X-ray Phase Contrast Imaging by Grating Interferometry

Dissertation

zur

Erlangung der naturwissenschaftlichen Doktorwürde
(Dr. sc. nat.)

vorgelegt der

Mathematisch-naturwissenschaftlichen Fakultät

der

Universität Zürich

von

Vincent Revol

aus

Frankreich

Promotionskomitee

Prof. Dr. Ulrich Straumann (Vorsitz)
Dr. Rolf Kaufmann (Leitung der Dissertation)

Zürich 2011

Die vorliegende Arbeit wurde von der Mathematisch-naturwissenschaftlichen Fakultät der Universität Zürich im 2011 semester SS 2011 als Dissertation angenommen.

Promotionskomitee: Prof. Dr. Ulrich Straumann (Vorsitz) and Dr. Rolf Kaufmann (Leitung der Dissertation).

SUMMARY

Conventional x-ray imaging methods rely on the measurement of the absorption of the radiation to produce an image of the sample studied. On the contrary, phase contrast x-ray techniques are based on the refraction of the beam inside the object. In the x-ray domain of interest to industrial and medical applications (photon energies from 10 to 100 keV), the interaction cross-sections underlying the refraction process can be up to three orders of magnitude higher than those of the absorption process. This is especially valid for elements of low density. For this reason, phase contrast techniques are expected to provide a significant contrast enhancement, in particular for low-absorbing materials such as biological soft tissues or plastics.

In the last decade, a method based on the Talbot-Lau grating interferometer was developed. It uses three x-ray gratings associated with an x-ray source and a digital detector. The method delivers, in a single acquisition, a phase contrast image as well as the conventional transmission image. In addition, a third image, called the scatter dark field, is obtained. The latter is sensitive to the small angle scattering of the wave caused by variations in the electron density which occur at a length scale smaller than the typical size of the detector pixels (for example, porosity in the sample). Thus, information on the microscopic structure of the specimen below the resolution limit can be gained.

With regards to an implementation in medical or industrial environments, the method is most promising. Indeed, the requirements in terms of spatial and temporal coherence of the used radiation are fulfilled by standard x-ray tube sources, as those found in the hospitals. Furthermore, grating interferometry is compatible with computed tomography. Thus, the three-dimensional geometry of the sample can also be reconstructed. However, additional demands of commercial applications (such as throughput, size of the field of view, robustness or dose efficiency...) still represent tough challenges for the instrumentation.

This manuscript is dedicated to the developments of concepts in view of an implementation of grating interferometry in functional environments. The work was carried out at the "Centre Suisse d'Electronique et Microtechnique" in Zürich. In a first phase, an experimental bench with specialized hardware and software was designed and built. Based on this platform, instrumental and methodological advancements could be tested together with the characterization of diverse grating configurations and the measurements of multiple samples. As summarized in the following paragraphs, important contributions could be realized in four complementary domains.

In terms of theory, a complete model of the underlying physical and geometrical effects is presented. It allows for the description of the contrast formation and, in particular, of the artifacts specific to grating interferometry. For each type of artifact, methods are reviewed or suggested to reduce their impact. A special emphasis is put on the quantitative analysis of the noise sources that occur during the acquisition process. Expressions of the signal-to-noise ratios for all three contrast mechanisms are derived and confirmed experimentally. These estimators are then used to compare phase contrast imaging (with a grating interferometer) to absorption-based imaging for a constant ionization dose.

Secondly, a series of methodological developments are proposed. Thus, an image reconstruction algorithm with improved robustness is demonstrated. The latter is particularly adapted to short acquisition times, as required in industry. Furthermore, a method is suggested, which allows, for instance, to determine the orientation of fibers in composite materials. This can be achieved with the help of a series of dark field images. Indeed, since the fibers (in this example) define a preferred direction in space, the small angle scattering displays an anisotropic pattern. Also, a specific gratings' configuration is presented, which is simultaneously optimized over two different x-ray energies domains. Thanks to such dual-energy measurements, information on the elemental composition of the object can be deduced.

From an instrumental point of view, the effort concentrates on the design of three additional grating interferometer configurations. Their characterization shows an enhancement of, respectively, the measurement sensitivity, the size of the field of view and the usable x-ray energies. A significant part of the work was dedicated to the testing of the different systems. This allowed to get a feedback on the gratings' quality and to optimize their fabrication processes.

Last but not least, the potential of phase contrast and scatter dark field imaging with regards to concrete applications is discussed. Indeed, although both methods provide fundamentally new insights into the object, this additional information may not systematically deliver a better diagnostic than conventional systems. For this purpose, a large number of representative samples are investigated. The results help to identify the most promising applications in medicine, non-destructive testing and security.

ZUSAMMENFASSUNG

Herkömmliche bildgebende Röntgensysteme nutzen die spezifische Absorption bzw. Transmission der Strahlung, um daraus ein Bild einer Probe zu gewinnen. Im Gegensatz dazu dient bei den sogenannten Phasenkontrastmethoden die physikalische Eigenschaft der Brechkraft bzw. Refraktivität als bildgebende Grösse. Die der Brechung zugrunde liegenden Wechselwirkungsquerschnitte harter Röntgenstrahlung (Photonenenergien von 10 bis 100keV) sind typischerweise mehrere Grössenordnungen grösser als jene der Absorption. Da dies insbesondere auch für leichte Elemente gilt, bietet sich Phasenkontrast an, gerade bei schwach absorbierenden Materialien den Bildkontrast erheblich zu verbessern.

Im vergangenen Jahrzehnt wurde eine Methode entwickelt, welche Phasenkontrast-Röntgenbilder auf dem Prinzip des Talbot-Lau Interferometers erzeugt. Das Prinzip der Methode basiert auf drei Beugungs- und Absorptionsgittern, welche zusammen mit einer Röntgenröhre und einem digitalen Röntgensensor verwendet werden. Die Methode liefert bei einer einzigen Aufnahme sowohl das Phasenkontrastbild als auch das herkömmliche Röntgenbild eines Objektes. Bemerkenswert ist, dass zudem ein drittes Bild gewonnen werden kann, das sogenannte Dunkelfeldbild. Für dessen Bildkontrast sind Variationen der Elektronendichte verantwortlich, welche sich auf einer Längenskala kleiner als die typische Grösse der Sensorpixel abspielen (z.B. Porosität). Auf diese Weise werden Struktureigenschaften weit unterhalb der Auflösungsgrenze abgebildet.

Hinsichtlich der Implementierung im medizinischen oder industriellen Bereich ist die Methode äusserst vielversprechend da die Anforderungen an die räumliche und zeitliche Kohärenz der verwendeten Strahlung durch konventionelle Röntgenröhren erfüllt sind. Dennoch stellen weitere Bedürfnisse kommerzieller Anwendungen, wie z.B. Probendurchsatz, Robustheit, Grösse des Bildfelds oder die Effizienz Herausforderungen dar, welchen die Technologie im aktuellen Stand nicht nachkommen kann.

Die vorliegende Arbeit beschäftigt sich mit der Entwicklung von Konzepten für die anwendungsspezifische Implementierung der Methode. Die Arbeit wurde am Centre Suisse d'Electronique et de Microtechnique SA (CSEM SA) in Zürich durchgeführt. In einer ersten Phase wurde ein Versuchsaufbau erstellt, für welchen spezifische Hardware und Software entwickelt werden musste. Mit diesem Aufbau wurden dann nebst den vielfältigen Messungen von Proben und der Charakterisierung der Gitterkonfigurationen vor allem die instrumentellen Weiterentwicklungen der Methode erarbeitet und getestet. In den folgenden Abschnitten wird präsentiert, wie wichtige Beiträge in vier Bereichen geleistet werden könnten.

Im theoretischen Teil der Arbeit wird ein Modell aufgebaut, welches die zugrunde

liegenden physikalischen Mechanismen, die Geometrie wie auch die Störeinflüsse berücksichtigt. Damit wurde eine präzise und realistische Beschreibung der Kontrastbildung erreicht, welche es erlaubt, die Ursachen bei der Entstehung von Bildartefakten zu ergründen. Ein spezieller Schwerpunkt bildet dabei die quantitative Untersuchung von Rausch- und Störsignalen, welche das Messverfahren mit sich bringt. Damit konnte die sogenannten signal-to-noise ratio (SNR) für alle drei Kontrastmechanismen vorhergesagt und anhand von Referenzmessungen experimentell bestätigt werden.

Anschliessend werden eine Reihe von methodischen Entwicklungen der Methode vorgestellt. So wurde ein robuster Algorithmus zur Bildrekonstruktion entwickelt, welcher die Möglichkeit für eine schnelle Datenaufnahme bietet. Das ist besonders für industrielle Anwendungen äusserst attraktiv. Weiter wurde eine Methode entwickelt, welche es unter anderem erlaubt, die Ausrichtung der Fasern in Faserverbundwerkstoffen zu bestimmen. Dies konnte mithilfe der Dunkelfeldaufnahmen erreicht werden, da sich die durch die Fasern verursachte Streuung in einer Anisotropie der Dunkelfeldaufnahmen niederschlägt. Zudem wird eine Gitterkonfiguration vorgestellt, welche gleichzeitig auf zwei unterschiedliche Energiebereiche der Röntgenstrahlung optimiert ist. Mithilfe solcher dual-energy Aufnahmen lassen sich Rückschlüsse auf die elementare Zusammensetzung der Materialien machen.

Im Zentrum der instrumentellen Weiterentwicklungen stehen drei Gitterkonfigurationen, welche in Bezug auf die Messempfindlichkeit, die Grösse des Bildfeldes und die verfügbare Röntgenenergie optimiert wurden. Die Messungen zur Charakterisierung dieser Gitter bzw. Gitterinterferometer lieferten wertvolle Rückschlüsse in Bezug auf die Optimierung der Herstellungsprozesse der Gitter.

Das letzte Kapitel befasst sich mit der Frage, inwiefern die Phasenkontrast und die Dunkelfeldbilder in der Lage sind, in den verschiedenen Anwendungen Informationen hervorzubringen, die über jene des klassischen Röntgens hinausgehen. Dazu wurde eine Reihe von Proben untersucht, welche für die verschiedenen Einsatzbereichen relevant sind. Die Ergebnisse tragen zur Identifizierung der vielversprechendsten Anwendungen in der medizinischen Diagnostik, der zerstörungsfreien Prüfung und Sicherheitsanwendungen bei.

RÉSUMÉ

Les systèmes de radiographie conventionnels se basent sur l'absorption des rayons X lors de leur propagation pour former une image de l'objet étudié. Par opposition, la radiographie par contraste de phase repose sur la mesure de la réfraction de l'onde dans le spécimen. Dans le domaine des rayons X dits "durs" (énergies des photons allant de 10 à 100 keV), la constante d'interaction du phénomène de réfraction est deux à trois ordres de grandeur supérieure à celle du processus d'absorption. Ceci est d'autant plus prononcé pour les éléments atomiques de faible densité. Par conséquent, une importante amélioration du contraste peut être attendue, précisément pour ces matériaux peu absorbants, tels que les tissus biologiques ou les plastiques.

Au cours de la dernière décennie, une méthode, basée sur l'interféromètre de Talbot-Lau, a été développée. Cette dernière s'appuie sur l'utilisation de trois réseaux pour les rayons X associés à une source et à un détecteur digital. Elle permet de réaliser simultanément la mesure de l'absorption et de la réfraction de l'onde. En outre, une troisième image, appelée image sur fond noir, est extraite, qui est liée à la diffraction aux petits angles des rayons X. Cette dernière est causée par des variations de la densité électronique, qui se produisent à l'échelle du micromètre, c'est-à-dire en dessous de la résolution des détecteurs standards (par exemple, de la porosité dans l'objet). Ainsi, une information, auparavant inaccessible, sur la microstructure de l'objet étudié est obtenue.

Pour ce qui est d'une implémentation dans le milieu médical ou industriel, cette méthode est particulièrement prometteuse. En effet, les contraintes sur la cohérence tant spatiale que temporelle de la radiation utilisée sont satisfaites par les tubes à rayons X standards, comme on peut en trouver dans les hôpitaux. D'autre part, l'interférométrie à base de réseaux est compatible avec la tomographie calculée, qui permet de reconstruire la géométrie de l'objet étudié en trois dimensions. Cependant, les contraintes additionnelles éxigées par les applications commerciales (la taille du champ de vue, le débit, la robustesse, l'utilisation efficace de la dose ionisante...) posent encore de sérieux défis pour l'instrumentation.

Ce manuscrit est consacré aux développements de concepts en vue d'une implémentation de l'interférence à base de réseaux dans un milieu fonctionnel. Le travail de thèse a été effectué au Centre Suisse d'Electronique et Microtechnique à Zürich, Suisse. Dans un premier temps, un banc de mesures comprenant un ensemble d'équipements et logiciels spécialisés a été conçu et construit. En se basant sur cette plateforme, des avancées aussi bien au niveau de l'instrumentation que des méthodes de mesure ont pu être testées en parallèle de la caractérisation des différentes configurations de réseaux et de l'inspection de nombreux échantillons. D'importantes contributions ont pu être réalisées dans quatres domaines complémentaires.

D'un point de vue théorique, un modèle complet des phénomènes physiques et géométriques sous-jacents cet instrument est présenté. Ce modèle permet de décrire la formation du signal et, en particulier, des artéfacts spécifiques à l'interférométrie à base de réseaux. Des méthodes sont revues et/ou suggérées pour réduire leur impact. L'accent est ensuite mis sur l'analyse quantitative des sources de bruit présentes lors du processus d'acquisition. Des expressions du signal-sur-bruit sont déduites et vérifiées expérimentalement pour les trois images obtenues. Ces estimateurs sont enfin utilisés pour comparer la sensibilité de la mesure par contraste de phase par rapport à celle par absorption.

En second lieu, de nouvelles méthodes de mesure sont proposées. Ainsi, un algorithme de reconstruction plus robuste est implémenté. Il permet de plus de réduire les temps d'acquisition, ce qui est particulièrement souhaitable dans de nombreuses applications industrielles. En outre, une nouvelle méthode est suggérée, qui permet, par exemple, de déterminer l'orientation des fibres dans un matériau composite. Cette information peut être extraite grâce à l'image sur fond noir. En effet, les fibres (dans cet exemple) définissent une direction privilégiée dans l'espace qui se reflète par une anisotropie de la diffraction aux petits angles. En complément, une configuration spécifique des réseaux est présentée, qui est optimisée simultanément autour de deux énergies différentes. Grâce à cette mesure à double énergie, une information sur la composition chimique de la matière peut être obtenue.

Pour ce qui est de l'instrumentation, les efforts sont concentrés sur la conception de trois configurations d'interféromètres additionnelles. Leurs caractérisations révèlent respectivement des améliorations de la sensibilité de la mesure, de la taille du champ de vue et des énergies des rayons X pouvant être utilisés. Le test de ces différents systèmes a permis en outre d'obtenir un retour sur la qualité des réseaux et d'optimiser leur processus de fabrication.

La dernière partie se focalise sur l'évaluation du potentiel de la radiographie par contraste de phase et sur fond noir en ce qui concerne des applications concrètes. En effet, bien que ces deux nouveaux outils offrent de nouvelles vues sur l'objet étudié, il n'est pas dit que l'information supplémentaire permette de fournir un diagnostic plus avancé qu'avec les systèmes conventionnels. A cette fin, un grand nombre d'échantillons représentatifs de différents champs d'applications sont inspectés. Les résultats permettent d'identifier les applications les plus prometteuses, que ce soit dans le domaine médical, de l'inspection non-destructive ou des contrôles de sécurité.

ACKNOWLEDGMENTS

This work was prepared at the Photonics Division of the Centre Suisse d'Electronique et Microtechnique (CSEM) directed by Dr. Nicolas Blanc. I would like to thank him and Dr. Claus Urban for offering me the possibility to accomplish this project in a motivating environment.

I would like to express my gratitude towards my academic supervisor, Prof. Dr. Ulrich Straumann from the Physics Institute of the University of Zürich, who always offered me his support and encouraged me to broaden my horizon through workshops and conferences.

I am honored that Prof. Dr. Mats Danielsson from the Royal Institute of Technology in Stockholm, Sweden and Dr. Ewald Roessl from Philips Research in Hamburg, Germany accepted to review this work.

I acknowledge the financial support from the Competence Center for Materials Science and Technology (CCMX) under grant Nr. 0206088.

A special thank goes to Rolf and Christian, my two x-ray colleagues at CSEM, for the time and energy that they dedicated to the supervision of this project. In a complementary manner, you both allowed me to develop my physical and technological understanding of numerous phenomena/devices. None of the results presented in this manuscript would have been achieved without your help.

The time I spent at CSEM has always been pleasant and enriching because I was surrounded by colleagues that made the meetings as well as the coffee breaks interesting. In particular, I would like to thank Barbara for the support and Edith and Hans-Ruedi with whom I shared my office during three years. Merci aussi à mes trois collègues doctorants, Dali, Christian et Lysandre pour les discussions passionantes pendant et en-dehors du travail.

Philippe Niedermann, Francis Cardot, Jean-Paul Morel et toutes les personnes de la Division Microsystems du CSEM impliquées dans la fabrication des réseaux ont réalisé un travail excellent, qui a contribué grandement au succès de ce projet. Merci.

Kurt Boesiger, Reto Meier und die Mitarbeiter der Werkstatt des Physik Institut der Universität Zürich haben mir geholfen, das mechanische Design des Aufbau zu realizieren. Ich werde die Hilfe und die gute Zusammenarbeit nicht vergessen.

Part of this work was realized in collaboration with the ”Eidgenössische Materialprüfungs- und ForschungsAnstalt” in Dübendorf. I would like to thank particularly Dr. Iwan Jerjen for the intense debates on differential phase contrast imaging as well as Dr. Thomas Lüthi, Dr. Philipp Schutz and Dr. Urs Sennhauser for their expertise on inspection techniques and materials.

I thank Prof. Dr. med. Caroline Maake, Prof. Dr. med. Thomas F. Lüscher, Christine Lohmann and all the rest of the collaborators from the University of Zürich for the collect and cross-analysis of the biological samples. I acknowledge also the help of Dr. Eva Knop from the Department of Community Ecology of the University of Bern for providing the snails.

For the study of composite materials, I would like to express my gratitude towards Prof. Dr. Philip Withers and Jordan Rouse from the University of Manchester as well as Dr. Michael Schulz and Oxana Weber from the Karlsruhe Institute of Technology for allowing me to access to interesting samples.

I acknowledge thankfully the work done by Graham Lang and Roger Cook that corrected this manuscript for misspellings and grammatical errors.

Finalement, je remercie tout particulièrement ma famille et mes amis, qui m'ont soutenu tout au long de cette thèse, malgré la distance. Et bien sur, ma Muriel avec qui j'ai partagè toutes les èmotions de la frustration jusqu' la joie, qui accompagnent le travail de recherche.

"Ils ont échoué parce qu'ils n'avaient pas commencé par le rêve" [William Shakespeare dans Hamlet].

CONTENTS

Summary **I**

Zusammenfassung **III**

Résumé **V**

Acknowledgments **VII**

1 Introduction **1**

1.1 Introduction to X-ray Imaging 1
1.2 Motivation 6
1.3 Extent of the Present Work 14

2 Grating Interferometer **17**

2.1 The Talbot-Lau Geometry 18
  2.1.1 Overview 18
  2.1.2 Beam-Splitter Grating and the Talbot Effect 19
  2.1.3 Sample and Interactions 25
  2.1.4 Analyzer Grating and Large Detector Pixels 30
  2.1.5 Source Grating and Standard X-ray Tubes 33
2.2 Image Reconstruction 40
  2.2.1 Phase Stepping Method 40

2.2.2 Image Content 44

2.3 Computed Tomography 46

2.3.1 Filtered Back Projection Algorithm 47

2.3.2 Absorption Tomography 51

2.3.3 Phase Tomography 53

2.3.4 Dark Field Tomography 54

3 Noise Analysis 57

3.1 Systematic Errors 58

3.1.1 Beam Hardening 58

3.1.2 Fixed Pattern Noise 61

3.1.3 Phase Wrapping and Clipping 63

3.1.4 Impact and Comparison 66

3.2 Stochastic Errors 73

3.2.1 Detector Quantum Noise 74

3.2.2 Mechanical Jitter Noise 79

3.2.3 Other Noise Sources 79

3.2.4 Experimental Confirmation 79

3.2.5 Differential Phase Contrast vs. Absorption Imaging 81

4 Instrumentation 87

4.1 Experimental Bench 87

4.1.1 Components of the Setup 88

4.1.2 Control and Acquisition Software 91

4.1.3 X-ray Gratings 93

4.2 Interferometer Design 97

4.2.1 Design Rules 97

4.2.2 Visibility Simulations 98

4.3 First Setup and Characterization 98

5 Developments and Applications 107

5.1 Advanced Imaging Methods 108

5.1.1 Moiré Fringes Reconstruction Method 108

5.1.2 Directional Dark Field Imaging 113

5.1.3 Dual Energy Phase Contrast Imaging 118

5.2 Improvements in the Instrumentation 119

5.2.1 Bent Grating Interferometer for Large Fields of View . . . 119

5.2.2 Improving the Phase Sensitivity 123

5.2.3 Increasing the Effective Energy 126

5.3 Applications 129

5.3.1 Medical Imaging 130

5.3.2 Non-Destructive Testing and Evaluation 137

5.3.3 Security and Screening 153

5.4 Summary and Conclusions 156

Outlook 161

A Medical Imaging: More Examples 163

B Non-Destructive Testing: More Examples 171

List of Symbols and Abbreviations 175

Bibliography 180

Curriculum Vitae 193

CHAPTER
ONE

INTRODUCTION

The work presented in this manuscript is dedicated to the use of an x-ray grating interferometer for phase contrast and dark field imaging. The progress realized in the instrumentation and methods will be presented as well as experimental results obtained for applications in the medical and industrial fields.

Before starting the description of this specific method, let us introduce some history and background on x-ray imaging. This will allow the reader to position x-ray grating interferometry into a global perspective and to understand its specificities compared to other imaging techniques. Secondly, scientific and industrial needs, which are not yet met by current technologies, will give a motivation for the research project. Finally, the tasks and accomplishments realized by this PhD thesis will be summarized.

1.1 Introduction to X-ray Imaging

X-ray discovery

Wilhelm Röntgen reported in 1896 about a new type of radiation ”capable of penetrating black cardboard which is quite opaque to ultra-violet light, sunlight, or arc-light” (Röntgen 1896). He summarized in these words one fundamental property of ”x-rays”, namely their high penetration depth in matter. For his research, he received the Nobel price in 1905 (Nob 1967). Other scientists like J. Hittorf, F. Sanford or I. Pulyui made similar observations but only Wilhelm Röntgen went through the systematic process of characterizing this new type of radiation. He also understood quickly that x-rays could be used for imaging

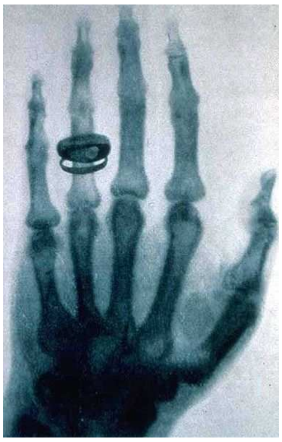

Figure 1.1: *One of the first X-ray photograph taken by Wilhelm Röntgen, which shows the hand of his wife acquired on a photographic plaque in December 1895*

purposes and started acquiring x-ray photographs, for example of the hand of his wife as shown in Figure 1.1. X-ray imaging was born.

Many measurement methods using x-rays appeared at the beginning of the 20^{th} century driven by the development of improved x-ray sources such as the Coolidge tube (Coolidge 1916) and new photosensitive elements. X-ray techniques are exceptionally rich in terms of variety and from the number of domains which can be addressed.

The purpose of the next paragraphs is to give an overview of the standard methods used for imaging purposes rather than providing an exhaustive description. The focus is put on x-ray imaging methods in a transmission geometry. In that configuration, the object to be studied is placed between the x-ray source and some kind of x-ray detector, which recovers information on the propagation of the beam within the sample.

In the x-ray energy domain of interest to industrial and medical applications (from 10 keV to 100 keV), the dominant interactions are photoelectric absorption, Compton (inelastic) scattering and coherent (elastic) scattering as shown in Figure 1.2 (Als-Nielsen & McMorrow 2001, Chap. 1).

Absorption-based X-ray Imaging

X-ray absorption-based imaging (ABI) was the first historical application suggested by Wilhelm Röntgen (Röntgen 1896) and is still nowadays the most widely used x-ray technique. The most important market segment is medical diagnostics, where it is used to detect a wide range of malignancy from bone fractures to tumors and atherosclerotic plaques. In the field of non-destructive testing and evaluation, ABI enables the quality control of manufactured goods in high end technologies, such as for aerospace and medical equipment. In a completely different application, it is present in the food chain to recognize packaging defects or contaminants. Finally, x-ray portals are implemented at borders (for instance

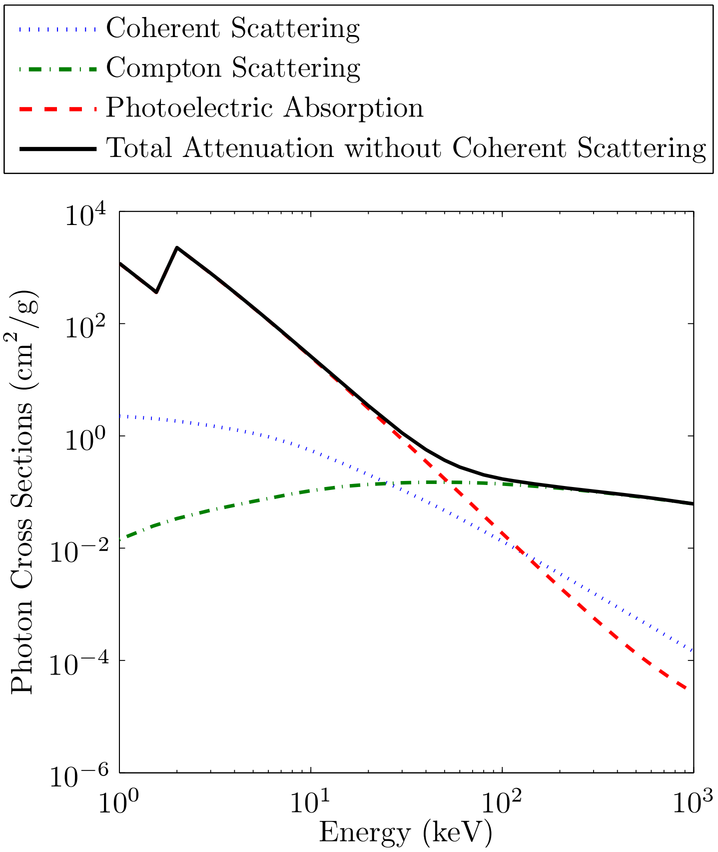

Figure 1.2: *Cross Sections of photoelectric absorption, Compton and Coherent Scattering in aluminum from the NIST database (Berger et al.).*

at airports) for the detection of explosives and illicit products in luggage and packages. Some examples of x-ray absorption-based imaging systems are shown in Figure 1.3.

ABI systems measure the decrease in the intensity I of the beam after propagation through the sample. The latter is given by the Beer-Lambert law (Als-Nielsen & McMorrow 2001, Sect. 1.3)

$$I = I_0 \exp(-\mu t) \tag{1.1}$$

Where I_0 is the intensity of the incoming wave, t is the object thickness and μ is the linear attenuation coefficient of the object, supposed to be homogeneous here.

The attenuation of the beam results from two different mechanisms. The photons are either absorbed by photoelectric absorption or deflected by Compton scattering away from the detector. In both cases, the detector records a decrease in the intensity of the pixel of interest. For this reason, the attenuation coefficient is usually expressed as

$$\mu = \mu_{pe} + \mu_{cs} \tag{1.2}$$

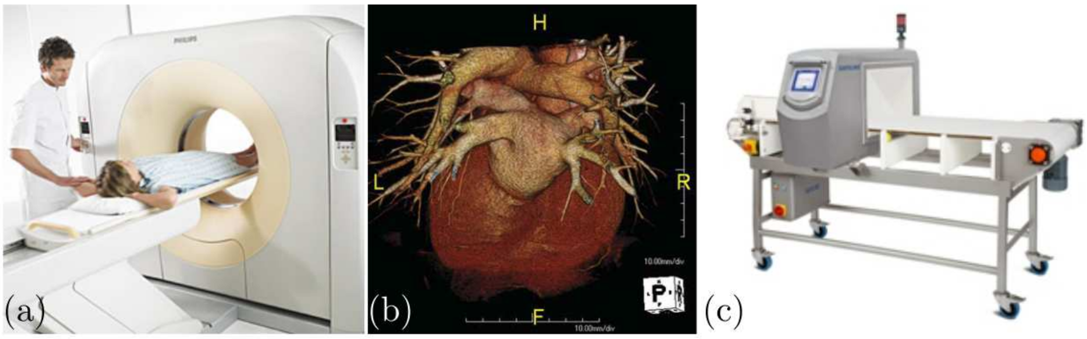

Figure 1.3: *(a) High-end dual energy computed tomography scanner from Philips. (b) Three-dimensional rendering of a human heart acquired by computed tomography (Wijesekera et al. 2010). (c) Scanning system from Mettler-Toledo for the detection of metal in packaged products.*

Where μ_{pe} represents the contributions from the photoelectric absorption and μ_{cs} from the Compton scattering. Photoelectric absorption is essentially dominant below 70keV (Figure 1.2) and μ_{pe} is in the first order proportional to Z^4/E^3, where Z is the atomic number and E the photon energy (Als-Nielsen & McMorrow 2001, Sect. 1.3). As a consequence from the strong dependence of the attenuation coefficient on the atomic number, a large contrast can be achieved between heavy and light elements, such as between bones (rich in Calcium) and soft tissues (rich in water).

Small Angle X-ray Scattering

Small Angle X-ray Scattering (SAXS) was invented later in the 20^{th} century. In contrast to absorption-based imaging, SAXS is a specialized inspection technique implemented for the study of colloids or inhomogeneities in metals, polymers or pharmaceuticals but also for the investigation of different kinds of fiber composite materials as illustrated in Figure 1.4-b for bones. Grating-based interferometry (as discussed later on in the thesis) enables the measurement of SAXS and could compete in some domains with existing technologies. For this reason, the principles of SAXS are introduced in the following paragraphs.

Similarly to Wide Angle X-ray Scattering (WAXS), which is commonly used in crystallography, Small Angle X-Ray Scattering (SAXS) is based on the measurement of the scattering pattern of a collimated beam impinging on the sample (see Figure 1.4-a). The angular deviations of interest in SAXS are however much smaller (below 1°) and call for a detector with smaller pixels and/or a larger distance between the sample and the detector.

The scattering angle, and consequently the scattering pattern, is related to the autocorrelation function of the electron density (Kak & Slaney 1999, Chap. 1). The angular deviation depends on the length scale of the electron density varia-

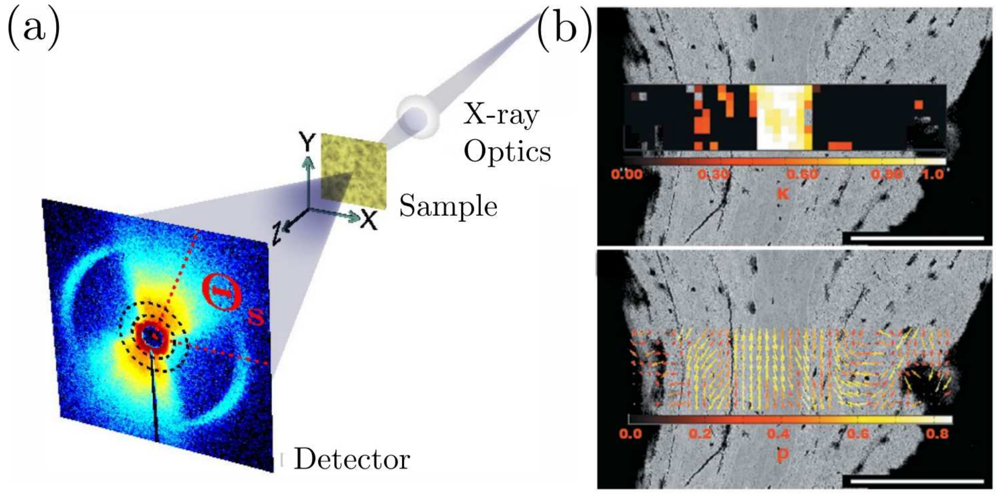

Figure 1.4: *(a) Standard setup for the measurement of Small Angle X-ray Scattering from (Bunk et al. 2009). (b) Example of the reconstruction of the anisotropic scattering intensity (top) and orientation (bottom) for a thin slice of bone (from (Gourrier et al. 2010).*

tions[1] while the intensity of the scattered beam depends on the density, size and composition of the inhomogeneities. In SAXS, the range of recorded scattering angles corresponds to inhomogeneities at a length scale of 1-100nm, much below the spatial resolution of x-ray absorption-based imaging systems.

Note that the phenomenon described above is a consequence of the elastic scattering of each atom, which sums up coherently for given directions in space depending on the electron density distribution. For example, a sample composed of fibers oriented along a given direction $\mathbf{P}$ will scatter more in the plane perpendicular to $\mathbf{P}$. So, not only can the density and size of the inhomogeneities be recovered but also their shape and preferred orientation.

The drawback of existing equipment based on laboratory x-ray tube sources lies in the high demand on the spatial coherence of the beam impinging on the sample. Most often, a collimator is used to form either a point or line source, which strongly reduces the photon flux and limits SAXS to niche applications with thin samples.

---

[1] The smaller the length scale of the electron density variations, the larger the scattering angle.

1.2 Motivation

Although x-ray absorption-based imaging is a standard tool for the inspection of the inner structure of objects, it suffers from a lack of sensitivity, especially for samples composed of simultaneously light and dense materials. The radiologist is indeed then confronted with a dilemma. Due to the highly absorbing elements, the x-ray energy must be high in order to penetrate through. At the same time, the linear absorption coefficient drops quickly with the energy and the light elements then become hardly detectable. For example, in medical imaging, the contrast is excellent for bones but insufficient in many cases to resolve features of biological tissues like tendons. Contrast agents can be employed, which fix specifically to target tissues[2] and thus allow the lack of sensitivity to be overcome. However, such agents are usually made of heavy elements, which cause undesired secondary effects for the patient.

More generally, there is a need from industry and medicine for an increase in the sensitivity of x-ray imaging. Other techniques like Magnetic Resonance Imaging (MRI) (Hendee & Morgan 1984), Single Photon Emission Computed Tomography (SPECT) or Positron Emission Tomography (PET) do provide an excellent sensitivity, and selectivity in the case of SPECT and PET. These technologies, as well as ultrasonic imaging, compete nowadays with the x-ray technology. The main advantage of x-ray imaging lies however in its polyvalence. It offers indeed a good spatial resolution and a simple measurement process at a relatively low cost.

In the second half of the last century, phase sensitive methods, which measure the phase shift of the x-ray beam within the sample instead of its absorption, received a growing interest. The reason is that, if the index of refraction is written in its complex form $n = 1 - \delta + i\beta$ (Als-Nielsen & McMorrow 2001, Chap. 3) with δ the refraction coefficient and β the extinction coefficient, δ is larger by two to three orders of magnitude compared to β. The interaction cross sections of X-ray absorption and phase shift are shown in Figure 1.5 at 5keV, 10keV, 20keV and 40keV. It can thus be seen that the phase contrast cross section is much larger, especially for elements with low atomic numbers and at high x-ray photon energies. As an example, the propagation of a monochromatic beam of energy 20keV through 25.7µm of silicon results in an absorption of only 0.026 but a large phase shift of π. Phase contrast imaging thus tries to take advantage of this difference in order to improve the measurement sensitivity.

Even though phase sensitive microscopy with visible light was already discovered in 1931 by Zernike (Zernike 1934), the first phase-sensitive x-ray instrument was invented by Bonse et al. "only" in 1965 (Bonse & Hart 1965). This delay

---

[2] Typical applications are angiography or urography.

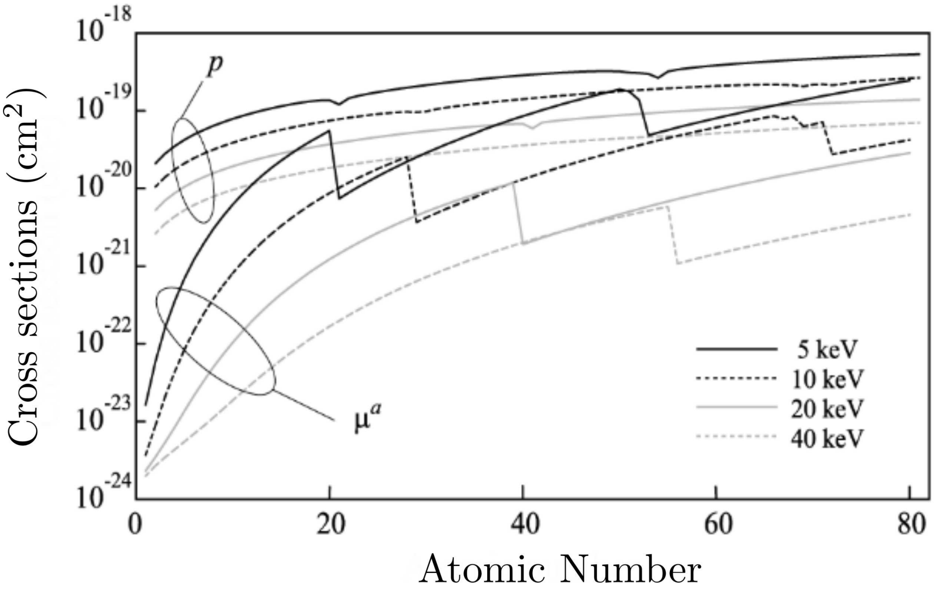

Figure 1.5: *Interaction cross sections of X-ray absorption (μ^a) and phase shift (p) as a function of the atomic number for x-ray energies of 5, 10, 20 and 40keV (from (Momose et al. 2001)).*

stems from the difficulty to design and produce proper x-ray optics (for instance, lenses with short focal length)[3] as well as from the nonexistence at that time of quasi-monochromatic x-ray sources with large photon flux. In contrast to lasers (monochromatic and collimated light) in the optical domain, standard x-ray tube sources produce photons over a wide-band energy spectrum and have limited photon flux.

Much progress was then triggered by the emergence of synchrotron light sources of the third generation in the eighties, which have a high brilliance and a low divergence angle (see Figure 1.6). Nearly monochromatic radiation could then be achieved with a reasonable photon flux by the insertion of crystal monochromators in the beam.

The various phase-sensitive methods can be separated into five categories, namely crystal interferometry, propagation-based imaging, analyzer-based imaging, grating-based projection imaging and grating-based interferometry.

Crystal Interferometry

Crystal interferometry was invented by Bonse et al. in 1965 (Bonse & Hart 1965).

---

[3] The index of refraction is indeed very close to one. Thus, the refraction occurs at very small angles (in the order of millidegrees) compared to visible light.

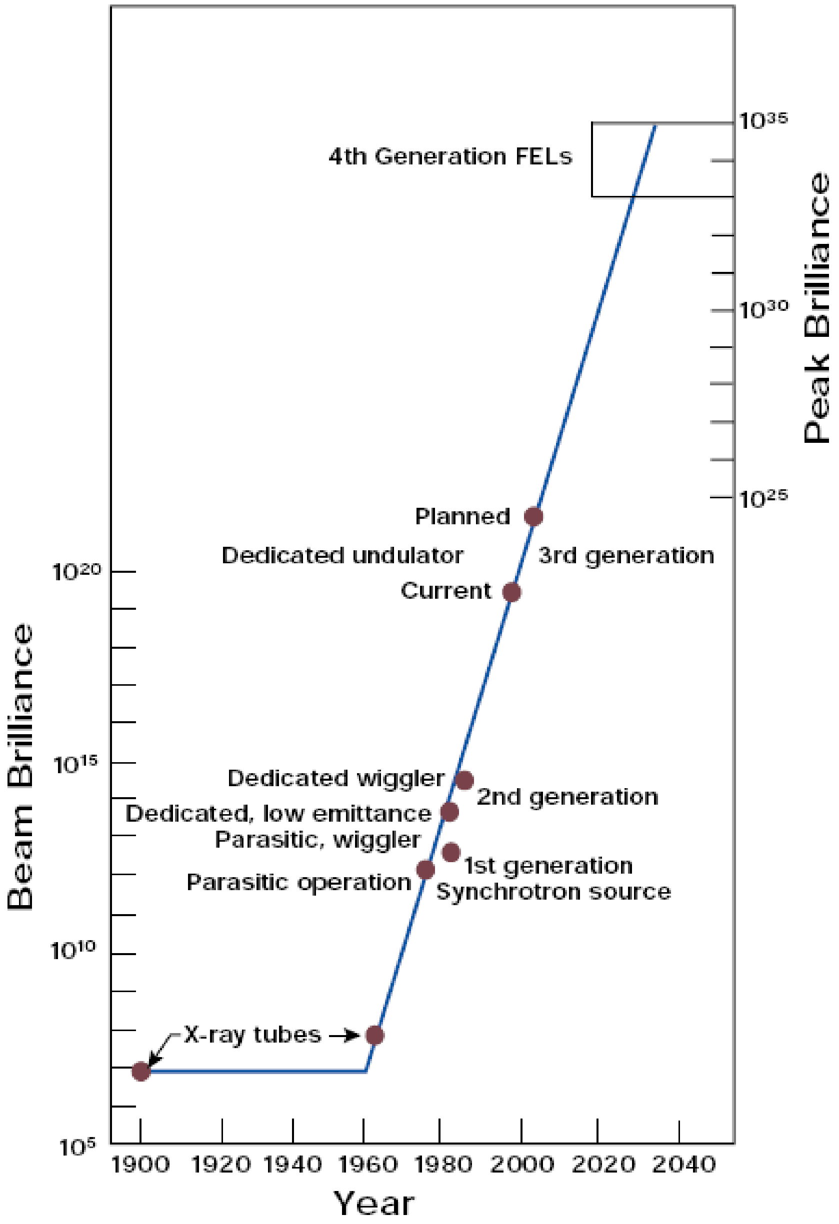

Figure 1.6: *History of (8-keV) x-ray sources. Beam brilliance vs. time.* Courtesy of David E. Moncton, Argonne National Laboratory

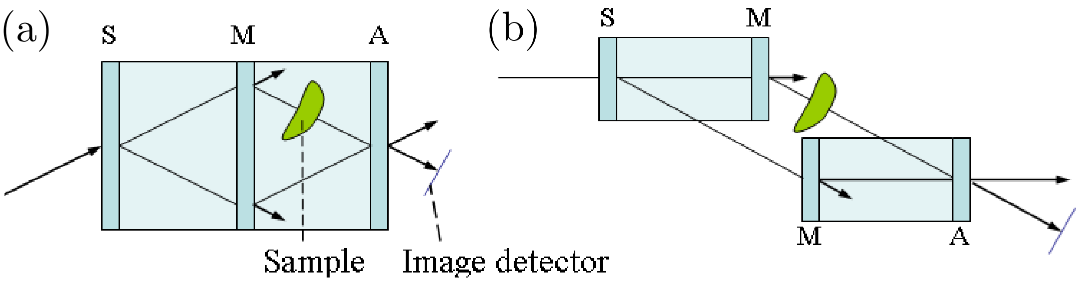

Figure 1.7: *(a) Monolithic LLL crystal interferometer and (b) interferometer consisting of two separated crystal blocks (from (Momose 2003)).*

It consists of three perfect silicon crystals placed in a Laue geometry as shown in Figure 1.7-a. The first crystal (S) acts as a beam splitter and divides the incoming beam into two beams. The second (M) reflects the two beams, which are finally recombined by the analyzer crystal (A). The sample, placed in one of the arms of the interferometer, induces a phase shift of one beam relative to the other and, consequently, an interference pattern is recorded on the x-ray detector. A phase shifting method is used to reconstruct the phase image and Computed Tomography can be implemented to get a full three-dimensional mapping of the refraction coefficient δ (Momose 1995).

The phase sensitivity of this method is excellent and impressive results could be demonstrated for medical applications (Momose *et al.* 1996; Takeda *et al.* 2000). This technique suffers however from some drawbacks. First, a large part of the photon flux is lost due to the different beam splitting stages as well as due to the crystals, which act as a monochromator in such a way that only a narrow energy band contributes to the contrast formation. Secondly, the field of view is actually limited to $7{\times}7$ cm^2 since the three crystals are cut out of a single silicon ingot and can hardly be made larger.

Another configuration was implemented based on two separated crystal blocks, which allows for a larger field of view (see Figure 1.7-b) (Yoneyama *et al.* 2002). The requirements on the alignment of the two blocks are however extremely high, which makes this system impractical for industrial applications.

Propagation-based Imaging

Propagation based imaging was introduced and developed by different groups at the end of the 20^{th} century (Snigirev *et al.* 1995; Wilkins *et al.* 1996; Nugent *et al.* 1996; Cloetens *et al.* 1996). Its principle is fairly straightforward since it consists in the observation of the intensity pattern at a distance d from the object and does not use any optical element (see Figure 1.8). In the Fresnel region, interference fringes appear which are related to the Laplacian of the phase shift (Bronnikov 2002). It is thus not a direct measurement of the phase shift of the wave in contrast to crystal interferometry.

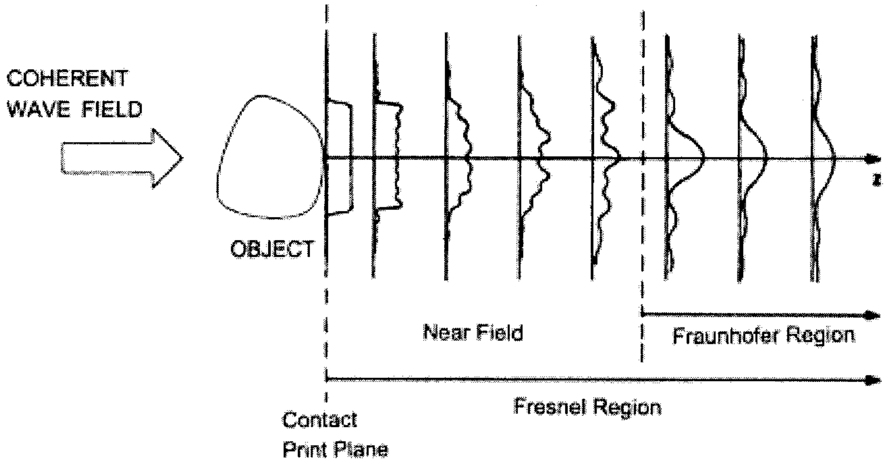

Figure 1.8: *Principle of Propagation-Based Imaging (from (Bronnikov 2002)). The intensity pattern at large distances from the object contains information on the phase shift in the object due to Fresnel diffraction.*

This method requires a high degree of spatial coherence and can only be implemented with synchrotron radiation or micro-focus x-ray tubes[4]. It however does not call for monochromatic radiation. This technique can be used in edge-enhancement mode, where a single acquisition is required (Lewis *et al.* 2005). Quantitative information on the refraction coefficient can also be recovered under some conditions by recording the intensity on different planes downstream of the object and applying specific reconstruction algorithms (Cloetens *et al.* 1996; Bronnikov 2002).

Due to its simplicity, propagation-based imaging was the first technique implemented into industrial products with a micro-focus x-ray tube. Such x-ray sources have however a weak photon flux[5] and the phase sensitivity of the method is relatively low.

Analyzer-based Imaging

Analyzer-based imaging, also called diffraction enhanced imaging, relies on the formation of a collimated beam by a single or double crystal monochromator. The latter impinges, after propagation through the sample, on an analyzer crystal. (Ingal & Beliaevskaya 1995) suggested to use a Laue geometry to detect simultaneously the transmitted and diffracted beam as shown in Figure 1.9-a. The

---

[4] Micro-focus x-ray tubes are x-ray tube sources with a focal spot of the order of some microns or tens of microns.

[5] The photon flux is limited by the heat generated by the deceleration of the electrons in the anode. Cooling and a rotating anode can be employed to evacuate or distribute the heat but for the same technology, the photon flux is roughly proportional to the focal spot size (Krestel 1990).

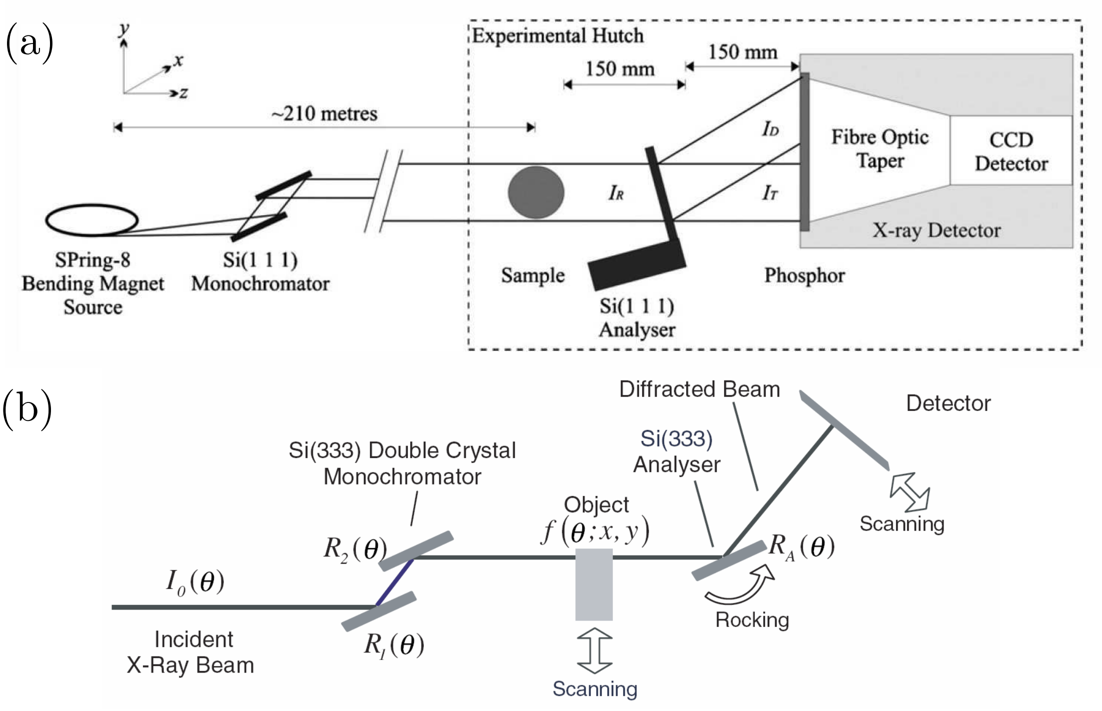

Figure 1.9: *Analyzer-based imaging in the (a) Laue configuration (from (Kitchen et al. 2011)) and (b) Bragg configuration (from (Wernick et al. 2003)).*

absorption and phase (refracted beam) can then be reconstructed as described in (Kitchen *et al.* 2008; Kitchen *et al.* 2011).

An alternative method consists in using the crystal in Bragg reflection as depicted in Figure 1.9-b (Chapman *et al.* 1997). Since the reflectivity is highly dependent on the angle of incidence (so-called rocking curve), the intensity recorded on the detector is extremely sensitive to the refraction of the beam in the sample. By varying the orientation of the crystal, the absorption and refraction effects can be separated (Chapman *et al.* 1997; Kitchen *et al.* 2007) as well as ultra small angle scattering (Wernick *et al.* 2003). Note that, since the refraction angle is linked to the derivative of the phase shift of the beam, analyzer-based imaging delivers a differential measurement.

Analyzer-based imaging has a high phase sensitivity, although only along one direction[6]. It can be implemented with x-ray tube sources but, since the beam has to be made monochromatic, the useful photon flux is limited.

Grating-based Projection Imaging

Grating-based projection imaging uses an absorbing grating placed in front of

---

[6] From Figure 1.9, it can be seen for example that the analyzer-based imager is only sensitive to refraction along direction y.

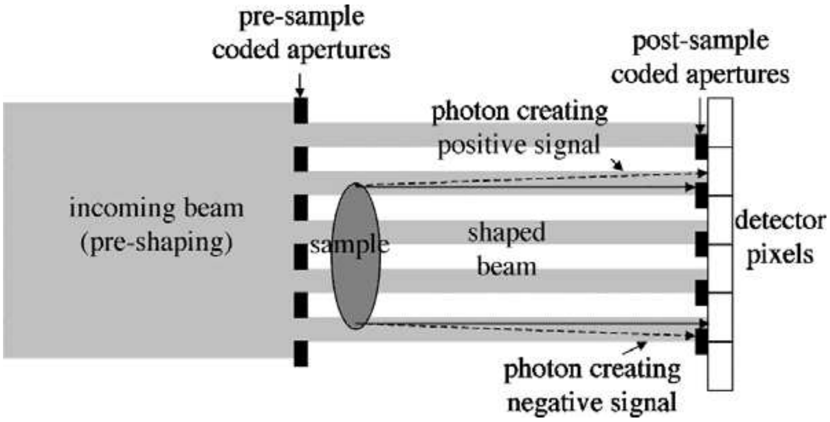

Figure 1.10: *Principle of grating-based projection imaging (from (Olivo & Speller 2007b)).*

the object. Thus, the grating forms an intensity pattern by shadowing part of the beam. Due to the refraction of the beam in the sample, the intensity fringes will be translated by an amount proportional to the refraction angle (hence, to the derivative of the phase shift of the beam). This translation can either be recovered directly if the pixel size is much smaller than the pattern periodicity (Wen *et al.* 2008; Wen *et al.* 2009), by inserting another absorbing grating in front of the detector (Olivo & Speller 2007b; Olivo & Speller 2007a) or, as was suggested more recently, by aligning the detector pixel precisely with the intensity pattern (Krejci *et al.* 2010a; Krejci *et al.* 2010b).

Grating-based projection imaging is thus a differential method, which can be implemented with two-dimensional gratings in order to detect refraction along two directions (Olivo *et al.* 2009). Polychromatic sources can be employed without loss of sensitivity. One of its main drawbacks is that it requires a good spatial coherence of the radiation[7]. Thus, x-ray tube sources with small focal spots have to be used, which limits the usefulness of the technique in industrial applications.

Grating-based Interferometry

Grating-based interferometry was introduced for visible light in 1971 by Lohmann and Silva (Lohmann & Silva 1971) and then translated to the x-ray domain (Clauser 1998; David *et al.* 2002; Momose 2003; David & Weitkamp 2006; David & Pfeiffer 2008). Similarly to the previous method, the contrast formation is based on the formation of an intensity pattern thanks to a transmission grating. However, this time the pattern stems from interferences (and not a projection of the absorption grating) resulting from the diffraction of the beam by a phase grating[8]. This so-called Talbot effect was already described by H. Talbot in 1836

---

[7] Although, this depends strongly on the exact periodicities and distances.

[8] A phase grating induces periodic modulations of the phase front without absorbing the

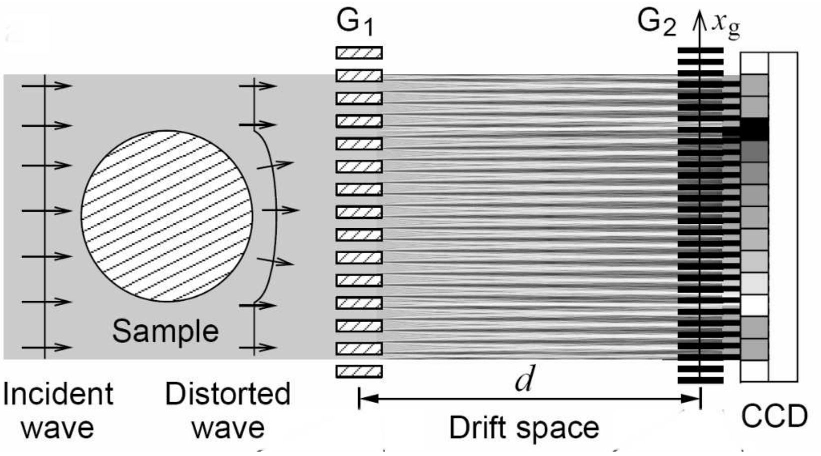

Figure 1.11: *Principle of grating-based interferometry (from (Weitkamp et al. 2005)).*

for visible light (Talbot 1836).

The displacement of the intensity pattern due to the sample can either be recorded directly with a high resolution x-ray detector (Takeda *et al.* 2007) or by means of an analyzer grating (Weitkamp *et al.* 2005) and leads to a differential measurement of the phase shift of the beam. Ultra small angle scattering can also be extracted simultaneously (Pfeiffer *et al.* 2008). Although the requirements in terms of spatial coherence are high, an absorption grating can be introduced in front of the x-ray source, which decouples the focal spot size from the spatial coherence requirements (Pfeiffer *et al.* 2006). Thus, conventional, high power, x-ray tubes with large focal spots and polychromatic spectra can be employed (Kottler *et al.* 2007b).

One- or two-dimensional gratings can be used to extract the phase derivative along two directions (Kottler *et al.* 2007a; Zanette *et al.* 2010). This method is compatible with computed tomography (Pfeiffer *et al.* 2007) and scanning setups (Kottler *et al.* 2007c).

Industrial Needs and Requirements

The goal of the research project is to transfer phase sensitive imaging from the laboratory to industrial or medical environments. This presents two challenges.

First, the successful method must provide an added value to standard imaging systems. This can be a significant improvement in the contrast for current applications. For example, the visualization of soft tissues in medical imaging. It can also be the combination of new modalities with standard contrast mechanisms. Here, we think of the simultaneous acquisition of absorption, refraction and ultra small

---

radiation.

angle scattering. This additional information could benefit known x-ray inspection tasks, or could be used to address new applications, previously unachievable with absorption-based radiography.

On the other hand, industrial requirements in terms of throughput, stability, dose efficiency, reliability, object size or cost must be met. The latter already exclude all techniques based on synchrotron radiation as well as those with a limited x-ray flux.

To our knowledge, among the phase sensitive methods presented above, grating-based imaging with a Talbot-Lau interferometer (Pfeiffer *et al.* 2006) has the highest potential to be successfully implemented in industrial environments. Grating-based interferometry is indeed compatible with conventional x-ray tube sources with large focal spots and polychromatic spectra. It provides three different contrast mechanisms within one acquisition and displays a good phase sensitivity. Moreover the requirements in terms of stability, although not trivial, are manageable.

Nevertheless, many challenges are still to be solved and new ideas to be proposed in order to make a success story out of this method. On the instrumentation side, the range of usable x-ray energies and the size of the field of view must be increased. In addition, the reproducibility and quality of the grating production process involves large efforts in process engineering. From the point of view of the data treatment, new methods have to be proposed to correct for artifacts and distortions and to extract all possible information out of the measurements. Finally, applications with a high potential must be found. This calls for the screening of a large variety of samples of different compositions for the identification of the most promising.

1.3 Extent of the Present Work

The research carried out in this thesis took place in the facilities of the "Centre Suisse d'Electronique et Microtechnique" (CSEM SA) in Zürich. Part of it was funded by the Competence Center for Materials Science and Technology (CCMX) under grant Nr. 0206088 and done in association with the "Eidgenössische Materialprüfungs- und ForschungsAnstalt" (Empa).

The first task consisted of the design and construction of an experimental bench for the testing of different grating interferometers as reported in Chapter 4. This included the selection and commissioning of the setup components (x-ray source, detector, positioning and alignment stages) and the conception of a mechanical model using Solidworks (drawings of interface parts). The control and acquisition software was developed in the Labview framework while the reconstruction algorithms and simulation tools were programed with Matlab. Finally, the x-ray gratings were fabricated at CSEM in Neuchâtel with our support and feedback.

Secondly, the theory of contrast formation and noise propagation was investigated (Chapters 2 and 3). The model allows for explaining the artifacts present in the image. Methods to reduce those artifacts are discussed and experimentally demonstrated. Furthermore analytical formulae for the noise contributions were derived and confirmed experimentally. A criterion is presented to compare phase contrast imaging to absorption-based radiography taking into account the radiation dose received by the sample.

From the experimental point of view, a large effort was invested in the characterization of the different grating interferometers (Chapter 4). Notably, the testing of the quality of the x-ray gratings (more than 100 configurations tested) was of prime importance in order to provide feedback to the process engineers and improve the fabrication processes. Moreover improvements in the instrumentation and in the measurement methods were suggested and demonstrated. They enable, for example, grating interferometry to be done with a large field of view or to extract new information on materials with fibers (Chapter 5).

Finally, a large variety of test specimens were investigated and analyzed, from human organs to explosives and aluminum weld. The measurements covered applications in the fields of medical imaging, non-destructive testing and security screening. This allows for the identification of the applications, for which differential phase contrast imaging with a grating interferometer has the highest potential. The conclusions are summarized in the second half of Chapter 5.

Part of the work presented in this thesis could be published in peer-reviewed journals. Notably, the results of Sections 3.2, 3.1.4, 5.1.3, 5.2.1, 5.2.2 and 5.3.2 have been published or submitted to journals (Revol *et al.* 2010c; Jerjen *et al.* 2011; Kottler *et al.* 2010b; Revol *et al.* 2011b; Revol *et al.* 2011a). Other research outcomes were published in conference proceedings (Revol *et al.* 2010b; Revol *et al.* 2010a; Jerjen *et al.* 2010; Kottler *et al.* 2010a; Kottler *et al.* 2010c).

CHAPTER

TWO

GRATING INTERFEROMETER

This chapter is dedicated to the contrast formation in grating interferometry. It provides information and notations which will be required for the understanding of the following chapters. It is inspired by publications that have been produced by different groups over the last decade but were revisited in order to offer a consistent model. It should be emphasized here that such a model is not to be found in any textbook and that much effort was devoted to its completion.

Section 2.1 starts with an overview, which should provide a rough understanding of the method studied, and then deepen into the impacts of each element of the grating interferometer. It is intended for the reader to come back to these parts later in the text when confronted with diverse observations.

Section 2.2 deals with the data analysis required for the reconstruction of the desired images of the transmission T, differential phase contrast DP and dark field V signal. Examples are provided which allow the reader to intuitively understand the information contained in these three images.

Finally, in Section 2.3, the basis of computed tomography will be presented, which allows for the reconstruction of three-dimensional information from a series of two-dimensional projections acquired under different viewing angles. It will be seen that all three contrast mechanisms can be combined with a tomographic approach.

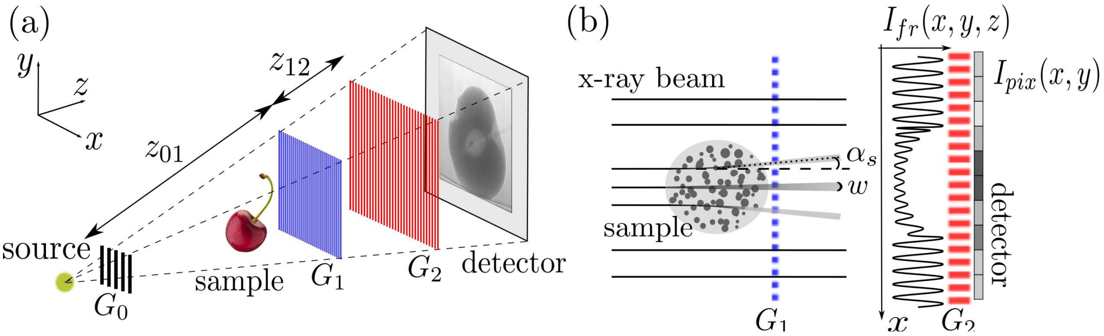

Figure 2.1: *(a) Talbot-Lau grating interferometer with an x-ray source and an x-ray detector supplemented by three x-ray gratings, called the source grating G_0, the beam-splitter grating G_1 and the analyzer grating G_2. The distances are z_{01} between G_0 and G_1 and z_{12} between G_1 and G_2. (b) The modulations of the wavefront induced by G_1 result in an interference pattern I_{fr} downstream of G_1. The local changes of the interference pattern due to the sample (attenuation, angular deviation α_s and beam broadening w) can then be recorded on the detector with the help of grating G_2.*

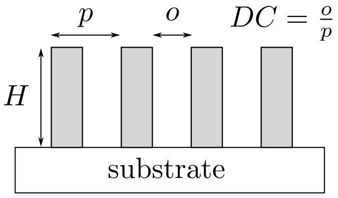

Figure 2.2: *Definition of the periodicity p, depth H and duty cycle DC for a rectangular grating.*

2.1 The Talbot-Lau Geometry

2.1.1 Overview

Grating interferometry in the x-ray domain was first introduced and developed in parallel by two research groups at the beginning of the 21^{st} century (Clauser 1998; David *et al.* 2002; Momose 2003; Momose 2005; Weitkamp *et al.* 2005; David & Weitkamp 2006; Pfeiffer *et al.* 2006; David & Pfeiffer 2008; Pfeiffer *et al.* 2008). Figure 2.1-a shows a schematic overview of the Talbot-Lau interferometer. The instrument consists of a conventional x-ray source, an x-ray detector and three x-ray gratings G_0, G_1 and G_2 with periodicities p_0, p_1 and p_2, depths H_0, H_1 and H_2 and duty cycles DC_0, DC_1 and DC_2,respectively. The definition of the periodicity, depth and duty cycle for a one-dimensional grating can be found in Figure 2.2.

The phase sensitive part consists of the beam-splitter grating G_1 and the analyzer grating G_2. G_1 (Figure 2.1-a) is a phase grating, which induces periodical phase modulations on the x-ray wavefront and acts as a beam-splitter. The divided beams then interfere downstream of G_1 and an intensity pattern I_{fr} is produced in the plane of G_2.

G_2 is an absorbing mask with a periodicity matching that of the interference fringes. Depending on the position of G_2 relative to the interference pattern, a varying amount of radiation is transmitted and recorded by the x-ray detector. Thus, for a given position of G_2, any change in the intensity modulations (for example, of the mean, amplitude or position) locally induces a change of the intensity I_{pix} recorded by the corresponding pixel of the x-ray detector. Note that G_2 is only required since the periodicity of the interference fringes, in the order of some microns, is much smaller than the pixel size of conventional x-ray detectors, which is in the order of some tens of microns.

Now, the beam propagation is modified in the presence of a sample mainly due to attenuation, refraction and ultra-small angle scattering and translates into changes in the intensity modulations as shown in Figure 2.1-b (attenuation, angular deviation α_s and beam broadening w). Diverse reconstruction methods are used to decouple the different contributions and extract three images. The transmission image (T) is linked to the absorption in the sample. The differential phase contrast image (DP) is proportional to the deflection angle α_s after refraction in the sample. And, in the end, the dark field image (V) reflects the ultra-small angle scattering produced by the inhomogeneities in the sample at the micron-scale (i.e. below the detector resolution).

Finally, the source grating G_0 is an absorbing grating used to transform the large focal spot into a series of line sources, which are individually coherent but mutually incoherent. Thus, G_0 allows for the grating interferometer to function with conventional high-flux x-ray tube sources. The role and influence of each parameter introduced in this overview will now be discussed in detail in the following paragraphs.

2.1.2 Beam-Splitter Grating and the Talbot Effect

Before starting to explain the fundamental role played by the beam-splitter grating G_1, let us lay down the assumptions made in this thesis. It is assumed that all media of interest here are dielectric, optically linear (no wave-mixing effect), isotropic (independent of the direction of polarization of the wave) and non-magnetic. Such media are characterized by a complex index of refraction $n = 1 - \delta + i\beta$. δ is defined here as the refraction coefficient and indicates the phase speed while the extinction coefficient β reflects the amount of absorption loss during the propagation. These assumptions allow us to use the scalar diffraction theory as introduced in (Goodman 2005, Sect. 3.2 and 3.3). Monochromatic electromagnetic waves of wavelength λ are modeled by a scalar field $u(\mathbf{r}, t) = Re\Big[U(\mathbf{r})\exp\big(-i2\pi\frac{c}{n\lambda}t\big)\Big]$, where c is the speed of light and t is the time. The complex amplitude $U(\mathbf{r})$ must satisfy the time-independent Helmholtz

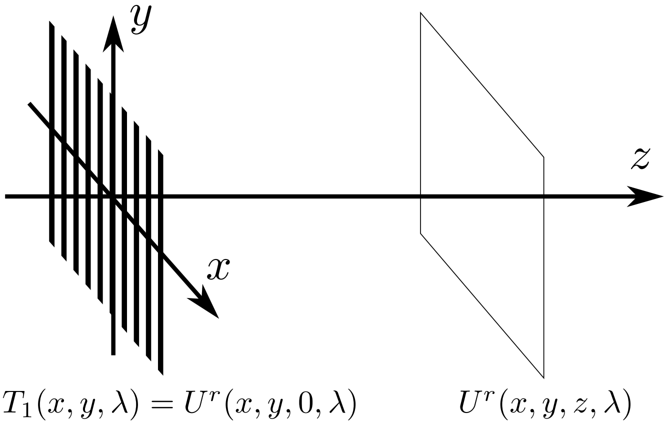

Figure 2.3: *Schematic view of the field propagation. A unit wave of wavelength λ is impinging onto a grating defined by its amplitude transmission function $T_1(x,y\lambda)$. After propagation along the optical axis z, the field is called $U^r(x,y,z,\lambda)$.*

equation

$$(\nabla^2 + k^2)U = 0 \tag{2.1}$$

Where $k = 2\pi/\lambda$ is the wave number.

So, let us consider the ideal case of a monochromatic plane wave of unit amplitude and wavelength λ incoming perpendicularly onto G_1. The grating G_1 consists of a periodical structure, either in one or two dimensions, which induces modulations either of the beam intensity or of the wavefront. In the first case, we will talk about an absorption grating while we refer to a phase grating in the second case.

In the following work, we restrain to one-dimensional gratings, which vary along the x-direction as drawn schematically in Figure 2.3, where the coordinate system is defined. Most of the results can however be extended to two-dimensional gratings without qualitatively changing the conclusions.

The periodical complex amplitude transmission function of G_1 can be expressed as a Fourier series

$$T_1(x,y,\lambda) \widehat{=} \sum_{\ell} B_\ell(y,\lambda) \exp(-i2\pi\frac{\ell x}{p_1}) \tag{2.2}$$

Where p_1 is the period of G_1 and B_ℓ are the complex Fourier coefficients, which depend on the exact shape of the grating . $\widehat{=}$ will be used in all the manuscript to indicate that this equation has the value of a definition. The electrical field $U^r(x,z,\lambda)$ at a distance z downstream of G_1 (see Figure 2.3) can be calculated using the Fresnel diffraction formula under its convolution form by (Goodman 2005,

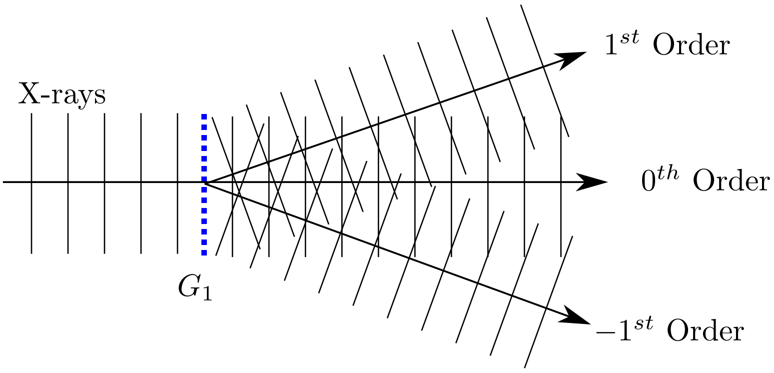

Figure 2.4: *Schematic view of the beam-splitting downstream of grating* G_1. *In the case of* $\pi/2$*-phase gratings, the energy is essentially divided in orders* 0 *and* ± 1.

Sect. 4.2):

$$\begin{aligned} U^r(x,y,z,\lambda) &= T_1(x,y,\lambda) * H_d(x,z,\lambda) && (2.3)\\ \text{with } H_d(x,z,\lambda) &= \frac{\exp(i2\pi z\lambda)}{i\lambda z}\exp\big(\frac{i\pi x^2}{z\lambda}\big) && (2.4)\end{aligned}$$

Where H_d is called the Fresnel kernel and $*$ is the convolution operator. Note that the Fresnel formula is valid under the sufficient condition $\pi p_1^4/4\lambda z^3 \ll 1$ (see (Goodman 2005, Sect. 4.2)). Typical values are $z \sim 10\,\mathrm{cm}$, $p_1 \sim 3\,\mu\mathrm{m}$ and $\lambda \sim 0.06\,\mathrm{nm}$ so that $\pi p_1^4/4\lambda z^3 \sim 10^{-9}$.

Combining Equations 2.2 and 2.3, it can be deduced that

$$U^r(x,y,z,\lambda) = \exp\big(i2\pi\frac{z}{\lambda}\big)\sum_\ell B_\ell(y,\lambda)\exp\big(-i\pi\frac{\lambda z}{p_1^2}\ell^2\big)\exp\big(i2\pi\frac{\ell x}{p_1}\big) \tag{2.5}$$

This expression can be interpreted as the superposition of waves propagating at different angles or orders (hence the name of "beam-splitter grating") as illustrated in Figure 2.4 (Hecht 2002, Sect. 10.2). Depending on the exact shape and nature (phase or absorption grating), the energy distributes differently between the different orders. In any case, for coherent waves, the superposition of waves induces interferences, which result in intensity modulations at some positions downstream of grating G_1.

Practically, the intensity can be calculated from Equation 2.5 as

$$\begin{aligned} I^r_{fr,par}(x,y,z,\lambda) &\widehat{=} |U^r(x,y,z,\lambda)|^2 && (2.6)\\ &= \sum_\ell b_\ell(y,z,\lambda)\exp\big(i2\pi\frac{\ell x}{p_1}\big) && (2.7)\end{aligned}$$

Where the subscript "*fr*" should be interpreted as "fringes" and "*par*" will be used to indicate that the expression is valid for a parallel beam i.e. plane waves.

b_ℓ are the Fourier coefficients of the intensity pattern, which can be expressed as

$$b_\ell(y,z,\lambda) = \sum_{\ell'} B_{\ell'+\ell} B^*_{\ell'} \exp\Big(-i\pi\lambda z \frac{\big((\ell'+\ell)^2 - \ell'^2\big)}{p_1^2}\Big) \tag{2.8}$$

Where B^* designates the complex conjugate of B. Equation 2.7 tells us that the intensity is a function of period p_1. The exact values of coefficient b_ℓ depend on the shape of the grating G_1 and of the distance z.

From Equation 2.5, a property of prime importance can be deduced. At a distance $z = mD_T$ with

$$D_T = 2p_1^2/\lambda \tag{2.9}$$

and m a positive integer, it can be observed that:

$$\begin{aligned} U^r(x,y,mD_T,\lambda) &= \exp\big(i4\pi m\frac{p_1^2}{\lambda^2}\big)\sum_\ell B_\ell(y,\lambda)\exp\big(i2\pi\frac{\ell x}{p_1}\big) && (2.10)\\ &= \exp\big(i4\pi\frac{p_1^2}{\lambda^2}\big)T_1(x,y,\lambda) && (2.11)\\ I^r_{fr,par}(x,y,mD_T,\lambda) &= |T_1(x,y,\lambda)|^2 && (2.12)\end{aligned}$$

So, the field at distance $z = mD_T$ is a replica of the complex amplitude transmission function of the grating. In the case of absorbing gratings, the intensity will then be an image of the grating as shown in Equation 2.12. On the contrary, phase gratings will display a constant intensity on these planes.

Note that we did not restrict here to any particular shape of the grating G_1. This effect is indeed valid for any periodic object and is named after Henry Talbot, who first observed this phenomenon in 1836 (Talbot 1836) for visible light. D_T is thus called the Talbot distance. The Talbot effect was later theoretically explained by J. T. Winthrop (Winthrop & Worthington 1965).

Even more interesting is the field at fractional orders of the Talbot distance $z = (M/P)D_T$, where M and P are integers prime to each other. On such planes, the field can be expressed (Arrizòn & Rojo-Velazquez 2001) as the superposition of translated unit cells $T_1^0(x,y) = T_1(x,y)\mathrm{rect}(x/p)$, where $\mathrm{rect}(x)$ is the rectangular function, equal to one between $-1/2$ and $1/2$ and zero elsewhere.

$$\begin{aligned} U^r(x,y,\frac{M}{P}D_T,\lambda) &= \exp\big(i4\pi\frac{Mp_1^2}{P\lambda^2}\big)\times \\ &\quad \sum_{L=-\infty}^{+\infty} C(L,M,P)T_1^0\big(x - L\frac{p_1}{P},y\big) && (2.13)\\ \text{with } C(L,M,P) &= \frac{1}{P}\sum_{\ell=0}^{P-1}\exp\big(i\frac{2\pi}{P}\ell(L-M\ell)\big) && (2.14)\end{aligned}$$

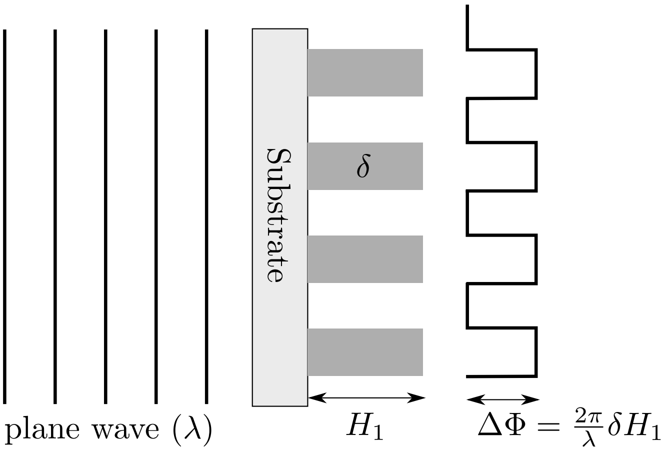

Figure 2.5: *Schematic view of a plane wave impinging on a rectangular phase grating. The wavefront after the grating has a rectangular profile of amplitude $\Delta\Phi$, which is proportional to the height H_1 of the grating trenches.*

Again, the superposition of the translated unit cells results in the formation of a complex intensity pattern, which can be calculated analytically from Equation 2.13. More on this rich phenomenon can be read in (Berry & Klein 1996; Berry *et al.* 2001).

Let us now restrict to a rectangular phase grating of duty cycle 0.5 (see Figure 2.2), meaning a grating which induces periodical rectangular modulations of the wavefront without attenuating the beam. The amplitude of the phase modulations are given by $\Delta\Phi = (2\pi/\lambda)\delta H_1$, where H_1 designates the height of the grating profile and δ the refraction coefficient of the grating material (see Figure 2.5). The design wavelength λ_{des} (or photon energy $E_{des} = hc/\lambda_{des}$ with h the Planck constant and c the speed of light) is defined as the wavelength for which the phase shift $\Delta\Phi$ is equal to $\pi/2$. Such a grating will be called a $\pi/2$-phase grating in the rest of the text.

The unit cell of a $\pi/2$-phase grating is given by:

$$T_1^0(x,y) \widehat{=} \begin{cases} 1 & -p_1/2 < x \leq 0 \\ \exp(i\pi/2) & 0 < x < p_1/2 \\ 0 & |x| \geq p_1/2 \end{cases} \tag{2.15}$$

The intensity was simulated numerically for such a phase grating as a function of the distance z using Equation 2.3. The results are plotted in Figure 2.6. It illustrates the Talbot effect for a $\pi/2$-phase grating. Clearly, self-images of the grating appear at distance $z = (2m+1)D_T/4$ (m integer). On these planes, the intensity forms a rectangular pattern of period p_1. This can also be verified analytically from Equation 2.13. Typically, for a period $p_1 \sim 3\,\mu\text{m}$ and $\lambda \sim 0.06\,\text{nm}$, a quarter of the Talbot distance is $D_T = 7.5\,\text{cm}$.

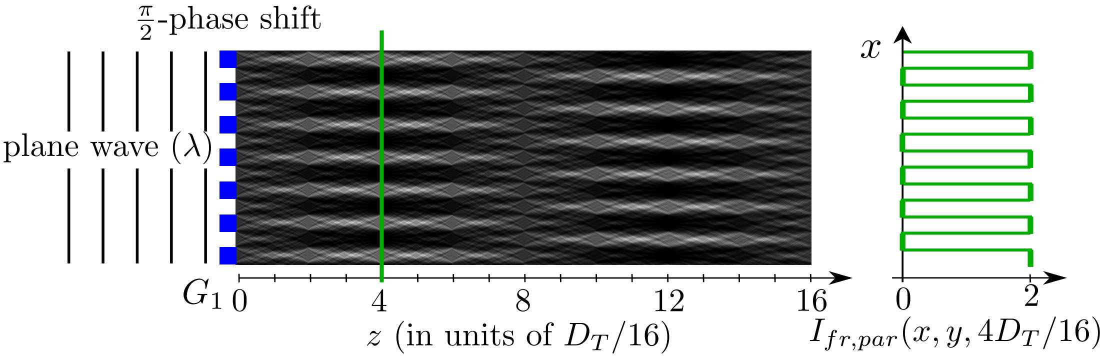

Figure 2.6: *Talbot effect illustrated for a plane wave impinging on a one-dimensional $\pi/2$-phase shifting grating. The intensity is displayed as a function of the distance z from the grating in units of quarters of the Talbot distance $D_T = p_1^2/2\lambda$. The intensity is coded as a gray value where white represents a high intensity. It can be observed that self-images are formed for $z = (2m+1)D_T/4$ for m positive integer. A cross section at position $z = D_T/4$ is plotted as a function of x on the right of the figure showing a perfect rectangular profile.*

In the case of a rectangular phase grating with π-phase shift, the self-images appear at distances $z = (2m+1)D_T/16$ (m integer) and have a period equal to half of the period of the grating, that is $p_1/2$. (Weitkamp *et al.* 2006) offers a detailed comparison of different grating types. It should be underlined here that phase gratings are preferred over amplitude gratings since a higher photon flux is then reaching the detector, which results in a better signal to noise ratio.

By convention, the fractional Talbot order N will be defined as $N \widehat{=} z/D_1$, where $D_1 \widehat{=} D_T/16$ is the first fractional Talbot distance for which the electrical field is a perfect reproduction of a π-phase shifting rectangular grating. The N^{th} fractional Talbot distance is then defined as

$$D_N \widehat{=} N D_1 \tag{2.16}$$

Let us also call p_{fr} the period of the interferences, which is equal to p_1 for a $\pi/2$-phase shifting grating and for a plane wave.

In summary, it was shown that interference fringes appear at certain distances from grating G_1 due to the diffraction of the beam. The positions of these planes depend on the type of grating used and their geometry. More precisely, for a phase grating inducing a rectangular phase profile of duty cycle 0.5 with $\Delta\Phi = \pi/2$, the interference pattern at distance $(2m+1)D_T/4$ (m integer) from grating G_1 is rectangular and displays a full modulation (meaning from zero to twice the incoming intensity). In the next paragraphs, it will be explained how this intensity pattern can be used to recover information about the absorption, refraction and ultra small-angle scattering occurring during the propagation of the wave in the sample.

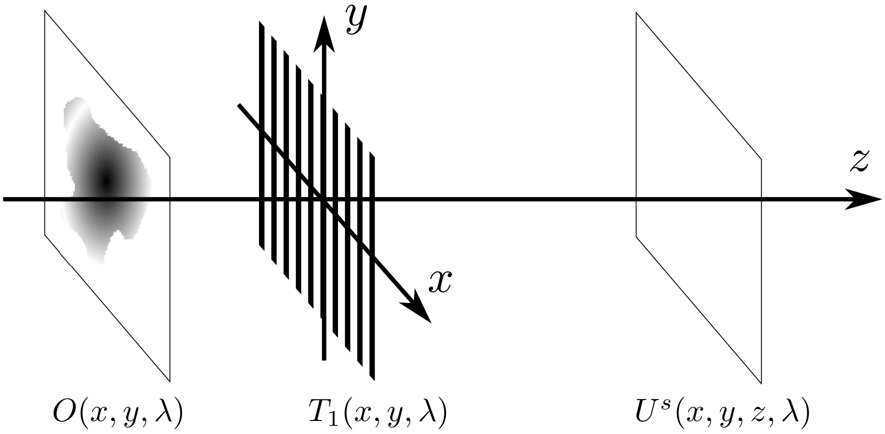

Figure 2.7: *Schematic view of the field propagation with an object in the field of view. The amplitude transmission function of the grating G_1 and of the object (placed either before or after the grating G_1) are $T_1(x,y,\lambda)$ and $O(x,y,\lambda)$, respectively. After propagation along the optical axis z, the field is $U^s(x,y,z,\lambda)$.*

2.1.3 Sample and Interactions

Let us see now how the intensity pattern introduced in the previous paragraph will be affected by an object placed in the field of view, either before or after the grating G_1. The object will be modeled by its amplitude transmission function $O(x,y,\lambda)$ (see Figure 2.7). The field intensity at a distance $z = D_N$ from grating G_1 in the presence of the sample will be denoted $I^s_{fr,par} = |U^s|^2$ and compared to $I^r_{fr,par}$, the field without sample.

Note that we will consistently use in this manuscript the superscripts (^{r}) and (^{s}) to refer, respectively, to the case without an object (”reference”) and with the object (”sample”) in the field of view. When the superscript is absent, this means that the statement is valid for both the reference and sample cases.

Generally, the amplitude transmission function is written as the product of a real and an imaginary function.

$$O(x,y,\lambda) \;\widehat{=}\; \exp\big(-\frac{A(x,y,\lambda)}{2}\big)\exp\big(-i\Phi(x,y,\lambda)\big) \tag{2.17}$$

If the index of refraction is expressed in its complex form as $n = 1-\delta+i\beta$, the following relations can be used

$$A(x,y,\lambda) \;\widehat{=}\; \frac{4\pi}{\lambda}\int_{\text{path}} \beta(x_o,y_o,z_o,\lambda)ds \tag{2.18}$$

$$= \int_{\text{path}} \mu(x_o,y_o,z_o,\lambda)ds \tag{2.19}$$

$$\Phi(x,y,\lambda) \;\widehat{=}\; -\frac{2\pi}{\lambda}\int_{\text{path}} \delta(x_o,y_o,z_o,\lambda)ds \tag{2.20}$$

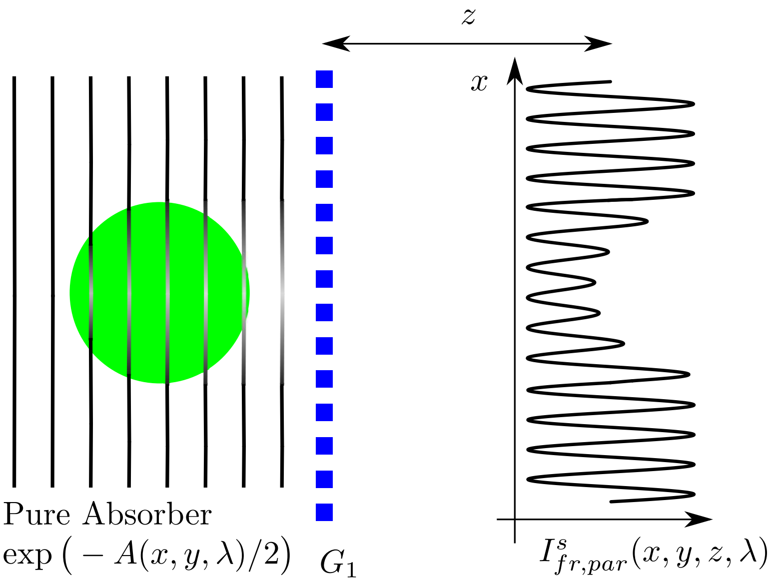

Figure 2.8: *A pure absorber with real amplitude transmission function* $\exp\big(-A(x,y,\lambda)/2\big)$ *induces a decrease of the mean intensity* $I^s_{fr,par}(x,y,z,\lambda)$.

Where (x_o,y_o,z_o) is the coordinate system fixed to the sample and $\mu\widehat{=}(4\pi/\lambda)\beta$ is the linear absorption coefficient. A is called the attenuation function while Φ is the phase shift or phase function of the sample. The integration is done along the x-ray path inside the sample. Note that scattering at large angles as resulting from inelastic Compton scattering induces a loss of flux on the detector and, as such, is included in the absorption coefficient i.e. $\mu = \mu_{PE}+\mu_{CS}$ where μ_{PE} is due to the photoelectric absorption and μ_{CS} is related to the Compton scattering.

Absorption

Let us consider first a purely absorbing object placed in the field of view. The amplitude transmission function $O(x,y,\lambda)$ of the object is then defined as $\exp\big(-A(x,y,\lambda)/2\big)$, a real function. Let us assume additionnally that $\exp\big(-A(x,y,\lambda)/2\big)$ is varying slowly compared to $T_1(x,y,\lambda)$.

In that case, the intensity $I^s_1(x,y,z,\lambda)$ at a distance D_N from G_1 can be expressed as

$$I^s_{fr,par}(x,y,D_N,\lambda) \quad = \quad \exp\big(-A(x,y,\lambda)\big) I^r_{fr,par}(x,y,D_N,\lambda) \qquad (2.21)$$

As expected, the presence of an absorbing object will induce a decrease of the intensity $I^r_{fr,par}$ proportional to the square of the amplitude transmission function. This is illustrated in Figure 2.8 in the case of a sphere.

Refraction

A purely phase-shifting object is now placed in the field of view. In that case, the amplitude transmission function of the object $O(x,y,\lambda)$ can be expressed

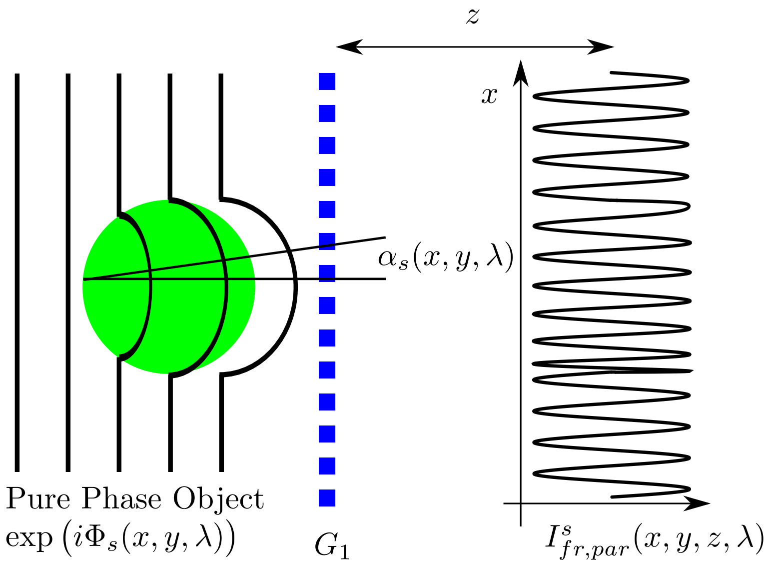

Figure 2.9: *A pure phase object with imaginary amplitude transmission function* $\exp\big(i\Phi_s(x,y,\lambda)\big)$ *induces a deviation of the x-ray beam by an angle* $\alpha_s(x,y,\lambda) = \frac{\lambda}{2\pi}\frac{\partial\Phi_s}{\partial x}(x,y,\lambda)$*. This results, locally, in a translation of the intensity pattern* $I^s_{fr,par}(x,y,z,\lambda)$*.*

as $\exp\big(i\Phi_s(x,y,\lambda)\big)$. It is assumed that $\Phi_s(x,y,\lambda)$ is varying slowly compared to $T_1(x,y,\lambda)$ (meaning over a period p_1), more precisely that $\frac{\partial^2\Phi_s}{\partial x^2}(x,y,\lambda) \ll \frac{\partial\Phi_s}{\partial x}(x,y,\lambda)/p_1$ such that the phase shift can be considered as linear. $\frac{\partial\Phi_s}{\partial x}$ (resp. $\frac{\partial^2\Phi_s}{\partial x^2}$) represents the first (resp. second) derivative of Φ_s along x.

The field at distance $z = D_N$ can be written as

$$\begin{aligned}
I^s_{fr,par}(x,y,D_N,\lambda) &= I^r_{fr,par}\Big(x - \frac{\lambda D_N}{2\pi}\frac{\partial\Phi_s}{\partial x}(x,y,\lambda), y, D_N, \lambda\Big) && (2.22)\\
&= \sum_\ell b_\ell(y,D_N,\lambda)\exp\big(i\frac{2\pi\ell x}{p_{fr}} + i\ell\varphi\big) && (2.23)\\
\text{with } \varphi &= \frac{\lambda D_N}{p_{fr}}\frac{\partial\Phi_s}{\partial x} && (2.24)\\
&= \frac{Np_1}{8}\frac{\partial\Phi_s}{\partial x} \quad (\text{ for } \lambda = \lambda_{des}) && (2.25)
\end{aligned}$$

Where λ_{des} is the design wavelength introduced in Section 2.1.2. This equation shows that the intensity $I^s_{fr,par}$ is equal to a locally translated version of $I^r_{fr,par}$, the intensity without object in the field of view. Equivalently, this effect can be seen as a phase shift $\ell\varphi$ of the Fourier coefficient b_ℓ. Indeed, refraction occurs in presence of a gradient of the wavefront and the beam is deviated (see Figure 2.9) by an angle

$$\alpha_s(x,y,\lambda) = \frac{\lambda}{2\pi}\frac{\partial\Phi_s}{\partial x}(x,y,\lambda) \tag{2.26}$$

Note that the phase shift of the interferences φ increases with the fractional Talbot order N.

Ultra-Small Angle Scattering

Finally, Ultra-Small Angle X-ray Scattering (USAXS or USAS) is induced by the inhomogeneities present in the sample. Inhomogeneities refer here to variations in the electron density at a length scale close to or below the grating period p_1. Those result in fast fluctuations of the wavefront $\Phi_f(x,y,\lambda)$ such that the assumption made in the previous paragraph about $\Phi_s(x,y,\lambda)$ is not valid anymore.

Since these multiple refracting events cannot be resolved individually, they have to be treated as a stochastic process, which will be characterized by the scattering cross section $\sigma_{usas}(\mathbf{q};\mathbf{r_0})$, where $\mathbf{r_0}$ is a point in the object and $\mathbf{q}$ is the three-dimensional scattering vector. We restrict here to small forward angle elastic scattering. $\sigma_{usas}(\mathbf{q};\mathbf{r_0})$ can be linked to the electron density ρ under the Born approximation[1] (Jackson 1999, Sect. 10.2) by

$$\sigma_{usas}(\mathbf{q};\mathbf{r_0}) \;\widehat{=}\; r_e^2 \int R(\mathbf{u}) \exp(-i\mathbf{q}.\mathbf{u}) d^3\mathbf{u} \tag{2.27}$$

$$\text{with } \mathcal{R}(\mathbf{u};\mathbf{r_0}) \;\widehat{=}\; \int_{\text{vicinity } \mathbf{r_0}} \rho(\mathbf{v})\rho(\mathbf{u}+\mathbf{v}) d^3\mathbf{v} \tag{2.28}$$

$\mathcal{R}(\mathbf{u};\mathbf{r_0})$ is the autocorrelation function of ρ in the vicinity of $\mathbf{r_0}$.

Following the demonstration from (Wen *et al.* 2008), the intensity $I^s_{1,par}$ can then be expressed, in the case of a pure scatterer, as:

$$I^s_{fr,par}(x,y,D_N,\lambda) = \sum_\ell b_\ell(y,D_N,\lambda) \times \exp\big(-S_\ell(x,y) + i\frac{2\pi\ell x}{p_{fr}}\big) \tag{2.29}$$

$$\text{with } S_\ell(x,y) = \lambda^2 r_e^2 \int_{\text{path}} \mathcal{R}_2\Big(\frac{\ell z_{12}\lambda}{p_{fr}}, 0; \mathbf{r_0}\Big) ds \tag{2.30}$$

$$\mathcal{R}_2\big(\Delta x, \Delta y; \mathbf{r_0}\big) \;\widehat{=}\; \int_{\text{vicinity } \mathbf{r_0}} \mathcal{R}\Big(0,0,w;\mathbf{r_0}\Big) - \mathcal{R}\Big(\Delta x, \Delta y, w; \mathbf{r_0}\Big) dw \tag{2.31}$$

Where $\mathbf{r_0}$ is taken along the x-ray path. Equation 2.29 tells us that the USAS induces an exponential decrease of all frequency components except the zeroth order component ($\mathcal{R}_2(0,0;\mathbf{r_0}) = 0$). Equation 2.30 indicates that the signal decrease (as given by S_ℓ) is related to the autocorrelation of the electron density over the distance $\ell\lambda D_N/p_{fr}$. Note that only the electron density variations along the x-direction have an impact on S_ℓ while those along the y-direction stays, in a first

---

[1] The Born approximation consists in taking the incident field as the driving field at each point of the scatterer instead of the total field. This ensues from the perturbation method where it is assumed that the scattering field is small compared to the incident field.

order, without effect. This is of course related to the fact that one-dimensional gratings are used here. For two-dimensional gratings, the intensity modulations would be affected by the USAS in both the x and y directions as demonstrated in (Zanette *et al.* 2010).

Furthermore, for $\lambda = \lambda_{des}$ and $z_{12} = D_N$, the interrogated autocorrelation distance becomes equal to $Np_1/8$. This corresponds to the length scale for which the grating interferometer is most sensitive and thus depends on the fractional Talbot order N and on the period p_1. This topic is further discussed in the case of spherical inhomogeneities in Section 5.3.2.

Moreover, the link between the phase shift and the integral of the electron density along the x-ray path is given by

$$\Phi(x,y) \sim \lambda r_e \int_{path} \rho(\mathbf{r_0}) ds \tag{2.32}$$

Where $\mathbf{r_0}$ is taken along the x-ray path. This expression can be used to further developp Equation 2.30 as

$$\begin{aligned} S_\ell(x,y) &= \int_{\text{path}} \frac{\partial}{\partial s}\Big[\sigma^2_{\Phi_f}\Big(1-\gamma\big(\frac{\ell z_{12}\lambda}{p_{fr}},0\big)\Big)\Big](\mathbf{r_0})ds && (2.33)\\ \text{with} \quad \sigma^2_{\Phi_f} &= \frac{1}{P^2}\int_{\text{unit area}} \Phi^2_f(x,y)dxdy && (2.34)\\ \text{and } \gamma\big(\Delta x,\Delta y\big) &= \frac{1}{\sigma^2_{\Phi_f}P^2}\int_{\text{unit area}} \Phi_f(x,y)\Phi_f(x+\Delta x, y+\Delta y)dxdy && (2.35) \end{aligned}$$

$\sigma^2_{\Phi_f}$ is the variance and $\gamma\big(\Delta x,\Delta y\big)$ the normalized autocorrelation function of the phase shift function Φ_f over a unit area around (x,y). The latter is defined by the minimal resolvable feature, which is given by the periodicity of the grating G_1 in the present case, i.e. $P = p_1$. As will be introduced in the following section, the width of the point spread function of standard detectors is usually larger than the periodicity p_1. In that case, the unit area has to be redefined such that P is then equal to the pixel size. From Equation 2.33, the formulation proposed by (Yashiro *et al.* 2010) can be derived directly. $\frac{\partial}{\partial s}\Big[\sigma^2_{\Phi_f}\Big(1-\gamma\big(\frac{\ell z_{12}\lambda}{p_{fr}},0\big)\Big)\Big](\mathbf{r_0})$ is then to be understood as the local contributions around $\mathbf{r_0}$ to the variations in the phase shift.

Intuitively, the USAS can also be interpreted as a blurring of the interference fringes as a consequence from the beam broadening after the multiple scattering events. In most cases, it is assumed that the latter follows a Gaussian distribution of width $w(x,y,\lambda)$ as shown in Figure 2.10. The formulation introduced above is however more general.

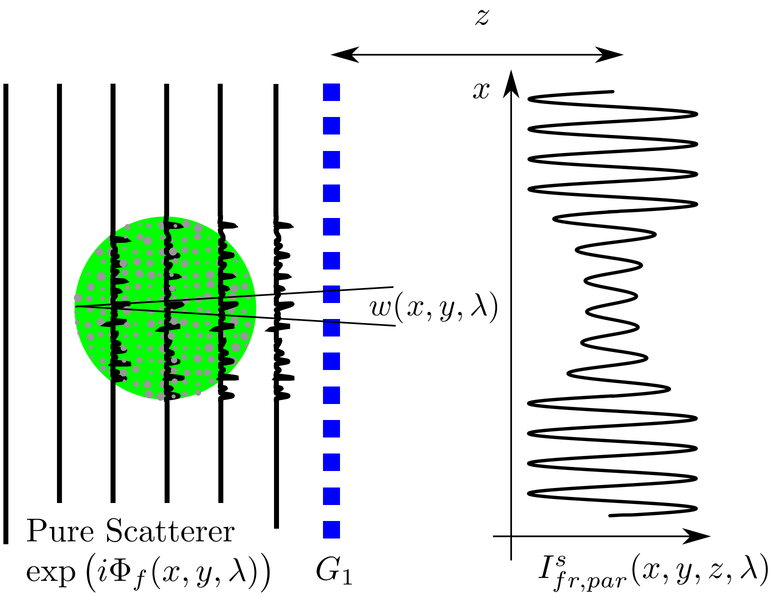

Figure 2.10: *A pure scatterer with imaginary amplitude transmission function* $\exp\big(i\Phi_f(x,y,\lambda)\big)$ *induces fast variations of the wavefront. Such unresolved variations are equivalent to a broadening of the beam, usually assumed to follow a Gaussian distribution of width* $w(x,y,\lambda)$*. As a result, the intensity pattern* $I^s_{fr,par}(x,y,z,\lambda)$ *is blurred and the amplitude of the modulations decreases.*

Note that the ultra small angle scattering is thus probing the variations in the electron density below the resolution of the imaging system. In the Chapter 5, this will prove to be a key advantage in numerous applications.

2.1.4 Analyzer Grating and Large Detector Pixels

In the previous section, it was shown that three different mechanisms (absorption, refraction and ultra-small angle scattering) have an impact on the interference pattern $I^r_{fr,par}$ and induce local changes of the mean, amplitude or position of the interference fringes. Assuming that the resolution of the detector is sufficiently good to resolve the fringes, these local changes can be recovered using the Fourier transform method (Takeda *et al.* 1982). This method has the advantage of using only one phase grating and is, for this reason, sometimes called the "single grating" method (Takeda *et al.* 2007; Wen *et al.* 2010). However, since the resolution of x-ray detectors is limited to some microns at best, such a setup calls for large periodicities. This translate into large Talbot distances[2] and, thus, instruments too large to be implemented in industrial environments. It should also

---

[2] The Talbot distance is proportional to the square of the grating periodicity (see Equation 2.9).

be added that such detectors with micron-scale pixels are expensive and have a weak stopping power.

In order to work with conventional detectors with pixel size p_{pix}, in the range of 10 - 500 μm, much larger than the fringes' periodicity in the order of some microns, another grating G_2 needs to be introduced. This grating is placed on a plane where self-images form i.e. at distances $z_{12} = D_N$, where D_N is the N^{th} fractionnal Talbot distance (definitions in Section 2.1.2). It is usually an absorbing grating with periodicity p_2 equal to the interferences' periodicity p_{fr}. As a result, depending on the exact position of the interference pattern with respect to G_2, a varying amount of the radiation is absorbed, as shown in Figure 2.11. Therefore, it serves as a mask to artificially improve the resolution of the detector and recover the fringes' characteristics. For this reason, it is called the analyzer grating.

The analyzer grating G_2 is modeled by its intensity transmission function T_2^2. The latter is periodic of period p_2 and can be expressed as a Fourier series:

$$T_2^2(x,y,\lambda) \widehat{=} \sum_{\ell} c_\ell(y,\lambda) \exp\big(-i2\pi\frac{\ell x}{p_2}\big) \tag{2.36}$$

Where c_ℓ are the Fourier coefficients of the intensity function T_2^2. Let us now assume that $p_2 = p_{fr}$. In addition, the variables will be written without showing explicitly their dependence on other parameters[3].

Combining Equations 2.7 and 2.36, the intensity right after grating G_2 with a sample in the field of view, can be expressed as

$$\begin{aligned} I^s_{2,par}(x,y,\lambda) &= T_2^2 \times I^s_{1,par} && (2.37)\\ &\widehat{=} \exp(-A) && (2.38)\\ &\quad \times \sum_{\ell,N} c_\ell b_{\ell+N} \exp\big(-S_{\ell+N}\big) \exp\big(i2\pi\frac{xN}{p_2} + i(\ell+N)\varphi\big) \end{aligned}$$

Where A, S and φ are related to the interactions of the beam with the sample, as presented in Section 2.1.3. Let us now introduce a detector placed right after grating G_2 (see Figure 2.11). The point spread function of the detector pixels is known as $PSF(x,y)$ and $\mathcal{D}(\lambda)$ designates the detector gain at this wavelength. The intensity of a pixel centered around (x,y) is then given by

$$\begin{aligned} I^s_{pix,par}(x,y,\lambda) &= \mathcal{D}\int PSF(x-x',y-y') I^s_{2,par}(x',y',\lambda)dx'dy' && (2.39)\\ &\widehat{=} \mathcal{D}p_{pix}\exp(-\bar{A})\sum_{\ell} c_\ell b_\ell \exp\big(-\bar{S}_\ell\big)\exp\big(i\bar{\varphi}_\ell\big) && (2.40)\\ I^r_{pix,par}(x,y,\lambda) &\sim \mathcal{D}p_{pix}\sum_{\ell} c_\ell b_\ell && (2.41) \end{aligned}$$

---

[3] For example, $T(x,y,\lambda)$ will now be written T.

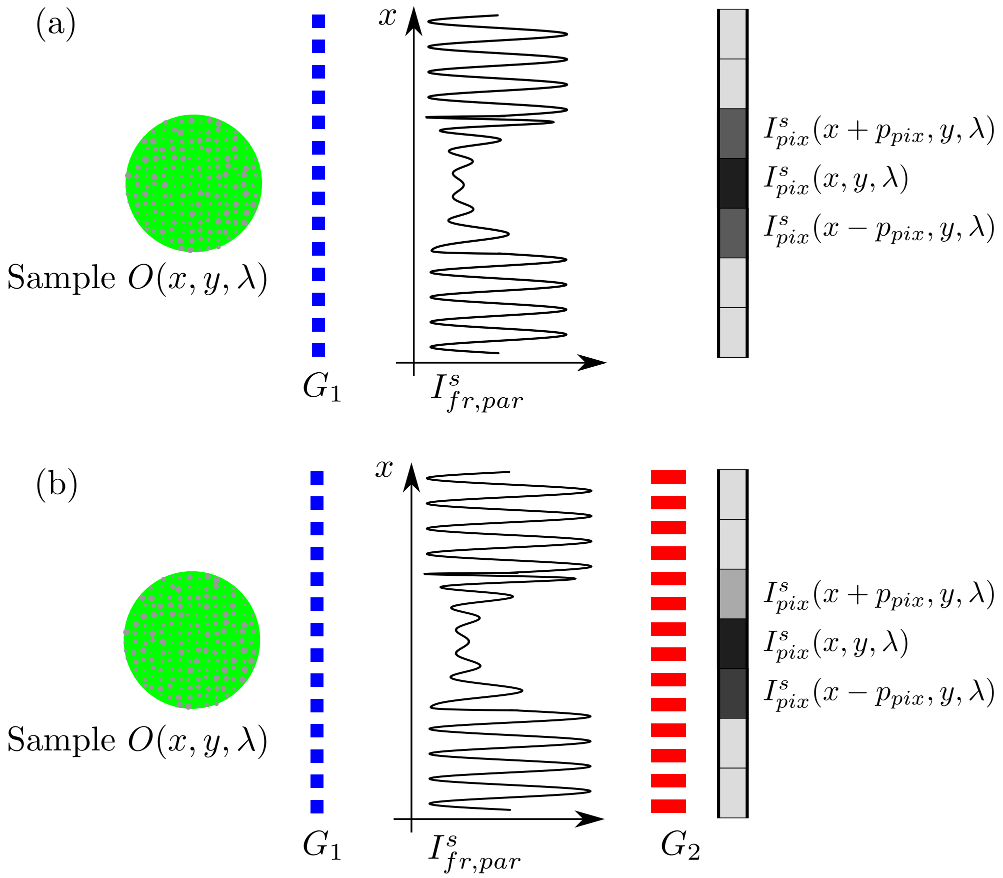

Figure 2.11: *In the presence of a sample of amplitude transmission function O, the intensity pattern $I^s_{fr,par}$ is modified. A detector with large pixels compared to the fringe periodicity p_{fr} is placed on the plane of the interferences. (a) Without grating G_2, the interference pattern is averaged out due to the pixel size and the pixel intensity I^s_{pix} is only sensitive to the attenuation in the sample but not to the phase effects. (b) For this reason, an analyzer grating G_2 has to be used, which masks a varying amount of the incoming flux depending on the position of the interference pattern with respect to G_2. As a result, the pixel intensity is also a function of the refraction and ultra-small angle scattering occurring in the sample. Note, for example, that the values of $I^s_{pix}(x+p_{pix}, y)$ and $I^s_{pix}(x - p_{pix}, y)$ are modified when G_2 is added.*

Where $\bar{A}$, $\bar{S}_\ell$ and $\bar{\varphi}_\ell$ are the results of the convolution with the point spread function of the detector. In a first order, $\bar{A}$, $\bar{S}_\ell$ and $\bar{\varphi}_\ell$ can be seen as blurred or averaged versions of A, S_ℓ and $\ell\varphi$. This however does not hold when the variations of φ are fast compared to the pixel size. In this case, the averaging will result in an additional loss of visibility, which is included in the factor $\bar{S}_\ell$. A more detailed approach of this topic is given in Section 3.1.3.

It can be observed that the pixel intensity depends, simultaneously, on the absorption ($\bar{A}$), phase ($\bar{\varphi}_\ell$) and ultra-small angle scattering ($\bar{S}_\ell$). As a consequence, specific reconstruction methods are required to decouple the three contributions. This is the subject of Section 2.2.

2.1.5 Source Grating and Standard X-ray Tubes

This paragraph is dedicated to the extension of the previous equations, when standard x-ray tubes are used to generate the radiation. Indeed, it was previously assumed that the incoming radiation consisted of monochromatic plane waves. This obviously does not hold for conventional x-ray tubes (Krestel 1990), which are spherically divergent point sources with extended focal spot and polychromatic spectrum. Let us deal with each point separately.

Point Sources and Spherical Divergence

In this paragraph, the x-ray source will be considered as a monochromatic point source with an infinitely small focal spot size placed at a distance z_{01} in front of the beam splitter grating G_1. The emitted wave is then spherically divergent as can be seen in Figure 2.12.

Let us first assume that the grating G_1 (respectively G_2) is spherical with radius of curvature equal to z_{01} (respectively $z_{01} + z_{12}$). In that case, the coordinate system (x, y) is mapped onto the spherical surface. The more realistic case of plane gratings is treated in Section 5.2.1. Due to the divergence of the beam, the N^{th} fractional Talbot distance d_N and the periodicity of the interference fringes at distance z_{12} have to be corrected for the magnification as follows (Engelhardt *et al.* 2007):

$$d_N \;\widehat{=}\; M_g D_N \tag{2.42}$$

$$p_{fr} \;\widehat{=}\; M_g p_1 \tag{2.43}$$

$$b_\ell(y,z,\lambda) \;\widehat{=}\; \sum_{\ell'} B_{\ell'+\ell} B^*_{\ell'} \exp\Big(- i\pi\lambda z \frac{\big((\ell'+\ell)^2 - \ell'^2\big)}{p_1^2} \frac{z_{12}}{M_g}\Big) \tag{2.44}$$

$$\text{with } M_g \;\widehat{=}\; \frac{z_{01}+z_{12}}{z_{01}} = \frac{p_0+p_2}{p_0} \tag{2.45}$$

Note that the magnification of the grating's periodicity M_g does not correspond

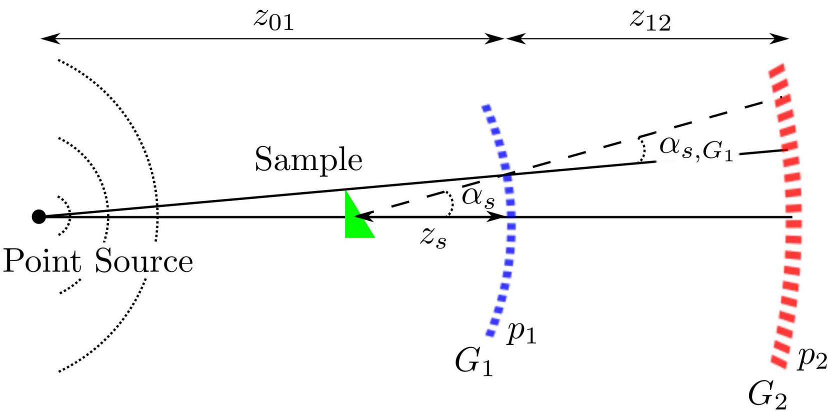

Figure 2.12: *For a point source, the emitted waves have spherical wavefronts as represented by the solid line. The periodicities* p_1 *and* p_2 *as well as the distances* z_{01} *and* z_{12} *have to be corrected due to the subsequent magnification. Additionnally, the apparent angular deflection* α_{s,G_1} *on* G_1 *is reduced compared to the angular deflection in the sample* α_s*.*

to the magnification of the sample

$$M_s \widehat{=} \frac{z_{01}+z_{12}}{z_{01}+z_s} \tag{2.46}$$

Where z_s is the distance between the sample and grating G_1 (see Figure 2.12). z_s can be negative, meaning that the sample is placed between the x-ray source and G_1, or positive when the sample is placed between G_1 and G_2. In Equation 2.41, $\bar{A}(x,y,\lambda)$, $\bar{\varphi}_\ell(x,y,\lambda)$ and $\bar{S}_\ell(x,y,\lambda)$ have to be replaced due to the magnification by

$$A_M(x,y,\lambda) \;\widehat{=}\; A\big(x/M_s, y/M_s, \lambda\big) \tag{2.47}$$
$$\varphi_M(x,y,\lambda) \;\widehat{=}\; \varphi\big(x/M_s, y/M_s, \lambda\big) \tag{2.48}$$
$$S_{\ell,M}(x,y,\lambda) \;\widehat{=}\; S_\ell\big(x/M_s, y/M_s, \lambda\big) \tag{2.49}$$

Furthermore, the apparent angular deviation on grating G_1, α_{s,G_1} (see Figure 2.12), is smaller than the angular deviation in the object α_s as explained in (Donath *et al.* 2009). As a consequence,

$$\varphi' = \varphi f(z_s) \tag{2.50}$$

$$\text{with } f(z_s) \;\widehat{=}\; \begin{cases} 1 + z_s/z_{01} & -z_{01} < z_s < 0 \\ 1 - z_s/z_{12} & 0 \le z_s < z_{12} \\ 0 & \text{elsewhere} \end{cases} \tag{2.51}$$

So the phase sensitivity decreases linearly as a function of the distance from grating G_1. Note, for example, that for a given interferometer, the phase sensitivity is

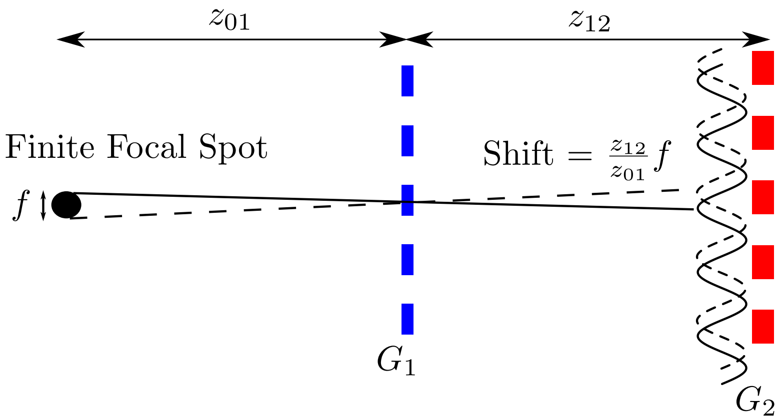

Figure 2.13: *The points of the focal spot of size f each emit a wave and induce interference fringes, which are shifted with respect to each other and produce a blurring of the ideal interference pattern. If the maximum shift $(z_{12}/z_{01})f$ is larger than the fringes' periodicity p_{fr}, the interference are completely blurred out.*

optimized when the sample is placed as close as possible to grating G_1. Geometrical magnification of the object (meaning placing the object closer to the focal spot) can be realized but at the expense of phase sensitivity.

Equivalently, the beam broadening due to ultra-small angle scattering, as given by the Equation 2.29, will also be reduced in the same way i.e.

$$S'_\ell = S_\ell f(z_s) \tag{2.52}$$

Finally, the intensity of the fringe pattern for a point source $I_{fr,pt}$ can be rewritten as

$$I^r_{fr,pt}(x,y,\lambda) = \frac{1}{(z_{01}+z_{12})^2} \sum_\ell b_\ell \exp\big(i2\pi \frac{x\ell}{p_{fr}}\big) \tag{2.53}$$

$$\begin{aligned} I^s_{fr,pt}(x,y,\lambda) &= \frac{1}{(z_{01}+z_{12})^2} \exp(-A_M) \qquad (2.54)\\ &\times \sum_\ell b_\ell \exp\big(-f(z_s)S_{\ell,M}\big) \exp\big(i2\pi \frac{x\ell}{p_{fr}} + i\ell f(z_s)\varphi_M\big) \end{aligned}$$

Extended Focal Spots

Let us now extend the previous relations to the case of a focal spot of finite size. The effect of an extended source can be understood as follows. In the limit of the paraxial approximation (i. e., the focal spot size is much smaller than distance z_{01}), each point of the focal spot induces interference fringes $I^r_{fr,pt}$ on the plane of G_2. If (x_f, y_f) designates the coordinate of a point of the focal spot, the generated interference fringes will be shifted with respect to the optical axis by

$\Delta x = x_f(z_{12}/z_{01})$ and $\Delta y = y_f(z_{12}/z_{01})$. This is illustrated in Figure 2.13. The sum of these interference patterns is then a blurred version of $I_{fr,pt}$ (Equation 2.55) expressed as

$$\begin{aligned} I^r_{fr}(x,y,z_{12},\lambda) &= I^r_{fr,pt} * \big(\frac{z_{01}}{z_{12}}\big)^2 T^2_f\big(x(\frac{z_{01}}{z_{12}}), y(\frac{z_{01}}{z_{12}})\big) && (2.55)\\ &= \frac{1}{(z_{01}+z_{12})^2}\sum_\ell b_\ell \tau_\ell \exp\big(i2\pi\frac{\ell x}{p_{fr}}\big) && (2.56)\\ \text{with } \tau_\ell &= \mathcal{F}_x(T^2_{f,Y})\big(\frac{z_{12}}{z_{01}}\frac{\ell}{p_{fr}}\big) && (2.57)\\ \text{and } T^2_{f,Y}(x) &= \int T^2_f(x,y)dy && (2.58) \end{aligned}$$

Where $T^2_f(x_f, y_f)$ is the intensity distribution of the focal spot. $\mathcal{F}_x(T^2_{f,Y})$ denotes the Fourier transform of $T^2_{f,Y}$ along the x-direction.

τ_ℓ can be linked to the mutual coherence function of the radiation in the x-direction τ by $\tau_\ell = \tau(\ell N p_1)$ (Yashiro *et al.* 2010). If the source distribution can be approximated by the product of two Gaussian functions of widths ϖ_x and ϖ_y in the x and y direction, the mutual coherence function is given by

$$\begin{aligned} \tau(L) &= \exp\big(-\frac{L^2}{2L^2_{coh}}\big) && (2.59)\\ \text{with } L_{coh} &= \frac{\lambda z_{01}}{2\pi\varpi_x} && (2.60) \end{aligned}$$

L_{coh} is called the spatial coherence length. From this expression, it can be seen that the blurring in the y-direction (parallel to the G_1 grating's lines) does not impact (at least in the first order) on the interference pattern. The coherence length in the x-direction is, on the contrary, critical. The Fourier coefficients, except the 0^{th} order, are decreased by a function depending strongly on the order itself (l), on the size of the focal spot (ϖ_x) and the distances, especially the fractional Talbot order. Note, for example, that for one given focal spot size and periodicity p_1, the blurring increases with the fractional Talbot order N.

If the focal spot is larger than the scaled fringes' periodicity, i.e. $\varpi_x > p_{fr}(z_{01}/z_{12})$, the interference pattern is completely washed out and the phase information is lost.

So for typical distances $p_{fr} = 3$ µm, $z_{01} = 1$ m and $z_{12} = 0.1$ m, the focal spot has to be smaller (in the x-direction) than 30 µm. This can only be achieved with microfocus x-ray sources (Engelhardt *et al.* 2007) or some exotic sources like sources with a liquid metal jet anode (Tuohima 2007). This method is sometimes referred to as the "two-gratings" method or Talbot interferometry and is usually applied when microscopic resolutions are desired (Engelhardt 2008). Its main

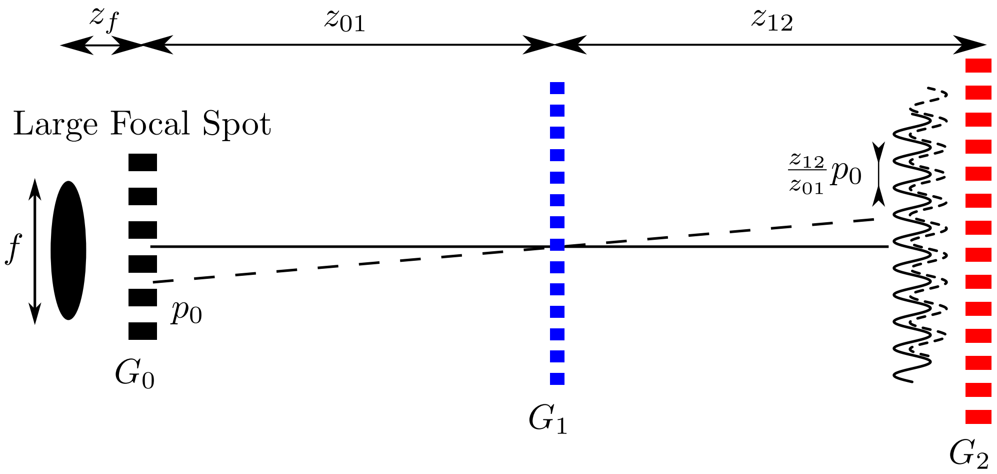

Figure 2.14: *When x-ray sources with large focal spots are used, an absorbing grating called the "source grating" G_0 is placed between the focal spot and the grating G_1. It acts as a mask and each opening becomes a single line source, which is sufficiently coherent to produce an interference pattern on the plane of grating G_2. The period p_0 of grating G_0 is chosen such that the interference patterns from different line sources add up constructively as illustrated for the central opening (solid line) and the opening immediately below (dashed line). The condition is $p_0 = (z_{01}/z_{12})p_{fr}$.*

disadvantage is that the photon flux of microfocus sources is low and limits the method in many applications where speed is required.

Source Grating

However, Pfeiffer et al. suggested in 2006 (Pfeiffer *et al.* 2006) to introduce a third grating in front of the focal spot, the "source grating" G_0, which allows for the use of x-ray tubes with a large focal spot. This grating configuration is usually called the Talbot-Lau interferometer. Grating G_0 is an absorbing mask of periodicity p_0 such that its intensity transmission function T_0^2 can be expressed as

$$T_0^2(x,y) \widehat{=} \sum_{\ell} a_\ell \exp\left(i2\pi\frac{\ell x}{p_0}\right) \tag{2.61}$$

where a_ℓ are the Fourier coefficients of the periodical function T_0^2. The role of G_0 can be intuitively understood by looking at Figure 2.14. Each opening of grating G_0 corresponds to a line source, which is sufficiently coherent in the x-direction to induce an interference pattern on the plane of G_2. In this way, the size of the focal spot f does not influence anymore the coherence of the radiation. Obviously, the line sources are mutually incoherent but, provided that the translation from one interference pattern to another is a multiple of the pattern periodicity (i.e. $p_0 = j\frac{z_{01}}{z_{12}}p_{fr}$ with j strictly a positive integer), the interference patterns will add constructively.

In mathematical terms, T_0^2 can be substituted to T_f^2 in Equation 2.58 and the intensity pattern becomes

$$I^r_{fr}(x,y,z_{12},\lambda) = \sum_{\ell}\Big(\sum_{\ell'} a_{\ell'}\delta_K\big(\ell' - \ell\frac{p_0}{p_{fr}}\big)\Big) b_\ell \exp\big(i2\pi\frac{\ell x}{p_{fr}}\big) \tag{2.62}$$

Where δ_K is the symbol of Kronecker[4]. It can then be deduced that I^r_{fr} will be equal to zero, except if $p_0 = j\frac{z_{01}}{z_{12}}p_1$ with j strictly a positive integer. If this condition is satisfied, the intensity can be rewritten as

$$I^r_{fr}(x,y,z_{12},\lambda) = \sum_{\ell} b_\ell a_{\ell\frac{z_{12}p_0}{z_{01}p_{fr}}} \exp\big(i2\pi\frac{\ell x}{p_{fr}}\big) \tag{2.63}$$

In all this manuscript, the choice was made to have

$$p_0 = \frac{z_{01}}{z_{12}}p_{fr} \tag{2.64}$$

So that the previous expression can be simplified. Note that for a fully absorbing rectangular grating of duty cycle DC_0, the coefficient a_0 is equal to DC_0 and implies that the average of the intensity pattern I^r_{fr} (as given by $|a_0b_0|$) is decreased by a factor DC_0 compared to the average without using grating G_0[5].

As a conclusion, an interference pattern can be obtained also in the case of an extended focal spot provided that a source grating is used. The resulting pixel intensity is given by

$$\begin{aligned} I^r_{pix}(x,y,\lambda) &= \frac{\mathcal{D}p_{pix}}{(z_{01}+z_{12})^2}\sum_\ell a_\ell b_\ell c_\ell && (2.65)\\ I^s_{pix}(x,y,\lambda) &= \frac{\mathcal{D}p_{pix}}{(z_{01}+z_{12})^2}\exp\big(-\bar{A}_M\big) && (2.66)\\ &\quad\times\sum_\ell a_\ell b_\ell c_\ell \exp\big(-f(z_s)\bar{S}_{\ell,M} + if(z_s)\bar{\varphi}_{\ell,M}\big) && (2.67)\end{aligned}$$

For simplification, the following notations will be used in the rest of the text.

$$\begin{aligned} q^r_\ell &\mathrel{\widehat{=}} a_\ell b_\ell c_\ell && (2.68)\\ q^s_\ell &\mathrel{\widehat{=}} a_\ell b_\ell c_\ell \exp\big(-\bar{A}_M - \bar{S}_{\ell,M}f(z_s)\big)\exp\big(if(z_s)\bar{\varphi}_{\ell,M}\big) && (2.69)\end{aligned}$$

As a reminder, a_ℓ, b_ℓ and c_ℓ are the complex Fourier coefficients of functions T_0^2, $I_{fr,pt}$ and T_2^2 that are linked to the source grating G_0, the beam splitter grating G_1 and the analyzer grating G_2.

---

[4] $\delta_K(\ell)$ is equal to 0 except for $\ell = 0$, where it is equal to 1.

[5] The collimation effect of the grating is not taken into account here.

Polychromatic Radiation

As seen in the previous paragraphs, each wavelength results in a pixel intensity $I_{pix}(x, y, z, \lambda)$ at distance $z = d_N$ given by Equation 2.63. When a polychromatic spectrum is used, the resulting pixel intensity is the weighted (incoherent) sum, where the weight function is $\mathcal{S}_{in}(\lambda)$, the number of photons emitted by unit solid angle by the x-ray source at wavelength λ during the exposure time. We then obtain

$$\begin{aligned}
I^j_{pix}(x, y) &= \int I^j_{pix}(x, y, \lambda) d\lambda && (2.70)\\
&\widehat{=} \sum_\ell Q^j_\ell \sin(\psi^j_\ell) && (2.71)\\
\text{with } Q^j_\ell &= \frac{\eta p_{pix}}{(z_{01} + z_{12})^2} \times \Big| \int \mathcal{D}(\lambda)\mathcal{S}_{in}(\lambda) q^j_\ell(x, y, \lambda) d\lambda \Big| && (2.72)\\
\text{and } \psi^j_\ell &= \frac{\pi}{2} - \arg\Big(\int \mathcal{D}(\lambda)\mathcal{S}_{in}(\lambda) q^j_\ell(x, y, \lambda) d\lambda \Big) && (2.73)
\end{aligned}$$

Where $j = r$ or s and η is equal to 1 for $\ell = 0$ and 2 otherwise. In the case of a polychromatic source with large focal spot, the terms Q_ℓ drop quickly for $\ell > 2$ such that the intensity can be approximated by its first two terms (Pfeiffer *et al.* 2006):

$$I^i_{pix}(x, y) \sim Q^i_0 + Q^i_1 \sin(\psi^i_1) \qquad (2.74)$$

Although this expression is particularly simple, the information contained in coefficients Q_0, Q_1 and ψ_1 is complex and depends, in a first order, on the properties of the sample but also simultaneously on the wavelength used and the gratings' geometry. When working with polychromatic radiation, these contributions may not be separated perfectly and will lead to artifacts in the images. This will be the topic of Section 3.1.

This paragraph highlights one of the key advantage of grating interferometry - that is its ability to function with polychromatic radiation. Indeed, although the interferometer is optimized for the energy E_{des}[6], x-ray photons of different energies do also produce an interference pattern and, most importantly, with the same periodicity p_{fr} (independent of the photon energy). As a consequence, the intensity patterns of different photon energies add up (incoherently) and all contribute to the phase contrast. Of course, the modulations of the intensity pattern (as given by the coefficient b_1 introduced in Equation 2.8) are maximal for the energy E_{des} and drop for higher/lower x-ray energies. As a rule of thumb, it is usually considered that grating interferometry supports spectral widths of

---

[6] The energy E_{des} is defined such that the grating G_1 induces a $\pi/2$-phase shift as discussed in Section 2.1.2.

up to 30% (Kottler *et al.* 2010b). This is considerably larger than the tolerated spectral widths of most other phase sensitive techniques introduced in Section 1.2 and allows most of the radiation emitted by the x-ray tube source to be used efficiently.

2.2 Image Reconstruction

In the previous paragraphs, it was shown that the intensity recorded by the detector pixels is a function of the absorption, refraction and ultra-small-angle scattering occurring in the sample. In the following paragraph, the most general method to decouple the three contrast mechanisms, called the phase stepping method (Weitkamp *et al.* 2005), will be presented. Other methods do exist (Momose *et al.* 2009; Zhu *et al.* 2010, Section 5.1.1) but usually relies on stronger assumptions about the object and/or system.

2.2.1 Phase Stepping Method

Let us consider that grating G_2 is displaced by an amount χ in the x-direction. Consequently, x is replaced by $x+\chi$ in Equation 2.36 and the new transmission function becomes

$$T_2^2(x,y,\lambda)=\sum_{\ell}\Big[c_\ell(y,\lambda)\exp\big(i2\pi\frac{\chi}{p_2}\big)\Big]\exp\big(-i2\pi\frac{\ell x}{p_2}\big) \tag{2.75}$$

Clearly, this expression is equivalent to the original, except that the coefficient $c_\ell(y,\lambda)$ was replaced by $c_\ell(y,\lambda)\exp\big(i2\pi\chi/p_2\big)$. A translation of a grating induces in fact a phase shift of the Fourier coefficients. Considering Equations 2.73 and 2.74, it can be finally found that

$$I_{pix}(x,y,\chi) \quad\sim\quad Q_0+Q_1\sin\big(2\pi\frac{\chi}{p_2}+\psi_1\big) \tag{2.76}$$

This expression tells us that the intensity forms approximately a sine function when the grating G_2 is shifted over one period p_2. Indeed, depending on the position of the interference pattern I_{fr} relative to the grating G_2, a varying amount of the radiation is transmitted onto the corresponding pixel, as illustrated in Figure 2.15. This so-called phase stepping curve is characterized by its mean Q_0, amplitude Q_1 and phase ψ_1. Note that the phase ψ_1 depends on the initial (relative) position of the x-ray gratings. The displacement χ can be realized by translating any of the gratings G_0, G_1 or G_2 by a distance $\frac{z_{01}}{z_{12}}\chi$, $\frac{z_{01}}{z_{01}+z_{12}}\chi$ and χ, respectively.

Usually, the pixel intensity is recorded at discrete positions, called phase steps. The total number of phase steps will be called N_{ps}. The pixel intensity at phase

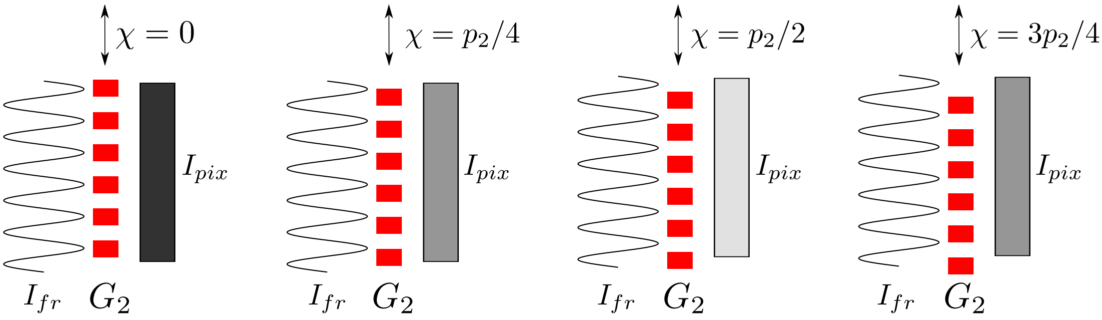

Figure 2.15: *Illustration of the phase stepping principle. From left to right, the grating* G_2 *is shifted by a displacement* $\chi = 0$, $p_2/4$, $p_2/2$ *and* $3p_2/4$ *in the* x*-direction. The recorded pixel intensity* I_{pix} *varies accordingly to the alignment of* G_2 *to the alignment fringes and the resulting curve is called the phase stepping curve.*

step $m = 1 \dots N_{ps}$ is then equal to

$$I_{pix}(x, y, j) \quad \sim \quad Q_0 + Q_1 \sin\left(2\pi m \frac{N_{per}}{N_{ps}} + \psi_1\right) \tag{2.77}$$

Where N_{per} is the number of periods p_2 covered during the phase stepping. Note that N_{ps} should at least be higher than three times N_{per} to satisfy the Nyquist condition. In practice, higher orders are also often present in Equation 2.77 such that it is usually preferable to take at least five and up to twenty phase steps per period.

Fundamentally, the idea to separate the contributions from the absorption, the refraction and the ultra-small angle scattering is to compare the phase stepping curve $I^s_{pix}(x, y, m)$, when a sample is present in the field of view, to a reference measurement $I^r_{pix}(x, y, m)$ without an object, and thereby deduce the local changes in the beam propagation due to the object.

Indeed, the coefficients Q_0, Q_1 and ψ_1 can be extracted from the acquired data set $I_{pix}(x, y, m)$ of the phase stepping curve by using the Fast Fourier Transform (FFT) (Bronshtein *et al.* 2003). The data set after FFT is called $\hat{I}_{pix}(x, y, m)$ and the coefficients are given by

$$Q_0 \quad = \quad \frac{\mid \hat{I}_{pix}(x, y, 0) \mid}{N_{ps}} \tag{2.78}$$

$$Q_1 \quad = \quad 2\frac{\mid \hat{I}_{pix}(x, y, N_{per} + 1) \mid}{N_{ps}} \tag{2.79}$$

$$\psi_1 \quad = \quad \arg(\hat{I}_{pix}(x, y, N_{per} + 1)) \tag{2.80}$$

Let us now consider, for a moment, the ideal case of a monochromatic wave

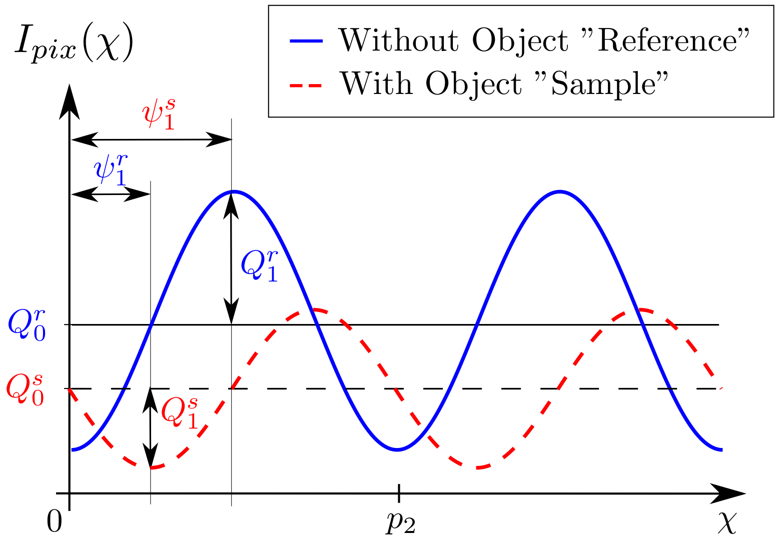

Figure 2.16: *The solid blue line represents the reference phase stepping curve (without object) while the dashed red line defines the sample phase stepping curve. The coefficients Q_0, Q_1 and ψ_1 can be calculated using the Fast Fourier Transform algorithm and used to calculate the absorption, refraction and ultra small angle scattering due to the sample.*

(wavelength λ) and remind the reader that, in that case (Equation 2.67),

$$Q_\ell^r = \frac{\eta p_{pix}}{(z_{01}+z_{12})^2} |\mathcal{D}\mathcal{S}_{in} a_\ell b_\ell c_\ell| \tag{2.81}$$

$$Q_\ell^s = \frac{\eta p_{pix}}{(z_{01}+z_{12})^2} |\mathcal{D}\mathcal{S}_{in} a_\ell b_\ell c_\ell| \exp\big(-\bar{A}_M - \bar{S}_{\ell,M} f(z_s)\big) \tag{2.82}$$

$$\psi_\ell^r = \arg(b_\ell c_\ell s_\ell) \tag{2.83}$$

$$\psi_\ell^s = \arg\Big(b_\ell c_\ell s_\ell \exp\big(i\bar{\varphi}_{\ell,M} f(z_s)\big)\Big) \tag{2.84}$$

Recall that a_l (resp. c_l) are the complex Fourier coefficients of the periodical transmission function of grating G_0 (resp. G_2) as defined in Equation 2.61 (resp. Equation 2.36). b_l are the Fourier coefficients of the interference pattern and are linked to the Fourier coefficients B_l of grating G_1 and to the Talbot distance d_m between grating G_1 and G_2 (see Equation 2.7). $\mathcal{D}$ is the detector sensitivity and $\mathcal{S}_{in}$ the number of photons emitted at wavelength λ. $\bar{A}_M$, $\bar{\varphi}_{\ell,M}$ and $\bar{S}_{l,M}$ represent the absorption, refraction angle and ultra-small angle scattering broadening as introduced in Section 2.1.3. η is equal to 1 for $\ell = 0$ and 2 otherwise

The first interesting quantity that can be formed, is

$$T(x,y) \mathrel{\widehat{=}} \frac{Q_o^s(x,y)}{Q_o^r(x,y)} \tag{2.85}$$

$$= \exp\big(-\bar{A}_M(x,y,\lambda)\big) \qquad \text{[monochromatic wave]} \tag{2.86}$$

Clearly, by forming the ratio between the mean Q_0^s with the object in the field of view and the mean Q_0^r without, the influence of the gratings' geometry and variations in the detector sensitivity or beam intensity is essentially removed. The remaining quantity is related to the intensity transmission function of the sample. For this reason, $T(x, y)$ is called the transmission image and is equivalent to the image that would be obtained if the gratings were removed (standard absorption-based radiography).

Secondly, it can be observed that

$$
\begin{aligned}
DP(x, y) &\;\widehat{=}\; \big(\psi_1^s(x, y) - \psi_1^r(x, y)\big)/2\pi && (2.87)\\
&= f(z_s)\bar{\varphi}_{1,M}(x, y, \lambda) \qquad \text{[monochromatic wave]} && (2.88)\\
&= \frac{\lambda z_{12}}{p_2} f(z_s) \frac{\partial \bar{\phi}_s}{\partial x}\Big(\frac{x}{M_s}, \frac{y}{M_s}, \lambda\Big) && (2.89)
\end{aligned}
$$

The image DP, formed by the difference of the phases ψ_1^s and ψ_1^r is thus linked to the phase shift $\bar{\varphi}_{1,M}$ due to the refraction in the sample and, consequently, to the derivative of the phase $\bar{\phi}_s$ along the x-direction. This image is called the differential phase contrast image. Note that the phase variations along the y-direction do not appear in this image.

Finally, let us define the visibility of the phase stepping curve v as

$$
v(x, y) \;\widehat{=}\; \frac{Q_1(x, y)}{Q_o(x, y)} \qquad (2.90)
$$

The visibility is an important parameter of the interferometer and defines its noise performance, as will be seen in Section 3.2. The visibility goes from 1, in the ideal case, to 0, where the phase information is completely lost. Now the ratio of the visibilities v^s and v^r defines the quantity $V(x, y)$:

$$
\begin{aligned}
V(x, y) &\;\widehat{=}\; \frac{v^s(x, y)}{v^r(x, y)} = \frac{Q_1^s(x, y)Q_o^r(x, y)}{Q_o^s(x, y)Q_1^r(x, y)} && (2.91)\\
&= \exp\Big(- \bar{S}_{1,M}(x, y, \lambda) f(z_s)\Big) \qquad \text{[monochromatic wave]} && (2.92)
\end{aligned}
$$

The image $V(x, y)$ is related to the ultra-small angle scattering $\bar{S}$ in the sample along the x-direction and is called the dark field image. This name has been given by association with dark field microscopy (Hecht 2002, Sect. 13.2.5), where a patch stop blocks the zero-frequency component (absorption essentially) such that only the scattered light is imaged onto the detector. As for image DP, the dark field image is insensitive to the ultra-small angle scattering along the y-direction.

Note that, since T and V are exponential functions, it is usual to represent images of the logarithms $-\log(T)$ and $-\log(V)$, which are directly proportional to the thickness and composition of the object.

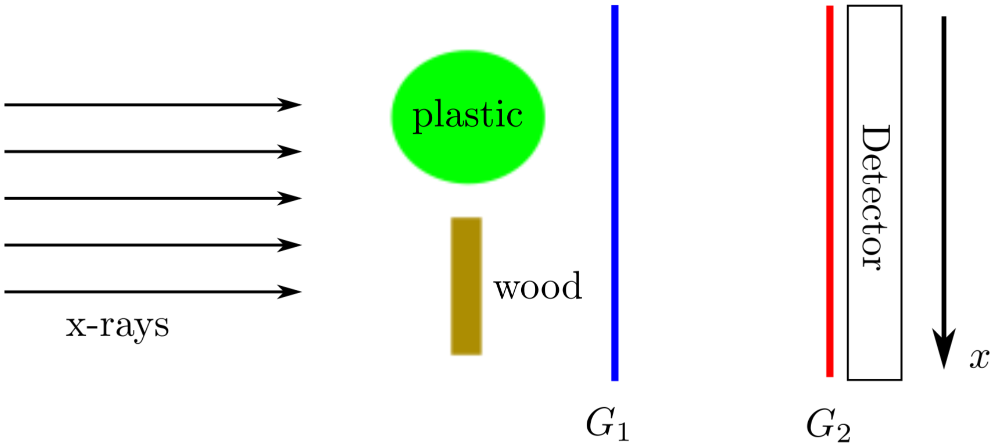

Figure 2.17: *Schematic view of the test sample composed of a plastic rod and a wood plate placed in the field of view of the grating interferometer.*

2.2.2 Image Content

A didactic example of the phase stepping reconstruction method is shown in Figure 2.18 for a sample composed of a plastic rod and a thin wood plate placed next to each other (see Figure 2.17). The reference and sample phase stepping curves are depicted for four different pixels (Figure 2.18-(abcd)) as indicated by the round, square, diamond and triangle markers. The images T, DP and V after reconstruction appear in Figure 2.18-(efg) and will be commented further in the next paragraphs.

The round markers refer to a pixel of the background (i.e. outside the object). In that case, the reference and sample phase stepping curve are identical except for some noise contributions. The coefficients Q_0, Q_1 and ψ_1 stay unchanged, meaning that the transmission T and dark field V are equal to one and the differential phase contrast DP to zero.

The square markers refer to a pixel placed in the middle of the plastic rod. In that case, the change between the reference and sample phase stepping curves is dominated by the absorption in the sample. The mean (coefficient Q_0) is strongly decreased and, consequently, the transmission T is smaller than one.

The diamond markers refer to a pixel at the edge of the plastic rod. The sample phase stepping curve is slightly attenuated but also shifted to the left compared to the reference measurement (coefficient ψ_1). The phase gradient is indeed strong at the edge of the rod and the beam is deflected ("lensing effect"). This angular deflection leads to a phase shift of the phase stepping curve, which translates in the image DP as a bright fringe on the left of the object. Note that fringes of opposed sign (dark) appear on the right of the plastic rod, indicating that the beam is deflected in the opposite direction.

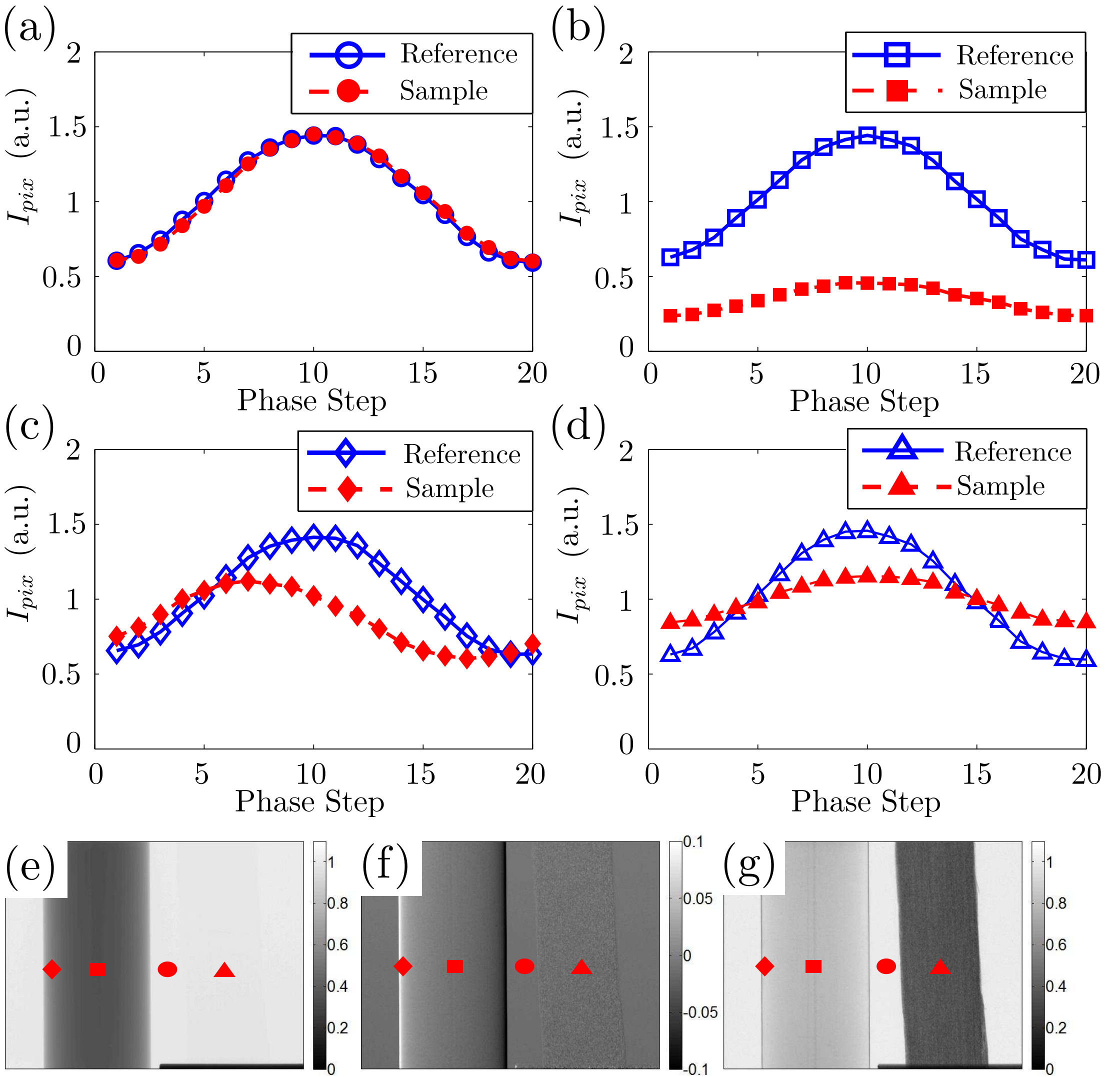

Transmission Image T

Differential Phase Contrast Image DP

Dark Field Image V

Figure 2.18: *Example of the phase stepping reconstruction method for a sample composed of a plastic rod and a thin wood board. The phase stepping curves (intensity as a function of the phase step) are shown for pixels (a) in the background (round markers), (b) in the middle of the plastic rod (square markers), (c) on the side of the plastic rod (diamond markers) and (d) in the middle of the wood plate (triangle markers). The solid blue line indicates the reference measurement while the dashed red line refers to the sample measurement. The mean* Q_0*, amplitude* Q_1 *and phase* ψ_1 *can be extracted by Fourier transform in both the reference and sample cases and used to reconstruct images* T*,* DP *and* V *as shown in (e,f,g). A detailed analysis of this example is provided in the text.*

The triangular markers refer to a pixel placed in the middle of the wood sample. The mean and phase of the sample phase stepping curve are, in that case, unchanged. However, the amplitude is strongly decreased. Let us remember that wood is composed of multiple fibers with sizes on the micron-scale, which induce a strong ultra-small angle scattering. This results in a decrease of the amplitude (coefficient Q_1) of the phase stepping curve and the dark field signal V is reduced.

Note that the three images rely on different physical interactions and, thus, display fundamentally different properties of the object. For example, the plastic rod is well resolved in images T and DP while it gives a weak contrast in the dark field image V. Obviously, due to its differential nature, the image DP provides a strong contrast a the edges of the plastic rod. Conversely, the wood appears most clearly in the dark field image V while it is nearly invisible in the transmission image T. This highlights the complementarity of the three images, which will be discussed further in the next chapters.

The interpretation of the images T, DP, and V given in this section assumes ideal conditions (monochromatic radiation, smoothly varying objects...). In practice, non-idealities do make the quantitative analysis of the images more complex (beam hardening, phase clipping...). Such effects will be discussed in details in Chapter 3.

2.3 Computed Tomography

Any acquired image on a flat panel detector is inherently two-dimensional (2D). The sample, itself, is however a three-dimensional (3D) object and this 3D information gets projected or compressed onto a 2D plane. Such compression leads to a loss of information such that, for example in absorption radiography, a thick object from a light material cannot be distinguished from a thin object of a dense material.

Tomography refers to diverse methods, which allow for the reconstruction of the 3D information from a series of 2D images of the sample acquired under different viewing angles. In radiography, we talk about ”transmission” tomography as opposed to ”emission” tomography, which is used, for instance, in Positron Emission Tomography (PET) and Single Photon Emission Computed Tomography (SPECT).

There are essentially two types of reconstruction algorithms. The iterative algorithms have the advantage of flexibility, since they are based on the minimization of a cost function, which can include some a-priori knowledge on the object. Iterative algorithms (Byrne 2007) are however slow, especially for large data sets, which explains why they are mostly used for specific tasks, such as scatter or motion-artifacts corrections (Isola *et al.* 2010).

The most standard algorithm is called the "Filtered Back Projection" algorithm (FBP) (Kak & Slaney 1999, Chap. 3), which has the advantage of speed and provides good results in most cases. It displays however artifacts, when the data set shows some non-idealities like beam hardening, which will be explained in Section 3.1. In this work, all tomographic reconstructions have been done with the FBP algorithm. In the first paragraph, the concept of Computed Tomography (CT) will be presented and the FPB algorithm will be briefly discussed. The implementation of the FBP algorithm for the different contrast mechanisms (absorption tomography, phase contrast tomography and dark field tomography) will then be described.

2.3.1 Filtered Back Projection Algorithm

Computed Tomography (CT) was invented and developed independently by Cormack in 1963 (Cormack 1963) and Hounsfield in 1973 (Hounsfield 1972; Hounsfield & Ambrose 1973) for medical applications. Their work greatly improved the diagnostic capabilities in various domains and was rewarded by the Nobel Price in Medicine in 1979. The mathematical reconstruction of a function from its projections was however already treated by Radon in 1917 (Radon 1986).

In the following paragraphs, the concept and notations required for the understanding will be introduced. For a detailed description of the mathematics and algorithms, the reader should however refer to textbooks (Kak & Slaney 1999; Buzug 2008).

Let us first formulate the problem for a two-dimensional function $g(x_o, y_o)$, which is projected perpendicularly onto a one-dimensional detector. It is considered that the incoming x-rays form a parallel beam. More realistic situations like fan or cone-beam will be discussed later on.

The starting point is based on the assumption that the x-rays propagate straight through the object as represented in Figure 2.19. The projection p_θ at angle θ can then be expressed as the line integral

$$\begin{aligned} p_\theta(x) &= \int_{\theta,x} g(x_o, y_o) ds & (2.93) \\ &= \int_{-\infty}^{\infty}\int_{-\infty}^{\infty} g(x_o, y_o)\delta(x_o\cos\theta + y_o\sin\theta) dx_o dy_o & (2.94) \end{aligned}$$

Where $x = x_o\cos\theta + y_o\sin\theta$ is the coordinate along the detector line and δ is the Dirac distribution. p_θ is the Radon transform of g and will be acquired with different angles θ by rotating the detector and the source around the object. The ensemble of the projections p_θ is called a sinogram.

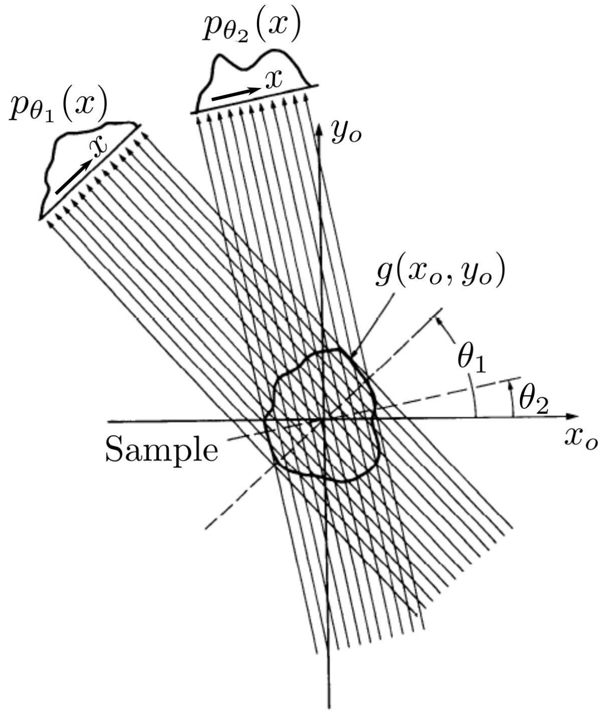

Figure 2.19: *Parallel projections are taken by measuring a set of parallel rays for a number of different angles (adapted from (Rosenfeld & Kak 1982)).*

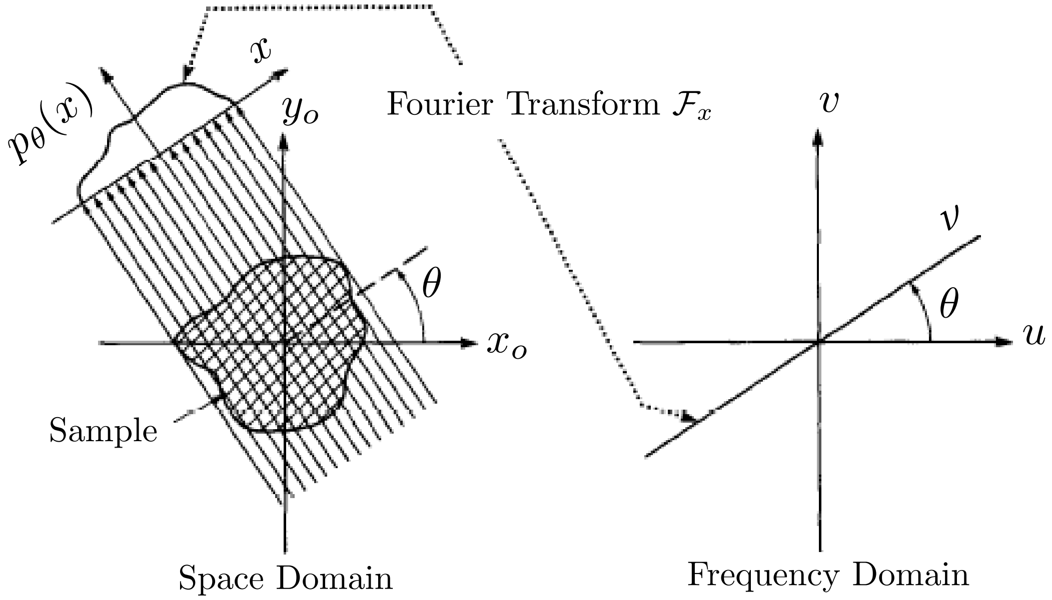

Figure 2.20: *The Fourier Slice Theorem relates the Fourier transform of a projection to the Fourier transform of the object along a radial line (from (Pan & Kak 1983)).*

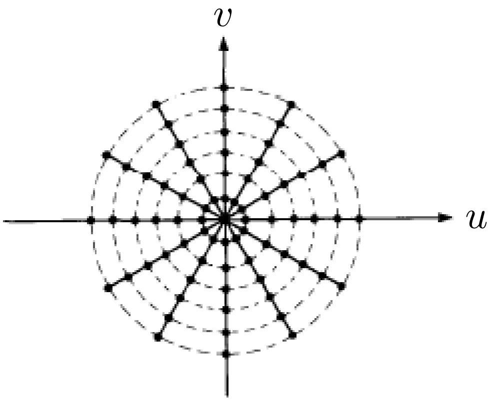

Frequency Domain

Figure 2.21: *Collecting projections of the object at a number of angles gives estimates of the Fourier transform of the object along radial lines. Additionally, the finite number of pixels of the detector implies that the estimates are only known at discrete positions as represented by the dots (from (Pan & Kak 1983)).*

The essence of any reconstruction technique is based on the Fourier Slice Theorem or Central Section Theorem (Kak & Slaney 1999, Sect. 3.2). This theorem stipulates that the one-dimensional Fourier transform $\mathcal{F}_x\big(p_\theta\big)$ of a projection p_θ is equal to the two-dimensional Fourier transform $\mathcal{F}_{x_o,y_o}\big(g\big)$ of function g along a radial line. This is illustrated in Figure 2.20. In mathematical terms, this translates into

$$\mathcal{F}_x\big(p_\theta\big)(\nu) \quad = \quad \mathcal{F}_{x_o,y_o}\big(g\big)(\nu\cos\theta, \nu\sin\theta) \qquad (2.95)$$

A demonstration of this expression is given in (Kak & Slaney 1999, Sect. 3.2). This result indicates that the Fourier transform $\mathcal{F}_{x_o,y_o}\big(g\big)$ can be calculated along radial lines given by the viewing angle θ. Assuming that the projections are known for all θ and x, the Fourier transform $\mathcal{F}_{x_o,y_o}\big(g\big)(u,v)$ can be calculated for any u and v. As a result, the object function g can be exactly reconstructed by taking the two-dimensional inverse Fourier transform of $\mathcal{F}_{x_o,y_o}\big(g\big)$.

In practice, only a finite number of angles $(\theta_n)_{n=1..N}$ are used and the projections are only measured at (discrete) pixel positions. This implies that the Fourier function $\mathcal{F}_{x_o,y_o}\big(g\big)$ is only known on a radial grid as shown in Figure 2.21. Yet, the inverse Fourier transform requires the knowledge of the points along a square grid. The first intuitive solution would be to interpolate the radial grid onto a square grid. However, it can be noticed that the radial grid is denser for the low frequencies than for the high frequencies. As a consequence, the interpolation error gets bigger for high frequencies, which leads to artifacts in the image.

For this reason, more involved algorithms are required to deal with the missing information, like the Filtered Back Projection (FBP) algorithm

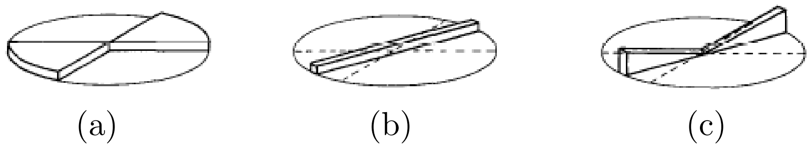

Figure 2.22: *This figure shows the frequency domain available from one projection. (a) is the ideal situation. A reconstruction could be formed by simply summing the reconstruction from each angle until the entire frequency domain is filled. What is acually measured is shown in (b). As predicted by the Fourier Slice Theorem, a projection gives information about the Fourier transform of the object along a single line. The FBP algorithm takes the data in (b) and applies a weighting in the frequency domain so that the data in (c) are an approximation to those in (a). (from (Kak & Slaney 1999)).*

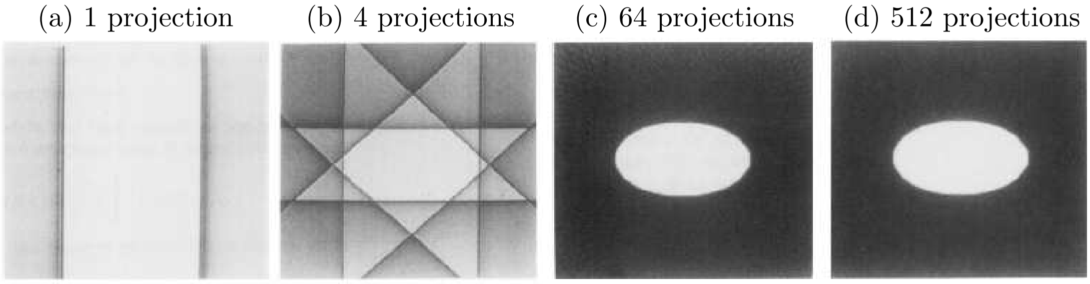

Figure 2.23: *The result of back projecting the filtered projections onto the image plane for (a) a single projection, (b) 4 projections, (64) projections and (d) 512 projections. (from (Kak & Slaney 1999)).*

(Kak & Slaney 1999, Sect. 3.3). The idea behind this algorithm is relatively simple to understand. As has been stated before, the radial grid (Figure 2.21) becomes sparser as the frequency increases. One way to compensate for this loss is to increase the weight of the Fourier components as a function of the frequency by filtering the projections by a ramp filter as shown on Figure 2.22. Now, remembering that each filtered projection represents the values of function g along one line, they can be back projected onto the image plane as illustrated in Figure 2.23 for an elliptic object. As the number of projections (taken under different angles) used in the reconstruction increases, the approximation of the function g improves.

In mathematical terms, the function g can indeed be expressed as (Kak & Slaney 1999)

$$g(x_o, y_o) = \int_0^{\pi} q_\theta(x_o \cos\theta + y_o \sin\theta) d\theta \tag{2.96}$$

$$\text{with } q_\theta(x) = \int_{-\infty}^{\infty} |\nu| \mathcal{F}_x\big(p_\theta\big)(\nu) \exp(j2\pi\nu x) d\nu \tag{2.97}$$

q_θ is the filtered projection of p_θ. The FBP algorithm can be implemented from a set of projection data p_θ acquired for angles θ between 0 and 180° in the following manner.

1. Calculate the Fast Fourier Transform of the projections p_θ.
2. Multiply the Fourier transformed projections by the ramp function.
3. Take the inverse FFT of the results of step 2 to obtain the filtered projections q_θ.
4. Back project the filtered projections into the image space to reconstruct function g.

Note that all steps are computationally efficient and can be accomplished within seconds with a standard office computer. Especially the implementation of the filtering process with the FFT is much faster for large data sets than the convolution operation.

When working with punctual sources, the approximation of a parallel incoming beam does not hold anymore. In that case, the shape of the "fan beam" for line detectors or "cone beam" for flat panel detectors have to be considered (see Figure 2.24). Applying the previous algorithm will induce a blurring of the reconstructed image since the filtered projections will not be back projected at the correct positions in the image space. However, some modifications can be made to account for the shape of the beam as described in (Feldkamp *et al.* 1984; Kak & Slaney 1999) and provide a sharp reconstruction. In this work, both parallel beam and cone beam algorithms have been used, where the cone-beam algorithm was developed in a collaboration with the Swiss Federal Institute for Materials Science and Technology (Empa) (Jerjen *et al.* 2010).

Note also that we restrict here to circular trajectories around the object. Other methods, like helical computed tomography (Buzug 2008, Sect. 8.7), use more complex trajectories in order to image longer object (for example in full-body CT) but are out of the scope of this work.

2.3.2 Absorption Tomography

Let us now investigate the implementation of this algorithm for absorption data. We shall remember (Equations 2.20) that the transmission image T_θ of a sample under the viewing angle θ (as provided by a standard absorption-based radiographic equipment[7] or by the approach presented in Section 2.2.1) is equal, for a

---

[7] By standard absorption-based radiographic equipment, we mean a setup formed by an x-ray source and a detector, where the sample is placed in-between. The transmission image is

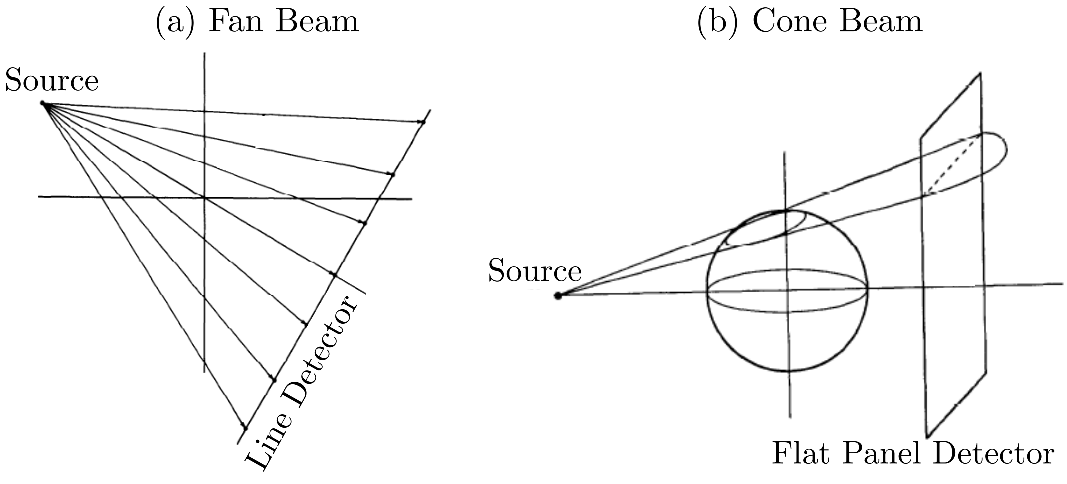

Figure 2.24: *For a point source, the x-rays cannot be considered anymore as a parallel beam. The Filtered Back Projection algorithm has then to take into account the shape of (a) the fan beam for a line detector or (b) the cone beam for a flat panel detector (from (Kak & Slaney 1999)).*

monochromatic source of wavelength λ, to

$$\begin{aligned} T_\theta(x,y,\lambda) &= \exp(-A_{M,\theta}(x,y,\lambda)) && (2.98)\\ \text{with } A_{M,\theta}(x,y,\lambda) &= \frac{4\pi}{\lambda}\int_{path}\beta(x_o,y_o,z_o,\lambda)ds && (2.99)\end{aligned}$$

Where s is the coordinate along the line going from position (x,y) of the detector to the center of the focal spot and (x_o,y_o,z_{1s}) is the coordinate system fixed to the sample, hence rotated (and scaled) compared to the coordinate system (x,y,z) linked to the source-detector system. By introducing the linear absorption coefficient $\mu=\frac{4\pi}{\lambda}\beta$, the quantity $\mathcal{T}_\theta \widehat{=} -\log(T_\theta)$ can be written as

$$\mathcal{T}_\theta(x,y,\lambda) = \int_{\text{path}}\mu(x_o,y_o,z_{1s},\lambda)ds \qquad (2.100)$$

The ensemble of the projections $\mathcal{T}_\theta(x,y_0,\lambda)$ for a given detector row y_0 and a set of angles θ is called a sinogram. An example for a plastic toy (playmobil$^{©}$) is shown in Figure 2.25-a. In Equation 2.100, a line integral of the form introduced in Section 2.3.1 with $p_\theta=\mathcal{T}_\theta$ can be recognized. The Filtered Back Projection algorithm can thus be used to reconstruct quantitatively the cross-section of the three-dimensional linear absorption coefficient μ as depicted in Figure 2.25-b. The full volume is then recovered by repeating the procedure for each detector row (illustrated later in Figure 4.9).

---

then simply equal to the ratio of the image acquired with the object in the field of view and the image acquired without.

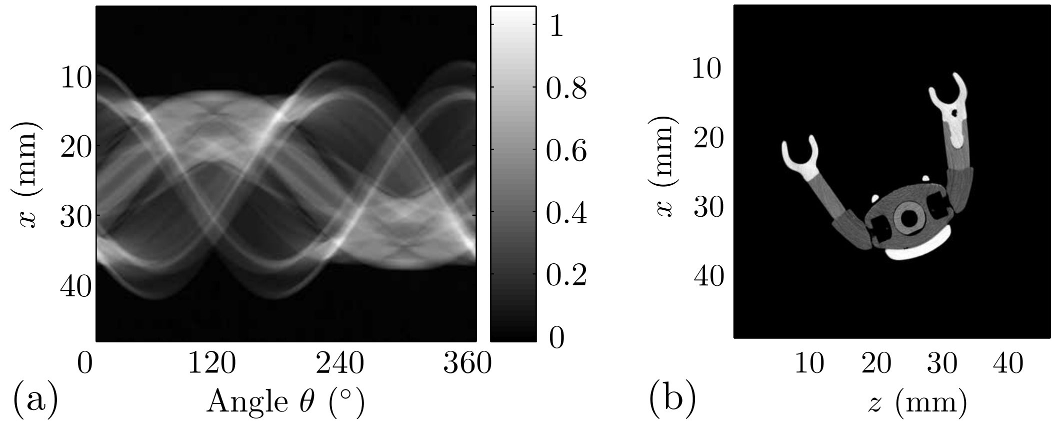

Figure 2.25: *Example of computed tomography realized on a plastic figurine (playmobil©). (a) Sinogram of the values of image $\mathcal{T}$ for a given detector row and a set of angles $\theta = 0...360°$. (b) Corresponding cross-section of the linear absorption coefficient μ reconstructed with the filtered back-projection algorithm.*

Note that in practice, since a polychromatic spectrum is used, Equation 2.100 is only a good approximation but not completely valid. This will lead to beam-hardening artifacts, which will be presented in Section 3.1.1.

2.3.3 Phase Tomography

The differential phase contrast information DP_θ of a sample under the viewing angle θ requires a slightly different treatment due to its differential nature. Indeed, if we consider a monochromatic wave of wavelength λ, Equations 2.88 and 2.20 tell us that:

$$DP_\theta(x,y,\lambda) = \frac{\lambda z_{12}}{p_2} f(z_s) \frac{\partial \bar{\phi}_{s,M,\theta}}{\partial x}\Big(x,y,\lambda\Big) \tag{2.101}$$

$$\text{with } \Phi_{s,M,\theta}(x,y,\lambda) = -\frac{2\pi}{\lambda}\int_{\text{path}} \delta(x_o,y_o,z_o,\lambda)ds \tag{2.102}$$

Again, s is the coordinate along the line going from position (x,y) of the detector to the center of the focal spot and (x_o,y_o,z_o) is the coordinate system fixed to the sample.

One first idea (and the most intuitive) would be to integrate image DP_θ along the x-direction in order to get directly the phase information $P_\theta = \int_x DP_\theta$. In that case, image P_θ is expressed as a line integral and the Filtered Back Projection algorithm can be directly applied without modifications. However, it turns out that the numerical integration of DP_θ leads very often to artifacts in P_θ as can be seen in Figure 2.26. Obviously, such artifacts propagate in the tomographic reconstruction.

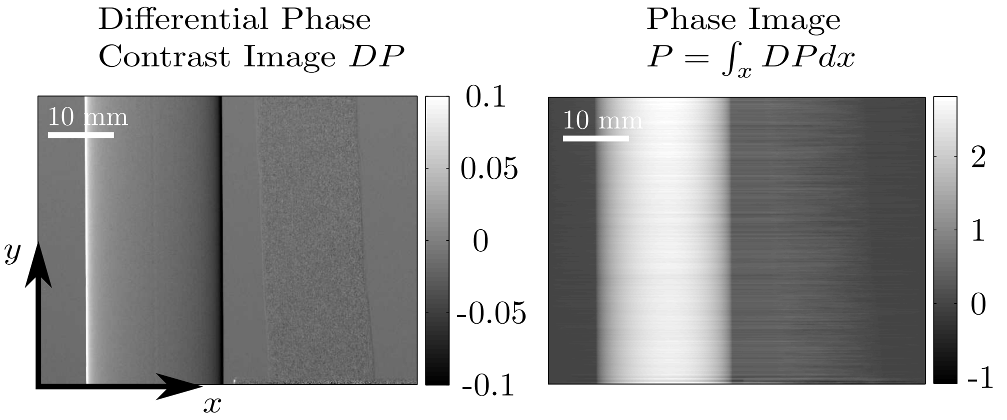

Figure 2.26: *Differential phase contrast image DP (left) and integrated phase image P (right) of a test sample composed of a plastic rod and a thin wood plate.*

Pfeiffer et al. suggested in 2007 (Pfeiffer *et al.* 2007) a method, inspired by the work done by Faris in the visible domain (Faris & Byer 1988), which allows for the reconstruction of the 3-dimensional phase information directly from the differential phase contrast image. This method is based on the observation that $\mathcal{F}_x\Big(\frac{\partial f}{\partial x}\Big)(\nu) = i2\pi\nu\mathcal{F}\big(f\big)(\nu)$. Equation 2.97 can then be rewritten as:

$$f(x_o, y_o) \;=\; \int_0^{\pi} q_\theta(x_o\cos\theta + y_o\sin\theta)d\theta \qquad (2.103)$$

$$\text{with } q_\theta(x) \;=\; \int_{-\infty}^{\infty} \frac{\text{sign}(\nu)}{i2\pi}\mathcal{F}_x\Big(\frac{\partial p_\theta}{\partial x}\Big)(\nu)\exp(j2\pi\nu t)d\nu \qquad (2.104)$$

Where $\text{sign}(\nu) = \frac{|\nu|}{\nu}$ is the sign function equal to 1 for $x > 0$, -1 for $x < 0$ and 0 for $x = 0$. So the derivative $\frac{\partial p_\theta}{\partial x}$ can be used directly in the Filtered Back Projection algorithm provided that the filtering is done with filter $\text{sign}(\nu)/i2\pi$ instead of $|\nu|$.

Now, by introducing the quantity $\mathcal{DP}_\theta \widehat{=} \big(p_2 f(z_s)/z_{12}\big)DP_\theta$, Equation 2.102 transforms into

$$\mathcal{DP}_\theta(x, y, \lambda) \;=\; \frac{\partial}{\partial x}\Big(\int_{\text{path}} -\delta(x_o, y_o, z_o, \lambda)ds\Big) \qquad (2.105)$$

For $p_\theta = \int_{path} -\delta(x_o, y_o, z_o, \lambda)ds$, the modified FBP algorithm presented in Equation 2.104 can be used and allows for the determination of the three-dimensional refraction coefficient δ.

2.3.4 Dark Field Tomography

Finally, we shall consider the case of dark field tomography. From Equations 2.92, 2.30 and 2.33, the dark field image V_θ of a sample under viewing angle θ and for a monochromatic wave of wavelength λ, is equal to

$$\begin{aligned}
V_\theta(x,y,\lambda) &= \exp\big(-f(z_s)\bar{S}_{1,M,\theta}(x,y,\lambda)\big) && (2.106)\\
\text{with } S_{1,M,\theta}(x,y,\lambda) &= \frac{2\pi^2 z_{12}^2}{p_2^2}\int_{\text{path}} \epsilon_\theta(x_o,y_o,z_o)ds && (2.107)\\
\text{and } \epsilon_\theta(x_o,y_o,z_o) &\widehat{=} \frac{p_2^2}{2\pi^2 z_{12}^2}\frac{\partial}{\partial s}\Big[\sigma_{\Phi_f}^2\Big(1-\gamma_\theta\big(\frac{\lambda z_{12}}{p_2},0\big)\Big)\Big](x_o,y_o,z_o) && (2.108)
\end{aligned}$$

Where (x_o,y_o,z_o) is the coordinate system link to the sample. ϵ_θ can be thought of as a linear scattering coefficient, which is related to the variations of the electron density (see Section 2.1.3). Then the quantity $\mathcal{V}$ can be defined as[8]

$$\mathcal{V}_\theta \widehat{=} -\big(2\pi^2 z_{12}^2 f(z_s)/p_2^2\big)\log\big(V_\theta\big) \qquad (2.109)$$

A line integral similar to the case of absorption radiography can be recognized. However, it should be noted that ϵ_θ does depend on the viewing angle θ. The autocorrelation function γ_θ is indeed linked only to the variations along the x-coordinate, which rotates compared to system (x_o,y_o).

Nevertheless, in most cases, the medium is isotropic such that ϵ can be considered as independent of θ and can be reconstructed using the standard FBP algorithm. Note, that σ_{Φ_f} and γ can be decoupled by reconstructing the linear scattering coefficient ϵ for different values of $\lambda z_{12}/p_2$. For anisotropic media, the FBP algorithm will lead to artifacts in the reconstruction.

---

[8] The linear scattering coefficient ϵ has been defined here to be compatible with the definition given in (Bech *et al.* 2010). Our expression is however more general and expresses formally ϵ as a function of the electron density.

CHAPTER
THREE

NOISE ANALYSIS

In Chapter 2, grating interferometry was introduced and it was shown that phase effects can be recovered which are indiscernible with conventional absorption-based x-ray systems. Such phase effects, as given by the differential phase contrast image DP and the dark field image V, rely on fundamentally different physical interactions (refraction and ultra-small angle scattering) and could potentially reveal features previously invisible.

The ability to detect a given feature - for example, a void in an aluminum plate - strongly depends on the exact sample geometry and composition. As a result, this assessment commonly relies on a first experimental trial, which often ends in a loss of time and/or money. This underlines the need for an understanding of the systematic and stochastic errors occurring during the data acquisition and analysis, which determine the measurement sensitivity. Let us restrict the following discussion to the phase stepping reconstruction method introduced in Section 2.2.1. However, most results are directly applicable to other reconstruction methods.

First of all the systematic errors or artifacts, which degrade or distort the different images, are presented in Section 3.1. Their impact and the methods to reduce them are discussed. Secondly, in Section 3.2, a model is developed for the stochastic errors present in the three images T, DP and V. This model includes the noise transfer characteristics of the scintillation-based x-ray detector and the mechanical jitter of the phase stepping stage, which are the two major noise contributions. In conclusion a comparison of absorption versus phase contrast imaging is suggested, in particular with respect to the radiation dose.

3.1 Systematic Errors

In this section, the focus is put on errors made on the recorded images T, DP and V (as defined in Section 2.2), which are of systematic nature. This means that these errors are identical for two different measurements repeated under the exact same conditions. The errors of stochastic nature are discussed in Section 3.2.

The systematic errors usually stem from nonidealities in the acquisition process, which lead to deviations of the reconstructed images compared to the theoretical expectations. These errors are also often called artifacts and lead to a degradation of the image quality. This obviously results in a loss of the measurement sensitivity. In the next paragraphs, fixed pattern noise and beam hardening, which are well-known artifacts for absorption-based radiography, are discussed in the frame of grating interferometry. Furthermore, two specific distortions of the differential phase contrast signal, named phase wrapping and phase clipping, are introduced. The impact of these artifacts on the three-dimensional volumes reconstructed by computed tomography is finally presented and methods to reduce this impact are considered.

3.1.1 Beam Hardening

Beam hardening follows from the energy-dependence of the linear absorption coefficient μ (Kak & Slaney 1999, Sect. 4.1). Indeed, if we consider an x-ray beam of energy spectrum $\mathcal{S}_{in}$ impinging on an homogeneous absorber of absorption coefficient μ and thickness t, the intensity recorded on the detector will be given by

$$I_{pix} = \int \mathcal{D}(E)\mathcal{S}_{in}(E)\exp\big(-\mu(E)t\big)dE \tag{3.1}$$

Where $\mathcal{D}$ is the gain of the x-ray detector. Except at the K-edges of the elements constituting the sample, μ decreases as a function of the energy (Als-Nielsen & McMorrow 2001, Sect. 1.3). Consequently, the photons of lower energies are absorbed more strongly than the high energy ones. The energy spectrum of the x-ray radiation after propagation through the sample $\mathcal{S}_{ex}$ is given by

$$\mathcal{S}_{ex}(E) = \mathcal{S}_{in}(E)\exp\big(-\mu(E)t\big) \tag{3.2}$$

Thus, $\mathcal{S}_{ex}$ is usually shifted toward the higher energies as illustrated in Figure 3.1-a for a 1 mm-aluminum filter placed in the field of view of the source operated with an acceleration voltage of 40 kVp. The shift of the energy spectrum is called beam hardening.

Now, as the thickness of the sample t increases, the spectrum gets harder (shifted toward the high energies). As a result, the measured linear absorption coefficient, defined as $\mu_{eff} \widehat{=} -\log(T)/t$, decreases with the increasing thickness. μ_{eff} can be approximated by (Kak & Slaney 1999, Sect. 4.1)

$$\mu_{eff} \quad \approx \quad \frac{\int \mu(E)\mathcal{S}_{ex}(E)dE}{\int \mathcal{S}_{ex}(E)dE} \tag{3.3}$$

This phenomenon is demonstrated for a plastic (polyvinyl chloride) wedge (sample of triangular shape) placed in the field of view (schematic view shown in Figure 3.1-b). In Figure 3.1-c, the measured signal $-\log(T)$ is plotted as a function of the x-coordinate (solid blue line) as well as the "ideal" signal expected for a monochromatic wave (red dashed line). Instead of displaying a perfectly triangular profile, the measured signal is "rounded" as a consequence of beam hardening.

Obviously, beam hardening will also impact on the images DP and V. In Figure 3.1-d, the differential phase contrast signal DP is plotted as a function of the x-coordinate for the same plastic wedge. For a monochromatic beam, one would expect to see a perfect rectangular shape (red dashed line) since the differential phase contrast is proportional to the first derivative of the phase shift (Equation 2.89). The latter is indeed constant - for each side of the wedge - in the present case. However, the measured signal (solid blue line) decreases as a function of the thickness. Again, the refraction coefficient δ of the homogeneous sample is a decreasing function of the x-ray energy (Als-Nielsen & McMorrow 2001, Sect. 1.3). The same argument presented for the linear absorption coefficient in the previous paragraph (beam hardening of the energy spectra) holds for the measured refraction coefficient and explains the observed decrease as a function of the thickness.

Finally, the dark field signal $-\log(V)$ is illustrated in Figure 3.1-e. In the monochromatic case, the visibility is not expected to change since the plastic sample is essentially homogeneous (no ultra small angle scattering). Thus, the signal $-\log(V)$ is supposed to stay null (dashed red line). However, the measured signal (solid blue line) displays a pronounced triangular shape. Indeed, the visibility $v = Q_1^s/Q_0^s$ (Equation 2.90) depends strongly on the photon energy and, in most cases, decreases when the mean energy of the spectrum increases due to the beam hardening[1]. This explains the observed increase of signal $-\log(V)$.

---

[1] The coefficients a_1 and c_1 introduced in Equations 2.36 and 2.61 decrease monotonically with the x-ray energy E. On the other hand b_1 (Equation 2.8) is optimized for the design energy E_{des} defined in Section 2.1.2 such that the phase grating G_1 induces a $\pi/2$ phase shift. So, if the center of gravity of the input x-ray spectrum $\mathcal{S}_{in}$ lies at or above the design energy E_{des}, the visibility will be reduced in the presence of an absorbing sample due to the shift of $\mathcal{S}_{ex}$ towards higher energies. However, in some cases where the center of gravity of the spectrum lies below E_{des}, the visibility can be increased.

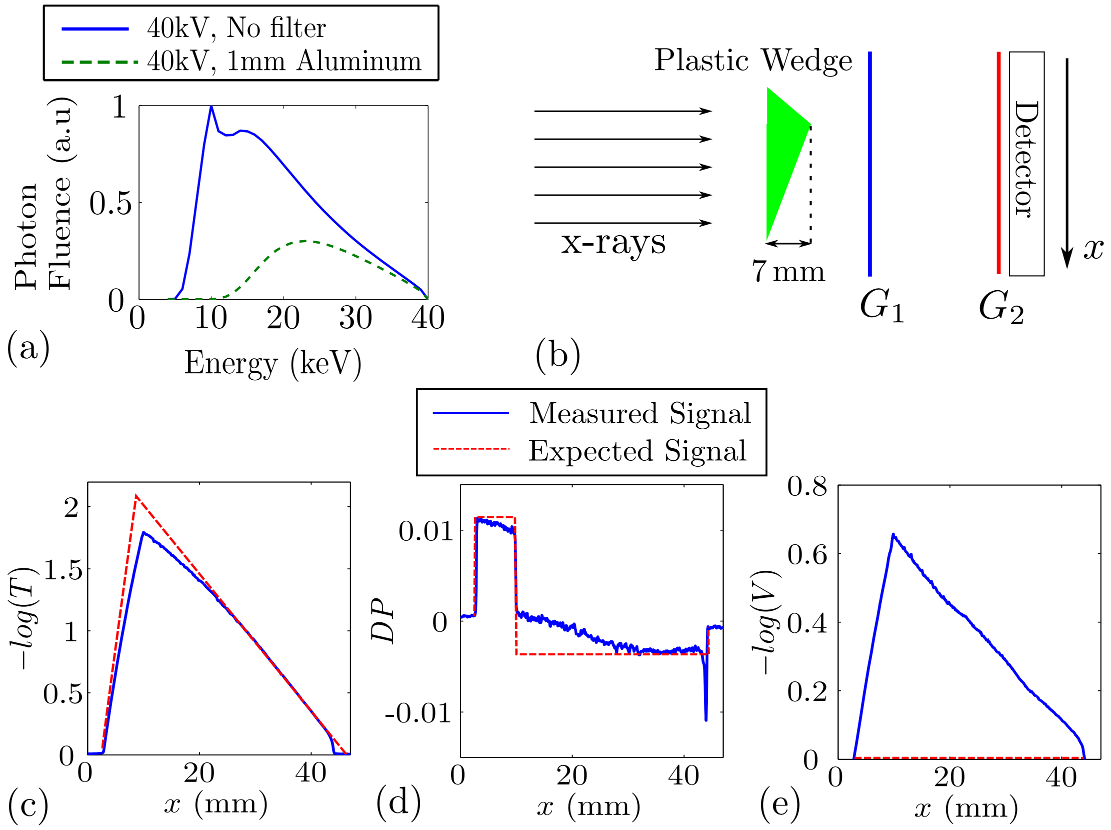

Figure 3.1: *(a) Normalized energy spectra of the x-ray tube with and without a 1mm-aluminum filter for an acceleration voltage of 40kVp simulated with the software SpekCalc (Poludniowski et al. 2009). (b) Schematic view of the setup with a plastic wedge in the field of view. The acquired signals* $-\log(T)$*,* DP *and* $-\log(V)$ *are plotted in (c), (d) and (e), respectively. The solid blue line (resp. dashed red line) represents the measured (resp. expected) signal. The measured signal is distorted due to beam hardening artifacts.*

Beam hardening artifacts can be partially compensated either by pre-processing of the data (correction of the signal by an empirical function), post-processing of the data (iterative algorithms) and by dual or multiple energy schemes (Kak & Slaney 1999, Sect. 4.1). A recent work by (Chabior *et al.* 2011) suggests an empirical correction to reduce beam hardening artifacts in the differential phase contrast image.

3.1.2 Fixed Pattern Noise

Fixed Pattern Noise (FPN) refers here to all (temporally constant) spatial variations of the pixel intensities recorded by the detector under an uniform illumination. FPN stems thus from differences in the responsivity of individual pixels. Looking at a simplified model as depicted in Figure 3.2, the conversion by the detector of the incoming photons into Arbitrary Digital Units (ADU) involves a number of conversion stages. The incoming photons are characterized by the spectrum $\mathcal{S}(E)$, considered to be uniform over the field of view.

The overall gain[2] of the detector is defined as

$$\begin{aligned} \mathcal{D}_0 &\mathrel{\widehat{=}} I/\mathcal{S}_0 \qquad (3.4) \\ \text{with } \mathcal{S}_0 &\mathrel{\widehat{=}} \int \mathcal{S}(E)dE \qquad (3.5) \end{aligned}$$

S_0 is the total number of photons impinging on the detector pixel during the exposure time. $\mathcal{D}_0$ ensues from the different conversion gains (scintillation, light collection, photo-diode quantum efficiency, amplifiers...). In addition, the photo-diode usually produces a so-called dark current, which adds to the photo-generated electrons. The dark current is due mainly to the background radiation and to the saturation or leakage current of the photo-diode. It results in an intensity I_{dark} (often called the dark field), which is summed onto the signal generated by the x-ray photons. The dark field is independent of the illumination but varies with the integration time and temperature.

$\mathcal{D}_0$ and I_{dark} depend among others on the scintillation crystal doping, the size of the pixel, the photo-diode junction and the amplifier gain. As a result, both $\mathcal{D}_0$ and I_{dark} vary from pixel to pixel since each pixel displays slightly different parameters from another due to the fabrication process. These variations can be partially corrected for by a calibration process.

First, I_{dark} is measured by recording the intensity without illumination (x-ray source off) and then subtracted from the output signal I_{pix}. This is called the

---

[2] Note that the stochastic variations of the different signals and gains are not taken into account here. Thus, only the average values of the gains and signals are considered.

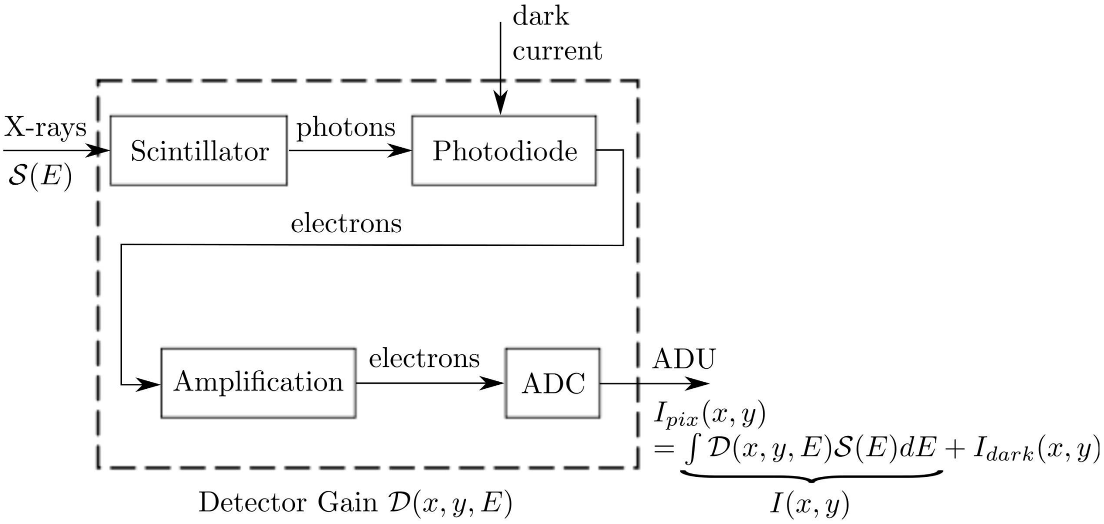

Figure 3.2: *Simple model of the x-ray detector illustrating the different conversion stages involved. ADC stands for Analog-to-Digital Converter and ADU for Arbitrary Digital Units.*

dark current correction, which lowers significantly the non-uniformities in the signal.

$$I \;=\; I_{pix} - I_{dark} = \int \mathcal{D}(x,y,E)\mathcal{S}(E)dE = \mathcal{D}_0\mathcal{S}_0 \tag{3.6}$$

Secondly, a map of the intensity I^r (with dark current correction) is acquired with illumination but without a sample in the field of view. The intensity I^s (with dark current correction) with sample can then be normalized as

$$\begin{aligned} T_{norm} = \frac{I^s}{I^r} &= \frac{\mathcal{D}_0^s}{\mathcal{D}_0^r}\frac{\int \mathcal{S}(E)\exp\big(-\mu(E)t\big)dE}{\int \mathcal{S}(E)dE} & (3.7)\\ &\sim \exp\big(-\mu_{eff}t\big) & (3.8)\end{aligned}$$

Where it was assumed that the sample is uniform of thickness t and linear absorption coefficient $\mu(E)$. In Equation 3.7, the gain $\mathcal{D}_0$ appears both in the numerator and denominator. In a first order, $\mathcal{D}_0^s$ is equal to $\mathcal{D}_0^r$ and the impact of the gain is removed from T_{norm}, which is equal to the transmission image, where μ_{eff} is the effective linear absorption coefficient, as introduced in Section 3.1.1. Note that this "bright field correction" is automatically built in the phase stepping reconstruction method (Equation 2.85).

Although the differences in gain are strongly reduced in this way, some non-uniformities usually remain. On the one hand, the photo-response curve[3] is not

---

[3] The photo-response curve is the curve of the output intensity I in ADU as a function of the input photon flux $\mathcal{S}_0$.

perfectly linear, particularly for low recorded intensities. Since this non-linearity behavior varies for different pixels, FPN do appear. This issue can be partially accounted for by doing a quadratic correction of the photo-response curve[4]. It is however impossible to fully correct the intensity signal and some non-uniformities are left.

On the other hand, the gain $\mathcal{D}_0$ varies also with the energy of the incoming x-rays since the absorption efficiency and the number of re-emitted photons per x-ray quanta of the scintillator are a function of the x-ray energy (see Section 3.2.4 for the experimental proof). Again, this phenomena is not corrected for in Equation 3.7.

In summary, FPN can be reduced by proper calibration methods but some non-uniformities do remain in the acquired intensities I. The calculation of the transmission T with the phase stepping reconstruction algorithm (Equation 2.85) is directly affected by the FPN. In Figure 3.3, it can be seen that our detector displays a FPN, which shows a vertical pattern. This hints at non-uniformities in the amplification stage, which is done column-wise in this detector architecture. This phenomenon is particularly pronounced for strongly absorbing samples.

However image DP (Equation 2.88)) is not strongly affected by FPN since the calculation of the phase (Equation 2.80) does not depend on the amplitude or mean of the phase stepping curve[5]. Consequently, variations of the gain do not affect image DP in the first order.

Similarly, the visibility (see Equation 2.90), which is formed by the ratio of the amplitude of the phase stepping curve divided by its mean, is essentially independent on the gain. Indeed the intensities recorded during the phase stepping curve are all of the same order of magnitude and are acquired with the same energy spectrum, thus with a similar gain. In conclusion, the phase contrast image DP and dark field image V usually do not show FPN while image T is affected.

3.1.3 Phase Wrapping and Clipping

Phase Wrapping

Phase wrapping follows from the 2π-phase ambiguity which results from the calculation of the argument of a complex number $\exp(i\Delta\phi)$. The calculated signal $\Delta\phi_{meas}$ is indeed "wrapped" into the interval $[-\pi;\pi]$ and is equal to $\Delta\phi_{meas} = \Delta\phi + m2\pi$, where integer m is unknown in practice.

---

[4] The quadratic correction consists in fitting the photo-response curve by a quadratic function, for each single pixel. In this way, the non-linearities are partially accounted for.

[5] For example, scaling a sine curve or adding a constant does not impact on the phase calculation.

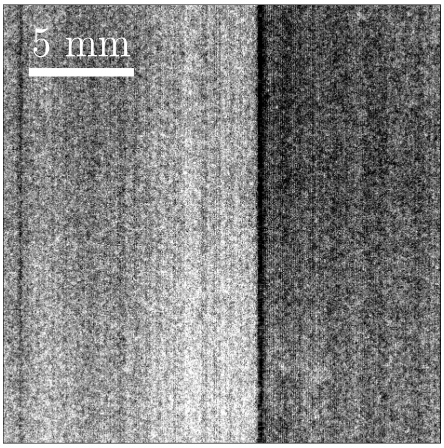

Figure 3.3: *Image T of a 3 mm-aluminum plate showing Fixed Pattern Noise in the form of vertical stripes. The latter could be attributed to variations of the gain of the column amplifier.*

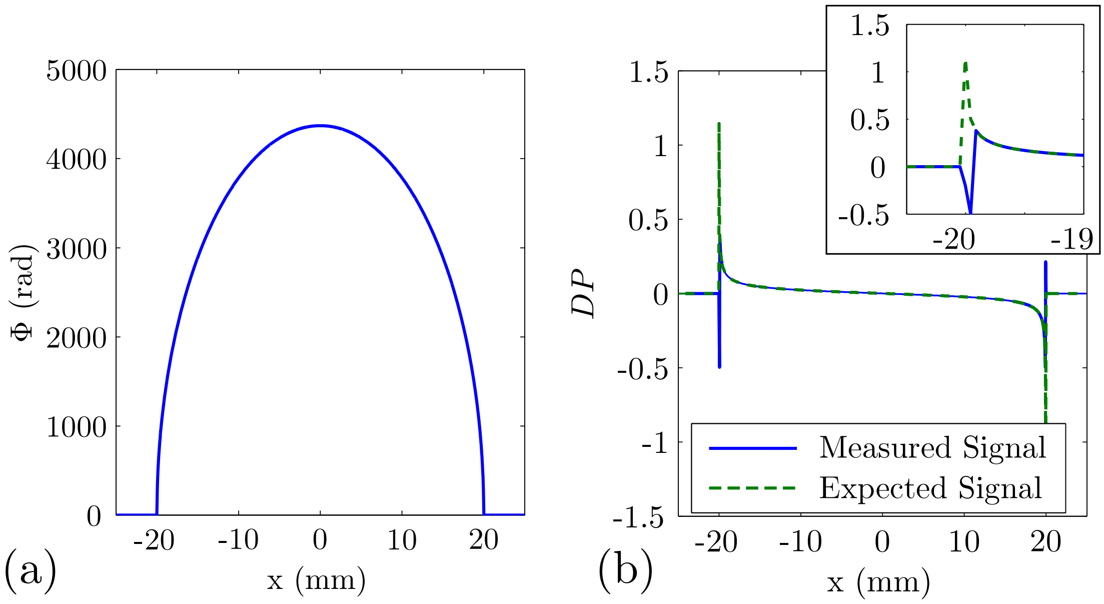

Figure 3.4: *(a) Simulated phase shift of the x-ray beam after propagation through a 40 mm diameter aluminum cylinder under the conditions described in the text. (b) Plot of the simulated signal DP as a function of coordinate x. The green dashed line represents the expected signal while the blue solid line shows the signal after phase wrapping. A zoom around one edge of the cylinder is plotted in the inset.*

In the differential phase contrast signal, phase wrapping occurs when the absolute value of the phase signal $\Delta\varphi = \varphi^s - \varphi^r$ gets higher than π, i.e. when the angular deviation is such that the interference pattern is laterally shifted by more than one period of grating G_2. For an homogeneous sample, this translates into the condition (see Chapter 2)

$$\frac{\Delta t}{p_{pix}} > \frac{p_2}{2z_{12}f(z_s)\Delta\delta} \tag{3.9}$$

where Δt is the average thickness variation of the sample over one pixel, p_{pix} is the pixel size, $\Delta\delta$ is the difference of refraction coefficient between the sample and the medium, p_2 is the periodicity of the analyzer grating G_2, z_{12} is the distance between gratings G_1 and G_2 and $f(z_s)$ is defined in Equation 2.51.

As an example, let us consider a sample made out of aluminum acquired with an interferometer such that $p_2 = 3\,\mu\text{m}$, $z_s = 0\,\text{mm}$ and $z_{12} = 69\,\text{mm}$. Equation 3.9 becomes then $\frac{\Delta t}{p_{pix}} > 16$ for a photon energy of 20 keV. This, of course, happens solely at abrupt interfaces. In Figure 3.4, phase wrapping was simulated for an aluminum cylinder of diameter 40 mm placed in air. The phase is depicted in (a) as a function of coordinate x, while the signal DP is shown in (b). The dashed green line represents the expected signal while the solid blue one is the simulated wrapped signal (the one that would be measured experimentally). A zoom at one edge of the cylinder is shown in the inset, where the phase wrapping artifact appears.

Phase Clipping

Phase clipping refers to a deformation of the signal due to the averaging of the phase over one pixel. Coming back to Equation 2.39 and considering a pure phase object illuminated by a parallel beam, the pixel intensity simplifies to:

$$\begin{aligned} I^s_{pix,par}(x,y,\lambda) &\sim \mathcal{D}\sum_\ell c_\ell b_\ell \times \\ &\int PSF(x-x',y-y')\exp\big(i\ell\phi\big)dx'dy' \end{aligned} \tag{3.10}$$

So it is seen that the impact of the phase variations are given by the terms

$$k_\ell \widehat{=} \frac{1}{p_{pix}}\int PSF(x-x',y-y')\exp\big(i\ell\phi\big)dx'dy' \tag{3.11}$$

where the integral is normalized by the pixel size p_{pix}. When the variations of the phase are slow compared to the pixel size, we have $|k_1| = 1$ and $\arg(k_1) = \phi$. However, when the variations of the phase are fast compared to the pixel size, the averaging of the complex exponential terms can result in a decreased amplitude, i.e. $|k_1| < 1$ (hence a loss of visibility), as well as a change in the phase signal $\arg(k_1) \neq \phi$.

Note that this phenomena is similar to the ultra small angle scattering (USAS) introduced in Section 2.1.3 in the sense that both effects result from the averaging of fast phase variations. However, in USAS, the phase variations are considered to be fast compared to the grating periodicity (in the order of some microns) and lead to loss of the interference pattern itself. In phase clipping, the interference fringes are preserved but the averaging over one detector pixel (in the order of tens of microns) leads to a loss of the visibility of the phase stepping curve and to a distorted phase signal. It should however be underlined that, in practice, the micro-structure of the sample often induces phase variations both at the length scale of the grating periodicity and of the pixel size. In that case, small angle scattering and phase clipping occur simultaneously and cannot be distinguished from each other. In the model introduced in Chapter 2, this is accounted for by the term $\bar{S}_\ell$ introduced in Equation 2.40, which includes both ultra-small-angle scattering and phase clipping.

Phase clipping can be particularly pronounced and detrimental for samples with strong edges. Indeed, when an edge is closely aligned with the x-ray beam direction, it can happen that, over one pixel, part of the x-rays are strongly deviated while the rest are not. In the averaging process, the signal then gets lost.

This is illustrated in Figure 3.5 by the example of an aluminum piece. The sample, as depicted in (a), is composed of two aluminum plates welded together at a right angle. It is oriented in such a way that three edges (one on each side and one in the middle) are closely aligned with the beam propagation direction. Each edge induces strong phase jumps, which in an ideal case should appear in the differential phase image in the form of strong peaks.

However, in the acquired signal DP, only the right edge appears clearly while the middle edge looks reduced and the left one is nearly suppressed. This phase loss is accompanied by a loss of visibility, which is revealed by large peaks in the dark field signal V. Note that the edges are then highlighted in the dark field image. This property is sometimes called ”edge enhancement”.

3.1.4 Impact and Comparison

Precision of Dark Field Imaging

Although, much effort has been dedicated in the literature to the understanding of the dark field image (Chen *et al.* 2010; Yashiro *et al.* 2010; Bech *et al.* 2010), none of the models includes all observed features. As was seen in the previous paragraphs, three different phenomena, namely ultra small angle scattering, beam hardening and phase clipping, impact on the measured dark field signal. These phenomena are in practice difficult to distinguish from another and make the quantitative analysis often challenging. However, the qualitative information

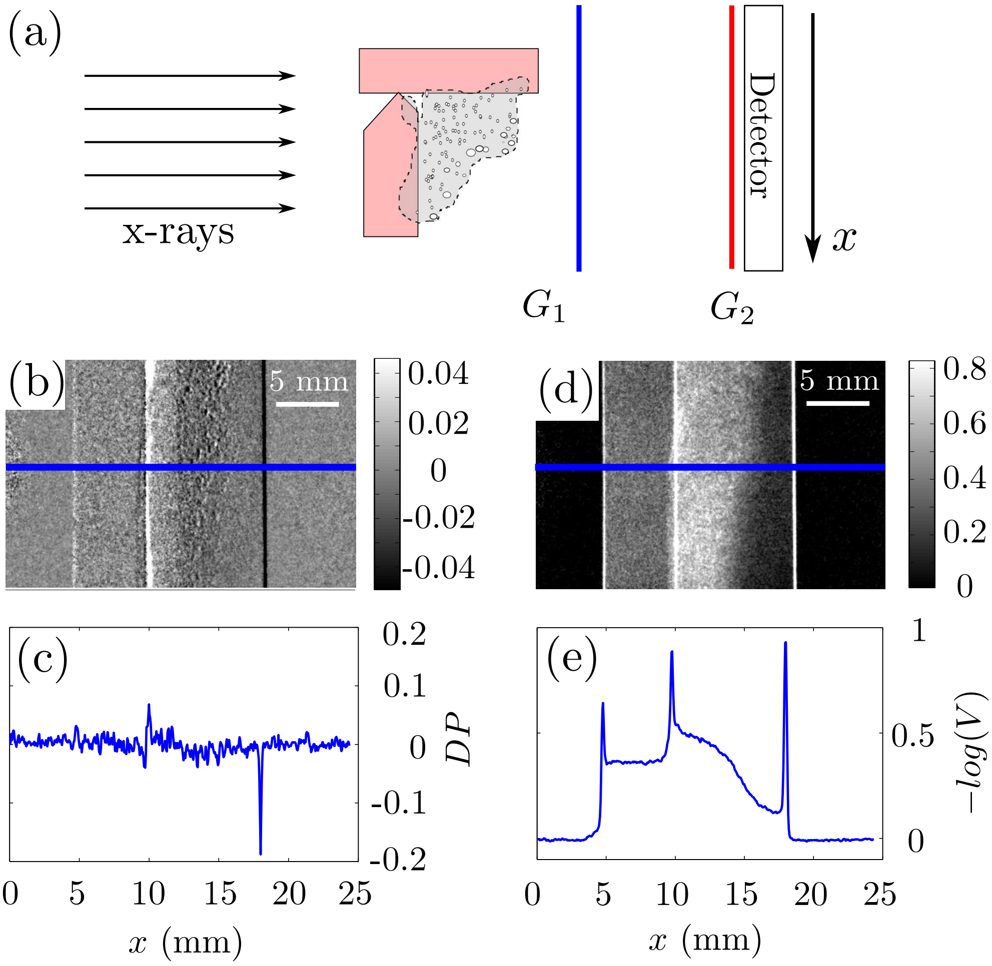

Figure 3.5: *(a) A sample composed of two aluminum plates welded together is placed in the field of view. Image DP (respectively V) as well as a cross section along the blue line are depicted in (b) and (c) (respectively in (d) and (e)).*

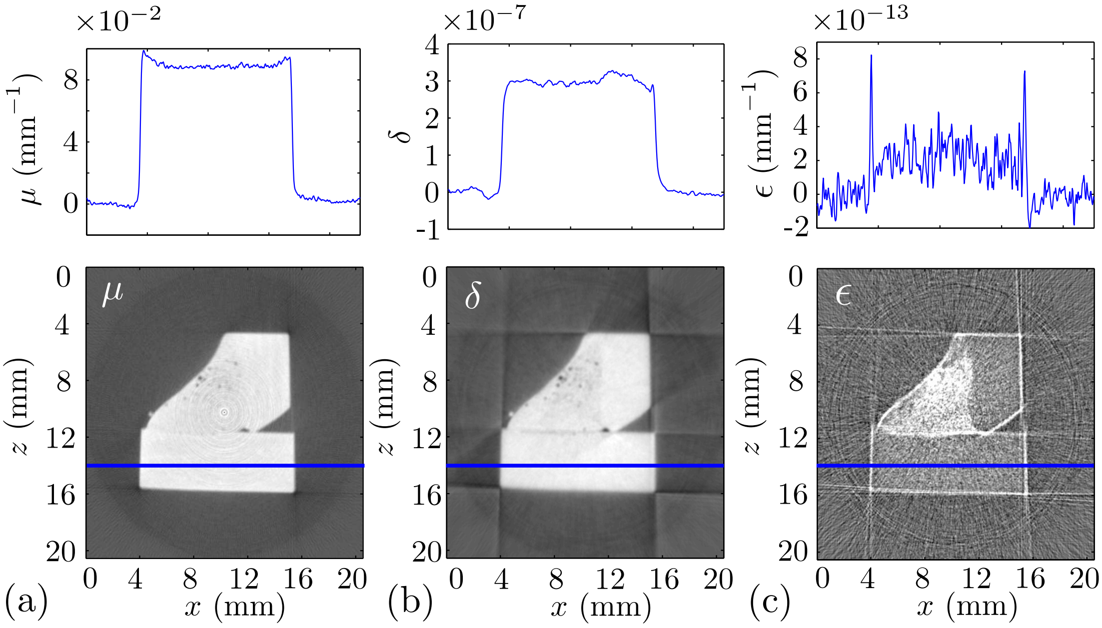

Figure 3.6: *Axial slice within the reconstructions of the (a) linear absorption coefficient μ, (b) refraction coefficient δ and (c) linear scattering coefficient ϵ for an aluminum piece using the filtered back projection algorithm presented in Section 2.3. Plot of μ, δ and ϵ along coordinate x at the position of the solid blue line are drawn at the top.*

contained in the dark field image is particularly valuable in some applications as will be seen in Chapter 5.3.

Tomographic Reconstruction

Let us finally discuss the impact of the presented systematic errors onto the three-dimensional reconstructions of the linear absorption coefficient μ, refraction coefficient δ and linear scattering coefficient ϵ as obtained by computed tomography (see Section 2.3). For this purpose, a computed tomography was realized for the aluminum weld sample introduced in Figure 3.5-a.

As shown in Figure 3.6-a, the reconstruction of μ displays essentially two types of artifacts. First are the ring artifacts, which appear as concentric circles in the middle of the object. They are the consequence of the fixed pattern noise (FPN) of the detector (see Section 3.1.2), which causes a consistent underestimation or overestimation of the linear absorption coefficient in each projection (Buzug 2008, Sect. 9.6.5).

The second dominating effect is the cupping or dishing artifact (Kak & Slaney 1999, Sect. 4.1), which appears as an underestimation of the linear absorption coefficient in the middle of an homogeneous sample while it should be constant. This can be seen, for example, in the plot of μ as a function of coordinate x in Figure 3.6-a, where μ is larger close to the edges than in the

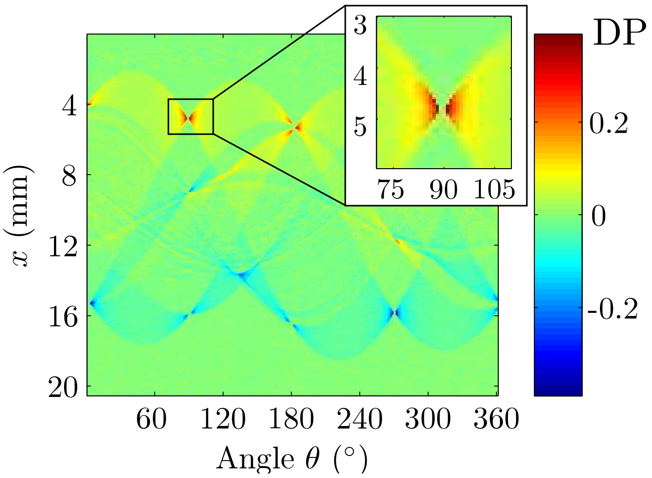

Figure 3.7: *Sinogram of the differential phase contrast signal DP as a function of the projection angle for the aluminum sample. The inset shows a zoom around one of the edges between angle $75°$ and $105°$.*

middle. Cupping artifacts are due to beam hardening (see Section 3.1.1). Indeed, the x-rays passing through the middle of the objects are more hardened[6] than those passing through the sides. As a result, the measured linear absorption coefficient μ_{eff} is lower in the middle than on the sides.

As illustrated in Figure 3.6-b, the dominating artifacts in the reconstruction of δ are the streaks or bands, which form close to the edges of the sample. These streaks propagate inside and outside the object and cause serious errors in the reconstructed δ. This can be observed in the plot of δ, where ideally a rectangular shape would be expected. However, δ is distorted for example around position $x = 3$ mm (outside) and around position $x = 13$ mm (inside). These artifacts are the consequence of phase wrapping and clipping (see Section 3.1.3), which cause a loss of the phase signal over some projection angles. This is highlighted in the inset in Figure 3.7, which shows the sinogram[7] of image DP for one detector row. Clearly, around angle 90°, the DP signal seems interrupted. This missing DP signal will result in errors in the filtered back-projection for those angles. Note also that the edges of the sample do not appear as sharp in δ as in μ as a consequence of the DP signal loss.

The reconstruction of ϵ, presented in Figure 3.6-c, displays bright streaks extending from the sides of the sample. The latter follow from the so-called edge enhancement caused by phase clipping, which results in a large dark field signal

---

[6] Hardened means that the x-ray energy spectrum is shifted to higher energies as introduced in Section 3.1.1.

[7] As a reminder, the sinogram is the visualization of the signal for one detector row as a function of the projection angle as acquired by computed tomography.

V at the edges of the sample. However, edge enhancement is a pure geometrical effect and does not ensue from a line integral. Thus, the assumption of the filtered back projection algorithm is not fulfilled and leads to errors in the reconstructed ϵ.

As already mentioned, the differential phase contrast and dark field images are less sensitive to fixed pattern noise and, consequently, δ and ϵ do not show ring artifacts in the object. Note that the rings appearing at the edges of the reconstructed slice in Figure 3.6-c are due to boundary effects at the end of the field of view and not to fixed pattern noise.

Other artifacts in CT

There are a number of artifacts that generally affect the reconstruction from computed tomography in addition to the ones presented before (Buzug 2008, Sect. 9.6), as for example

- Under-sampling or aliasing artifacts, which are due either to a lack of projection angles or an insufficient detector resolution. They appear as streaks or bands appearing close to the edges of the reconstructed structure.
- Scatter artifacts, which are due to the Compton scattering of the x-ray beam within the sample, usually appear as streaks behind highly scattering objects.
- Incomplete projections, which occur when the sample is larger than the field of view. The missing information will lead to streaking or shadowing artifacts.

These artifacts are similar for absorption-based radiography and phase contrast radiography. Moreover, they are not the dominant effects in the reconstructed volumes presented in this thesis and, as a consequence, will not be discussed in detail.

Artifact Reduction

The previous paragraph illustrated the typical artifacts that penalize the reconstruction of μ, δ and ϵ. In some cases, their impact can be particularly detrimental and destroys the original information. Thus, it is necessary to find ways of reducing or suppressing these artifacts in order to provide images of industrial quality.

Methods to correct for beam hardening/cupping and fixed pattern noise/ring artifacts were mentioned in Sections 3.1.1 and 3.1.2, respectively. Here, the focus is put on the reduction of phase wrapping and clipping artifacts.

One technique consists in immersing the object into a fluid whose refraction coefficient is close to that of the sample. In this way, the jump at the edges of

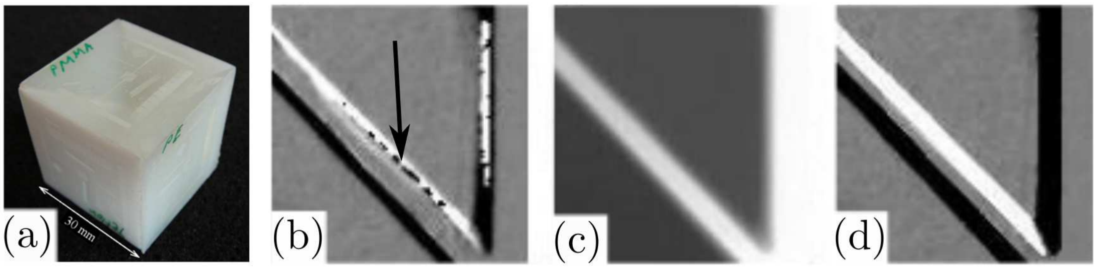

Figure 3.8: *Illustration of the phase clipping correction. (a) Photograph of the test cube composed of different plastics. (b) Image DP before correction, (c) the image T used for the correction and (d) the corrected image DP of one of the interfaces of the test cube at a given projection angle (adapted from (Jerjen et al. 2011)).*

the sample is decreased, which prevents the formation of phase wrapping and clipping artifacts. Such a method performs well and has been used in various measurements presented later in this thesis. However, it is not implementable in numerous applications, where the sample cannot be immersed.

Another way consists in correcting the phase wrapping and clipping errors in image DP thanks to the absorption contrast image[8]. Iwan Jerjen from Empa developed a correction algorithm for phase clipping and wrapping artifacts for grating interferometry - the first of this kind to our knowledge. I realized the measurements of a test sample to experimentally demonstrate the improvements of the algorithm. This work has been published in (Jerjen *et al.* 2011).

The basic idea is to correct the erroneous projections DP thanks to the absorption contrast images T. In principle, a numerical derivative of the logarithm of image T is used to identify the pixels where the signal changes abruptly (at the edges of the sample) by applying a threshold. Then, at these locations, the value of image DP is replaced by the value of the numerical derivative of the logarithm of image T multiplied by a factor, which depends on the materials at the interface[9].

However, most samples are composed of different materials. Thus, the material-dependent factor should be adapted to each interface. In practice, this is however not realizable and it was chosen to take the factor corresponding to the interface with the largest difference of refraction coefficient. This follows from the observation that the phase wrapping and clipping artifacts are stronger for larger differences of indexes of refraction. As a consequence, the strongest artifacts will be correctly accounted for in the algorithm, while the value of signal DP will be slightly under- or over-evaluated at other interfaces.

---

[8] Note that the transmission image T is obtained simultaneously and does not require an additional measurement.

[9] For example, air and teflon.

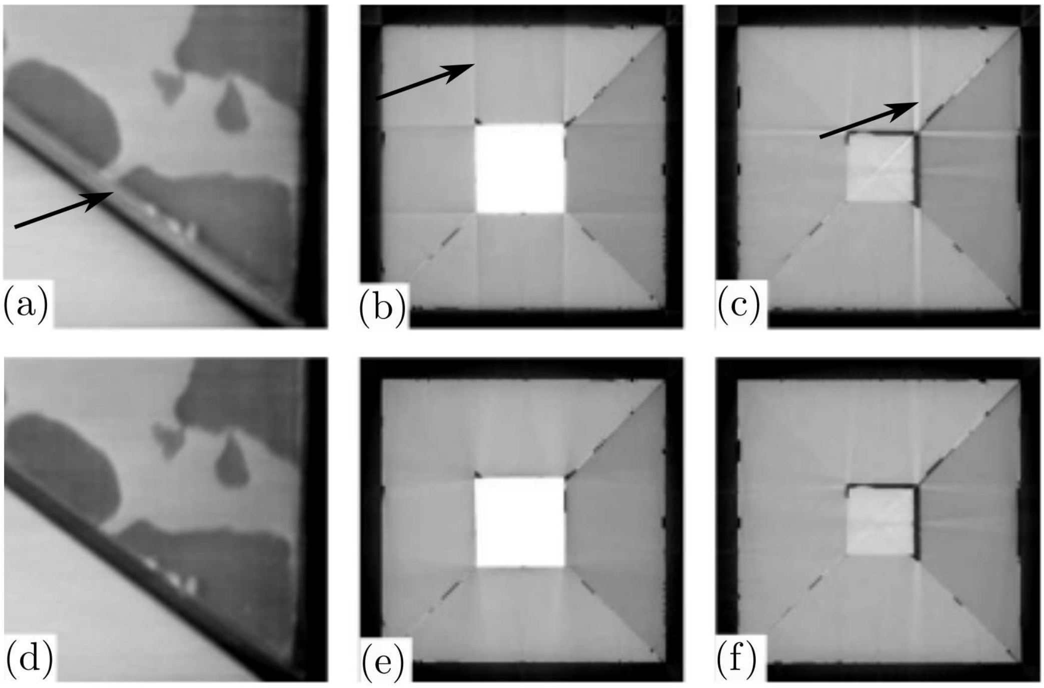

Figure 3.9: *(a), (b) and (c) are slices within the three-dimensional volume of δ reconstructed with the filtered back-projection algorithm without implementing the phase wrapping and clipping correction algorithm. (d), (e) and (f) show the same slices after correction (adapted from (Jerjen et al. 2011)).*

In order to evaluate the performance of the algorithm, a test cube ($30 \times 30 \times 30\,\mathrm{mm}^3$) assembled from six pyramids made of different plastics (polyethylene PE, polycaprolactam PA6, nylon PA66, plexiglass PMMA, polyoxymethylene POM, and teflon PTFE) was investigated. This test cube depicted in Figure 3.8-a was chosen since it shows a multitude of interfaces between different materials. The measurements were realized on setup **S20-4** (see Section 4.3) for an acceleration voltage of 40 kVp. 722 projection angles were acquired, evenly distributed over 360° and T and DP were reconstructed at each angle from a series of 10 phase steps. The exposure time for each step was set to 6.7 s.

Figure 3.8-b displays the image DP at one interface within the object. Phase wrapping and clipping artifacts can be observed as indicated by the black arrow, for example. Figure 3.8-c shows the corresponding image T used in the correction algorithm and Figure 3.8-d the image DP after applying the correction algorithm. Clearly, the artifacts have been strongly reduced.

Secondly the three-dimensional volume δ was reconstructed using a Feldkamp algorithm adapted for the differential phase contrast tomography (Feldkamp *et al.* 1984; Jerjen *et al.* 2010) where the cone beam geometry is taken into account (see Section 2.3.1). The top row of Figure 3.9 shows three different slices within the volume of δ obtained without applying the correction algorithm. The bottom row illustrates the same slices after correction.

In Figure 3.9-a, the junction between two plastic pyramids can be seen. The darker regions indicate the position of the glue used to bind the pyramids together. The gap between the two plastics (diagonal dark band) appears to be erroneously filled as marked by the black arrow. In contrast, the gap in the corrected image is then fully visible and sharp edges are recovered, as shown in Figure 3.9-d. In Figure 3.9-b and 3.9-c, stripes and bands are visible within the reconstruction as pointed out by the black arrows. Those are strongly reduced in Figure 3.9-e and 3.9-f although not completely suppressed. This imperfect correction is due to the fact that the correction factor is valid only for one interface.

In conclusion, two approaches to reduce the phase wrapping and clipping artifacts have been discussed and experimentally verified. The latter are particularly penalizing for manufactured objects with flat surfaces. First, the sample can be immersed in a phase-matching liquid to reduce the phase gap at the interface. This method can however not be implemented in many applications due to practical constraints. A second technique based on an algorithm to correct the phase signal by using the absorption-based radiography has been demonstrated. A significant decrease of the artifacts could be shown. Such a method would be implementable for a wide range of investigations and is particularly interesting for non-destructive testing or evaluation.

3.2 Stochastic Errors

Stochastic errors refer to the fluctuations of the signal observed when a series of measurements is repeated under the exact same conditions. The stochastic errors are the result of the diverse random processes involved in the signal formation chain. Thus, only a single pixel will be taken into account here and not pixel-to-pixel variations as in Section 3.1.

So, let us only consider the stochastic error of the intensity $I_{pix}(x,y)$ of a single pixel and drop the indexes (x,y) for clarity. The measurement of T (resp. DP and V) as defined by Equation 2.85 (resp. 2.88 and 2.91) is affected by various noise sources. Its statistical distribution will be characterized by the mean $\overline{T}$ (resp. $\overline{DP}$ and $\overline{V}$) and the standard deviation σ_T (resp. σ_{DP} and σ_V). Two major sources of uncertainties will be studied in detail, namely the contributions $\sigma_{T,det}$ (resp. $\sigma_{DP,det}$ and $\sigma_{V,det}$) from the detector noise at the digital output and $\sigma_{T,jitter}$ (resp. $\sigma_{DP,jitter}$ and $\sigma_{V,jitter}$) from the phase stepping jitter in the sampled positions χ. Other possible sources of error $\sigma_{T,other}$ will finally be reviewed briefly. The total uncertainty of T (resp. DP and V) will then be given by

$$\sigma_T^2 = \sigma_{T,det}^2 + \sigma_{T,jitter}^2 + \sigma_{T,other}^2 \tag{3.12}$$

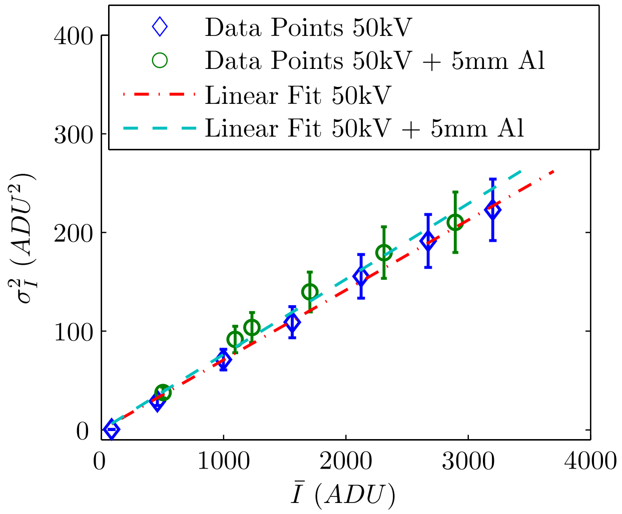

Figure 3.10: *The variance σ_I^2 is plotted as a function of the mean output $\overline{I}$ for a tube acceleration voltage of 50 kVp. The error bars represent the standard deviation of σ_I^2 due to the pixel-to-pixel inhomogeneities. In one case, 1.5 mm of silicon was used as filter (round markers) while in the other case, an additional 5 mm-thick aluminum plate was added (square markers). In both cases, the data were fitted with a linear function (resp. dashed and dot-dashed lines). As appears in the plot, the fitting coefficients depend on the energy spectrum of the incoming photons.*

3.2.1 Detector Quantum Noise

Our starting point is the measurement of the noise characteristics of our detector. We used a RadIcon Shad-o-Box 2k with 2048×1024 pixels of size 48 × 48 µm ^{2} and scintillator Min-R 2190 from Kodak. The variance of the stochastic distribution of the digital output I of the x-ray detector (after dark current correction as defined in Equation 3.6) was measured as a function of the mean intensity. The latter was controlled by changing the anode current for a fixed tube voltage and exposure time. For this purpose, 100 successive exposures were recorded for each anode current. For each pixel, the mean and variance of the acquired intensity histogram were then estimated. Finally, the calculated means and variances were averaged over a 100 × 100 pixels area to obtain the average mean intensity $\overline{I}$ and average variance σ_I^2.

In Figure 3.10, σ_I^2 is plotted as a function of $\overline{I}$ for a tube acceleration voltage of $V_{tube} = 50$ kVp, once with 1.5 mm of silicon (equivalent to the beam hardening due to the three gratings) as filter and once with 1.5 mm of silicon and 5 mm aluminum as filter. The error bars show the standard deviation of σ_I^2 over the 100 × 100 pixels area, which represents the pixel-to-pixel inhomogeneities of the detector.

From this plot, it can be seen that the variance σ_I^2 can be well approximated by a linear fit over most of the dynamic range. Indeed, the error between the linear fit and the measured variance stays below the level of the pixel-to-pixel inhomogeneities. It can therefore be assumed that

$$\sigma^2_{I,det} = f_1\overline{I} + f_0 \tag{3.13}$$

Where the slope f_1 is linked to the signal and noise transfer of the incoming x-ray photons to the output in Arbitrary Digital Units (ADU) while f_0 is an additive noise occurring during the acquisition chain. This additive noise is essentially due to the electronic noise of the detector, including the readout, thermal and quantization noises and does not depend on the illumination of the detector[10]. f_0 can be determined by acquiring series of images while the detector is not submitted to any radiation i.e. at $\bar{I} = 0$[11]. For our detector, it can be seen (see Figure 3.10) that this additive noise is less than 1 ADU and is consequently ignored i.e. $f_0 = 0$.

The slope f_1 is linked to the signal and noise transfer of the incoming x-ray photons to the output in Arbitrary Digital Units (ADU), which involves different conversion stages - each generating excess noise on the input signal (see Figure 3.2). Without entering into the details of the single conversion stages, the detective quantum efficiency (DQE) is defined as

$$DQE \ \widehat{=} \ \frac{SNR_I^2}{SNR_{ph}^2} = \frac{\bar{I}^2}{\sigma_I^2 \bar{\mathcal{S}}_0} \tag{3.14}$$

Where SNR_I and SNR_{ph} are the signal to noise ratios of the output signal I and of the incoming number photons, respectively. $\mathcal{S}_0$ is the total number of photons impinging on the detector during the exposure time. Thus, DQE characterizes the total noise transfer of the detector.

For thermal sources (typically the case of x-ray tube sources), $\mathcal{S}_0$ follows a Poisson distribution, which is characterized by $SNR_{ph} = \bar{\mathcal{S}}_0$, where $\bar{\mathcal{S}}_0$ is the mean number of recorded photons. In that case, the slope f_1 can be rewritten as

$$f_1 = \frac{\mathcal{D}_0}{DQE} \tag{3.15}$$

Where $\mathcal{D}_0 = \bar{I}/\bar{\mathcal{S}}_0$ is the overall gain of the detector (Section 3.1.2). The reader is referred to the literature(Zweig 1965; Rabbani *et al.* 1987; Cunningham *et al.* 1994) for more details about this topic, especially about the limitations of the linear model.

---

[10] This means that it is constant as a function of the average recorded signal $\bar{I}$, hence the denomination "additive noise".

[11] Note that I is the intensity after dark current correction and thus is indeed equal to 0 when the detector is not illuminated.

Additionally, note that the slope f_1 of the linear fit with a 5 mm-aluminum filter is higher than that without filter (see Figure 3.10). This increase is due to the beam hardening of the energy spectrum after propagation through the aluminum plate[12]. Indeed, both the gain $\mathcal{D}_0$ and the DQE are energy dependent, which implies that the slope f_1 depends on the energy spectrum of the incoming photons. Note that, for this reason, f_1 is in general different for the reference measurement f_1^r and for the sample measurement f_1^s.

Finally, the uncertainties in the acquired data set σ_I^i ($i = r$ or s) translate into uncertainties $\sigma_{T,det}$ (resp. $\sigma_{DP,det}$ and $\sigma_{V,det}$) in the reconstructed image T (resp. DP and V). These uncertainties can be calculated by using the error propagation formula (Bronshtein *et al.* 2003) on Equations 2.77 and 2.85 (resp. Equations 2.88 and 2.91) and the linear model of Equation 3.13. It is assumed that the number of phase stepping steps N_{ps} is sufficiently high to prevent aliasing, which is reasonable for normal experimental conditions ($N_{ps} \geq 5$). The resulting expressions are summarized in Table 3.1, where Q_0 is the mean intensity of the phase stepping curve and v the visibility (Section 2.2).

Background Case

Let us consider first a situation where no object is in the field of view. In this case, the mean intensity Q_0 and visibility v of the phase stepping curve are equal for the reference and sample measurements. Furthermore there is no beam hardening. Therefore $\overline{T} = 1$, $\overline{V} = 1$ and $f_1^s = f_1^r = f_1$. The expressions for the relative uncertainty due to the detector quantum noise can then be simplified as displayed in the right column of Table 3.1.

Remembering the definition of the slope f_1 (Equation 3.15), the ratio f_1^r/Q_0^r is then equal to $1/\bar{\mathcal{S}}_0^r DQE$, where $\bar{\mathcal{S}}_0^r$ is the average number of photons impinging on the detector during the phase stepping curve. Thus, the results show that, for each image (T, DP or V), the relative uncertainty decreases with the square root of the total integrated number of photons during the phase stepping curve $\bar{\mathcal{S}}_{total}^r \widehat{=} N_{ps}\bar{\mathcal{S}}_0^r$ as well as with the square root of the detective quantum efficiency DQE. This tells us that the image quality improves if the mean photon counts $\bar{\mathcal{S}}_0^r$ recorded by the detector at each phase step goes up or if we use more phase steps. Moreover, for DP and V, the relative uncertainty decreases linearly with the visibility v. This underlines the importance of optimizing the latter to obtain a good phase sensitivity with grating interferometers.

General Case

In the general case, the expressions are similar to the background case except for a multiplicative factor that depends on the absorption and visibility loss inside the

---

[12] Beam hardening refers to the shift of the mean of the energy spectrum towards higher energy in presence of an absorbing object. More on this phenomenon in Section 3.1.1

object. This factor is at its minimum when $\overline{T} = 1$ and $\overline{V} = 1$ i.e. in the background case. As $\overline{T}$ becomes smaller, the relative uncertainty increases monotonically for each image (T, DP or V). Qualitatively, the number of detected photons is lower when an object is present in the field of view and this degrades the quality of the images. However, note that $\sigma_T/_{\overline{T}}$ is not sensitive to a loss of visibility ($\bar{V} < 1$) while σ_{DP} and $\sigma_V/_{\overline{V}}$ are.

At the limit, when the object is a strong absorber ($T \ll 1$) and when the visibility loss is large ($V \ll 1$), the contributions from the phase stepping with sample (second term in the brackets) become dominant. The expressions then simplify and the relative uncertainties only depend on the characteristics of the sample phase stepping curve i.e. the total integrated intensity $\bar{\mathcal{S}}^s_{total} = TN_{ps}\bar{\mathcal{S}}^r_0$, the visibility $v^s = Vv^r$ and the detective efficiency DQE^s.

Table 3.1: *Expressions for the contributions to the uncertainties in T, DP and V from the detector quantum noise and the phase stepping jitter.*

	General Case	**Background Case**
$\left(\frac{\sigma_{T,det}}{\overline{T}}\right)^2 =$	$\frac{f_1^r}{N_{ps}Q_0^r}\left(1+\frac{f_1^s}{\overline{T}f_1^r}\right)$	$\frac{2f_1^r}{N_{ps}Q_0^r}$
$\left(\sigma_{DP,det}\right)^2 =$	$\frac{f_1^r}{2\pi^2 v^{r2} N_{ps} Q_0^r}\left(1+\frac{f_1^s}{f_1^r\overline{TV}^2}\right)$	$\frac{f_1^r}{\pi^2 v^{r2} N_{ps} Q_0^r}$
$\left(\frac{\sigma_{V,det}}{\overline{V}}\right)^2 =$	$\frac{f_1^r}{v^{r2} N_{ps} Q_0^r}\left(v^{r^2}(1+\frac{f_1^s}{f_1^r\overline{T}})+2(1+\frac{f_1^s}{f_1^r\overline{TV}^2})\right)$	$\frac{2f_1^r}{v^{r2} N_{ps} Q_0^r}\left(v^{r^2}+2\right)$
$\left(\frac{\sigma_{T,jitter}}{\overline{T}}\right)^2 =$	$\frac{2\pi^2 v^{r2}}{N_{ps}}(\frac{\sigma_\chi}{p_2})^2(1+\overline{V}^2)$	$\frac{4\pi^2 v^{r2}}{N_{ps}}(\frac{\sigma_\chi}{p_2})^2$
$\left(\sigma_{DP,jitter}\right)^2 =$	$\frac{3}{N_{ps}}(\frac{\sigma_\chi}{p_2})^2$	$\frac{3}{N_{ps}}(\frac{\sigma_\chi}{p_2})^2$
$\left(\frac{\sigma_{V,jitter}}{\overline{V}}\right)^2 =$	$\frac{2\pi^2}{N_{ps}}(\frac{\sigma_\chi}{p_2})^2(2+v^{r2}(1+\overline{V}^2))$	$\frac{4\pi^2}{N_{ps}}(\frac{\sigma_\chi}{p_2})^2(1+v^{r2})$

3.2.2 Mechanical Jitter Noise

The phase stepping is usually done by translating one of the three gratings. The actual position χ of the interference pattern with respect to G_2 (see Section 2.2.1) is distributed around its ideal position due to mechanical uncertainties. This distribution will be characterized by the standard deviation σ_χ and translates into uncertainties in the sampled intensity value I_{pix} and finally, in the images T, DP and V. The error propagation formula can again be applied to Equation 2.77 to obtain the contributions from the phase stepping jitter $\sigma_{T,jitter}$, $\sigma_{DP,jitter}$ and $\sigma_{V,jitter}$. The expressions are included in Table 3.1.

The results show that the relative errors in images T, DP and V due to the phase stepping jitter depend linearly on the relative error of the position with respect to the period of the phase stepping curve σ_χ/p_2. For image T, the relative uncertainty is also proportional to v^r. Indeed, the smaller the visibility, the smaller is the error of the estimation of the average intensity Q_0. Contrary to T, the uncertainty of DP is independent of v^r.

3.2.3 Other Noise Sources

Though negligible in most cases, some other noise sources can also contribute to the degradation of the image quality for particular designs or conditions. Notably, the mechanical drift of the gratings with respect to each other due to thermal instabilities can result in temporal fluctuations of the images T, DP and V. Practical solutions, such as an optimized mechanical design and temperature control, can however be implemented to reduce these factors.

3.2.4 Experimental Confirmation

A set of experimental data has been collected to verify the expressions summarized in Table 3.1. The data were acquired with the interferometer configuration **S20-4**, which will be described in Section 4.3. The conclusions however do not depend on the interferometer design .

Phase stepping series were repeated at different anode currents, hence different photon fluxes for a constant tube acceleration voltage of 50 kVp. Each phase stepping series was done over one period of G_0 for a total of 12 phase steps and the exposure time was set to 6.7 s for each raw image. The field of view was divided into two parts: on one side, no object was present in the field of view while on the other side a 5mm-thick aluminum plate (absorption $1 - T = 0.73$ and visibility loss $1 - V = 0.45$) was used to simulate a strongly absorbing object. This procedure was repeated for two different G_0 gratings with duty cycles 0.3 and 0.5, for which the visibilities v^r were 0.23 and 0.16, respectively.

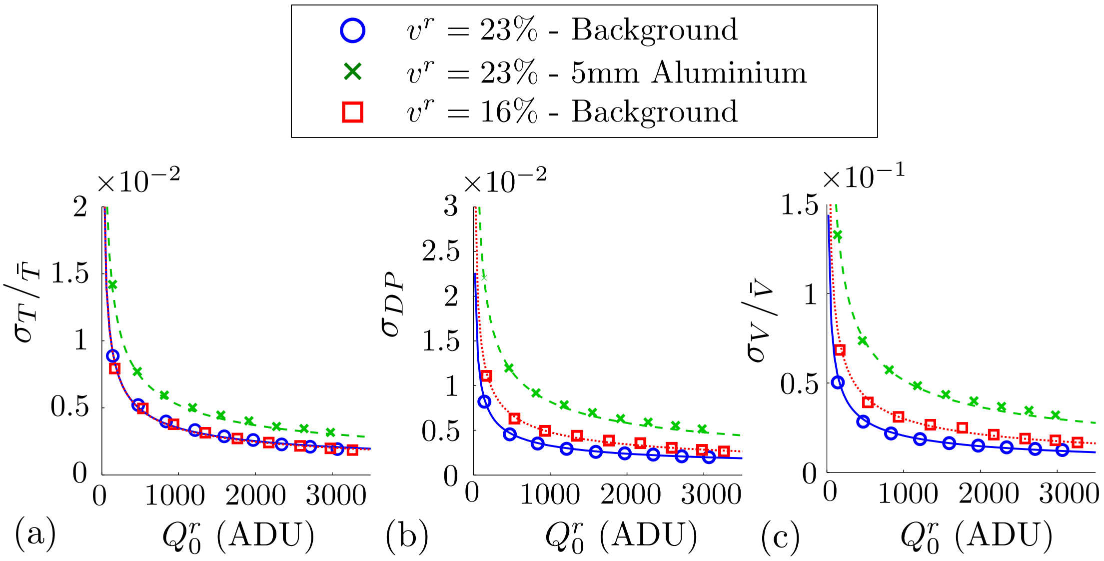

Figure 3.11: *The relative uncertainties in (a) T, (b) DP and (c) V were measured for a tube voltage of $50kV$ as a function of the mean intensity Q_0^r, in the background case with $v^r = 0.23$ (round markers), in the background case with $v^r = 0.16$ (square markers) and within the 5mm aluminum plate ($T = 0.27$ and $V = 0.55$) with a visibility $v^r = 0.23$ (cross markers). For each situation, the quantitative estimations of the model are indicated with solid lines (resp. dotted line and dashed lines).*

For each situation, the average intensity Q_0^r and the standard deviations σ_T, σ_{DP} and σ_V were extracted from an area of 200×200 pixels. Figure 3.11 shows the measured uncertainties as a function of Q_0^r as well as the predictions from the theoretical model (see Table 3.1). The conversion factors $f_1^r = 0.0709$ and $f_1^s = 0.0764$ used in the model estimations were extracted from the linear fit of the mean-variance plot at 50 kVp (see Figure 3.10). Moreover, the minimal incremental motion of the phase stepping stage is 0.3 µm (Newport), which corresponds to a jitter on the phase stepping $\sigma_\chi/p_2 \sim 0.0017$.

Figure 3.11 shows a good agreement between the measurements and the theoretical model over the full dynamic range of the detector. As discussed in the previous section, the relative uncertainties in T, DP and V decrease as a function of the inverse square root of Q_0^r and increase when an object is present in the field of view (here the 5mm aluminum plate). Moreover, the relative uncertainty in T is independent of the decrease of v^r (different source gratings) while it increases for DP and V.

Note that, under the present experimental conditions, the contributions from the detector quantum noise are dominant over the jitter noise. For example, for a visibility $v^r = 0.23$ without object (background case), the relative uncertainty in T due to the jitter is around $\sigma_{T,jitter}/\overline{T} = 0.67 \times 10^{-3}$, which is smaller than the contribution from the detector quantum noise $\sigma_{T,det}/\overline{T} > 1.5 \times 10^{-3}$.

In summary, the contributions from the detector noise are functions of the total integrated intensity during the phase stepping (number of phase steps times the average intensity), the visibility of the phase stepping curve, the noise transfer performance of the x-ray imaging system and the absorption and visibility loss in the imaged sample. To enhance the precision of a measurement, three approaches are thus available. First, the detective quantum efficiency (DQE) of the x-ray detector could be increased. But the gain margin is thin since commercially available detectors are already strongly optimized. Another possibility is to use longer exposure times, more phase steps or larger photon flux. However, since x-ray tubes have limited power, a trade-off has to be made between measurement time and sensitivity. Finally, the design and fabrication of the x-ray gratings can be improved, to obtain the best possible phase stepping visibility. This underlines the need for the development of optimized micro fabrication processes but also of simulation tools that allow for an a-priori estimation of the visibility. Significant improvement of the image quality with reasonably short exposure times could thus be realized using the last approach.

The contributions from the mechanical jitter of the phase stepping stage depend on the ratio of the jitter standard deviation to the periodicity p_2, the number of phase steps, the visibility of the phase stepping curve and the absorption and visibility loss in the sample. The phase stepping stage and number of phase steps should be chosen such that the jitter noise is negligible compared to the detector quantum noise.

3.2.5 Differential Phase Contrast vs. Absorption Imaging

Now that quantitative expressions have been given for the stochastic errors in the measurement of the phase contrast and absorption images, it is possible to study the sensitivity of differential phase contrast imaging compared to absorption imaging. A comparison criterion was first suggested by (Momose *et al.* 2008) for monochromatic waves and homogeneous objects based on the Talbot interferometer. Recall that the Talbot interferometer consists uniquely of the analyzer grating and beam splitter grating illuminated by a micro-focus tube, hence without source grating. In the next paragraph, this criterion is extended to Talbot-Lau interferometry with inhomogeneous objects i.e. inducing ultra small angle scattering.

Let us consider a cylinder of radius d made of a material A with refraction coefficient δ_A and absorption coefficient μ_a surrounded by a medium of thickness $t \gg d$, refraction coefficient δ_m and absorption coefficient μ_m. The inhomogeneities of the medium, which result in ultra small angle scattering, are modeled by the linear scattering coefficient ϵ_m. The sample is placed at a distance z_s from grating G_1.

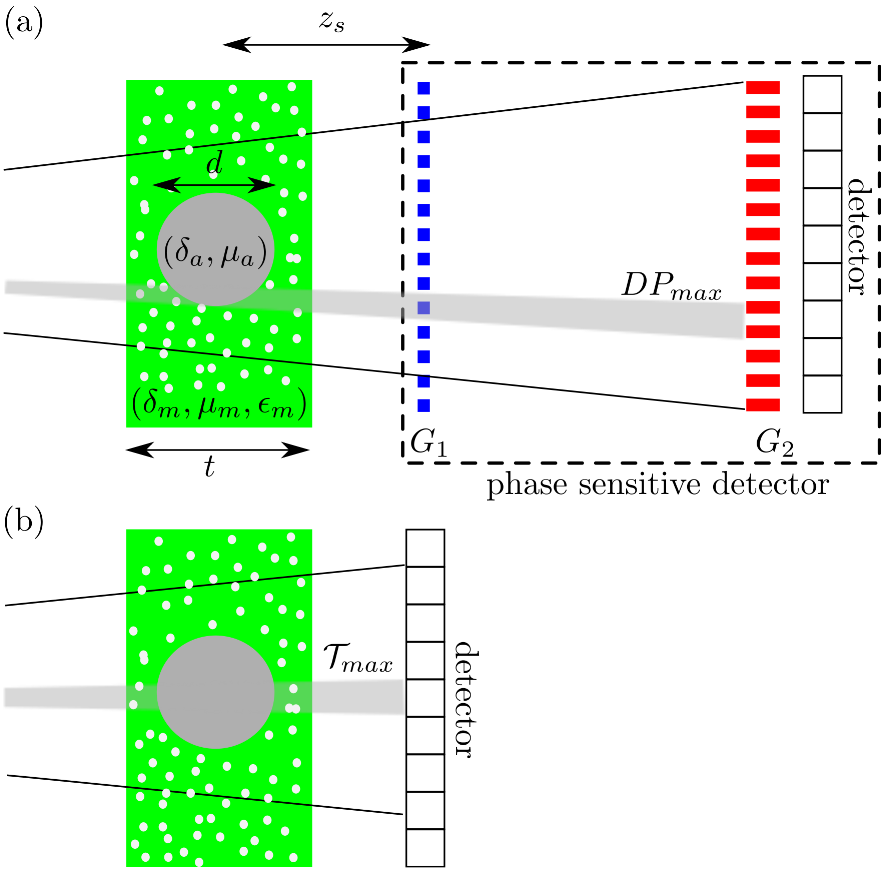

Figure 3.12: *(a) A sample made of a cylinder placed in a medium is placed at a distance z_s in front of grating G_1. The ensemble $\{G_1 + G_2 + detector\}$ is considered as a phase sensitive detector and compared to a conventional detector placed at the position of G_1 as shown in (b).*

Remember that z_s takes a negative value when the sample lies in front of the grating G_1 (see Section 2.1.5). The pixel size is given by p_{pix}, which is considered to be much smaller than d ($p_{pix} \ll d$).

In order to compare differential phase contrast imaging with absorption imaging, it is necessary to ensure that the dose received by the sample is the same in both case. The two following situations are considered, as illustrated in Figure 3.12. In the phase sensitive mode, the ensemble $\{G_1 + G_2 + \text{detector}\}$ is considered as a phase sensitive detector, which delivers a signal DP. In the absorption mode, the detector is placed right at the position of G_1 in order to have the same input flux and produces a signal $\mathcal{T} = -\log(T)$.

Let us start with a monochromatic wave of wavelength λ impinging on our system. The maximum signal $\mathcal{T}_{max}$ from the cylindrical inclusion measured in absorption mode occurs in the middle of the cylinder and is equal to $\mathcal{T}_{max} = \Delta\mu d$ with

$\Delta\mu = \mu_a - \mu_m$.

Due to the differential nature of the phase information, the maximum signal DP_{max} from the phase sensitive detector occurs on the side of the inclusion and its value is

$$DP_{max} = \frac{2\lambda z_{12}\Delta\delta}{p_1 M_s}\sqrt{\frac{d}{M_s p_{pix}}} \tag{3.16}$$

Where $\Delta\delta = \delta_a - \delta_m$ is the difference of refraction coefficient between the inclusion and the medium and $M_s = (z_{01} + z_{12})/(z_{01} + z_s)$ is the magnification of the object.

On the other hand, the noise levels in images $\mathcal{T}$ and DP are given by the expressions of Table 3.1 with $f_1^s = f_1^r$ (monochromatic radiation).

$$\begin{align} \sigma_{\mathcal{T}} &= \frac{\sigma_T}{\bar{T}} = \sqrt{\frac{1}{\bar{\mathcal{S}}^r_{tot} DQE^s}\Big(1 + \frac{1}{\bar{T}}\Big)} \tag{3.17}\\ \sigma_{DP} &= \sqrt{\frac{1}{2\pi^2 v^{r2}\bar{\mathcal{S}}'^{r}_{tot} DQE^s}\Big(1 + \frac{1}{\bar{V}^2\bar{T}}\Big)} \tag{3.18}\\ \text{with } \bar{\mathcal{S}}'_{tot} &= \bar{\mathcal{S}}_{tot}\frac{T_{12}}{M_g^2} \tag{3.19} \end{align}$$

Where $\bar{\mathcal{S}}_{tot}$ is the total number of photons recorded by the detector in the absorption mode. As seen in Equation 3.19, the total number of photons recorded in the phase contrast mode $\bar{\mathcal{S}}'_{tot}$ is reduced due to the additional propagation distance z_{12} between gratings G_1 and G_2 (magnification $M_g = (z_{01} + z_{12})/z_{01}$) and to the absorption within gratings G_1 and G_2 as given by the transmission T_{12}. Note, the absorption and visibility loss from the cylindrical inclusion are assumed to be negligible compared to those from the medium such that

$$\begin{align} \bar{T} &\sim \exp\big(-\mu_m t\big) \tag{3.20}\\ \bar{V} &\sim \exp\big(-\frac{2\pi^2 z_{12}^2 f(z_s)}{p_2^2}\epsilon_m t\big) \tag{3.21} \end{align}$$

Differential phase contrast imaging will be said to be equivalent to absorption contrast if the signal to noise ratio of signal DP (given by DP_{max}/σ_{DP}) is equal to that from signal $\mathcal{T}$ (given by $\mathcal{T}_{max}/\sigma_{\mathcal{T}}$). Assuming that $\lambda = \lambda_{des}$, this results in the following limit on $\Delta\delta$ as a function of $\Delta\mu$

$$\begin{align} \Delta\delta_{lim} &\widehat{=} \sqrt{p_{pix} d}\cdot\Big(\frac{M_s^{3/2}}{\sqrt{2}(N/8)p_1}\Big)\cdot\Big(\frac{a_0\sqrt{b_0 c_0}}{a_1 b_1 c_1}\Big)\cdot R\cdot\Delta\beta \tag{3.22}\\ \text{with } R &= \sqrt{\frac{1 + f_1^s/(f_1^r\bar{T}\bar{V}^2)}{1 + f_1^s/(f_1^r\bar{T})}} \tag{3.23} \end{align}$$

Where $\Delta\beta = (\lambda/4\pi)\Delta\mu$. The relations $v^r = 2(a_1 b_1 c_1)/(a_0 b_0 c_0)$ and $T_{12} = b_0 c_0$ were used in the calculations, which are valid uniquely for monochromatic radiation. (a_1, a_0), (b_0, b_1) and (c_0, c_1) are Fourier coefficients linked to the transmission functions of gratings G_0, G_1 and G_2, respectively (see Chapter 2).

So, if $\Delta\delta > \Delta\delta_{lim}$, differential phase contrast will give a better contrast than absorption-based radiography and vice versa if $\Delta\delta < \Delta\delta_{lim}$. Thus, this criterion tells us which inclusions can be detected better with differential phase contrast or absorption contrast, depending on their size, composition ($\Delta\delta$, $\Delta\beta$) and the system parameters. The first term on the right side of Equation 3.22 describes notably that the phase contrast is more favorable to imaging small samples with small pixels. The second term is related to the interferometer design. Note, for example, that the phase sensitivity increases with the fractional Talbot order N. The third term is linked to the Fourier coefficients of the gratings' transmission function and depends essentially on the quality of the gratings (shape, depth of the trenches, duty cycle...).

Compared to the expression given by Momose et al. in (Momose *et al.* 2008), this expression also includes the impact from the source grating (coefficient a_0 and a_1) and from an inhomogeneous medium. Indeed, the fourth term of Equation 3.22 involves the ratio R. The latter is equal to 1 for $V = 1$ and increases as the dark field signal V decreases[13]. Especially, this means that differential phase imaging gets penalized for strongly scattering samples, where the phase signal is partially lost.

$\Delta\delta_{lim}$ was calculated as a function of $\Delta\mu$ under the conditions $E = 20\,\text{keV}$, $p_{pix} = 48\,\mu\text{m}$, $p_1 = 2.85\,\mu\text{m}$, $z_{01} = 1315\,\text{mm}$, $z_{12} = 69\,\text{mm}$, $z_s = 45\,\text{mm}$ and $v^r = 0.44$. It was supposed additionally that $b_0 = 1$ (no absorption in the phase grating G_1) and $c_0 = 0.5$ (grating G_2 with a duty cycle of 0.5 and fully absorbing, which is a fair assumption for $E = 20\,\text{keV}$). The variables d, N and V were used as parameters. The results are plotted in Figure 3.13. In addition, the values of ($\Delta\delta$, $\Delta\mu$) for different plastics (torlon (PI), plexiglass (PMMA), teflon (PTFE), nylon (PA66) and polyoxymethylene (POM-C)) as well as aluminum and iron in a water or air medium were compiled from the database of the National Institute of Standards and Technologies (Berger *et al.*) and reported in the graph.

This graph tells us which material combinations can be better visualized using absorption-based radiography or differential phase contrast imaging. Thus, the markers that lie above the curve indicate material combinations favorable to differential phase contrast and vice versa for the point below the curve. Generally, it can be seen that heavier elements like aluminum or iron should preferentially be imaged using absorption contrast while phase contrast is favorable for lighter

---

[13] As a reminder, a decrease of V signifies a loss of visibility, either due to ultra small angle scattering or other phenomena, as was seen in Section 3.1

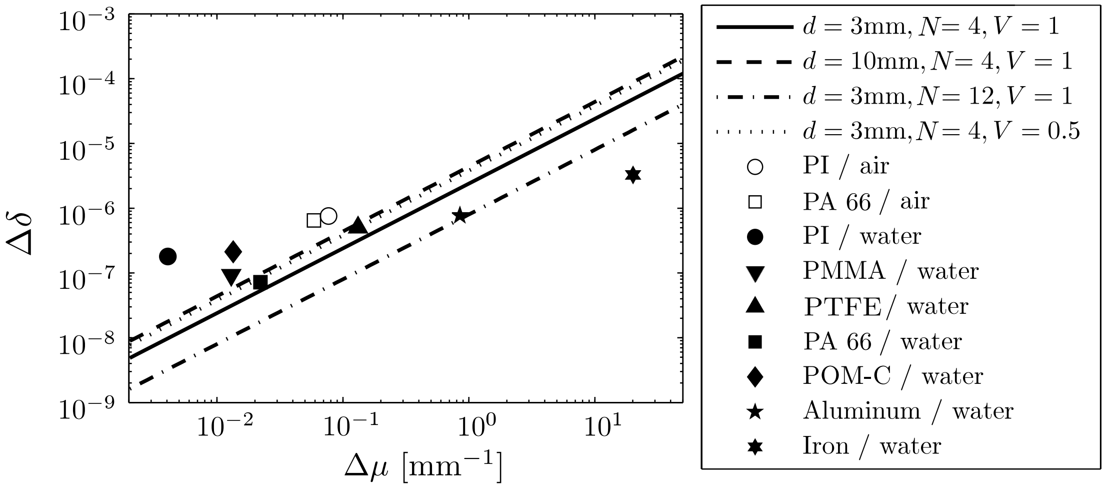

Figure 3.13: *Plot of the value of $\Delta\delta_{lim}$ as a function of Δ_{mu} for monochromatic radiation under the conditions described in the text. In addition, the values of $(\Delta\delta, \Delta\mu)$ for different material combinations were compiled from the NIST database (Berger et al.).*

elements like plastics. This however depends strongly on the medium used. For example, the combination PI/water gives a better phase contrast than PI/air while it is the opposite for PA66/water and PA66/air. The experimental proof of this model can be found in Section 4.3.

As a conclusion, let us recall that the calculations were done assuming that the sample receives the same radiation dose both for the absorption and differential phase contrast mechanisms. For living samples, this is of prime importance since DNA mutation and consequently tumors can be induced as a consequence of the ionizing radiation. This means that for a sample for which the material combination marker lies above the line: either the contrast obtained for an identical dose is improved or, inversely, the contrast can be kept identical but the dose reduced.

CHAPTER

FOUR

INSTRUMENTATION

This chapter describes the experimental bench built in the facilities of CSEM in Zürich as well as first characterization results. The design and assembly of the diverse components as well as the development of control and acquisition software was the first task to be accomplished in this thesis and was a prerequisite for the demonstration of new ideas and developments.

Section 4.1 introduces the different elements, which are part of the experimental bench. The mechanical model made during the planning phase as well as the dedicated control and acquisition software are then presented. Furthermore, the fabrication of the gratings using micro-fabrication processes is discussed.

In Section 4.2, the conception rules, which link the periodicities of the gratings to the distances and the x-ray design energy are summarized. In addition, a simulation framework was created to calculate numerically the performance of the interferometer for different system parameters and allows for its optimization.

In Section 4.3, the first grating interferometer design made during this thesis is examined. The performance is characterized and compared to simulations. This first configuration is the starting point for the developments and evolutions, which are the subject of Chapter 5.

4.1 Experimental Bench

Before starting the description of the system, let us recall the general requirements of the experimental bench design. The bench aims at providing a platform to test different grating combinations and methods. Thus, it has to be flexible in terms of dimensions and accommodate diverse equipments and test samples. In addition, it should be mechanically stable in order for the x-ray gratings to stay aligned, at least during the acquisition time of one image series.

4.1.1 Components of the Setup

Each component of the system was imported or drawn in the software Solidworks to form a Computed Assisted Design (CAD) model. A schematic view of the bench is shown in Figure 4.1. The components of the system, for which the requirements are discussed in the next paragraphs, are summarized in Table 4.1.

X-ray source

First, an x-ray source is needed, which should be sufficiently powerful and stable to address industrial applications. For this reason, an x-ray tube source with large focal spot (Comet MXR-160HP 20) was chosen. It is composed of an electron gun focused onto a tungsten target oriented at 20°, which emits a polychromatic Bremsstrahlung spectrum. The maximum acceleration voltage lies at 160 kV for a continuous power rating of 1 kW. The focal spot measures $1 \times 1\,\mathrm{mm}^2$ according to norm EN 12543 and the x-ray beam is emitted in a 40° cone through a 0.8 mm-Beryllium window. A collimator and a shutter from Electro-Optical Products Corporation (SH-10) are placed after the exit window to block the undesired radiation in order to preserve the lifetime of the detector.

X-ray detector

On the other side of the system, the x-ray beam intensity is recorded by an x-ray detector. The camera must be digital, since data processing is required to reconstruct the images T, DP and V. Otherwise, there are no requirements on the detector from a system point of view. The target applications however calls for a field of view in the order of some centimeters up to tens of centimeters and pixel sizes between 50 to 200 µm. Smaller pixels would provide a better contrast as was discussed in Section 3.2.5. However, for scintillation-based detectors, the achieved resolution is directly linked to the thickness of the scintillating layer. This means that small pixel sizes imply lower stopping powers, which in turn degrades the performance of the system. We chose a scintillator-based detector from the company RadIcon (Shad-o-box 2k). It counts 2048 × 1024 pixels of intrinsic size $48 \times 48\,\mu\mathrm{m}^{\ 2}$ and is equipped with a Gd_2O_2S:Tb scintillation crystal from Kodak (MinR 2190).

The detector is mounted onto a two-axis tilting stage and can be additionally manually translated along axes y and z. These degrees of freedom are required for the alignment of the rotation axis onto the camera pixel field (computed tomography).

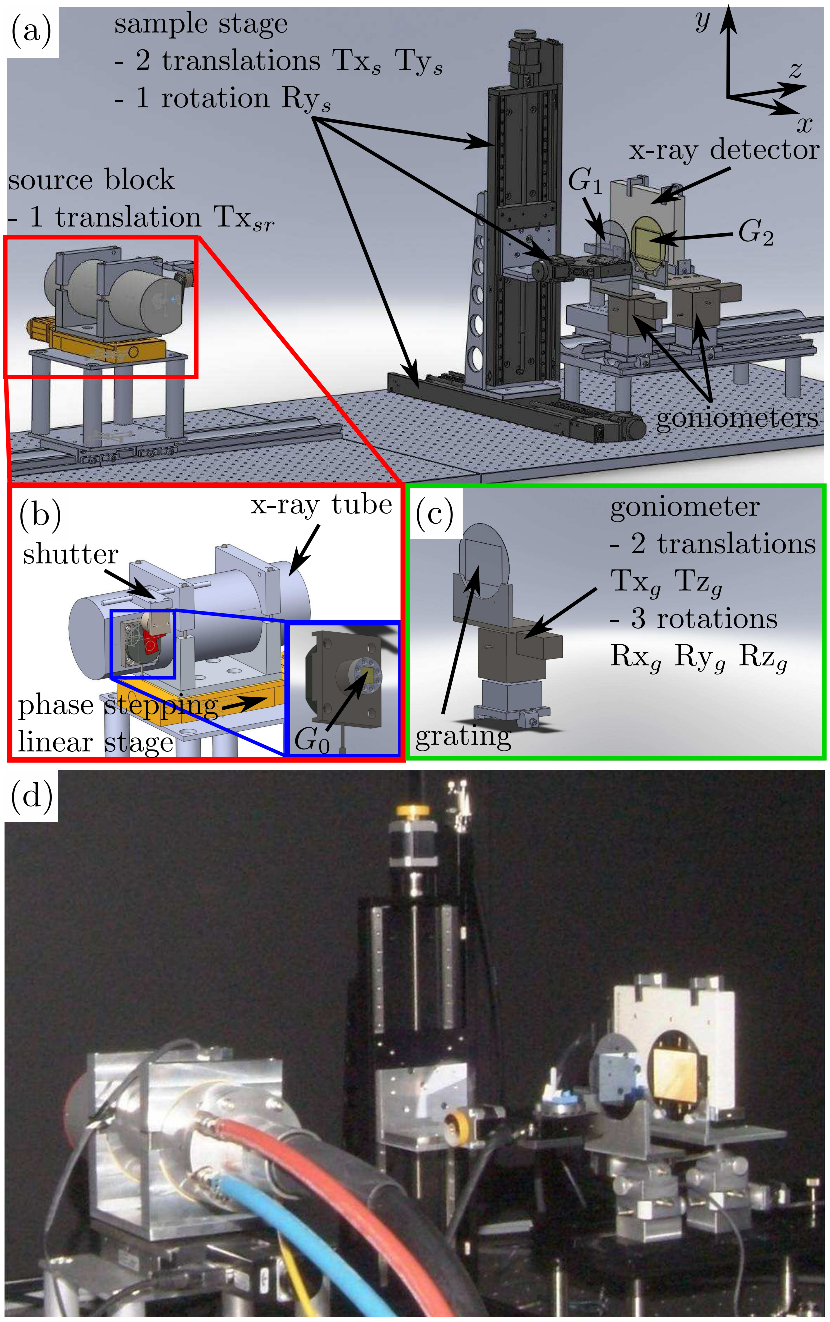

Figure 4.1: *(a) Isometric view of the interferometer with x-ray tube, detector and three gratings G_0, G_1 and G_2 taken from the Computer Assisted Design model done under Solidworks. The sample can be positioned thanks to two linear stages (horizontal and vertical) as well as a rotary stage. (b) The x-ray tube is placed onto a linear stage that is used to operate the phase stepping. The source grating G_0 is mounted directly on the source, as close as possible to the exit window as shown in the inset. (c) The gratings G_1 and G_2 are fixed onto goniometers with five degrees of freedom (two in translation and three in rotation). (d) Photograph of the experimental bench in the laboratory showing the same elements as in the CAD model.*

Sample positioning

Our system must adapt to diverse types and sizes of samples. For this reason, two motorized linear stages (Owis LTM120) are used, which enable the operator to position the object along the horizontal and vertical axes with travel ranges of 395 mm and 295 mm, respectively. The repeatability measures less than 15 µm and the positioning error is 25 µm per 100 mm travel range. In addition, a rotary stage (Owis DMT65) can be optionally mounted with a repeatability of 0.02° and allows for the realization of Computed Tomography by acquiring multiple projections at different angular positions of the sample. Various basins were also produced in order to immerse the sample into a fluid environment.

Grating Alignment

Obviously, the system performs at its best when the three gratings G_0, G_1 and G_2 are perfectly aligned. Most critical are the translation and the rotation along the z-direction of G_1 with respect to G_2, which require an alignment precision in the order of 10 µm and 0.5 millidegrees, respectively.

It was decided to mount G_0 directly onto the x-ray tube housing in order to minimize the distance between the focal spot and G_0 (maximization of the photon flux) and keep it fixed. The two other gratings G_1 and G_2 are then mounted onto goniometers (Huber 1003-MS). The latter possess two degrees of freedom in rotation and two in translation with travel ranges ±12.5 mm and ±18°, respectively. The translation and rotation along axis z are motorized such that the final alignment can be realized with a high degree of precision (0.5 µm in translation and 0.5 millidegrees in rotation). In addition, the gratings can be manually rotated about the y-direction when needed.

Phase stepping

As was seen in Section 2.2.1, the phase stepping consists in the translation of one grating over one or more periods while the two other gratings stay fixed. Moreover, the requirements in terms of positioning error scale with the periodicity[1] as demonstrated in Section 3.2.2. In our grating configurations, the periodicity of grating G_0 is always much larger than the periodicities of gratings G_1 and G_2. Thus, it was decided to operate the phase stepping on grating G_0. Since G_0 is mounted onto the x-ray tube, the tube itself was placed onto a motorized linear stage from Newport (UTS50-PP) with a travel range of 50 mm. The minimal step size is 0.3 µm for an unidirectional precision of 1 µm and a hysteresis repeatability of less than 5 µm.

Miscellaneous

---

[1] The smaller the periodicity, the stronger are the positioning requirements.

Function	**Equipment**
X-ray source	Comet MXR-160HP 20 with Shutter EOPC SH-10 and collimator
X-ray detector	RadIcon Shad-o-box 2k Kodak MinR 2190 Scintillator
Sample Positioning	Motorized XY stage : Owis LTM120 Motorized rotary stage: Owis DMT65
Gratings Alignment	Goniometers Huber 1003-MS with two axis motorized
Phase Stepping	Motorized linear stage Newport UTS50-PP

Table 4.1: *Summary of the components of the x-ray experimental bench*

The whole system was built onto an optical table in the facilities of CSEM in Zürich. A hutch made of lead coupled to an interlock system linking the doors to the x-ray source was installed, which allows the system to be operated in complete safety.

Most of the components described above can also be translated along the z-direction thanks to a rail system. Thus, a rough positioning can be achieved prior to realizing a fine adjustment of the distances with the motorized stages.

The mechanical parts needed for the interface between the different components were designed in CAD and produced at the workshop of the Physics Institute of the University of Zürich, which was always of great help for technical questions.

4.1.2 Control and Acquisition Software

The motorized stages (as listed above) are identified here by the abbreviations Tx_{sr}, Tx_s, Ty_s, Ry_s, Tz_g and Rz_g, where R refers to a rotation and T to a translation. The letters x, y and z are used indicate the direction and the subscripts sr, s and g designate the source stage, sample stage and goniometers, respectively.

In order to relay the command from the computer to the motors, three motor drives and controllers are implemented. A single axis controller from Owis (PS10) is used to operate the translation Ty_s. A four-axis controller (PXI 7334) combined with a motor drive (MID 7654) from National Instruments is linked to the motors Tx_s, Ry_s, Tz_g and Rz_g. One of the digital outputs triggers additionally the shutter. A single-axis controller from Newport (SMC100) commands the motor Tx_{sr}. Finally, a frame grabber is used to read the raw data from the x-ray detector. A summary of these connections is provided in Figure 4.2.

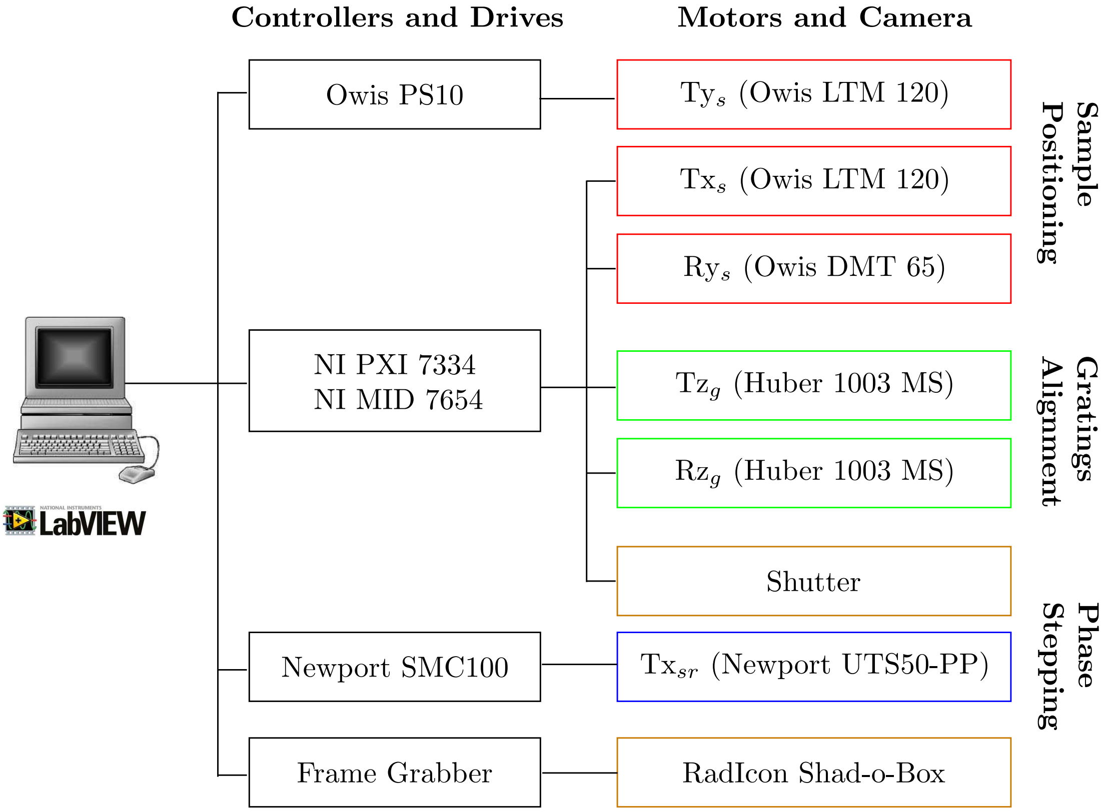

Figure 4.2: *Schematic overview of the control scheme. The motors, camera and shutter are controlled through divers drives and controllers by the dedicated software, developed using the software Labview from National Instruments.*

Dedicated software was developed using the software Labview from National Instruments in order to control the diverse motors and x-ray camera as well as to automate the measurements. Labview was chosen due to the ease of creation of virtual instruments (VI), which allows non-experienced operators to start a measurement by simple interactions with a graphical user interface. From an architectural point of view, the software is divided into functional blocks, which can be updated individually and provide a simple maintenance scheme.

From the user point of view, the software is divided into four VIs.

- A VI to initialize the controllers and the system parameters.
- An alignment VI to control single motors directly and align the interferometer.
- A VI to acquire a series of images with the x-ray detector.
- A VI to program any measurement, from single images to a full tomographic acquisition.

In addition, a simple interpreter was programed to allow the user to write commands in a text file and, thus, realize a series of measurements with changing parameters.

In Figure 4.3, the front view of the acquisition VI is displayed as an example. The parameters of the measurements, like the number of steps in a phase stepping series or the number of angles in the tomography, can be set through the graphical interface. Some information is returned in real-time through indicators like the estimated time for the measurement or the image currently recorded.

4.1.3 X-ray Gratings

The gratings G_0, G_1 and G_2 form the x-ray interferometer and are as a consequence the core elements of the experimental setup. A stable fabrication process is essential in order to ensure, for example, that the height is respected, that the gratings are as rectangular as possible, that no large defects are present and so on. Such parameters indeed impact on the visibility of the phase stepping curve and finally on the noise level or artifacts in the reconstructed images, as shown in Section 3.2.1.

X-ray grating periodicities vary typically from 2 to 5 μm for G_1 and G_2 to up to 60 μm for G_0. The depths range however from 30 to 100 μm and a maximal aspect ratio in our case of 20. Such structures are particularly difficult to produce due to the high aspect ratio of the trenches[2].

---

[2] The aspect ratio of a grating structure is defined as the height divided by the periodicity.

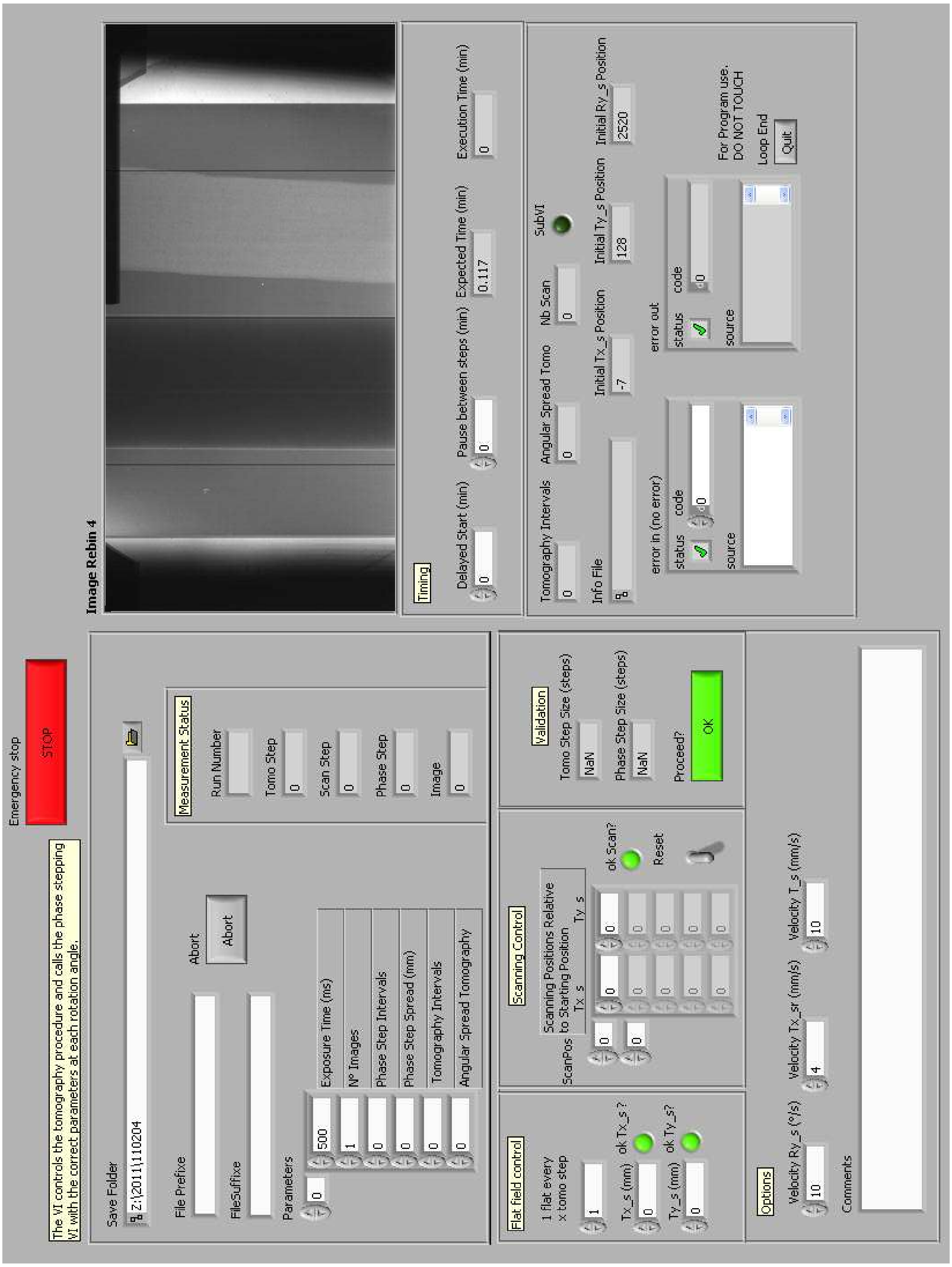

The VI controls the tomography procedure and calls the phase stepping VI with the correct parameters at each rotation angle.

Save Folder: Z:\2011\110204

File Prefix

FileSuffixe

Parameters: 0

Exposure Time (ms): 500

N° Images: 1

Phase Step Intervals: 0

Phase Step Spread (mm): 0

Tomography Intervals: 0

Angular Spread Tomography: 0

Measurement Status

Run Number

Tomo Step: 0

Scan Step: 0

Phase Step: 0

Image: 0

Image Rebin 4

Timing

Delayed Start (min): 0

Pause between steps (min): 0

Expected Time (min): 0.117

Execution Time (min): 0

Tomography Intervals: 0

Angular Spread Tomo: 0

Nb Scan: 0

Info File

Initial Tx_s Position: -7

Initial Ty_s Position: 128

Initial Ry_s Position: 2520

error in (no error): status, code 0, source

error out: status, code d0, source

For Program use. DO NOT TOUCH

Flat field control

1 flat every x tomo step: 1

Tx_s (mm): 0

Ty_s (mm): 0

Scanning Control

ScanPos: 0, 0

Scanning Positions Relative to Starting Position: Tx_s 0, Ty_s 0

Validation

Tomo Step Size (steps): NaN

Phase Step Size (steps): NaN

Options

Velocity Ry_s (°/s): 10

Velocity Tx_sr (mm/s): 4

Velocity T_s (mm/s): 10

Comments

Figure 4.3: *Front view of the Virtual Instrument dedicated to the control of data acquisition. It offers a complete range of options for the measurement from single images to complete computed tomography data sets with stitching.*

CSEM invested a large effort in the development of fabrication processes for all three gratings, which are based on standard technologies from the silicon industry. The gratings were produced in the clean rooms of CSEM in Neuchâtel. I made a literature survey of different microfabrication processes in order to identify the most suitable and participated in the first production runs with my colleagues in Neuchâtel. Afterwards, I was not involved directly in the production but participated closely in the development of the processes by testing all fabricated gratings (more than 100 different grating combinations tested) and giving feedback on their quality.

The fabrication processes used for gratings G_1 and G_2 require for <110>-oriented Silicon wafers[3] and are similar to those described by (David *et al.* 2007). Since silicon is a relatively good phase shifting material[4], the phase grating G_1 is simply realized by forming trenches into the wafer by KOH wet etch (Kendall 1979; Lang 1996). The grating G_2 is achieved by deposition of a gold layer onto the silicon mold (obtained by wet etch) by electro-deposition (Christie & Cameron 1994). Gold is indeed one of the elements with the highest stopping power[5], which can be readily deposited. In the case of grating G_0, the trenches are formed by Deep Reactive Ion Etching (DRIE) and are then filled completely with gold by electroplating.

---

[3] Standard Silicon wafers are <100>-oriented.

[4] A good phase shifting material must have a large refraction coefficient but a low absorption coefficient.

[5] The stopping power of an element is directly linked to its density and atomic mass.

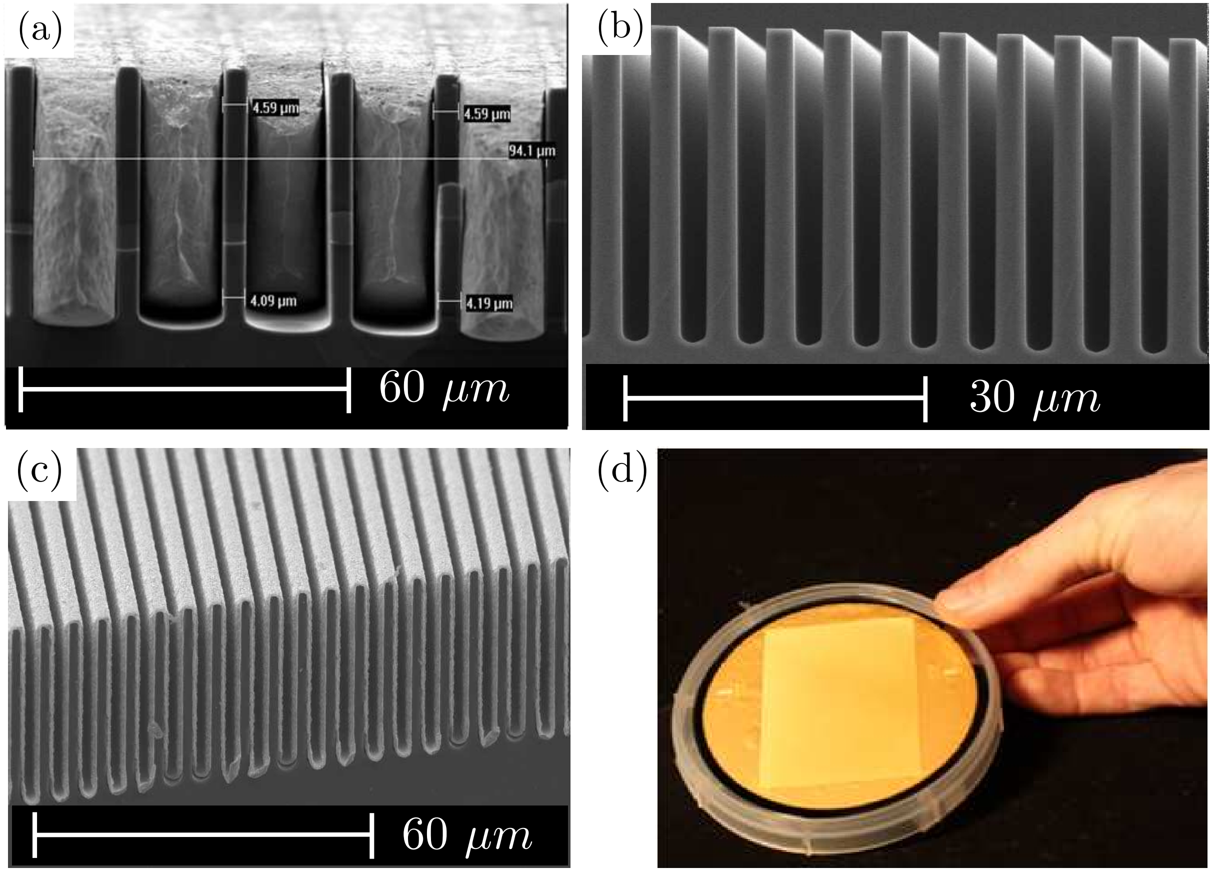

Figure 4.4: *Microscopic cross-sections acquired with the Scanning Electron Microscope (SEM with an acceleration voltage of 10 kV) of (a) the source grating G_0, (b) the beam splitter grating G_1 and (c) the analyzer grating G_2. [Courtesy of Philippe Niedermann and Francis Cardot, CSEM Neuchâtel] (d) Photograph of an analyzer grating. The sensitive area (size $5{\times}7\mathrm{cm}^2$) can be recognized due to the change in reflectivity of the gold layer deposited onto the etched silicon wafer.*

In Figure 4.4 microscopic views of one set of gratings acquired with a Scanning Electron Microscope are depicted. The x-ray gratings have a usable area of $5 \times 7\,\mathrm{cm}^2$.

4.2 Interferometer Design

4.2.1 Design Rules

During the description of the contrast formation in Chapter 2, different conditions on the grating periodicities and distances were introduced. They are summarized by the following three equations

$$\begin{aligned} z_{12} &= M_g N \frac{p_1^2}{8\lambda_{des}} && \text{Eqs. } 2.9, 2.16 \text{ and } 2.42 \\ p_2 &= M_g p_1 && \text{Eq. } 2.43 \\ p_0 &= \frac{z_{01}}{z_{12}} p_2 && \text{Eq. } 2.64 \\ \text{with } M_g &= \frac{z_{01}+z_{12}}{z_{01}} = \frac{p_0+p_2}{p_0} && \text{Eq. } 2.45 \end{aligned}$$

The system of equations has seven unknowns. Four parameters can thus be chosen in order to fix the rest of the unknowns. Since the production of x-ray gratings is costly, in particular for G_0 and G_2, it makes sense to define p_0 and p_2, which will be chosen among a set of available values. In addition, the visibility of the interferometer is optimized only for specific integer values of the fractional Talbot order N (see Section 2.1.2), where the interference pattern is the most pronounced. Thus, for a $\pi/2$-phase grating, N is preferentially taken equal to be 4 or 12 even though 2, 6 and 10 would be usable but with a sub-optimal visibility. Finally, the total length of the system $z_{01} + z_{12}$ is in practice given by the experimental conditions[6]. The periodicity p_1, wavelength λ_{des} and the ratio z_{12}/z_{01} can then be calculated from the set of equations.

In addition, it should be recalled here that, for a $\pi/2$-phase grating, the height H_1 is related directly to the wavelength by $H_1 = (\lambda_{des}/4\delta_{Si})$, where δ_{Si} is the refraction coefficient of silicon at wavelength λ_{des}. There are no strict conditions on the heights H_0 and H_2. Ideally, the transmission of the grating bars (given by $\exp(-\mu_{Au}H)$) should be as close as possible to zero, where μ_{Au} is the linear absorption coefficient of gold at wavelength λ_{des}. In practice, a compromise has to be drawn between the optimization of the visibility (requiring deeper gratings)

---

[6] Like the size of the hutch in an experimental setup or the size of the instrument for an industrial system.

and the complexity of the gratings' process (increasing with the gratings' depth). In order to make the best possible trade-off and save fabrication costs, it is essential to be able to simulate the visibility before producing the gratings. The development of simulation tools will be the subject of the next section.

4.2.2 Visibility Simulations

As seen in Chapters 2 and 3, numerous parameters play a role in the contrast formation and in the noise level of the images obtained with a grating interferometer. In order to make an educated choice of the system parameters, a simulation tool was developed in Matlab, which allows for the calculation of the intensity on different planes of our interferometer. The simulations are based on the numerical implementation of the wave propagation equations, which were presented in Chapter 2. An example of intensity plots was shown in Figure 2.6. Furthermore, a Graphical User Interface was conceived in order to facilitate the use of these simulations tools.

The energy spectrum of the source and detector response as well as the gratings' properties (periodicities, duty cycle, depths) and the distances are modeled within the framework. Typical defects of the gratings like a non-rectangular grating profile or non-uniformities in the height are also accounted for.

The visibility can then be calculated numerically as a function of these parameters. In this way, the influence of parameters such as the duty cycle DC_0 or the heights H_0 and H_2 can be understood. Moreover, specifications concerning the shape of the grating profile can be evaluated and transmitted to the process specialists.

As an example, the visibility is plotted as a function of the duty cycle of grating G_0 for a given interferometer design in Figure 4.5-a. It can be seen that there is an optimal duty cycle, which depends on the depth H_0. For a very deep grating, the maximal value v_{max} will occur for DC_{max} equal to zero[7]. As H_0 decreases, v_{max} is reduced and DC_{max} shifts towards 0.5.

4.3 First Setup and Characterization

The first interferometer design was done with relatively conservative parameters (see Table 4.2) since the whole technological knowhow in terms of gratings production had to be developed at CSEM. Thus, the focus was set on the quality of

---

[7] For an infinitely deep grating, the spatial coherence is indeed directly related to the duty cycle and the best visibility is obtained for a point source, i.e. $DC_0 = 0$.

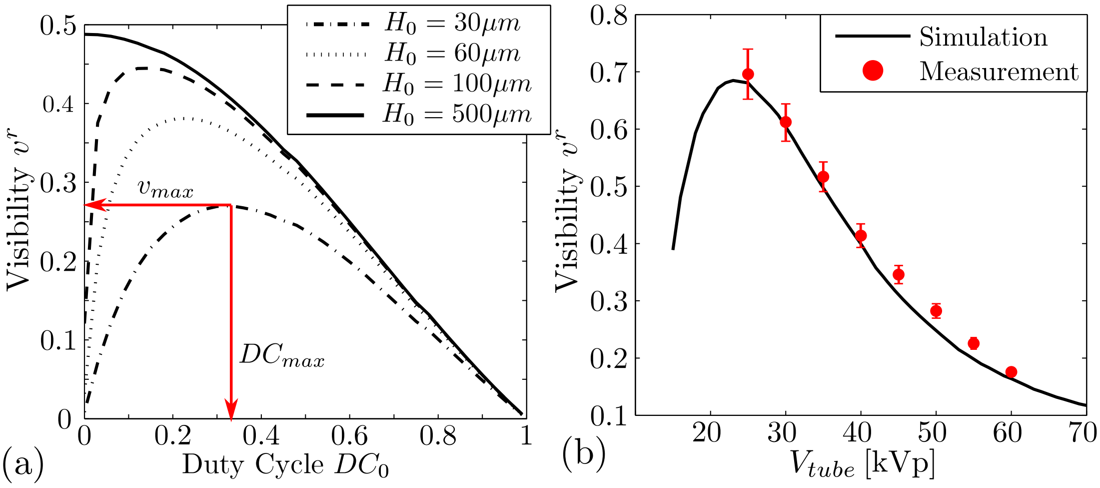

Figure 4.5: *(a) Simulation of the visibility as a function of the duty cycle DC_0 of grating G_0 for the interferometer configuration presented in Section 4.3 and for an acceleration voltage of the x-ray tube of 40 kVp (no filter). (b) Simulation and measurements of the visibility for the same interferometer configuration as a function of the acceleration voltage for a given duty cycle $DC_0 = 0.2$. The error bars indicate the variations or error on the visibility measured over the field of view.*

the gratings and not on achieving challenging specifications. The characterization of the setup consists of the verification of the grating specifications and of the estimation of the grating interferometer performance in terms of visibility and sensitivity, both for two-dimensional projections and for computed tomography. The setup is called **S20-4** after the design energy $E_{des} = 20\,\text{keV}$ and the fractional Talbot order $N = 4$, which are two of the most important parameters.

First, the visibility v^r was measured as a function of the tube acceleration voltage without filter. The results are plotted in Figure 4.5 superimposed on the simulated values. A good agreement can be seen between simulations and measurements, which confirms the validity of the developed tools. Furthermore, it can be seen that the visibility reaches a maximum around $V_{tube} = 25\,\text{kVp}$. The flux is however too weak at this tube voltage and a compromise had to be made. In most experiments, the acceleration voltage was set close to 40 kVp, where the visibility reaches 0.4. For polychromatic radiation, this value is completely satisfying and allows for the acquisition of low noise images.

As an example, a cherry was imaged with our grating interferometer operated with an x-ray source voltage of 40 kVp and an anode current of 22.5 mA. The phase stepping series was realized with 19 phase steps over one period and the exposure time for the detector readout was set to 33.5 s. The resulting T, DP and V images are shown in Figure 4.6.

The example illustrates the complementarity of the information contained by T,

	Parameter	**Setup S20-4**
General	Design Energy E_{des} [keV]	20
	Fractional Talbot order N	4
Distances	z_{01} [mm]	1310
	z_{12} [mm]	69
Source Grating	Periodicity [µm]	57
	Height [µm]	70
	Duty Cycle	0.2
Beam Splitter Grating	Periodicity [µm]	2.85
	Height [µm]	12.85
	Duty Cycle	0.5
Analyzer Grating	Periodicity [µm]	3
	Height [µm]	30
	Duty Cycle	0.5
Characteristics	Angular Range [µrad]	43.5
	Visibility v^r	0.4
		@ V_{tube}=40kVp

Table 4.2: *Summary of the parameters and characteristics of the first design*

DP and V. For instance,the structure of the stone, as indicated by the black arrow in Figure 4.6-b, appears most clearly in image DP. Image V allows for a much better delimitation of the stone but also for the visualization of fibers in the pulp (indicated by the white arrow in Figure 4.6-c). The size of these fibers is typically below the resolution of the detector which explains that they do not appear in T and DP. However, these fibers do lead to the ultra-small angle scattering of the beam (see Section 2.1.3). This then reflects in the dark field image V. Thus, details of the microstruture, that are invisible to conventional radiographic equipments, do appear in V.

Secondly, a sample composed of five plastic rods of diameter 3 mm (torlon (PI), plexiglass (PMMA), teflon (PTFE), nylon (PA66) and polyoxymethylene (POM-C)) was investigated by computed tomography. The rods were immersed in a water basin in order to limit the phase jumps at the interfaces and reduce the phase clipping and wrapping artifacts, as introduced in Section 3.1.3. A series of 721 projections were acquired over 360° using a tube acceleration voltage $V_{tube} = 35\,\text{kVp}$. Each projection was reconstructed from 10 phase steps acquired with an exposure time of 6.7 s. The average intensity of the phase stepping curve was $Q_0 = 222$ Arbitrary Digital Units (ADU) and the visibility $v = 0.44$.

The three-dimensional volumes of the linear absorption coefficient $\Delta\mu$, refrac-

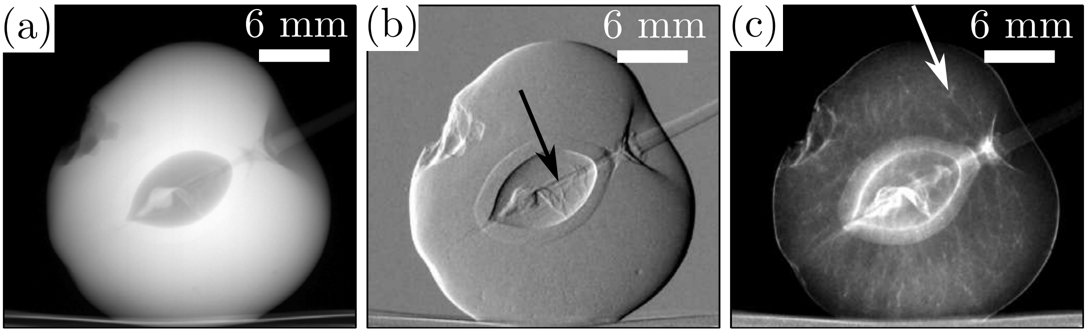

Figure 4.6: *(a) Transmission T, (b) Differential Phase Contrast DP and (c) Dark Field V images of a cherry acquired with the Talbot-Lau interferometer setup described in this section (adapted from (Revol et al. 2010b)).*

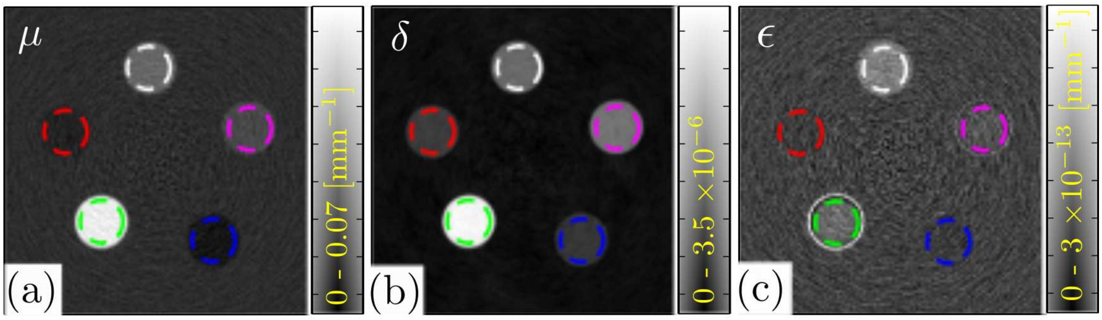

Figure 4.7: *Axial slice of the (a) linear absorption coefficient $\Delta\mu$, (b) refraction coefficient $\Delta\delta$ and (c) linear scattering coefficient $\Delta\epsilon$ reconstructed by computed tomography. The sample consists of five different plastic rods (from the top and going counterclockwise, torlon (white), plexiglass (red), teflon (green), nylon (blue) and polyoxymethylene (pink)) immersed in a water basin.*

tion coefficient $\Delta\delta$ and linear scattering coefficient $\Delta\epsilon$ were then reconstructed using the filtered back projection algorithms presented in Section 2.3. Note that $\Delta\mu$ (respectively $\Delta\delta$ and $\Delta\epsilon$) is actually the difference of the linear absorption coefficients (respectively, the indexes of refraction and the linear scattering coefficients) between the plastic of interest and water since the rods are placed in a water basin. An axial slice within the three volumes is shown in Figure 4.7, where the different rods are marked with colored circles.

The volumes were segmented and, for each plastic rod as well as for the background (i.e. the water), the average and standard deviation of $\Delta\mu$, $\Delta\delta$ and $\Delta\epsilon$ were extracted. The results are listed in Table 4.3. Table 4.4 compiles the values of the contrast to noise ratios CNR, where CNR_μ (respectively CNR_δ and CNR_ϵ) designates the contrast to noise ratio between the plastic of interest and the water i.e. the ratio $\Delta\mu_{plastic}/\sigma_{\mu,water}$ (respectively, $\Delta\delta_{plastic}/\sigma_{\delta,water}$ and $\Delta\epsilon_{plastic}/\sigma_{\epsilon,water}$).

In the present situation, the contrast to noise ratios (plastic/water) are higher

	Absorption $\Delta\mu \cdot 10^3$ [m^{-1}]	**Phase Contrast** $\Delta\delta \cdot 10^8$	**Dark Field** $\Delta\epsilon \cdot 10^{14}$ [m^{-1}]
PI	18.27 ± 1.75	20.57 ± 0.85	10.14 ± 2.23
PMMA	-3.49 ± 1.70	10.65 ± 0.80	-0.60 ± 2.08
PTFE	61.57 ± 2.02	54.27 ± 1.27	5.33 ± 2.71
PA66	-7.35 ± 1.71	9.06 ± 0.81	-0.91 ± 2.06
POM-C	8.95 ± 1.72	23.50 ± 0.84	2.32 ± 2.29
Water	0 ± 2.43	0 ± 1.00	0 ± 2.89

Table 4.3: *Mean and standard deviation of the segmented volumes $\Delta\mu$, $\Delta\delta$ and $\Delta\epsilon$ obtained from the computed tomography with setup **S20-4** as described in the text.*

in the phase contrast measurement than in the absorption-based computed tomography, which is consistent with the results of Section 3.2.5. The contrast improvement is particularly pronounced for POM-C/water and PMMA/water since μ_{PMMA} and μ_{POM-C} are close to μ_{water} and, consequently, cannot be readily distinguished from the medium (water) with the absorption contrast. Note especially that the contrast to noise ratio of phase contrast imaging is not generally better than that from absorption-based radiography. It depends on the material combination of the object under study and should be calculated, case by case, using tools similar to the ones presented in this thesis.

As for $\Delta\epsilon$, the contrast to noise ratio is poor. This was actually expected since the plastic rods are essentially homogeneous object and the contrast observed in Figure 4.7-c comes mainly from beam hardening and phase clipping (note the edge enhancement of the teflon rod). A significant contrast enhancement can however be observed when highly inhomogeneous objects are under study, as will be seen in Section 5.3.2.

For monochromatic radiation, the values of $\Delta\mu$ and $\Delta\delta$ are well-known and tabulated, for example, in the National Institute of Standards and Technologies database (Berger *et al.*). However, in our measurements, their values come from the weighted average of the different energies present in the energy spectrum. By analogy to monochromatic radiation, we define the effective energy of the absorption measurement $<E_\mu>$ as the energy for which the average $\bar{\Delta\mu}$ is equal to $\Delta\mu_{mono}(<E_\mu>)$, where $\Delta\mu_{mono}(<E_\mu>)$ is the tabulated value at energy $<E_\mu>$. Similarly, $<E_\delta>$ designates the effective energy of the measurement of $\Delta\delta$.

From Table 4.3, it can be found that $<E_\mu>\sim$ 27 keV while $<E_\delta>\sim$ 19 keV. The large difference looks surprising at first but can be explained easily. As was introduced in Section 3.1.1, the effective value of $\Delta\mu$ after propagation through a sample is essentially given by the weighted average over the exit energy spectrum,

	Absorption CNR_{μ}	**Phase Contrast** CNR_{δ}	**Dark Field** CNR_{ϵ}
PI	7.6	20.6	3.5
PMMA	1.5	10.6	0.2
PTFE	25.7	54.3	1.8
PA66	3	9.0	0.3
POM-C	3.7	23.5	0.8

Table 4.4: *The corresponding contrast to noise ratio CNR is defined as the ratio of the mean (either of μ, δ or ϵ) of the plastic of interest over the standard deviation in the media, here water.*

i.e. after filtering by the sample and the gratings[8]. In the present situation, the normalized energy spectrum from the tube operated with $V_{tube} = 35\,\text{kV}$ and after filtering by 1.5 mm Silicon and 20 mm water is plotted in Figure 4.8. The center of gravity of the spectrum lies around 27 keV, which agrees with the value obtained for $<E_{\mu}>$.

On the other hand, looking at Equation 2.72, it can be seen that the value of $\Delta\delta$ is linked to the average weighted not only by the energy spectrum but also by the coefficient q_1 (defined in Equation 2.69), i.e. indirectly by the visibility v^r. Now, since the visibility is maximal around the design energy E_{des} (equal to 20 keV in our case as displayed in Figure 4.8), the effective energy $<E_{\delta}>$ tends to be displaced towards E_{des}, as observed.

Note that the quantity $\Delta\epsilon$ is not tabulated in any database. Thus, the estimation of $<E_{\epsilon}>$ could not be achieved. Generally, it can however be considered that $<E_{\epsilon}>\sim<E_{\delta}>$ since the weighting of the different energies is identical for δ and ϵ.

As an example, a tomographic measurement of a plastic toy ("playmobil©") was realized by rotating the sample over 360° for a total of 721 steps. At each angular position, a phase stepping series was performed with 12 phase steps over one period. Each raw image was acquired during 4 s. The linear absorption coefficient $\mu(x, y, z)$, the refraction coefficient $\delta(x, y, z)$ as well as the linear scattering coefficient $\epsilon(x, y, z)$ were reconstructed as three-dimensional volumes using the algorithms introduced in Section 2.3. Figure 4.9-a displays a three-dimensional rendering of the surface of the playmobil© obtained by segmentation of the re-

---

[8] Here, it is assumed that the detector sensitivity does not vary strongly over the energy range of interest. Additionally, the coefficient q_0 (see Equation 2.69) is considered to be constant as a function of the energy. In a more detailed treatment, both phenomena could also be included without changing fundamentally the conclusions but it was decided to neglect them for the sake of simplicity.

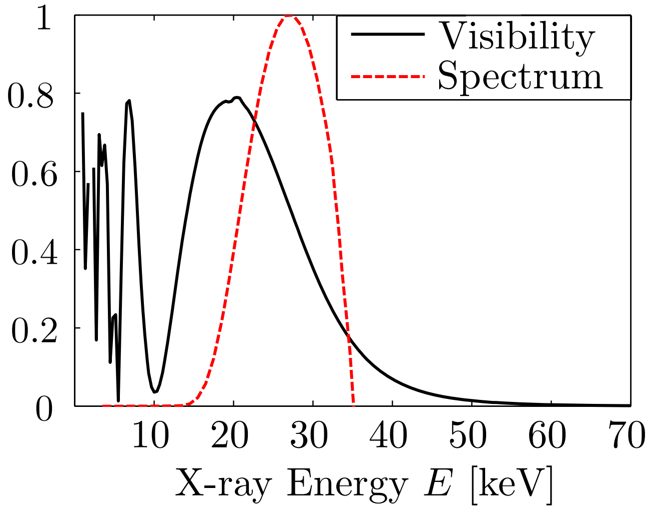

Figure 4.8: *The black solid curve shows the visibility as a function of the x-ray energy E (monochromatic wave) obtained using the simulation tool. The red dashed line represents the normalized energy spectrum for an acceleration voltage of 35 kVp after propagation through 1.5 mm of Silicon and 20 mm of water.*

fraction coefficient δ.

Finally, the three reconstructed volumes were combined into one (as shown in Figure 4.9-b) by using the Red-Green-Blue (RGB) coding where the R, G and B channels were attributed to δ, μ and ϵ, respectively. As a result, each combination of μ, δ and ϵ corresponds to a specific color. Thus, two materials with the same attenuation coefficient (and as such indistinguishable in conventional CT) but with different indices of refraction or different linear diffusion coefficients appear as two distinct colors and vice versa. These results as well as other examples were published in (Revol *et al.* 2010b; Kottler *et al.* 2010a).

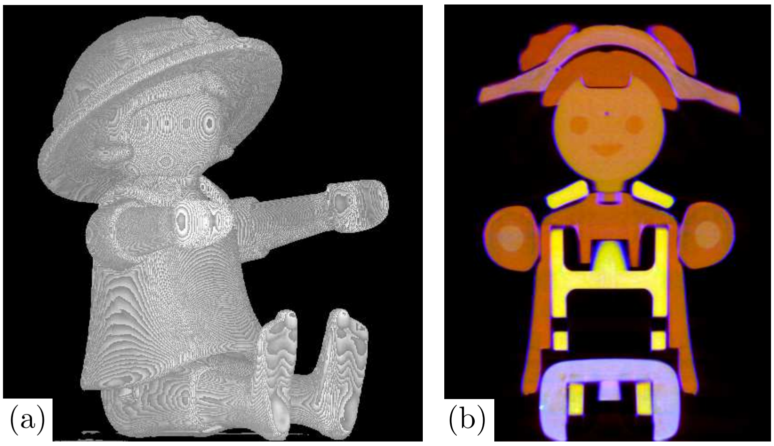

Figure 4.9: *(a) Three-dimensional rendering of the external surface of a playmobil*$^{\copyright}$ *done by segmentation of the refraction coefficient* $\delta(x, y, z)$*. (b) Tomographic reconstructed slice of a playmobil*$^{\copyright}$ *using RGB coding. Color channels Red, Green and Blue were attributed to the refraction coefficient* δ*, the attenuation coefficient* μ*, and the linear diffusion coefficient* ϵ*, respectively. The playmobil*$^{\copyright}$ *is made out of five different plastics, each identified by a specific color (adapted from (Revol et al. 2010b)).*

CHAPTER

FIVE

DEVELOPMENTS AND APPLICATIONS

Let us emphasize at this point that there is not one ideal grating interferometer that solves every problem for every sample. On the contrary, the design must be optimized for each application depending on the inspection task and the characteristics of the samples.

In Section 5.1, innovative methods are presented which address specific measurement needs. First, a reconstruction method based on Moiré fringes is implemented, which allows for a simple, fast and robust measurement procedure, particularly adapted to non-destructive testing. Secondly, dark field imaging can be combined with a rotation of the sample in order to extract information about the anisotropic micro-structure of a sample, for example the orientation of fibers in composite materials. Finally, dual energy phase contrast imaging with a grating interferometer is introduced.

Section 5.2 deals with developments in the instrumentation. An interferometer with bent gratings demonstrates that large fields of view are achievable in compact systems. Furthermore, it is seen that the phase sensitivity can be tuned by changing the fractional Talbot order. Additionally, the latest progress in the grating fabrication processes enabled the construction of a grating interferometer with a design energy of 50 keV, which allows for the investigation of thicker and/or denser samples.

Finally, the usefulness of the technique is discussed in Section 5.3 for applications in medical imaging, non-destructive testing and evaluation and security. The potential advantages are illustrated with the help of examples.

5.1 Advanced Imaging Methods

5.1.1 Moiré Fringes Reconstruction Method

Industrial applications, in particular in-line inspection, which is done directly on the production line, often require a large throughput, hence a fast image acquisition. In addition, the measurement must be done in demanding environmental conditions including vibrations and large temperature changes. In such situations, the phase stepping reconstruction method (see Section 2.2) is not optimal because it involves the translation of one of the gratings. This may lead to artifacts, for example when the gratings drift between the first and the last phase step. For this reason, a simpler reconstruction technique would be preferred.

This paragraph is dedicated to a method introduced in the domain of x-ray phase contrast imaging by Momose et al. in 2009 for synchrotron radiation (Momose *et al.* 2009). It has been successfully implemented in this work for conventional x-ray tubes. The method is based on the measurement of the changes in the Moiré fringes that appear when periodical signals are superimposed as illustrated in Figure 5.1 for two grids of periodicities p and p' (Hecht 2002). The modifications of these Moiré fringes are then analyzed by the Fourier-transform Method (introduced by (Takeda *et al.* 1982)) and allow for the calculation of the absorption, refraction and ultra-small angle scattering of the x-ray beam in the object.

Two types of Moiré fringes are distinguished here. First, the rotational Moiré fringes appear when the grids have the same periodicity $p = p'$ but are rotated with respect to each other by an angle $\vartheta \ll 1$. The resulting intensity variations are perpendicular to the grid lines and have a periodicity $p_m \sim p/\vartheta$. Secondly, the extension Moiré fringes occur when the grids are correctly aligned ($\vartheta = 0$) but have slightly different periodicities. In that case, intensity variations parallel to the grid lines with periodicity $p_m \sim p/|p' - p|$ are observed.

Let us now consider that the grating G_2 is slightly rotated by an angle $\vartheta \ll 1$ compared to grating G_1 as represented in Figure 5.1-c. It is assumed again that p_{fr}=p_2. The rotation of the coordinate system implies that, in the first order, x must be replaced by $x - y\vartheta$ and y by $y + \vartheta x$ in Equation 2.36. Considering Equations 2.73 and 2.74, the pixel intensity can finally be written as

$$\begin{aligned} I_{pix} &\sim Q_0 + Q_1 \sin\big(2\pi\frac{y\vartheta}{p_2} + \psi_1\big) && (5.1)\\ &\sim Q_0 && (5.2)\\ &\quad + \frac{1}{i2\pi}\Big[Q_1 \exp\big(i\psi_1\big)\exp\big(i2\pi\frac{y\vartheta}{p_2}\big) - Q_1\exp\big(-i\psi_1\big)\exp\big(-i2\pi\frac{y\vartheta}{p_2}\big)\Big] \end{aligned}$$

This expression tells us that the intensity I_{pix} varies now as a function of coordi-

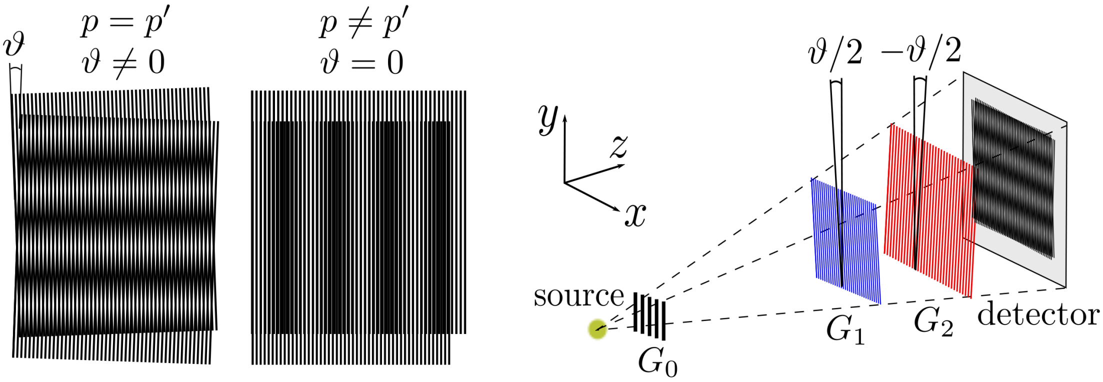

(a) (b) (c)

Figure 5.1: *(a) Rotational Moiré fringes perpendicular to the grating lines. (b) Extension Moiré fringes parallel to the grating lines. (c) Schematic view of the Talbot-Lau interferometer as prepared for the Moiré fringes Fourier transform method. Moiré fringes are induced by the rotation of grating* G_1 *and* G_2 *around the optical axis* z*.*

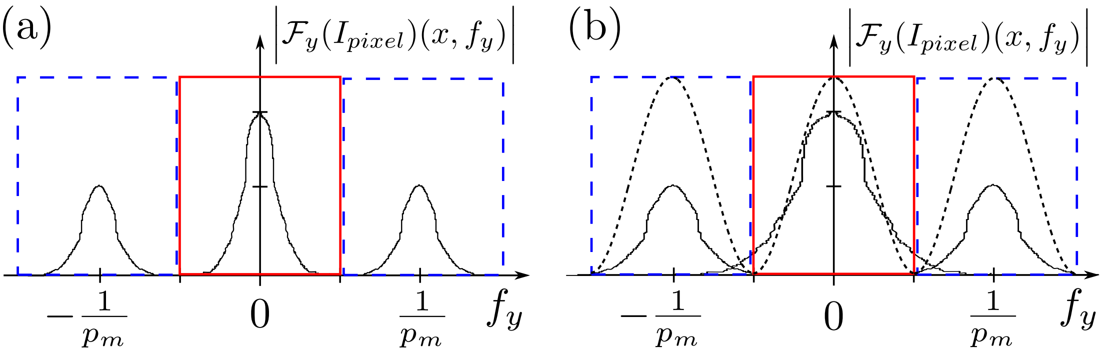

Figure 5.2: *(a) Schematic representation of the Fourier transformed pixel intensity* $|\mathcal{F}_y(I_{pix})(x, f_y)|$*. The central peak (in the red solid box) around* $f_y = 0$ *is equal to* $|\mathcal{F}_y(Q_0)(x, f_y)|$*. The side lobes (in the blue dashed boxes) around frequencies* $f_y = \pm 1/p_m$ *are equal to* $|\mathcal{F}_y(Q_1)(x, f_y)|$*. (b) When the sample's highest spatial frequency is larger than* $1/2p_m$*, aliasing artifacts appear due to the overlap of the central and side lobes. An anti-aliasing filtering window (dashed black curve) can be implemented to reduce this effect.*

nate y with periodicity $p_m \sim p_2/\vartheta$. Thus Moiré fringes act as a frequency carrier for the phase information. This means that the signals Q_1 and ψ_1 are shifted in the frequency domain from the zero frequency term Q_0 by the modulation frequency $1/p_m$ as can be seen in the following equation

$$\begin{aligned} \mathcal{F}_y(I_{pix})(x, f_y) &= \mathcal{F}_y\big(Q_0\big)(x, f_y) \\ &+\frac{1}{i2\pi}\mathcal{F}_y\big(Q_1\exp(i\psi_1)\big)(x, f_y - \frac{1}{p_m}) \\ &-\frac{1}{i2\pi}\mathcal{F}_y\big(Q_1\exp(-i\psi_1)\big)(x, f_y + \frac{1}{p_m}) \end{aligned} \tag{5.3}$$

Where $\mathcal{F}_y$ is the Fourier transform along the y-direction. So, provided that the signals $\mathcal{F}_y\big(Q_0\big)(x, f_y)$ and $\mathcal{F}_y\big(Q_1 e^{i\psi_1}\big)(x, f_y \pm \frac{1}{p_m})$ do not overlap in the frequency domain, i.e. $Q_0(x, y)$, $Q_1(x, y)$ and $\psi_1(x, y)$ vary slowly compared to p_m, the two terms can be isolated (see Figure 5.2-a) and the coefficients Q_0, Q_1 and ψ_1 can be recovered by

$$Q_0(x, y) = \mathcal{F}_y^{-1}\Big(\mathcal{F}_y(I_{pix})(x, f_y) \times \mathrm{rect}(p_m f_y)\Big)(x, y) \tag{5.4}$$

$$Q_1(x, y) = \Big|\mathcal{F}_y^{-1}\Big(\mathcal{F}_y(I_{pix})(x, f_y \pm \frac{1}{p_m}) \times \mathrm{rect}(p_m f_y)\Big)(x, y)\Big| \tag{5.5}$$

$$\begin{aligned} \psi_1(x, y) &= \frac{\pi}{2} \\ &\mp arg\Big[\mathcal{F}_y^{-1}\Big(\mathcal{F}_y(I_{pix})(x, f_y \pm \frac{1}{p_m}) \times \mathrm{rect}(p_m f_y)\Big)(x, y)\Big] \end{aligned} \tag{5.6}$$

Where $\mathrm{rect}(x)$ is the rectangular function equal to 1 for $|x| < 1/2$ and 0 elsewhere. From these results, the three images T, DP and V can be reconstructed, similarly to the phase stepping method, using Equations 2.85, 2.88 and 2.91, respectively. Note that, for the Moiré method, the data analysis is done per column whereas it is done for each pixel in the phase stepping method.

The results for a plastic toy are shown in Figure 5.3. The setup **S20-4** described in Section 4.3 was used for the measurements. The tube acceleration voltage was set to 40 kVp and the exposure time to 33 s. Rotational Moiré fringes with a periodicity p_m of 6 pixels (288 µm) were formed by rotating grating G_1 with respect to G_2. Images T, DP and V were then reconstructed using the algorithm discussed above.

Note that the extracted frequency windows have a width equal to $\pm p_m/2$ (Equations 5.4, 5.5 and 5.7). This implies that the spatial resolution in the y-direction (perpendicular to the Moiré fringes) in the final images is given by the periodicity of the Moiré fringes. The smaller p_m, the better is the resolution. In the example in Figure 5.3, the spatial resolution is thus equal to six times the detector pixel size. As a remark, zero padding[1] is in general done before taking the inverse Fourier

---

[1] Zero padding consists in extending the length of a signal by a series of zeros.

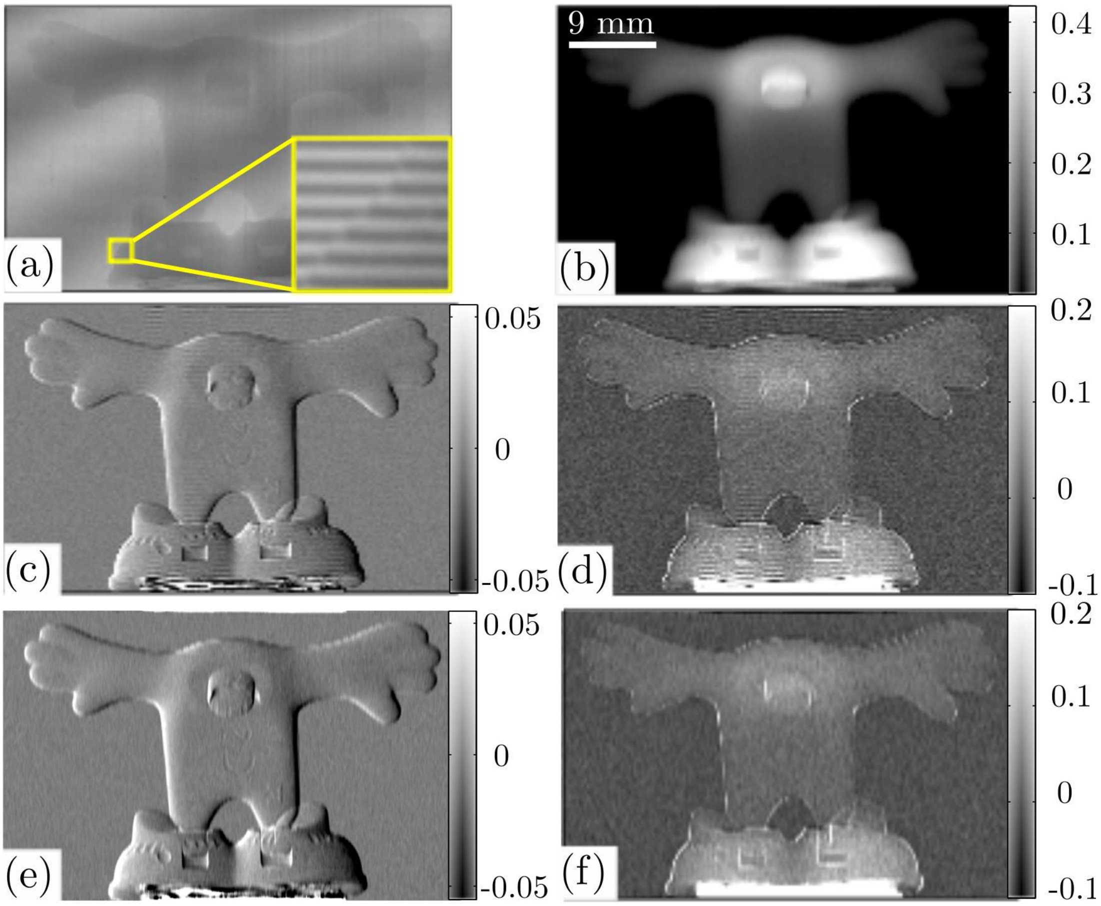

Figure 5.3: *(a) Intensity recorded by the detector in presence of Moiré fringes. The inset shows a zoom in of the intensity. A weak displacement of the fringes can be stated, although it may not be that clear for prints of poor quality. Reconstructed (b) transmission image* $-\log(T)$*, (c) differential phase contrast image* $\mathcal{DP}$ *and (d) dark field image* $-\log(V)$ *without anti-aliasing filter. (e) and (f) identical to (c) and (d) except that an anti-aliasing filter was used in the reconstruction.*

transform in order to recover the same signal length. The spatial resolution stays however unchanged in this operation.

The bottom limit of p_m is given by the Nyquist condition, which tells us that the sampling frequency should be at least twice the highest frequency in the acquired signal (Buzug 2008, Sect. 4.18). Assuming that the Moiré fringes form a perfect sine, this implies that p_m should be strictly larger than two pixels[2]. However, a second factor impacts on the choice of p_m. Indeed, the visibility of Moiré fringes decreases with the angular misalignment ϑ. This means that the noise in the images DP and V gets higher for smaller p_m. Thus, a trade-off must drawn between noise levels and spatial resolution. One way to get over this limitation would be to use extension Moiré (see Figure 5.1-b) thanks to gratings with adapted periodicities. This is probably the way that would be chosen for an industrial implementation.

Another interesting feature is the presence of bright and dark streaks in images DP and V like, for example, around the feet of the figurine in Figure 5.3-cd. Such artifacts occur when the highest spatial frequency of the object is higher than $1/2p_m$ (contrary to the assumption made for the reconstruction algorithm). In that case, the central peak overlaps with the side lobes in the frequency domain, as shown in Figure 5.2-b. Thus, high frequencies are wrongly added to the extracted spectra $\mathcal{F}_y\big(Q_0\big)(x, f_y)$ and $\mathcal{F}_y\big(Q_1 e^{i\psi_1}\big)(x, f_y \pm \frac{1}{p_m})$. This leads to the so-called aliasing artifacts.

Aliasing artifacts can be reduced by windowing the extracted spectra before taking the inverse Fourier transform (for instance, by a Hamming window (Buzug 2008, Sect. 7.2.1)). In this way, the undesired high frequencies are dampened. It however leads to a slight loss of spatial resolution in the final images. The images DP and V of the plastic toy after windowing are shown in the bottom row of Figure 5.3.

In conclusion, the Moiré fringes reconstruction method, in comparison to the phase stepping approach, has the following advantages. Although the image resolution is reduced compared to the phase stepping method, this technique does not require any mechanical movement of the gratings during the acquisition of the images. It is thus particularly robust and fast acquisition times are possible. Furthermore, the method is a lot less sensitive to mechanical drift of the gratings, caused by vibrations and/or temperature variations. This was tested by acquiring the sample image ten minutes after the reference image. No artifacts could be observed in the reconstructed images. In contrast, the same measurement done with the phase stepping method leads to drift artifacts. This method is envisioned to be particularly successful for fast scanning tasks in industrial environments.

---

[2] Note that p_m does not have to be a multiple of the pixel size. For example, it was confirmed experimentally that the method does function when p_m is equal to $2.6p_{pix}$.

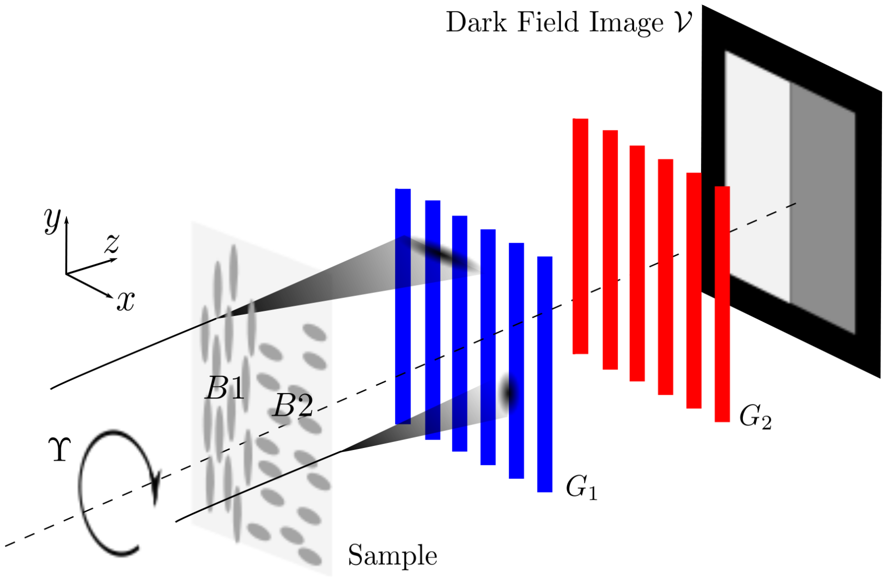

Figure 5.4: *A sample composed of ellipsoidal particles embedded in an homogeneous medium is placed in front of* G_1*. The sample can be rotated around the optical axis* z *by an angle* Υ*. Due to the unidirectional sensitivity of the dark field signal, the signal* $\mathcal{V}$ *varies as a function of* Υ*. It reaches a maximum when the long axis of the ellipsoidal particles is aligned with the grating lines. (Not to scale)*

5.1.2 Directional Dark Field Imaging

In this section, the emphasis is put on samples which have anisotropic microstructures. This is the case for example for modern composite materials, which are composed of fibers[3] embedded in a polymer medium. Such materials have normally a low weight but display excellent mechanical properties. For this reason, they receive a growing interest from the automotive and aerospace industries. However, the control of the production processes (injection molding, casting...) and their aging properties are still under intense study and the demand for adapted inspection tools is high.

As was seen before, dark field imaging is particularly sensitive to variations in the electron density at the micrometer scale and, thus, seems particularly adapted for the study of the fibers whose sizes range from hundreds of nanometers to hundreds of micrometers. Furthermore, only the contributions along the x-direction (perpendicular to the grating lines) are involved in the dark field contrast formation while variations along the y-direction simply result in a blurring of the image (Section 2.1.3).

This leads to the main idea of this paragraph, namely that the directional depen-

---

[3] For example, glass or carbon fibers.

dence of the dark field signal could be used to analyze the micro-structure of such anisotropic objects. This concept was also independently developed by another group (Jensen *et al.* 2010).

As an illustration, let us consider an object made of particles embedded in a homogeneous medium as shown in Figure 5.4. In one part $B1$ of the specimen, the particles have a highly anisotropic[4] ellipsoidal shape with their long axes oriented along the y-direction. In the other part $B2$, the anisotropy is less pronounced and the long axis is aligned with direction x.

Now, the (ultra small angle) scattering cross-section (as given by Equation 2.27) is related to the Fourier transform of the autocorrelation function of the electron density of the sample. Thus, fast spatial variations of the electron density along the x-direction will lead to scattering at large angles (along the x-direction) and vice versa for slow spatial variations.

To take an extreme example, let us consider a series of infinite planes $\mathcal{P}$ spaced by a constant distance and all perpendicular to the **u**-direction, where **u** is an arbitrary vector in space. In that case, the electron density only varies in the **u**-direction while it stays constant in other directions. As a consequence, the scattering cross-section is null in each direction except for the **u**-direction. Recalling that the normalized dark field signal $\mathcal{V}$ (see Section 2.3.4) is linked to the projection of the scattering vector along the x-direction (the direction perpendicular to the grating lines), $\mathcal{V}$ is equal to zero when the planes $\mathcal{P}$ are perpendicular to the x-direction and maximum when parallel to the latter.

Coming back to the case depicted in Figure 5.4, the dark field signal $\mathcal{V}$ is then higher in area $B1$ than in area $B2$. If the sample is now rotated by an angle Υ around the optical axis z, the signal $\mathcal{V}$ in area $B1$ decreases while that in area $B2$ increases. $\mathcal{V}$ is thus a periodic function of Υ with period π, which can be modeled as a sine curve (see Figure 5.5)

$$\mathcal{V}(\Upsilon) \quad \sim \quad X_0 + X_1 \sin\big(2\Upsilon + \Lambda_1\big) \tag{5.7}$$

Where X_0 is the mean, X_1 the amplitude and Δ_1 the phase of the sine. Thus, by acquiring a dark field image at different angles Υ, the coefficients X_0, X_1 and Δ_1 can be extracted, for example, by taking the Fourier transform of the signal $\mathcal{V}(\Upsilon)$.

The mean X_0 is linked to the isotropic part of the scattering (not dependent on the orientation). It is proportional to $\bar{\rho}^2$, the mean square of the variations in the electron density. The latter stems from the difference in electron density between the particles and the medium as well as from the size and density of particles. In

---

[4] This means that the ratio of the long axis over the minor axis is high.

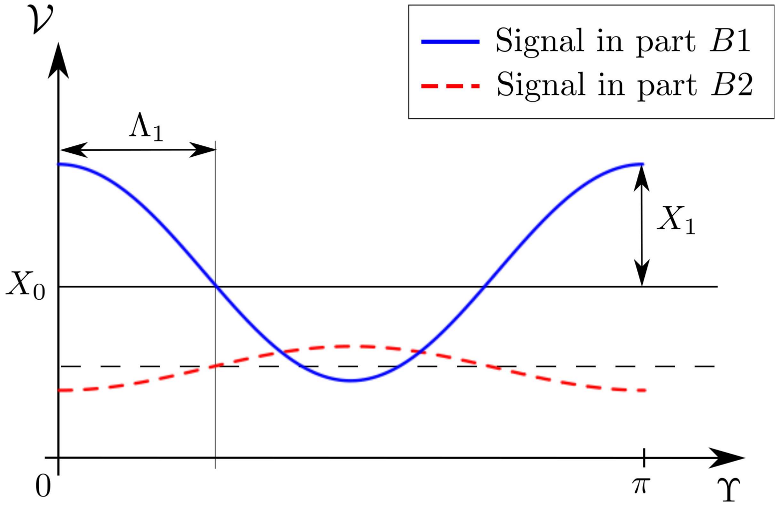

Figure 5.5: *The signal* $\mathcal{V}$ *as a function of angle* Υ *can be approximated by a sine curve of mean* X_0*, amplitude* X_1 *and phase* Λ_1*.*

Figure 5.4, the particle density is lower in part $B2$ than in $B1$. As a consequence, the mean X_0 must be lower for the signal in $B2$ than in $B1$.

Furthermore, the ratio $F = X_1/X_0$ relates to the degree of anisotropy. Thus, for spherical particles, F will be equal to zero since there is not preferred direction in space and the scattering remains constant as a function of the rotation angle Υ. However, when the particle is longer in a given direction, the ratio F will be larger than zero.

Finally, the phase Λ_1 depends on the initial orientation of the particles compared to the grating lines. For example, the particle in B_1 were initially aligned with the grating in such a way that the signal $\mathcal{V}$ was maximum for $\Upsilon = 0$. The phase Λ_1 is then equal to $\pi/2$. Inversely, the phase of the dark field curve in part B_2 is $3\pi/2$. It is thus possible to determine the preferred orientation of the particles.

Note that the dark field signal represents the average of the scattering over one pixel. As a consequence, the recovered information is not the orientation or shape of a single particle but the average over many particles at this position.

As an example, a piece of fabric was investigated with the setup **S20-4** described in Section 4.3. The sample consists of a mesh of fibers oriented along two different directions. A series of dark field images was acquired while rotating the sample around the optical axis by steps of 30°. The tube acceleration voltage was set 40 kVp and 20 phase steps with an exposure time of 6.7 s were realized.

In order to follow the signal $\mathcal{V}$ from one point of the sample at different angles, the

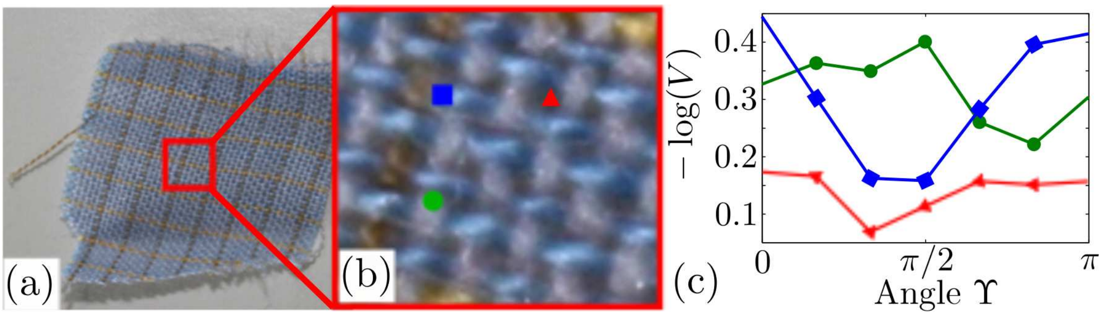

Figure 5.6: *(a) Photograph with (b) zoom of the fabric sample. (c) The signal $-\log(V)$ is plotted as a function of angle Υ for points in the hole of the mesh (triangle), in two fibers bundles of opposite orientation (round and square).*

acquired images have to be rotated before data analysis[5]. The curves $-\log(V)$ as a function of Υ of three different pixels are plotted in Figure 5.6-c. The triangles are taken in a part of the object where no fiber is present. Logically, the dark field signal stays low and does not vary with Υ. On the other hand, the squares, which represent a point in a fiber bundle, form a nice sine curve with a large amplitude X_1. The signal from a point of a fiber bundle oriented in the perpendicular direction also draws a sine curve but the phase Λ_1 is obviously shifted by π.

For each point of the fabric, the coefficients X_0, F and Λ_1 were reconstructed by taking the Fourier transform and are displayed in Figure 5.7. The mean X_0 represents the isotropic scattering and allows for the visualization of the density of the fibers. Note especially that X_0 is larger when the bundles of both directions overlap. The image of ratio F appears as an array of dots, which can be puzzling at first. However, remember that F is linked to the anisotropy of the sample microstructure. F is expected to be large within the bundle of fibers but not when they overlap. In that case, the signals from fibers oriented along two perpendicular directions are indeed out of phase and the resulting average signal looks more or less constant. Finally, the phase Λ_1 shows fast variations, which are due to the change of the fibers' direction from one bundle to another. Note that this image can be misleading, since the phase is not well defined in parts of the sample that are isotropic.

For this reason, the three images can be summarized into one compound image. The latter consists of dashes superimposed on a colormap. The latter represents the isotropic scattering (same as image X_0) while the dashes' length is proportional to the ratio F and their orientation is given by the phase Λ_1. This compound image enables a fast and efficient visualization of all three information channels.

As a conclusion, a method was developed which allows for the study of materials

---

[5] The sample is indeed rotated while the detector stays fixed.

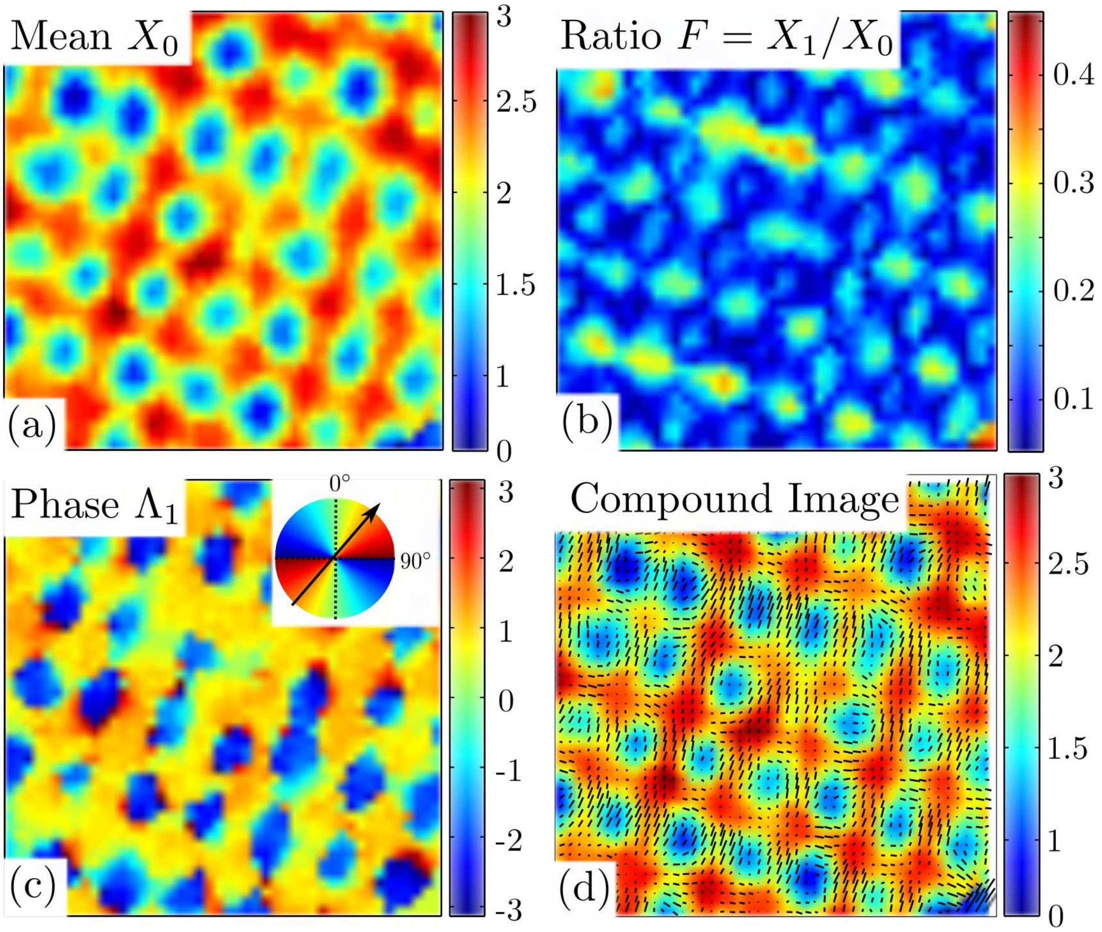

Figure 5.7: *(a) Isotropic scattering X_0, (b) anisotropic ratio $F = X_1/X_0$ and (c) phase Λ_1 reconstructed for the fabric specimen. (d) Compound image of all three sources of information, where the colormap (background) represents the isotropic scattering X_0. The dashes' length is proportional to ratio F and oriented according to phase Λ_1.*

with an anisotropic micro-structure. The method is based on the acquisition of a series of scatter dark field images while rotating the sample around the optical axis. Thus, not only the density and size of inhomogeneities can be reconstructed from the data but also the shape and orientation of these inhomogeneities. Such a method is of particular interest for fiber composite materials, for which no investigation method exists to determine the fibers' orientation and fulfills all requirements in terms of field of view and speed for an industrial implementation. This will be illustrated in Section 5.3.2.

5.1.3 Dual Energy Phase Contrast Imaging

Dual or multiple energy imaging (DE) is a conventional imaging method for absorption-based radiography. It is used to achieve elemental identification. In principle, DE relies on the measurement of the same sample over two different energy ranges. This can be done either by acquiring projections with different acceleration voltages of the x-ray tube or, more practically, by using an energy-sensitive detector.

Now, since the decrease of the linear absorption coefficient μ with the energy of the x-ray photons depends on the atomic number (Als-Nielsen & McMorrow 2001, Sect. 1.3), the measurement of the absorption over different energy ranges can be used to recover information on the composition of the sample. Such techniques are used for example in airports for the identification of explosives.

Such a dual-energy scheme could potentially also be beneficial for phase sensitive imaging methods. Its implementation is however not trivial, since most techniques have a limited energy bandwidth. A specific arrangement of the grating interferometer was recently suggested by (Kottler & Kaufmann 2009) that is simultaneously optimized over two energy ranges. Thus it could be used to achieve dual-energy phase sensitive measurements.

Generally, it should be recalled that the interference pattern follows from the diffraction of the x-ray wave onto a phase grating with phase shift $\Delta\Phi$. It was seen in Section 2.1.2 that, for a parallel beam, the interference periodicity is equal to twice the grating periodicity if $\Delta\Phi = \pi$. In any other case i.e. $\Delta\Phi \neq \pi$ (modulo 2π), the periodicity of the modulation is equal to the grating periodicity.

Thus, the idea lies in the use of a phase grating inducing a $\pi/2$-phase shift[6] at the design energy E_{des}. Indeed, the latter acts simultaneously as a $\pi/4$-phase grating at the double energy $2 \times E_{des}$. Recalling that the fringe periodicity do not depend on the energy, the interferometer can be used at the same time at

---

[6] Before this invention, the phase gratings were chosen to induce a π-phase shift at the design energy E_{des}.

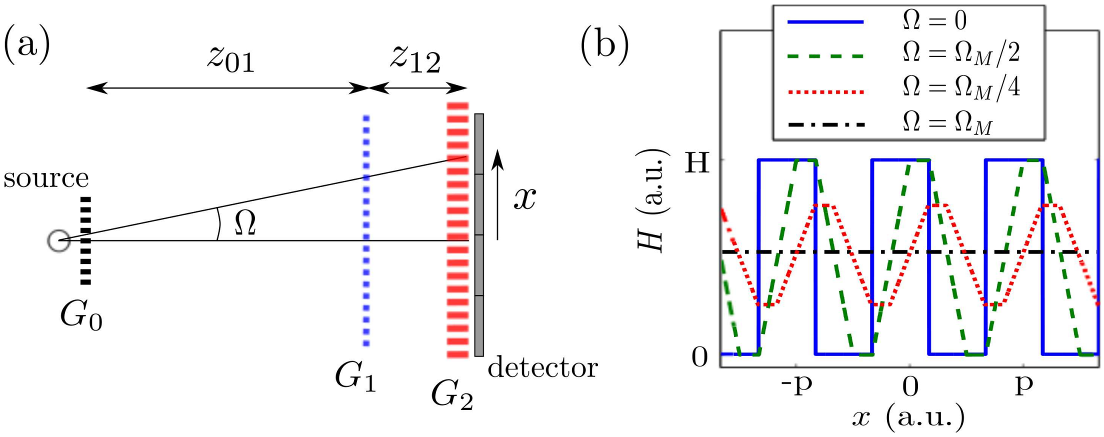

Figure 5.8: *(a) Standard Talbot-Lau geometry.* z_{01} *is the distance between the focal spot or* G_0 *and* G_1 *and* z_{12} *between* G_1 *and* G_2*. The incidence angle* Ω *increases with* x*, the distance from the optical axis. (b) Distorted profiles seen by the x-rays coming with different angles of incidence* Ω *onto a perfectly rectangular grating, where* $\Omega_M = \mathrm{atan}(p/H)$ *is the angular acceptance of the grating (adapted from (Revol et al. 2011b)).*

energies E_{des} and $2 \times E_{des}$. Note, that this is not the case for a π-phase grating since the periodicity of the interference differs then by a factor two.

The feasibility was demonstrated with the setup **S20-4** and the results are reported in (Kottler *et al.* 2010b).

5.2 Improvements in the Instrumentation

5.2.1 Bent Grating Interferometer for Large Fields of View

Up to now, it was assumed that the spherical divergence of the beam (as introduced in Section 2.1.5) did not cause any trouble. This is essentially true as long as the field of view is relatively small compared to the full system length $z_{01}+z_{12}$. However, for industrial systems, which often require compact geometries, the previous assumption does not hold anymore and leads to serious artifacts at the edges of the field of view.

Indeed, the x-rays do not impinge perpendicularly onto the gratings over the full field of view. If x is defined as the coordinate perpendicular to the gratings' lines (see Figure 5.8-a), whose origin is on the optical axis z, then $\Omega = \mathrm{atan}\big(x/(z_{01} + z_{12})\big)$ is the angle of incidence at the gratings. Clearly, Ω increases when x increases i.e. on the sides of the gratings.

Note that we only consider the direction x perpendicular to the grating's lines in the following study. The results can however be readily extended in two directions.

For one-dimensional gratings, a non-perpendicular angle of incidence onto the gratings along the y-direction, parallel to the gratings' lines will not affect the performance of the interferometer significantly since the grating profile does not vary along this direction. This remark does not hold for two-dimensional gratings, for which the effect will be similar along both gratings' directions.

As a consequence the x-ray beam, impinging onto the grating with an angle Ω, does not see the ideal rectangular grating as for $\Omega = 0$ but a distorted profile. This effect is illustrated in Figure 5.8-b for the angles of incidence $\Omega = \Omega_M/4$, $\Omega_M/2$ and Ω_M, where $\Omega_M = \text{atan}(p/H)$ is the angular acceptance of a grating of periodicity p and height H. For grating G_1, the distorted grating's profile leads to a distorted phase shift profile and, finally, to less pronounced intensity modulations, since the fractional Talbot effect is only optimal for one phase shift (Arrizòn & Ojeda-Castaeda 1994; Weitkamp *et al.* 2005). For grating G_2, the distorted grating's profile results in an additional blurring of the intensity pattern. Consequently, as the angle of incidence Ω increases, the performance of the Talbot-Lau interferometer decreases (Yashiro *et al.* 2008).

The method suggested here to counterbalance this effect is to use cylindrical gratings instead of plane gratings. The new geometry is displayed in Figure 5.9-a. It consists of the same elements as the standard interferometer except that G_1 and G_2 are bent with radii of curvature z_{01} and $z_{01} + z_{12}$, respectively and thus coincide with the x-ray wavefront. As a result, the angle of incidence Ω is constantly zero over the full field of view.

In order to verify the previous assertions, a compact grating interferometer named **S25-1b** was designed and built with distances $z_{01} = 515\,\text{mm}$ and $z_{12} = 77\,\text{mm}$. The sensitive area of the gratings being $5 \times 7\,\text{cm}^2$, the angles of incidence Ω run from -3.4° to +3.4°.

The x-ray gratings were optimized for an x-ray energy of 24.5 keV. The periodicities of G_0, G_1 and G_2 were $p_0 = 20\,\mu\text{m}$, $p_1 = 5.2\,\mu\text{m}$ and $p_2 = 3\,\mu\text{m}$ and the depths $H_0 = 45\,\mu\text{m}$, $H_1 = 30.9\,\mu\text{m}$ and $H_2 = 30\,\mu\text{m}$, respectively. The duty cycles were 0.25 for G_0 and 0.5 for G_1 and G_2. The corresponding angular acceptances are $\Omega_M^0 = 26.4°$, $\Omega_M^1 = 9.7°$ and $\Omega_M^2 = 5.74°$. In this configuration, the size of the field of view is clearly limited by gratings G_1 and G_2 and the effect of a non-perpendicular incidence on G_0 will be neglected.

Two types of frames were fabricated to mount the gratings G_1 and G_2. In the first type, the gratings are simply pinched punctually at the bottom and keep a plane profile (as shown in Figure 4.1). In the second type, the gratings are constrained onto a cylindrical metal frame (of adapted radius of curvature) thanks to two metal bars on each side of the grating (see Figure 5.9-c). The frame has a rectangular opening corresponding to the sensitive area of the gratings. Both frames were manufactured with standard machine tools (surface finished according to

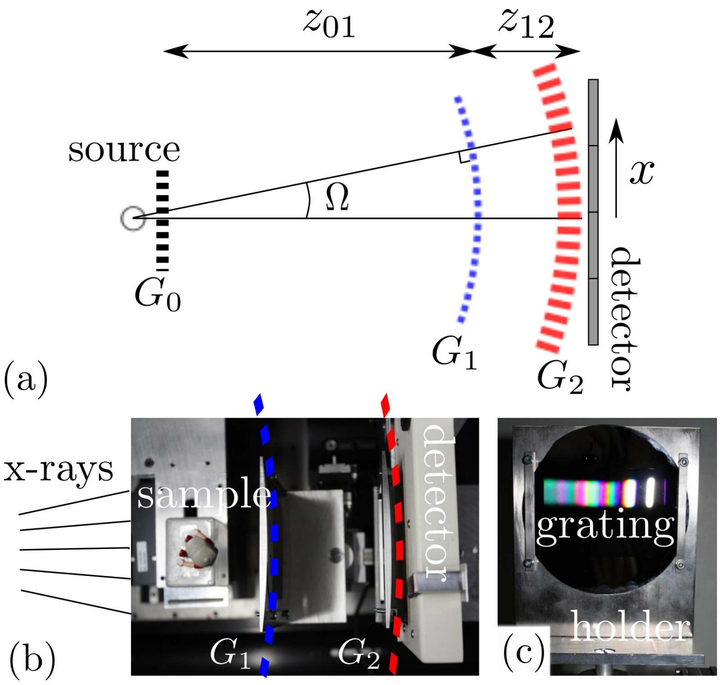

Figure 5.9: *(a) Proposed geometry with gratings G_1 and G_2 bent on a cylindrical shape of radii of curvature z_{01} and $z_{01} + z_{12}$, respectively. (b) Top view of the interferometer with the two cylindrical grating holders. (c) Front view of one of the cylindrical grating holders (adapted from (Revol et al. 2011b)).*

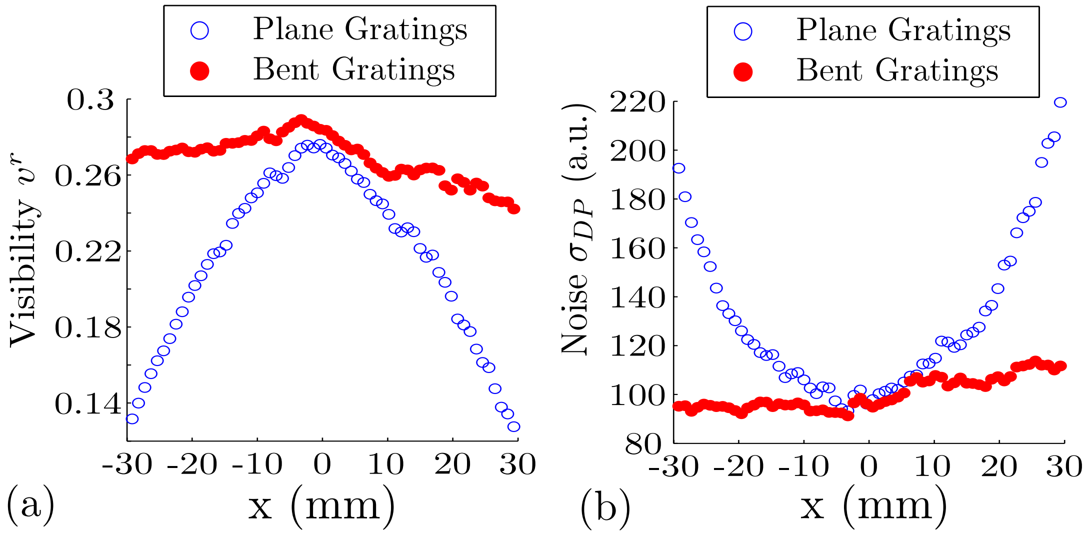

Figure 5.10: *(a) Visibility of the phase stepping curve v^r and (b) level of uncertainty σ_{DP} normalized by the value in the center of the field of view as a function of the coordinate x (adapted from (Revol et al. 2011b)).*

norm ISO-N7). A top view of the interferometer with bent gratings is shown on Figure 5.9-b.

For each type of frame, a series of 11 phase steps was realized by translating the source grating G_0 over one period p_0 in the direction perpendicular to the grating lines. At each position, an image was acquired with an acceleration voltage of the x-ray tube of 40 kVp and an anode current of 22.5 mA. The exposure time of the x-ray detector was set to 2 s. The visibility v^r was extracted and averaged over 100 pixels in the direction perpendicular to the gratings' lines. Additionally, a differential phase contrast image DP was calculated without an object in the field of view.

In Figure 5.10-a, the visibility v^r is plotted as a function of coordinate x (see Figure 5.8), once for the plane gratings and once for the bent gratings. A floating average of 10 pixels was realized along the x-direction to reduce the noise due to pixel-to-pixel variations. While, for plane gratings, the visibility v^r drops strongly as $|x|$ increases, v^r stays close to the center value for bent gratings.

Additionally, the level of uncertainties in the differential phase contrast image σ_{DP} was calculated as a function of the coordinate x by taking the standard deviation of the signal (without object) over an area of 10×100 pixels[7] and normalized by the value in the center of the field of view. Figure 5.10-b shows that σ_{DP} increases as $|x|$ increases for plane gratings but stays constant for bent gratings. The level

---

[7] The standard deviation is taken over an area of 10×100 pixels, where 10 refers to the x-direction and 100 to the y-direction

of uncertainty σ_{DP} is indeed inversely proportional to the visibility v^r (see Section 3.2). The increase of σ_{DP} in the plane gratings' configuration thus deteriorates the sensitivity of the measurement, which ultimately limits the usable size of the field of view. This limitation is overcome by the bent gratings' configuration.

The slight variations of the visibility and of the level of uncertainties for the bent gratings' configuration can be attributed to two contributions. First, the source grating G_0, which was not bent in our setup, also contributes to the decrease of the visibility away from the optical axis. Indeed, although the angles of incidence are small compared to the angular acceptance of grating G_0, its profile is slightly distorted, which results in a loss of spatial coherence of the x-rays and, consequently, a decrease of the visibility v^r. Secondly, imperfections in the curvature of the gratings' holders and defects of the gratings themselves, can impact locally on the visibility measurements.

In conclusion, a new geometry of the Talbot-Lau interferometer with gratings bent on cylindrical holders was demonstrated. Such a geometry allows for a perpendicular angle of incidence of the x-ray beam onto the gratings over the full field of view. It thus prevents the decrease of the visibility of our interferometer away from the optical axis, and consequently, the increase of the uncertainties in our measurement.

Such a demonstration removes one of the bottlenecks of grating-based phase contrast imaging, namely the limited size of the field of view. Compact systems with large fields of view, as used in micro-computerized tomography, can thus be envisioned. This work has been published in (Revol *et al.* 2011b).

5.2.2 Improving the Phase Sensitivity

Although contrast improvements in the measurement sensitivity could already be demonstrated by grating interferometry using setup **S20-4**, it is justified to wonder whether the phase sensitivity of the system could be further increased - under the same experimental conditions[8] - by tuning some of the design parameters. Obviously, such progress would allow new applications to be addressed, especially in medicine, where the requirements in terms of dose efficiency are extremely high.

In Section 3.2.5, an expression was derived for the signal to noise ratio of the differential phase contrast signal in the case of a cylindrical object. By revisiting this equation, the dominant factors can be identified as the visibility v^r of the phase stepping curve and the fractional Talbot order N. Taking the example of the setup **S20-4** introduced in Section 4.3, the visibility is principally limited by the

---

[8] Here is understood that the same energy spectrum is used and the same dose is imparted onto the sample.

energy bandwidth and not by the gratings' quality[9]. Much improvement is then not to be expected there. On the other hand, increasing the fractional Talbot order can be achieved by changing the periodicities of the different gratings. This provides a way to tune the phase sensitivity while keeping the same setup dimensions.

Accordingly, a new grating interferometer configuration **S20-12** was designed with fractional Talbot order $N = 12$ (previously $N = 4$) for the same design energy $E_{des} = 20$ keV and similar source-to-detector distance. The periodicities of G_0, G_1 and G_2 are $p_0 = 20\,\mu\text{m}$, $p_1 = 2.61\,\mu\text{m}$ and $p_2 = 3\,\mu\text{m}$ and the heights $H_0 = 45\,\mu\text{m}$, $H_1 = 12.85\,\mu\text{m}$ and $H_2 = 30\,\mu\text{m}$, respectively. The duty cycle of G_0 was chosen to be 0.2. For these parameters, the lengths are $z_{01} = 1265\,\text{mm}$ and $z_{12} = 189\,\text{mm}$.

In order to compare the sensitivities of the setups **S20-4** and **S20-12**, the experiment presented in Section 4.3 was repeated under the same conditions. Thus, 721 projections of the plastic rods (torlon (PI), plexiglass (PMMA), teflon (PTFE), nylon (PA66) and polyoxymethylene (POM-C)) were recorded over over 360° with an acceleration voltage of $V_{tube} = 35\,\text{kVp}$. Each projection was reconstructed from 10 phase steps acquired with an exposure time of 6.7 s. The average intensity of the phase stepping curve was $Q_0 = 260$ Arbitrary Digital Units (ADU) and the visibility $v = 0.20$ (for the measurement with setup **S20-12**).

The three-dimensional volumes of the linear absorption coefficient $\Delta\mu$, refraction coefficient $\Delta\delta$ and linear scattering coefficient $\Delta\epsilon$ were again reconstructed using the filtered back projection algorithms presented in Section 2.3. The volumes were segmented and, for each plastic rod as well as for the background (i.e. the water), the average and standard deviation of $\Delta\mu$, $\Delta\delta$ and $\Delta\epsilon$ were extracted. The results are listed in Table 5.1. The contrast to noise ratios for setups **S20-4** and **S20-12** are compiled in Table 5.2.

Table 5.1 shows that the values found for $\Delta\mu$ and $\Delta\delta$ are consistent with those measured with setup **S20-4**, as reported in Table 4.3. This is not the case for the linear scattering coefficient $\Delta\epsilon$. My explanation would be that the dominant effect in the formation of the dark field signal is not ultra small angle scattering in this measurement but beam hardening and phase clipping (see Section 3.1.4). Since both effects depend on the exact setup, this would explain the discrepancy in the measured values of $\Delta\epsilon$.

Next, by comparing the values to the NIST database (Berger *et al.*), it can be deduced that $<E_\mu>\sim 27\,\text{keV}$ while $<E_\delta>\sim 18\,\text{keV}$[10]. Those are logically similar

---

[9] For the cited setup, the measured visibility is indeed equal to the visibility predicted by the simulations. This implies that the gratings' quality does not suffer from large defects.

[10] As a reminder, $<E_\mu>$ and $<E_\delta>$ are the effective energies for the absorption and phase

	Absorption $\Delta\mu \cdot 10^3$ [m^{-1}]	**Phase Contrast** $\Delta\delta \cdot 10^8$	**Dark Field** $\Delta\epsilon \cdot 10^{14}$ [m^{-1}]
PI	19.00 ± 1.81	22.22 ± 0.65	1.17 ± 0.54
PMMA	-3.53 ± 1.75	11.50 ± 0.58	-0.18 ± 0.50
PTFE	64.70 ± 2.17	57.05 ± 1.32	0.56 ± 0.65
PA66	-7.46 ± 1.75	10.00 ± 0.58	-0.23 ± 0.50
POM-C	9.48 ± 1.78	25.21 ± 0.67	0.31 ± 0.66
Water	0 ± 2.53	0 ± 0.69	0 ± 0.69

Table 5.1: *Mean and standard deviation of the segmented volumes $\Delta\mu$, $\Delta\delta$ and $\Delta\epsilon$ obtained from the computed tomography with setup* ***S20-12*** *as described in the text.*

	Absorption CNR_μ		**Phase Contrast** CNR_δ	
	S20-4	**S20-12**	**S20-4**	**S20-12**
PI	7.6	7.5	20.6	31.9
PMMA	1.5	1.4	10.6	16.5
PTFE	25.7	25.6	54.3	81.8
PA66	3	2.9	9	14.3
POM-C	3.7	3.7	23.5	36.1

Table 5.2: *The table compiles the contrast to noise ratio CNR of the linear attenuation coefficient μ and refraction coefficient δ measured for the different plastic rods for both setups* ***S20-4*** *and* ***S20-12****.*

to the values found for setup **S20-4**.

Moreover, by looking at Table 5.2, it can be seen that that the contrast-to-noise ratios CNR_μ for different plastics are nearly identical in both tables. Indeed, the latter depends essentially on the total detected photon flux, which was the same for the two acquisition series (260 versus 222 ADU). On the other hand, the values of CNR_δ have been increased by ~50% for each plastic. This results essentially from two contributions: the increase of the fractional Talbot order by a factor three (from 4 to 12) which is mitigated by the halving of the visibility v^r (from 0.44 to 0.2). A substantial contrast improvement could thus be demonstrated for setup **S20-12** in comparison to setup **S20-4**.

In conclusion, it was seen that the phase sensitivity of the system can be tuned by changing the fractional Talbot order N and this, without modifying the setup length (hence the photon flux incoming on the detector). This is done at the cost of smaller x-ray grating periodicities. This, in turn, increases the challenges in terms of their production. Furthermore, it should be noticed that, as the system becomes more sensitive to phase variations, the impact of ultra small angle scattering also gets larger. This can be of course an advantage in some applications. It is however penalizing for strongly scattering samples, since the loss of visibility is then increased and can result in the destruction of the phase signal. Thus, higher fractional Talbot order may not always be beneficial. On the contrary, for strong scatterers, like for the inspection of wood or brick, it may even be interesting to lower the fractional Talbot order.

5.2.3 Increasing the Effective Energy

Choosing or shaping the energy spectrum of the x-ray photons contributing to the signal is one of the key parameters in x-ray imaging. Indeed, if the effective energy[11] is too low, most of the radiation will be absorbed in the sample before reaching the detector. This has two consequences. First, the noise in the image will be high since the former is inversely proportional to the square root of the acquired intensity (see Section 3). Secondly, a large dose will be imparted on the sample, which is a major concern for living samples. On the contrary, if the effective energy is too high, the interaction with the object will be too weak to obtain a good contrast in the image.

In absorption-based radiography, the spectrum, and hence the effective en-

---

contrast measurements as described in Section 4.3.

[11] The effective energy E_X of the measurement of a quantity X is defined as the energy for which the measured value $\bar{X}$ obtained for polychromatic radiation is equal to $X(E_X)$, where X is the value for monochromatic radiation. In our case, X can be the linear absorption coefficient μ, the refractive index δ or the linear scattering coefficient ϵ.

ergy, can be tuned easily by changing the acceleration voltage of the x-ray tube and/or by using x-ray filters placed between the source and the sample[12] (Sandborg *et al.* 1994; Okunade 2002). However, this becomes more complicated for differential phase contrast imaging with a grating interferometer. Indeed, not only the shape of the x-ray spectrum impacts on the effective energy but also the dependence of the visibility on the energy as was discussed in Section 4.3. The latter is typically maximum at the design energy E_{des}[13].

In the grating interferometers introduced up to now in this thesis, the effective energies for the phase measurements were close to 20 keV for setups **S20-4** and **S20-4** or 24.5 keV for setup **S25-1b**. Such energies are adapted for the investigation of thin samples made of light elements, for which significant contrast enhancements could be demonstrated. Nevertheless it is insufficient to image thick specimens - like, for instance, a human arm - or objects composed of dense elements, like metals. Since a large majority of medical and industrial tasks demand higher effective energies, a large effort was devoted to increasing the latter in grating interferometry and thus accessing new application domains.

Now, the effective energy of the phase measurement is driven first by the design energy E_{des} and secondly by the effective absorption of the source grating G_0 and analyzer grating G_2. In particular, the second effect should not be neglected. As illustrated in Figure 5.11-a, although $E_{des} = 50$ keV in these simulations, the maximum of the visibility, hence the effective energy, gets shifted towards lower energies as the height of grating G_2 decreases.

Thus, a larger effective energy requires increasing the heights H_0, H_1 and H_2 of the x-ray grating G_0, G_1 and G_2. H_1 scales nearly linearly with the effective energy while H_0 and H_2 grow exponentially except at the K-edges[14]. This appears in the plots of the penetration depth of the x-ray beam as a function of the energy for gold, lead and tungsten displayed in Figure 5.11-b.

For example, for an energy of 20 keV, H_1 is equal to 12.8 µm for a $\pi/2$-phase grating made out of silicon while H_2 should be equal to 11 µm to obtain an absorption of 75%. At 50 keV, H_1 becomes equal to 32.3 µm while G_2 has now to be 120 µm-deep to achieve the same performance. Furthermore, if the total

---

[12] Filters consist usually of thin plates of metal like copper or aluminum. As a result of beam hardening (see Section 3.1.1), the lower part of the energy spectrum is strongly attenuated. In some cases, K-edge filters, for which the characteristic energy of the K-edge of the filter element lies within the spectrum, are used. More information on filters can be found in (Sandborg *et al.* 1994; Okunade 2002).

[13] In our case, the design energy is defined in such a way that the phase shift of the wave after propagation through the silicon grating is equal to $\pi/2$ as defined in Section 2.1.2.

[14] K-edges describe the sudden increase in the linear absorption coefficient, which occurs at the binding energy of the electrons of the K shell.

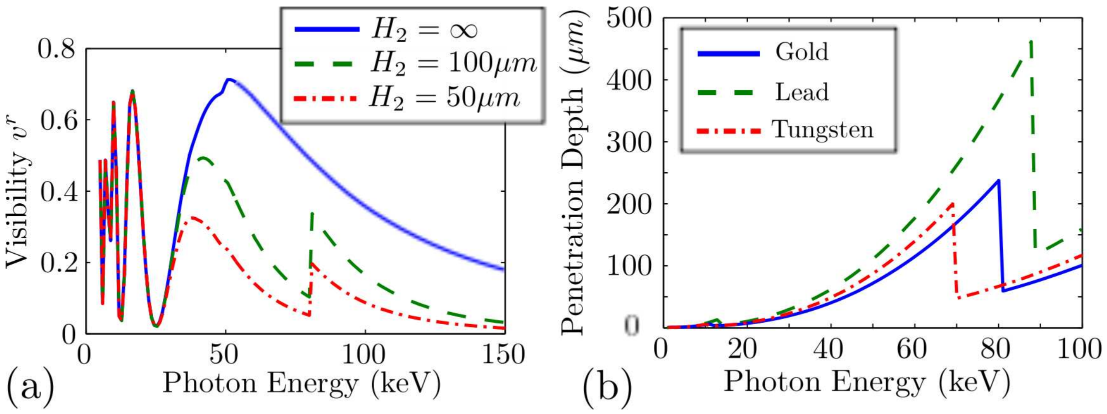

Figure 5.11: *(a) Simulated visibility as a function of the energy for a setup of design energy $E_{des} = 50\,keV$ assuming an infinitely deep source grating G_0. Different heights H_2 of grating G_2 were simulated. The sudden increase of the visibility around $E = 80\,keV$ is due to the K-edge of gold which is used here as the absorber for the grating G_2. (b) Penetration depth of the x-ray beam as a function of the energy for different metals. The K-edges of gold, lead and tungsten occur approximately at energies 80.7 keV, 88 keV and 69.5 keV respectively.*

length of the interferometer is kept constant, the increase of the design energies results in a decrease of the periodicities p_0, p_1 and p_2. All in all, the aspect ratio of the x-ray gratings increases drastically with the effective energy, in particular for G_0 and G_2.

This is of course a challenge for the processes used to produce the x-ray gratings. The progresses realized in this domain by my colleagues at CSEM Neuchâtel, in particular Francis Cardot and Philippe Niedermann, were nonetheless sufficient to design and manufacture a set of gratings, named **S50-4**, optimized for a design energy $E_{des} = 50\,\text{keV}$. The periodicities are $p_0 = 20\,\mu\text{m}$, $p_1 = 4\,\mu\text{m}$ and $p_2 = 5\,\mu\text{m}$ and the depths $H_0 = 100\,\mu\text{m}$, $H_1 = 32\,\mu\text{m}$ and $H_2 = 100\,\mu\text{m}$, respectively. The distances are set to $z_{01} = 1613\,\text{mm}$ and $z_{12} = 403\,\text{mm}$, which correspond to a fractional Talbot order $N = 4$.

The average visibility v^r achieved with setup **S50-4** was measured as a function of the tube voltage V_{tube} and compared to the values obtained by simulation (see Section 4.2.2) as reported in Figure 5.12. The error bars represent the standard deviation of the measured visibility over the field of view. The experiment was repeated with different thickness of aluminum filters. As can be observed, the measured visibility is lower than the expectations. This is due to some imperfections in the fabrication processes of grating G_2, notably to non-uniformity in the deposition of the gold layer along the trenches (see Section 4.1.3 for a reminder of the fabrication processes). As a result, the apparent grating profile is not perfectly rectangular, which causes a loss of visibility.

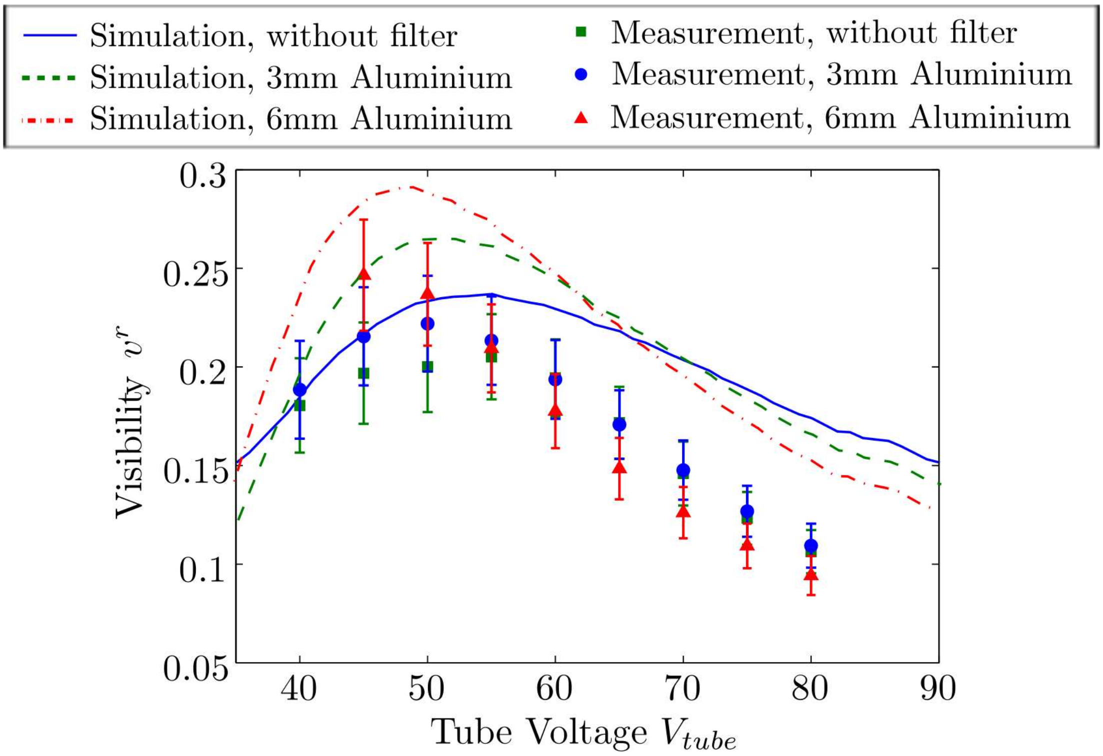

Figure 5.12: *Measured and simulated visibility of setup* ***S50-4*** *as a function of the tube voltage* V_{tube} *without filter and with an aluminum filter of thickness 3 mm or 6 mm. The error bars represent the standard deviation of the measured visibility over the field of view.*

Nevertheless, a visibility around 0.18 can be achieved for a tube voltage $V_{tube} = 60\,\text{kVp}$. This value is sufficient to achieve a good phase sensitivity. In addition, note that the measured visibility does not change significantly in the presence of the aluminum filters. This means that the contrast is not only due to the x-rays of low energies and, as a consequence, that the effective energy of the phase measurement has been significantly increased compared to setups **S20-4** and **S20-12**. This allows then for the investigation of thicker and denser samples, as will be illustrated for the inspection of porosity in an aluminum weld in Section 5.3.2.

5.3 Applications

Last but not least, the relevance of grating interferometry for diverse applications will be discussed in this section. The analysis are made with the help of measurements done on a large variety of samples. The results are summarized by application fields, namely medical imaging, non-destructive testing and evalua-

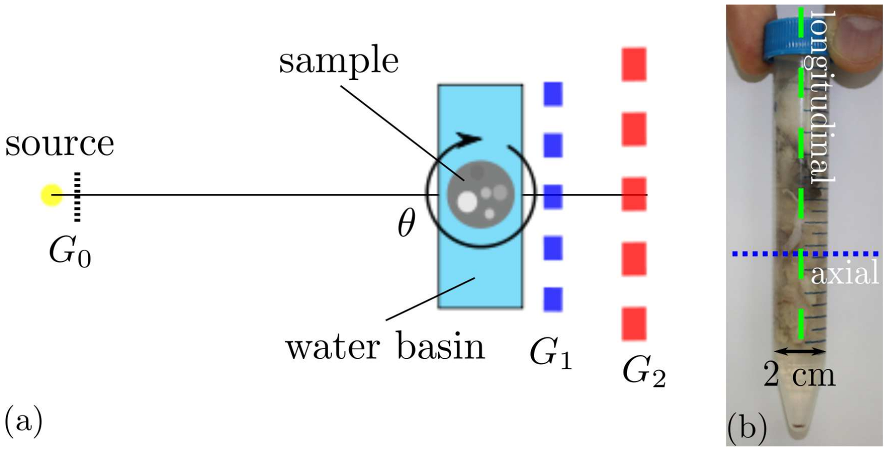

Figure 5.13: *(a) Schematic view of setup* ***S20-12*** *used for the screening of diverse organs. The experimental tube is placed in a water basin in front of G_1 and projections are acquired at different angles θ. (b) Photograph of one of the experimental tubes with the specimen embedded in agarose gel. The tube is rotated around its axis and the longitudinal and axial cross-sections are represented by the green dashed line and dotted blue line, respectively.*

tion and security.

The screening of the multiple specimens represents the largest part of the experimental effort. In total, more than 3000 measurement series (from a single image to a complete tomography) were acquired and generated more than 1.5 TeraBytes of raw data.

5.3.1 *Medical Imaging*

This section investigates the potential of x-ray phase contrast imaging for medical diagnostics. X-ray phase contrast imaging has attracted indeed a lot of interest in this field since it offers an increased contrast for light elements (for example, biological tissues) compared to conventional absorption-based systems.

However, medical diagnostics belong to the most challenging applications. Indeed, the requirements in term of dose efficiency[15] and reliability are extremely high. In addition, the features of interest are particularly complex. The body is composed of highly absorbing structures, the bones, and diverse soft tissues (organs, fat, connective tissue), whose electron densities are close to each other. Thus, the detection of variations of the morphology or composition of those tissues (for example, the development of a tumor) requires a high sensitivity.

---

[15] Dose efficiency relates to the usefulness of the extracted information compared to the radiation dose absorbed by the patient.

Organs Screening

In the following, the interferometer configuration **S20-12** (Section 5.2.2) is used to realize computerized tomography on specimens of various organs, both from human and animal donors. These initial results were used to identify potential applications, for which phase contrast imaging based on the grating interferometer could be of advantage to medicine.

The different human organs were gathered and prepared with the help of PD. Dr. med. Caroline Maake from the Anatomy department of the University of Zürich within a joint project supported by the Gerbert-Ruf Stiftung under contract GRS-033/08. The specimens were fixed in formalin before being placed in a 2 cm-diameter plastic tube (see Figure 5.14-a) and embedded in agarose gel to ensure that the sample does not move or alter during the measurement.

For the tomographic measurement, the tubes were placed in a 2.5 cm-wide rectangular water tank, as can be seen in Figure 5.13. Water is used as an immersion fluid in order to prevent phase clipping and phase wrapping artifacts (see Section 3.1.3). 721 projections over 360° were realized with an acceleration voltage of $V_{tube} = 40\,\mathrm{kVp}$. Each projection was reconstructed from 10 phase steps, acquired with an exposure time of 6.7 s. The three-dimensional volumes of the linear absorption coefficient μ, refraction coefficient δ and linear scattering coefficient ϵ were reconstructed using the filtered back projection algorithms presented in Section 2.3.

As an example, Figure 5.14 displays the results for a specimen of human adrenalin gland surrounded by fat and connective tissue. Cross sections (axial and longitudinal) are depicted within the reconstructed volumes μ, δ and ϵ. This allows for the direct comparison of the information delivered by the different contrast mechanisms. In both μ and δ, the fat and connective tissue can be visualized as well as the organ itself with medulla and cortex. Note that the contrast to noise ratio in phase contrast imaging is higher than in absorption contrast. For instance, the light halo around the medulla appears clearly in the reconstruction of δ while it can hardly be distinguished from the gelatin in the cross sections of μ. As for the linear scattering coefficient ϵ, it gives a completely different image of the sample. The septa (partition walls) of the connective tissue are highlighted while the soft tissues themselves are difficult to identify.

The results for other organs are summarized in Table 5.3 and some cross-sections can be found in Appendix A. It can be concluded that the contrast improvements of phase contrast imaging in comparison to absorption imaging depend strongly on the investigated tissues. For instance, for liver or lung specimens, the organ could not be rendered using either phase contrast or absorption-based imaging.

Nevertheless, our setup allowed significant breakthroughs in terms of contrast for samples of the adrenal gland, of the mesentery, of tendons embedded in

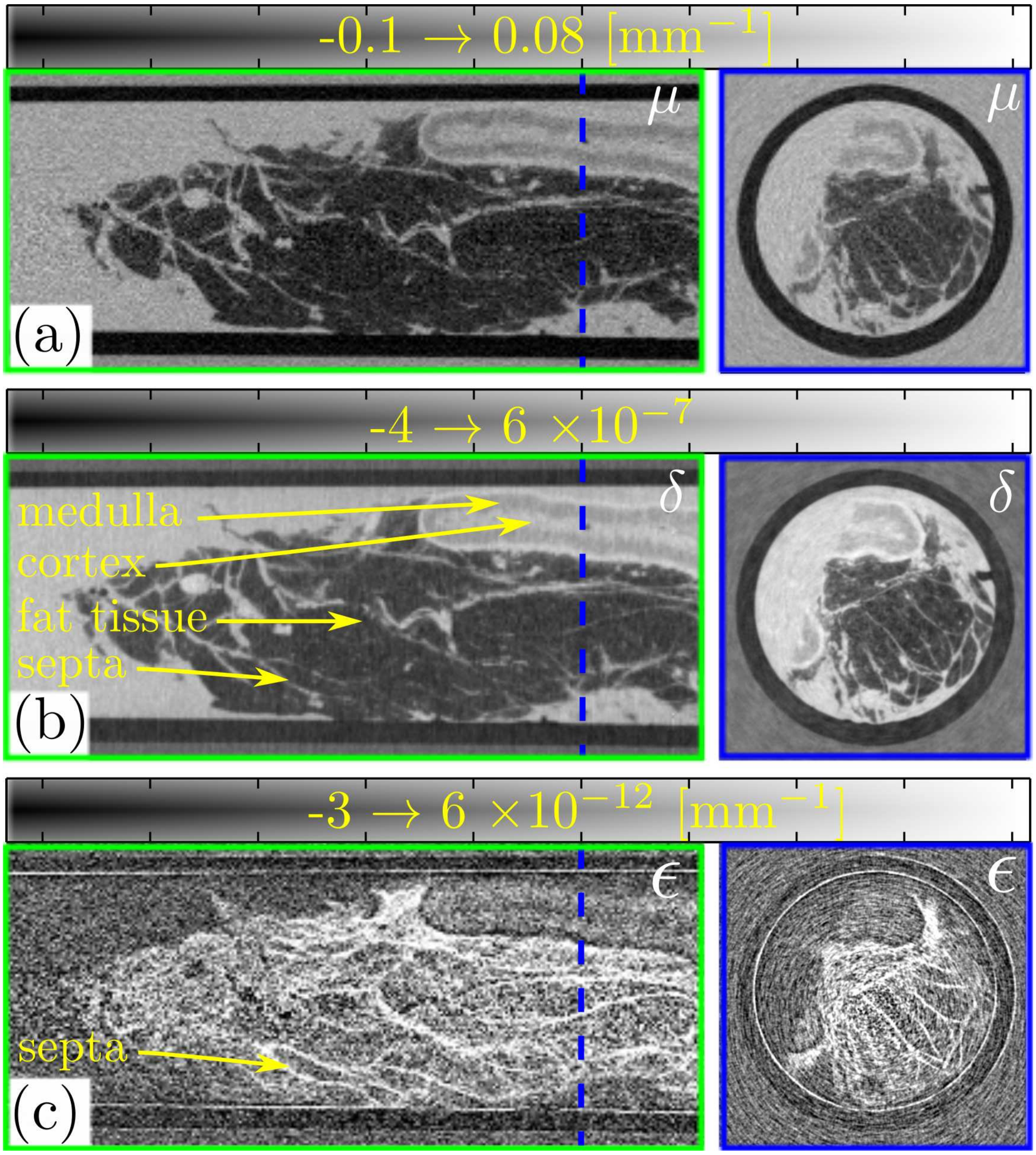

Figure 5.14: *(a), (b) and (c) show a longitudinal (left) and axial (right) cross-sections within the three-dimensional reconstructions of, respectively, the linear absorption coefficient μ, the refraction coefficient δ and the linear scattering coefficient ϵ for a specimen composed of a human adrenal gland surrounded by fat and connective tissue.*

muscles and of blood vessels and arteries. In particular for arteries, the contrast improvement was significant and allows for the visualization of structures previously invisible in absorption tomography. Initial results were published in (Kottler *et al.* 2010c) but the project is still on-going.

	Number of Samples	**Observations**
Adrenal Gland	2	Fat and connective tissue can be identified. Cortex and medulla appear in both absorption and phase contrast imaging but with a better signal to noise ratio in the latter.
Pancreas	1	Fat and connective tissue can be recognized. Otherwise, few anatomical structure can be distinguished from the background.
Vessels Arteries	4	Fat and connective tissue can be recognized. Structure of the vessel can be visualized with phase contrast imaging but not with absorption-based imaging. Notably the lumen, media and adventitia were identified. In the human samples, atherosclerotic plaques could be observed.
Liver	2	Few anatomical structures can be distinguished from the background.
Stomach	1	Few anatomical structures can be distinguished from the background.
Lungs	2	No anatomical structure can be distinguished from the background.
Mesentery	1	Fat and connective tissue can be recognized. Blood vessels can be distinguished with phase contrast imaging and not with absorption imaging.
Spleen	1	No anatomical structure can be distinguished from the background.
Tendons	1	The tendons can be distinguished from muscles with phase contrast imaging and not with absorption imaging.

Table 5.3: *Summary of the observations for different human organs investigated under the experimental procedure reported in the text.*

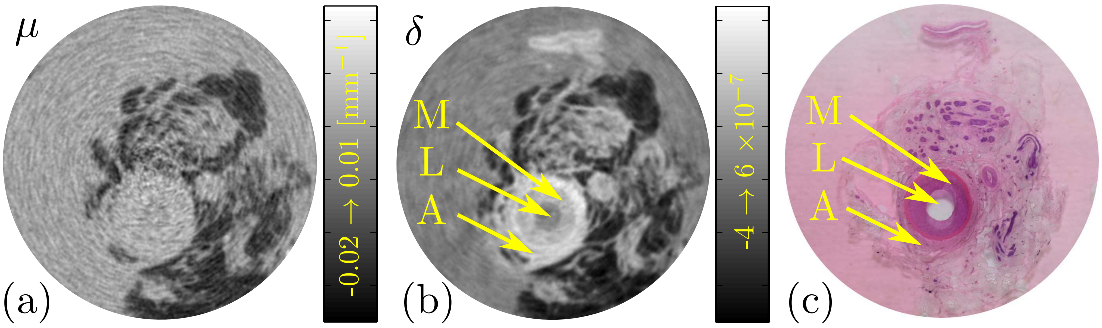

Figure 5.15: *Axial cross sections of the (a) linear absorption coefficient μ and (b) refraction coefficient δ for the artery of a calf. (c) Photograph of an histology slice stained with hematoxylin and eosin of the same specimen. The Lumen (L), Media (M) and Adventitia (A) could be identified.*

Cardiovascular Imaging

Cardiovascular diseases represent the main cause of fatalities in western countries. They are the result of defects in the circulatory system, which can potentially lead to a stroke or a heart infarct. It turns out that the arteries and vessels are particularly difficult to image by absorption-based radiography. For this reason, angiography[16] is usually realized with the help of a contrast agent[17] injected into the blood. However, contrast agents have two main disadvantages. First and foremost, contrast agents are typically made out of heavy elements and cause secondary effects on the health of the patient. Secondly, only the lumen (cavity between the vessel walls, where the blood flows) is highlighted by contrast agents but the medium (the vessel wall itself) stays invisible. Therefore only indirect conclusions on the malignancy can be made.

As was seen in Table 5.3, the structure of blood vessels and arteries can be well inspected by phase contrast tomography with a grating interferometer. Thus, it is envisioned that our method could help in the early detection of cardiovascular diseases. For this reason, a study was started in order to investigate this potential in more detail. Some first results will be presented in the following, with a particular focus on atherosclerotic plaques. This study is done in association with the Cardiology Research Group lead by Prof. Dr. med. Thomas F. Lüscher from the University of Zürich.

Samples from the artery of a calf were prepared in para-formaldehyde and subjected to computed tomography following the same experimental protocol as pre-

---

[16] Angiography is the imaging technique used to visualize for instance arteries, veins and the heart chambers.

[17] A contrast agent is a substance, typically made out of heavy metals, which is injected into the body in order to highlight a particular organ or tissue.

sented in the previous paragraph. Figure 5.15-ab shows axial cross-sections of the reconstructed linear absorption coefficient μ and refraction coefficient δ. At a first glance, it can be seen that δ reveals information on the artery that are completely invisible in the measurement of μ.

In order to confirm and identify the tissues appearing in δ, histology slices were prepared from the exact same specimen and stained with hematoxylin and eosin. A photograph of the corresponding slice of the artery is shown in Figure 5.15-c. This photograph allows for the identification of the different tissues, notably, the lumen (L), media (M) and adventitia (A). Furthermore, the histology slice can be mapped with the structure observed in the cross-section of δ. Thus, contrarily to absorption-based tomography, phase contrast tomography allows for the visualization of the media and adventitia. This could be of interest for the study of certain malignancy like, for example, the vulnerability of atherosclerotic plaques.

Indeed, although atherosclerotic plaques can usually be visualized with absorption-based radiography, it is impossible to distinguish between stable (innocuous) and unstable (vulnerable) plaques, which are weakly bounded to the lumen and can potentially be released in the blood. This can result in the formation of a thrombus and lead to a stroke or a heart attack. Our first results with phase contrast imaging let us envision that the liaison between the lumen and the plaques could be investigated. Studies on this topic are still on-going.

Small Animal Imaging

Finally, it is thought that differential phase contrast imaging could be of interest in small animal imaging. In particular, the required x-ray energies and the dimensions of the field of view lie in a range which is already achievable at this stage of the development. Although it represents a small market, small animal imaging would be a good starting point to gain clinical and in-situ technical experience. This could then be used to verify the usefulness of the technique and to enter more important markets in the future.

Measurements were done on relatively unusual animals, namely on snails called Arion rufus (Linnaeus 1758). The animals were provided by Dr. Eva Knop from the Department of Community Ecology of the University of Berne. The living snails were subjected to parallel-plate compression as is done typically in mammography. This procedure immobilizes the specimens and evens out the thickness, which allows for a better visualization of the structure of interest. The results for one specimen are shown in Figure 5.16. Different features can be observed in the differential phase contrast DP or dark field V images that are not revealed as clearly in the conventional absorption-based image T. Although not all organs could be allocated in the images, the winding structure was identified as the intestinal tract. Note that it is particularly well revealed in V.

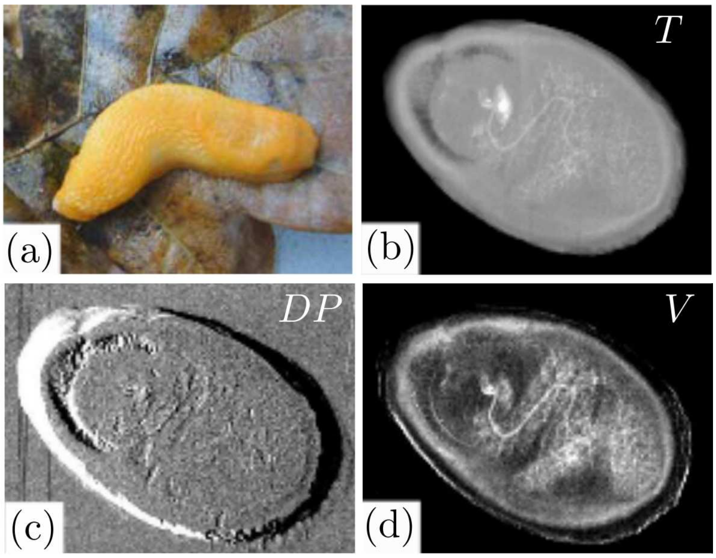

Figure 5.16: *(a) Photograph of the imaged snail Arion rufus after the experiment. (b) Absorption-based T, (c) differential phase contrast DP and dark field V images of the specimen (adapted from (Kottler et al. 2010a)).*

5.3.2 Non-Destructive Testing and Evaluation

Non-destructive testing and evaluation represents the second biggest market for x-ray imaging systems. On the one hand, in-line inspection refers more particularly to the systematic quality control of manufactured goods, implemented right on the production belt. Thus, it calls for high throughput and robustness, since the system must work continuously. On the other hand, evaluation is done on a limited number of samples in order to optimize or control the fabrication process.

Non-destructive testing and evaluation is used typically for critical parts in a wide range of activities, like for instance in the automotive, aerospace and medical supply industry. It is also implemented for the detection of impurities in packaged goods, as for instance in the food industry.

Obviously, the key advantage of non-destructive techniques is that the object stay intact after the measurement. This is essential on the production line, since the products must be delivered after the test. For evaluation purposes, it is also important in order to be able to proceed to different analysis (potentially, with complementary methods) on the exact same sample without altering its characteristics. In the following paragraphs, the potential of grating interferometry for non-destructive testing and evaluation was assessed experimentally for a variety of application domains.

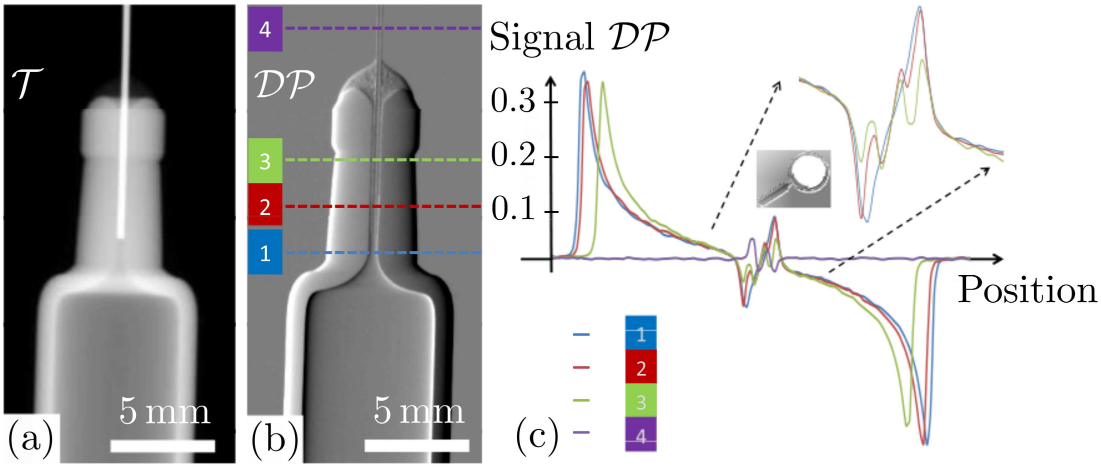

Figure 5.17: *Normalized (a) absorption-based $\mathcal{T}$ and (b) differential phase contrast $\mathcal{DP}$ images of a syringe. (c) Cross-sections of image $\mathcal{DP}$ at different vertical positions (adapted from (Kottler et al. 2010a)).*

Detection of Manufacturing Faults

During the production or assembly of manufactured goods, some errors may result in malformations like the deformation of one part, or the improper gluing or sealing of two pieces. In that case, the resulting product will not meet the specifications, which can hamper its future use. This is particularly important for critical objects such as for medical supply, where a failure may have dramatic consequences. Thus, inspection methods are needed to prevent such faulty products from reaching the user.

As an example, the usefulness of differential phase contrast imaging is evaluated here for the quality control of syringes. The samples were inspected with the grating interferometer **S20-4**. The syringes were composed of a metal needle glued into a glass body. The gluing of the needle represents a major issue for the fabrication process. An insufficient surface coverage leads to a weak bounding to the body and may cause the needle to be pulled out during its extraction from the patient. On the contrary, an excess of glue may result in the closing of the needle opening.

As can be seen in Figure 5.17, the absorption-based radiography does not provide a good contrast because the metal needle absorbs most of the radiation and saturates the signal. However, the differential phase contrast image allows for the visualization of the coverage of glue along the needle. This can be seen by a careful observation of the area between the needle and the body in image $\mathcal{DP}$. It becomes even clearer by looking at the plots of the signal $\mathcal{DP}$ as a function of the horizontal coordinate. Different vertical positions are marked by a number from "1" to "4".

The plots display series of peaks (positive or negative). Each peak indicates the presence of an interface between two materials of different refraction coefficient (strong phase jump). Thus, the plot ”1” reveals four interfaces that are due to the separations between the syringe body and the air (in the following sequence air/glass/air/glass/air). Similarly, four peaks appear in the middle of plot ”4”. Those are related with the interfaces between the metal needle and the air. Note that the differential phase signal is wrapped at this interface (see Section 3.1.3).

Now, the plots ”2” and ”3” are the most interesting. In both cases, one can count six symmetrical peaks. In plot ”2”, the peaks correspond to the interfaces air/glass/air/metal/air/glass/air. Plot ”3” is similar to plot ”2” except that the peaks corresponding to the interface glass/air and air/glass (in the middle) are not as pronounced. This reveals the presence of the glue (instead of the air) between the glass body and the metal needle. The difference of refraction coefficient between glass and glue is indeed much smaller than between glass and the air. As a consequence, the phase jump at the interface is smaller. This results in a smaller peak in the differential phase contrast signal DP.

Thus, the differential phase contrast image could be used to detect the presence of glue along the metal needle and test that the fabrication process fulfills the specifications. A similar study was realized to ascertain the presence of a polymer fiber (equivalent to any polymer like for example the glue) inside the needle opening. In such a case, the polymer would prevent the liquid from flowing in or out of the needle. As for the previous situation, differential phase contrast imaging allowed the presence of the fiber to be detected while this was impossible with absorption-based radiography. This example is reported in Figure B.1 in Appendix B.

Inspection of Sub-Pixel Porosity

The characterization of the micro-structure of manufactured goods is of paramount importance. The latter often impacts directly on the aging properties of the materials like the formation of cracks. In particular, porosity is a challenging issue in injection molding of plastics and for metal welding. The quantification of the density and size of the pores (both depend strongly on the process parameters) cannot be done using conventional x-raying systems (without magnification) because of the restriction in terms of spatial resolutions. Indeed, the latter lies in industrial systems at the best around 50 µm while the pores are often in the micron-range.

Magnification can be realized with the so-called micro-focus x-ray tubes[18] to achieve spatial resolutions in the order of a micrometer. However, the inspected

---

[18] Micro-focus x-ray tubes have a focal spot in the range of 1 to 50 µm. For comparison, for conventional x-ray tubes, the size lies around 1 mm.

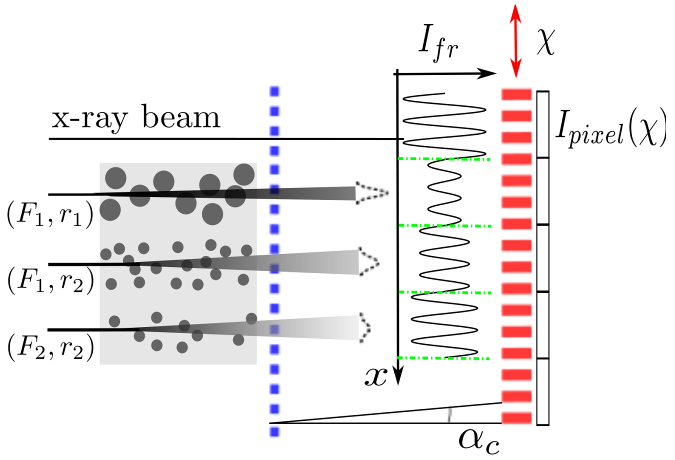

Figure 5.18: *A pure phase object composed of spherical inhomogeneities embedded in an uniform medium is placed in the x-ray beam. The interference I_{fr} induced by G_1 onto the plane of G_2 are blurred due to the ultra-small angle scattering. The decrease of the visibility (amplitude divided by the mean) of I_{fr} varies with the radius r and the volume fraction F of the particles as discussed in the text. The drawings are not to scale (adapted from (Revol et al. 2011a)).*

volume is accordingly reduced and moreover the power rating of such micro-focus sources is limited[19]. As a consequence, this method cannot be applied for the investigation of large samples within a reasonable measurement time.

This section explains how scatter dark field imaging can be implemented for the inspection of porosity and cracks at a sub-pixel length scale. As an example, a detailed study of a piece of aluminum weld is done with the grating interferometer **S50-4**. The conclusions are extended to other applications and fueled by experimental results.

Scatter Dark Field Imaging has been introduced in Section 2.1.3. Let us consider now a pure phase object (meaning not absorbing) composed of spheres of material A, which are smaller than the pixel size embedded in material B. In the case of porous materials, A would be for example air. The propagation of the x-ray beam through those multiple spheres (randomly positioned) results in variations of the wavefront Φ_f, which are fast compared to the pixel size. These unresolved phase variations cause a decrease of the visibility v^s as discussed in Section 2.1.3.

Using Equation 2.33, the expression of the dark field signal V developped by (Yashiro *et al.* 2010) can be calculated in the case of a monochromatic beam of wavelength λ. Assuming that the ensemble of the phase signals Φ_f over one pixel

---

[19] The achievable power rating is roughly proportional to the surface of the focal spot.

forms a Gaussian distribution, V can be expressed as

$$V(m,n) = \exp\Big(- \sigma^2_{\Phi_s}(m,n)\big(1 - \gamma(-Np_1/8, 0; m,n)\big)\Big) \tag{5.8}$$

Where σ_{Φ_s} is the width and γ is the normalized autocorrelation function of the Gaussian distribution Φ_f. As a reminder, p_1 is the periodicity of grating G_1 and N is the fractional Talbot order.

Clearly, V decreases with the width σ. In addition, it is weighted by the autocorrelation of the phase variations over the length $Np_1/8$. Perfectly uncorrelated phase variations ($\gamma = 0$) contribute fully to the visibility loss while correlated phase variations (in the extreme case, an uniform object) do not affect the signal V.

For spherical inhomogeneities of radius r, the quantities σ and γ can be calculated analytically and are given by (Yashiro *et al.* 2010)

$$\begin{aligned}
\sigma^2 &= \big(Ft\big) \cdot \big(\frac{3}{2} r \Delta\rho^2 r_e^2 \lambda^2\big) && (5.9)\\
\gamma(-Np_1/8) &= \Big(1 + \frac{R^2}{2}\Big)\sqrt{1-R^2} \\
&\quad + \Big(2R^2 - \frac{R^4}{2}\Big) \log\Big(\frac{|R|}{1+\sqrt{1-R^2}}\Big) && (5.10)\\
\text{with } R &= \frac{Np_1}{16r} && (5.11)
\end{aligned}$$

Where F is the volume fraction occupied by the spherical inclusions (equal to the number density multiplied by the volume of a single sphere), t is the thickness of the sample along the beam propagation, r_e is the classical electron radius and $\Delta\rho$ is the difference in the number density of electrons between materials A and B.

The quantity σ^2 is linked to the intensity of the ultra small angle scattering. For the same volume fraction, the latter increases with the radius of the spherical inhomogeneities (green dotted line in Figure 5.19-a). On the other hand, the factor (1-γ) is associated with the ratio of the scattering angle α over the critical angle of the interferometer $\alpha_c = p_2/z_{12} = 8\lambda/Np_1$ (see Figure 5.18). If α is larger than α_c, the blurring will affect fully the interference pattern (blurring window larger than one period p_2). Smaller scattering angles will on the contrary have a reduced impact. Remembering that the scattering angle scales with $\lambda/2\pi d$, this explains that $(1-\gamma)$ is equal to 1 until $r = Np_1/16$ and then decreases (red dot-dashed curve in Figure 5.19-a). The exact form of the curve depends on the shape of the particles.

Due to the combination of both effects, the dark field signal V reaches a minimum V_{min} as plotted in Figure 5.19-a (blue solid curve). V_{min} increases as a function

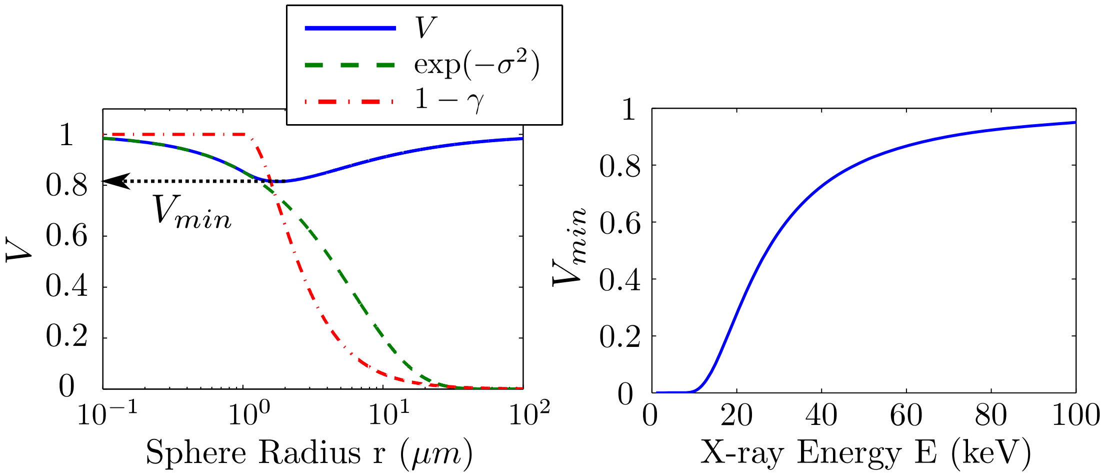

Figure 5.19: *(a) Calculated dark field signal V for spherical air pockets trapped in an aluminum piece as a function of the radius for an x-ray of 50 keV. The other parameters were fixed at values $p_1 = 4\,\mu\text{m}$, $N = 4$, $F = 0.5$, $t = 10\,\text{mm}$ and $\Delta\rho = 66 \times 10^{29}\,m^{-3}$. (b) Plot of the minimal dark field signal V_{min} as a function of the x-ray energy (adapted from (Revol et al. 2011a)).*

of the energy as can be seen in Figure 5.19-b. For lower energies, the visibility goes to zero, i.e. the interference modulations are completely blurred and the reconstructed dark field and differential phase contrast signals will be noisy (see Section 3.2).

In summary, the dark field signal V is related to the particles' (gas pockets in the present case) size and density. Thus, dark field imaging is a good tool for the investigation of porous materials. Since the length scale of the micro-structure contributing to the signal is not linked to the detector resolution, large samples can be imaged.

As an example, a sample, prepared by Audi AG, was produced by Metal Inert Gas (MIG) welding aluminum/aluminum of two plates placed at right angles. A photograph can be seen in Figure 5.20-a. During the process, pores appear in the weld pool, which are called blow holes. The density and size of the blow holes depend on the process conditions and determine partly the mechanical resistance of the joint.

For the dark field measurements, the x-ray grating interferometer **S50-4** introduced in Section 5.2.3 was used. The two-dimensional radiographs of the attenuation T and of the scatter dark field V of the sample were reconstructed from a series of 20 phase steps with an exposure time of 6.7 s at each step. The acceleration voltage of the x-ray tube was set to 70 kVp. Computed tomography was also realized by acquiring 361 projections of the sample by angular steps of 1°. The cone-beam filtered back projection algorithm developed for phase contrast

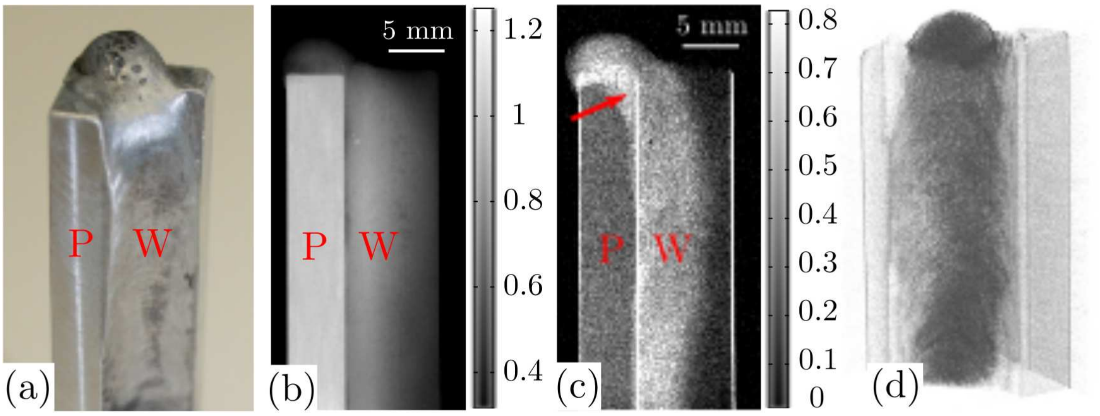

Figure 5.20: *(a) Photograph of the aluminum weld. (b) Logarithms of the absorption-based radiography* $-\log(T)$ *and (c) scatter dark field image* $-\log(V)$ *of the aluminum weld. The letters W and P have been placed to distinguish the weld from the plates. Note that the weld can be better differentiated from the plates in the scatter dark field image. (d) Three-dimensional rendering of the aluminum weld done using the reconstructed linear scattering coefficient* ϵ *(adapted from (Revol et al. 2011a)).*

imaging at Empa (Jerjen *et al.* 2010; Feldkamp *et al.* 1984) was used to reconstruct both the linear absorption coefficient μ and the linear scattering coefficient ϵ. The reconstruction algorithm of the linear scattering coefficient supposes that the inhomogeneities are isotropic. This is justified in the present case since the air inclusions are spherical. This can be verified by looking at the three-dimensional reconstructions of the linear absorption coefficient obtained by micro-tomography.

In order to confirm the results, comparative measurements were done with an x-ray micro-computed tomography instrument (µCT) located at Empa (Trtik *et al.* 2011). It comprises a micrometer-spot size X-ray tube, a high precision rotation table mounted on an XYZ stage made of three linear stages and an X-ray flat panel detector with pixels of size $50 \times 50\ \mu\text{m}^2$. 2×2 pixels were binned together for the measurement. The distance between the source and the detector was 500 mm while the test object was placed at a distance of 50 mm from the source. The spatial resolution of the reconstructed images is equal to 10 µm.

The x-ray tube was biased at an acceleration voltage of 70 kVp. 721 projected images, evenly distributed over 360°, were recorded. For each projection, 8 individual images with an integration time of 0.5 s were recorded. The three-dimensional image of the linear absorption coefficient in the test object was calculated by means of a filtered back projection Feldkamp algorithm (Feldkamp *et al.* 1984).

Two-dimensional radiographies of the sample are displayed in Figure 5.20-bc. A clear contrast improvement can be observed between the absorption-based image T and the scatter dark field image V. Indeed, while the density of the weld is very similar to the aluminum plates (same material hence a similar absorption), the micro-structures differ. The aluminum plates are essentially homogeneous while the weld is composed of a multitude of blow holes of various sizes. As explained above, such inhomogeneities result in a loss of visibility, as measured by the dark field signal V. Note that the image V allows us already to observe that the weld pool extends into the aluminum plates, as indicated by the red arrow in Figure 5.20-c.

Going to the results of the computed tomography, an axial slice within the coefficients μ and ϵ is depicted in Figure 5.21-ab. As expected, the value of μ is identical within the weld and the plates such that it is hard to distinguish one from the other. Although some large blow holes can be observed, the majority have a size below the spatial resolution of this measurement and thus stay invisible. On the other hand, the cross-section of ϵ reveals a clear contrast between the weld and the plates. Compared to two-dimensional projections, the three-dimensional reconstruction enables a precise visualization of the weld volume, notably to observe the interface between the weld and the plates. Figure 5.20-d displays a three-dimensional rendering of the weld volume.

Finally, these results were compared to the three-dimensional reconstruction of μ obtained with the x-ray micro-computer tomography instrument. Using VG-studio Max, the data were segmented in order to extract the positions and volumes of the blow holes using the built-in automatic threshold selection. For the same axial cross section, Figure 5.21-c shows the spatial distribution of the blow holes with the volume represented by a color code.

By comparison of the zoom-in images in Figure 5.21-d and e, two conclusions can be drawn. First, ϵ is close to zero for blow holes that are much larger than the pixel size. Indeed, such holes form a homogeneous area (trapped gas) and do not result in a SDFI signal. Secondly, the value of ϵ appears correlated with the density of the holes. The denser the holes, the larger is ϵ. Moreover, it can be observed that ϵ also takes large values in regions where no blow holes can be observed in Figure 5.21-d. In fact, the spatial resolution of the µCT instrument lies by 10 μm while USAS is maximum for inhomogeneities of size around 2 μm. Thus, the observed USAS must be related to blow holes of size smaller than 10 μm.

Note that the density of blow holes is lower close to the interface with the aluminum plates. We suppose that this distribution is due to the temperature profile of the workpiece during welding. These results were obtained in close collaboration with Iwan Jerjen and Philipp Schutz from Empa. They are published in (Revol *et al.* 2011a).

The method presented in this section was also applied to other types of scattering samples. The results are summarized in Table 5.4 and another measurement example can be found in Figure B.4 in Appendix B. In conclusion, the usefulness of

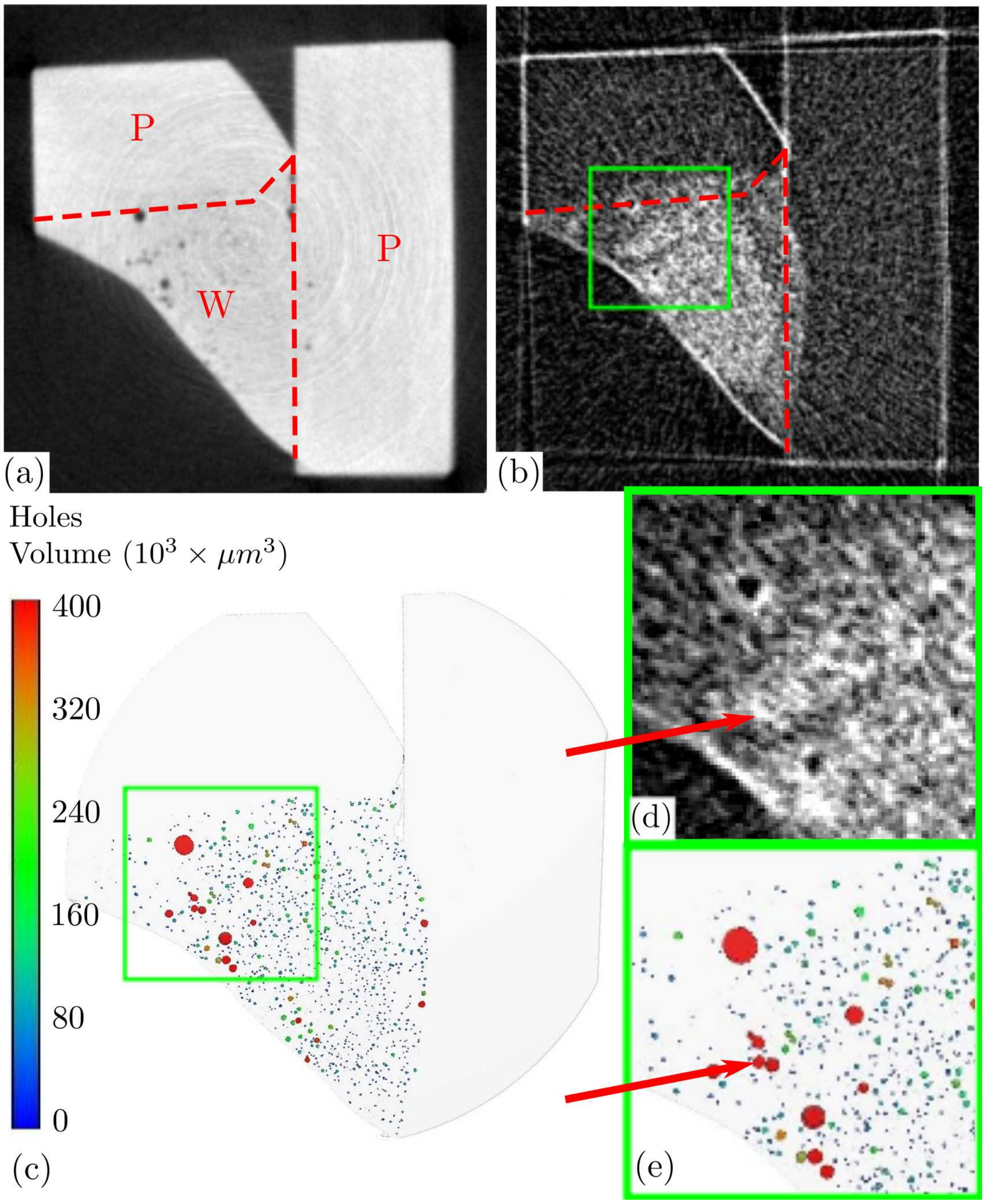

Figure 5.21: *Axial cross sections within (a) the linear absorption coefficient and (b) the linear scattering coefficient reconstructed using the grating interferometer with a spatial resolution ∼48 μm. The letters W and P indicate the positions of the aluminium weld and plates, respectively and the dashed red lines mark the position of the plates limits before welding. (c) Visualization of the holes distribution and volume (color coded) from the segmentation of the linear absorption coefficient using the micro-tomography setup with a spatial resolution of 10 μm. (d) and (e) are zoom-ins on the areas indicated by the green rectangles in (b) and (c), respectively. The arrows indicate specific areas that are discussed in the text (adapted from (Revol et al. 2011a)).*

x-ray scatter dark field imaging based on the grating interferometer was demonstrated for the inspection of the micro-structure of diverse types of materials. In particular, the quantification of porosity could be achieved for a sample of aluminum weld. The key point of this technology is that information is extracted at a sub-pixel length scale. For these reasons, scatter dark field imaging is envisioned to become a standard procedure for the inspection of porosity or inhomogeneities in diverse types of materials.

Sample Type	**Inspection Task**	**Measurement and Results**
Metal Weld	Gas inclusions form in the melted metal during the welding process. The size and density of these inclusions depend on the process parameters and are related to the formation of cracks in the weld.	The dark field signal could be used to analyze the distribution of the pores in a sample of aluminum weld and provided insight into the weld quality.
Plastics	During injection-molding of plastics, holes and pores are formed when wrong process parameters/mold shapes are used. Such defects impact strongly on the aging properties of the polymer. Optical non-destructive techniques exist for transparent polymers but not for opaque plastics.	Diverse opaque and transparent samples were measured. The porous areas in the piece could be identified by dark field radiography.
Brick / Wood	The drying and wetting properties of bricks and woods are of interest for the construction industry. The former are strongly related with the micro-structure of the materials.	Samples of bricks were investigated. A large difference in the dark field signal could be measured between wet and dry samples. Thus, the drying of a brick as a function of time could be studied (see Figure B.4).
Graphite	Homogeneity inspection	Some measurements were realized on a graphite sample. It was concluded that the graphite induces a large ultra-small angle scattering which destroys the phase information. No valuable results could be obtained.

Table 5.4: *Summary of the inspections of the micro-structure with scatter dark field imaging for diverse samples.*

Detection of Cracks, Delamination and Fibers in Composite Polymers

Composite polymers are engineered materials resulting from the association of one or more components embedded in a polymer binder. They represent a growing part of the structural materials used in the automotive and aerospace industries. They are appreciated for their excellent mechanical properties combined with a low weight. For instance, 50 percent of the new Boeing 787 "Dreamliner" is made out of composite materials.

In particular, fiber-reinforced plastics are typically made of glass or carbon fibers bounded in a polymer resin. Their mechanical properties are linked to the orientation of the fibers. For example, such materials have a good resistance to tensile forces along the fibers' direction but are fragile in the direction perpendicular to the latter. One common way to deal with this issue is to form a stack of such layers with alternating fibers' orientations.

Although such fiber-reinforced panels have excellent properties, their aging behavior still raises some concern. Notably, the delamination of the layers and/or the formation of cracks can occur as the consequence of an impact. Such defects are difficult to diagnose since they affect the internal structure of the panel and are hardly visible from the outside. Computed tomography and thermal imaging are often used to study the formation of such damage in the laboratory. However, they cannot be applied for testing in-situ because of practical constraints (size of the studied objects, time required for the measurements). Thus, the composite panels (for example the wings of a plane) are usually inspected by means of ultrasound. This technique gives however only a point measurement and must be repeated at different positions of the panel.

As was seen in the last example, dark field imaging is extremely sensitive to variations of the micro-structure at a scale below the resolution of standard detectors. It is thought that it could provide an excellent tool to detect crack and delamination in such fiber-reinforced plastics.

A study of composite panels was started in collaboration with the research group led by Prof. Dr. Philip Withers at the University of Manchester. The samples were composed of a stack of fiber-reinforced layers (100 µm thick carbon fibers) oriented alternatively at 0°, 45°, 90° and 135° compared to the length of the panel. The setup **S20-4** (Section 4.3) was used for the measurement. The tube acceleration voltage was equal to 35 kVp. 20 phase steps were acquired with an exposure time of 6.7 s. A photograph of the studied specimen is shown in Figure 5.22-a while the normalized absorption-based $\mathcal{T}$, differential phase contrast $\mathcal{DP}$ and dark field $\mathcal{V}$ images are displayed in Figure 5.22-bcd.

In image $\mathcal{T}$, the variations of the binder thickness can be observed (difference in the gray levels) as well as some cracks (dark streaks). Note that the cracks follow the orientation of the fibers (0°, 45°, 90° and 135°). The fibers themselves are

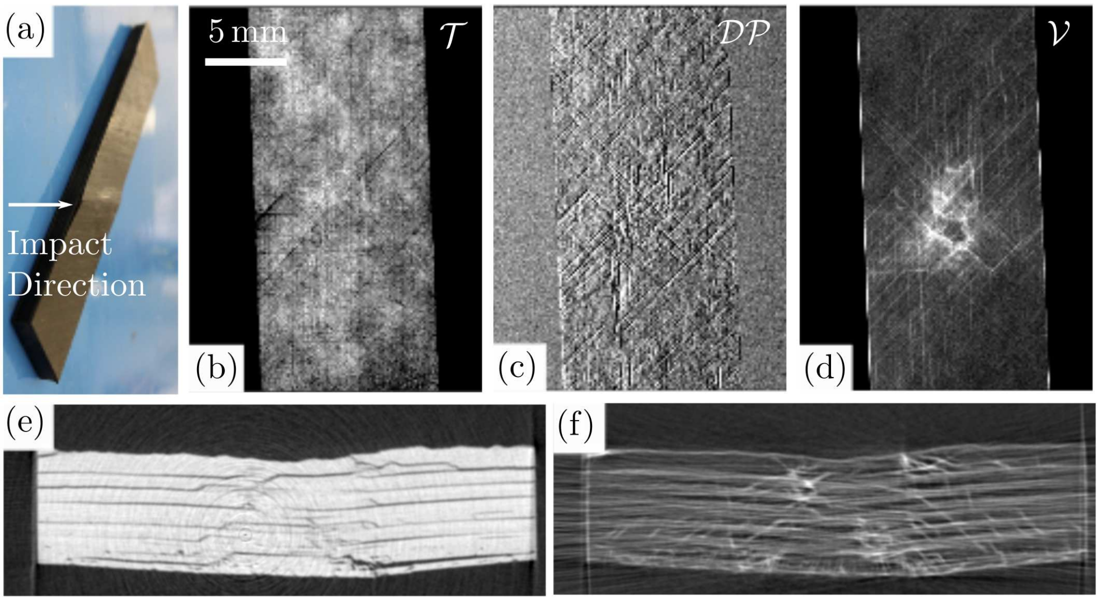

Figure 5.22: *(a) Photograph of the tested fiber-reinforced panel where the impact damage position is indicated by the white arrow. Normalized (b) absorption-based image $\mathcal{T}$, (c) differential phase contrast image $\mathcal{DP}$ and (d) dark field image $\mathcal{V}$. (e) and (f) show cross sections along the plane perpendicular to the panel length of the linear absorption coefficient μ and linear scattering coefficient ϵ, respectively.*

hardly visible. Image $\mathcal{DP}$ displays a large number of streaks, which correspond to the position of the fibers. Whether these streaks also reveal some cracks in the structure is difficult to diagnostic. However, the impact damage is clearly defined and delimited in $\mathcal{V}$. Its extent can be measured and the cracks which propagate from the delamination in the center and towards the outside are revealed. Other examples of composite materials can be found in Figures B.2 and B.3 in Appendix B.

The same sample was then subjected to computed tomography in order to confirm the observations done from the two-dimensional views. 721 projections were acquired over 360° and the linear absorption coefficient μ and scattering coefficient ϵ were reconstructed using the algorithms presented in Section 2.3. Cross-sections along the plane perpendicular to the length of the panel are shown in Figure 5.22-ef for μ and ϵ. The delamination and the multiple cracks are revealed in the cross section of μ. This result confirms the validity of the observations made with the help of the two-dimensional dark field image. In the cross section of ϵ the cracks, which propagate from the top (impact side) in the shape of a cone, are highlighted. In particular, ϵ also allows for the visualization of micro-cracks which are invisible in the cross section of μ due to insufficient spatial resolution.

Next, test parts produced by Micro Powder Injection Molding (MicroPIM)

(Zauner 2006) were graciously provided by Dr. M. Schulz and O. Weber from the Karlsruhe Institute of Technology (KIT) in Germany. MicroPIM is an emerging process for the production of small and complex-shaped parts at a low cost. It consists in the injection molding of fine metallic powders followed by debinding and sintering. Furthermore, KIT developed a process where micro-fibers are simultaneously injected with the powder. These fibers are thought to improve the mechanical stability of the produced parts. Obviously, the distribution and the orientation of the fibers is of paramount importance in this respect. However, it is typically difficult to determine with conventional micro-computed tomography techniques because the micro-fibers are smaller than the spatial resolution.

The sample studied consists of a thin disk. For this application, directional dark field imaging, as presented in Section 5.1.2, was used to reconstruct the local orientation and distribution of the fibers. The results are summarized in Figure 5.23 in the form of the compound image. On the one hand, the colormap (background) represents the isotropic scattering i.e. due to randomly oriented micro-structures of the sample. The latter is essentially homogeneous throughout the disk except for the center (the point where the powder and the fibers are injected).

On the other hand, the dashes are related to the average distribution and orientation of the fibers in the sample. Their length is proportional to the degree of anisotropy. In that particular case, it is determined by the combination of the degree of order (i.e. are the fibers all aligned along one direction or are they randomly positioned) and the relative density of the fibers compared to isotropic scatterers (i.e. the ratio of the number of isotropic scattering particles, such as binder particles, over the number of fibers in the volume of interest). Also, the dashes' orientation gives an indication of the average orientation of the fibers. Thus, it can be seen that the fibers are aligned on average along concentric circles. The zoom-in in Figure 5.23-b shows however that the orientation fluctuates locally, in particular close to the center of the disk.

In conclusion, the potential of dark field imaging for the investigation of fiber-reinforced composite has been demonstrated. On the one hand, its capacity to provide the two-dimensional mapping of impact damage makes it a particularly efficient and fast inspection tool for large composite panels. On the other hand, directional dark field imaging allows also for the measurement of the orientation of microscopic fibers for samples where conventional systems are limited by their spatial resolution. These two examples are real "show cases", which illustrate the merit of the new contrast mechanisms offered by grating interferometry.

Food Inspection: Sealing Defects and Contaminants

Finally, the food industry is pushing for the development of inspection techniques which can be implemented on the packaging lines. This industry is confronted essentially with two problems.

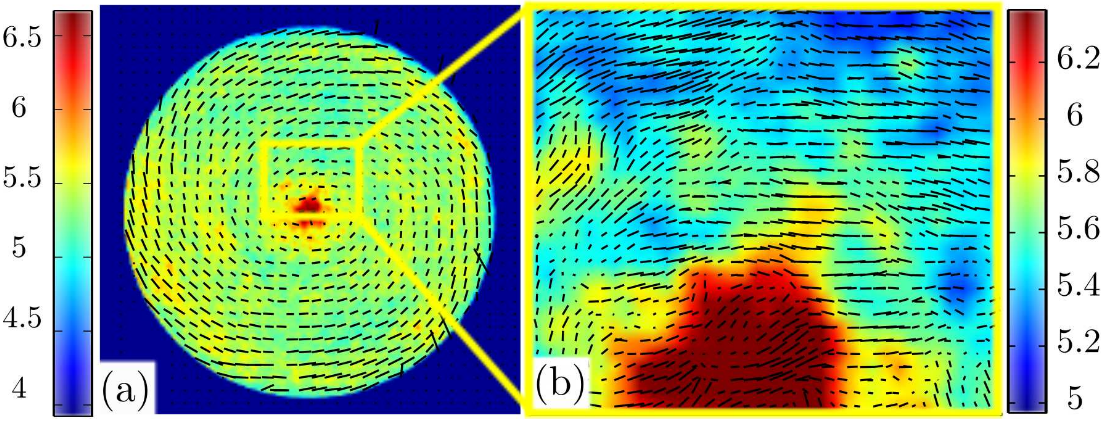

Figure 5.23: *(a) Compound image of the results of the directional dark field measurement for a composite disk. More details on the sample is given in the text. (b) Zoom in of the compound image around the center of the disk.*

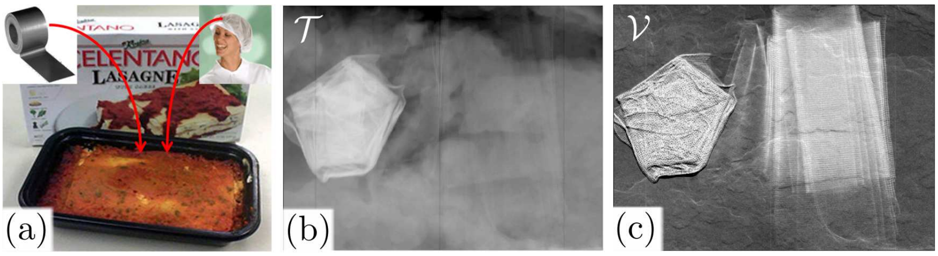

Figure 5.24: *(a) Photograph of a package of frozen lasagnas where a piece of rubber band and of fabric were added. Normalized (b) absorption-based image $\mathcal{T}$ and (c) dark field image $\mathcal{V}$ showing the different contaminants (adapted from (Kottler et al. 2010a)).*

First is the presence of contaminants in the food products, which appear undesired during production. Traditionally, x-ray systems are dedicated to the detection of dense elements like metals while the screening for lighter elements like wood or plastics is done manually by operators or even absent.

Frozen lasagnas as shown in Figure 5.24-a were taken as an example for the detection of different contaminants. The latter were inserted into the package and investigated with setup **S20-4**. The results of the measurement of the normalized absorption-based image $\mathcal{T}$ and dark field image $\mathcal{V}$ are depicted in Figure 5.24-bc in the presence of a piece of rubber band (relatively dense) and one of fabric. Clearly, the rubber band (left in the image) can be detected both in images $\mathcal{T}$ and $\mathcal{V}$. However, the piece of fabric only appears in $\mathcal{V}$. This test was repeated for different types of contaminants such as metals, wood pieces, plastics or bricks.

In general, heavy elements (metals, rubbers...) can be at the best detected with absorption-based radiography while dark field imaging is of advantage for scatterers (fabric, wood, brick...). The detection of plastic pieces remains difficult

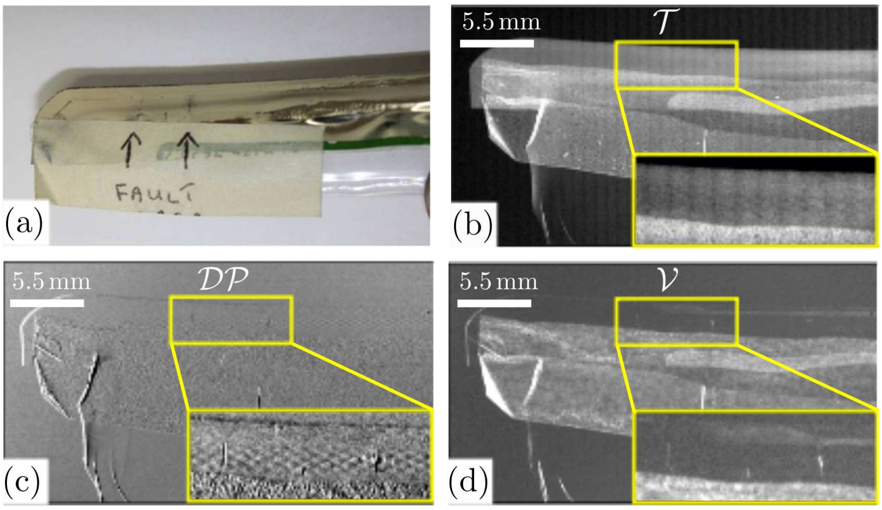

Figure 5.25: *(a) Photograph of a piece of package where some defects appear in the sealing as indicated by the arrows. Normalized (b) absorption-based image $\mathcal{T}$, (c) differential phase contrast image $\mathcal{DP}$ and (d) dark field image $\mathcal{V}$. The insets are zoom in of the defect area.*

although differential phase contrast does offer an increased contrast for this kind of contaminant. One of the main advantages of an inspection system based on grating interferometry is that it offers simultaneously all three contrast mechanisms, which complement each other and allow for the detection of a larger number of contaminants.

The second typical problem for food products consists in a non-conform sealing, which can lead to the corruption of the food. Sealing is usually realized by the welding of two plastics foils. During the process, a number of defects such as scratches / tears in one of the foil or an improper wrapping occur. Such defects were simulated on a plastic package. A photograph of the test sealing with tear defects can be seen in Figure 5.25-a. At the top of the photograph is the sealing itself (shinny appearance) and the tear defects are indicated by arrows. This package was investigated with the help of setup **S20-4**. The reconstructed normalized transmission $\mathcal{T}$, differential phase contrast $\mathcal{DP}$ and dark field $\mathcal{V}$ images are shown in Figure 5.25. The tear defects are absolutely invisible in image $\mathcal{T}$. However, the defects appear as fine streaks in images $\mathcal{DP}$ and $\mathcal{V}$. Those streaks may be hard to visualize in prints of poor quality.

Thus, the implementation of x-ray phase contrast imaging with a grating interferometer could overcome some of the limitations of the current food inspection systems. Accordingly, the quality of the production could be significantly improved.

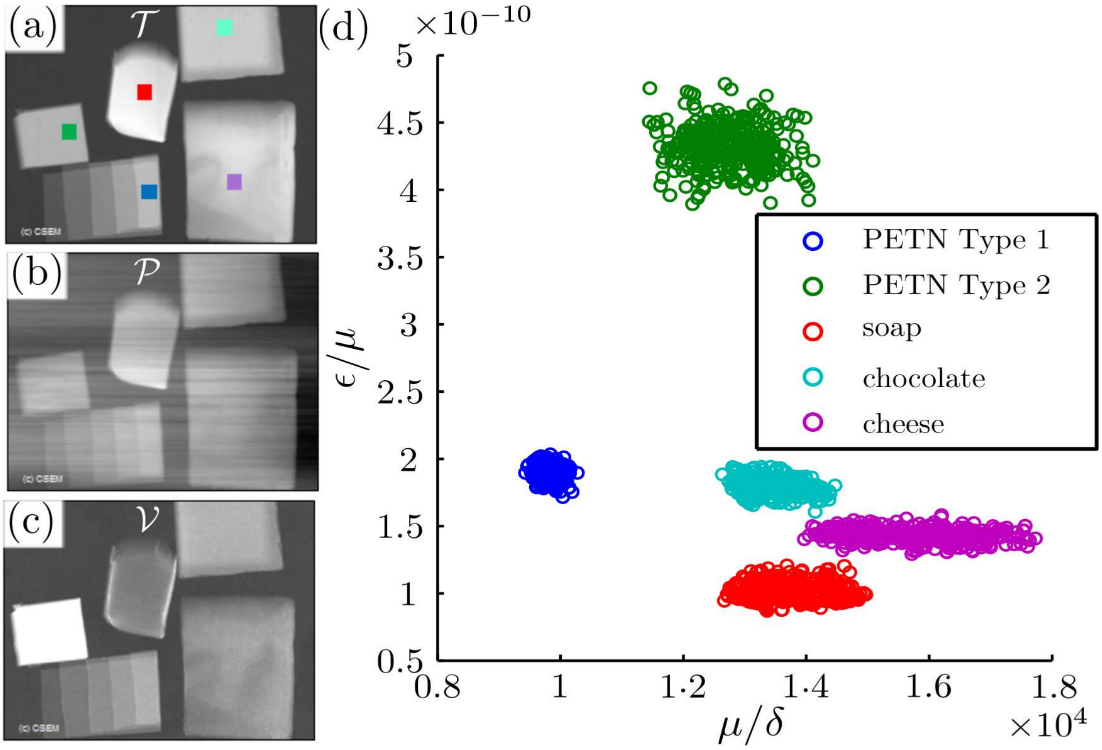

Figure 5.26: *(a) Absorption, (b) phase and (c) dark field images of chocolate, cheese, PETN type 1, PETN type 2 and soap (clockwise starting from the top right). (d) Two-dimensional plot of the ratio $R_{VT} = \epsilon/\mu$ as a function of $R_{TP} = \mu/\delta$ for the different materials (signals collected for the areas indicated by the colored squares on (a)) (Revol et al. 2010a).*

5.3.3 Security and Screening

Explosive Detection

Parcel screening presents great challenges for the instrumentation. First, it has to be fast in order to process the thousands of pieces of luggage transiting daily at airports and borders. Secondly, the rate of false negatives should lie truly near zero. Current systems, based on the absorption of the object, display a strong rate of false positives, which then require the intervention of a security officer. This consequently results in a loss of time. Even when multiple energy spectra are used, some typical fail objects like chocolate, soap and cheese are difficult to distinguish from explosives like PETN.

In order to investigate the potential of grating interferometry in explosive detection, a sample was prepared with cheese, chocolate, solid soap and two types of PETN. Images $\mathcal{T}$, $\mathcal{P}$ (integrated from $\mathcal{DP}$) and $\mathcal{V}$ as shown in Figure 5.26-a were acquired with 7 phase steps over one period with the setup **S20-4**. The exposure time was 6.7 s per phase step and the tube acceleration voltage was set to 40 kVp.

For each material, the signals $\mathcal{T}$, $\mathcal{P}$ and $\mathcal{V}$ were extracted for each pixel of a small area as shown on Figure 5.26-a.

Now, for a given uniform material of thickness t, let us recall that the signals at the x-ray energy E are given by Equations 2.100, 2.105 and 2.109:

$$\mathcal{T} = \mu t \tag{5.12}$$

$$\mathcal{P} = \delta t \tag{5.13}$$

$$\mathcal{V} = \epsilon t \tag{5.14}$$

Where μ is the linear absorption coefficient, δ is the refraction coefficient and ϵ is the linear scattering coefficient.

Consequently, the three signals $\mathcal{T}$, $\mathcal{P}$ and $\mathcal{V}$ are linearly dependent on the thickness t. Thus, the dependence on t can canceled by forming the ratios:

$$R_{TP} = \frac{\mathcal{T}}{\mathcal{P}} = \frac{\mu}{\delta} \tag{5.15}$$

$$R_{VT} = \frac{\mathcal{V}}{\mathcal{T}} = \frac{\epsilon}{\mu} \tag{5.16}$$

$$R_{PV} = -\frac{\mathcal{P}}{\mathcal{V}} = \frac{\delta}{\epsilon} \tag{5.17}$$

Note that these ratios depend only on the properties of the materials. The ratios are linked by the relation $R_{TP}R_{VT}R_{PV} = 1$ and we are left with two independent variables, which characterize the material.

In Figure 5.26 are plotted the values of ratio R_{VT} as a function of R_{TP} for the different materials under study. It can be seen that each material corresponds to a special position in the two-dimensional space and is separated from the other materials. For the targeted application, this implies that PETN explosives can be distinguished from cheese, chocolate and soap using the suggested method. Note particularly that the PETN of type 2 has a much higher ratio R_{VT} than the other materials due to its large scattering coefficient (Figure 5.26-d). PETN of type 2 has indeed a crystalline structure while the other materials are relatively homogeneous. The spread of the ratios for each material is essentially related to the noise in the measurements.

Thus, it was shown that two ratios can be formed using the three channels of information, which are characteristic of the elemental composition and microstructure of the object. In addition, these ratios are independent of the thickness. Such ratios could potentially be used to for the screening of packages in order to detect explosives.

Identification through the Scatter Signature

In the previous paragraph, the scattering signal was used to get additional information about the size, density and refraction coefficient of the inhomogeneities

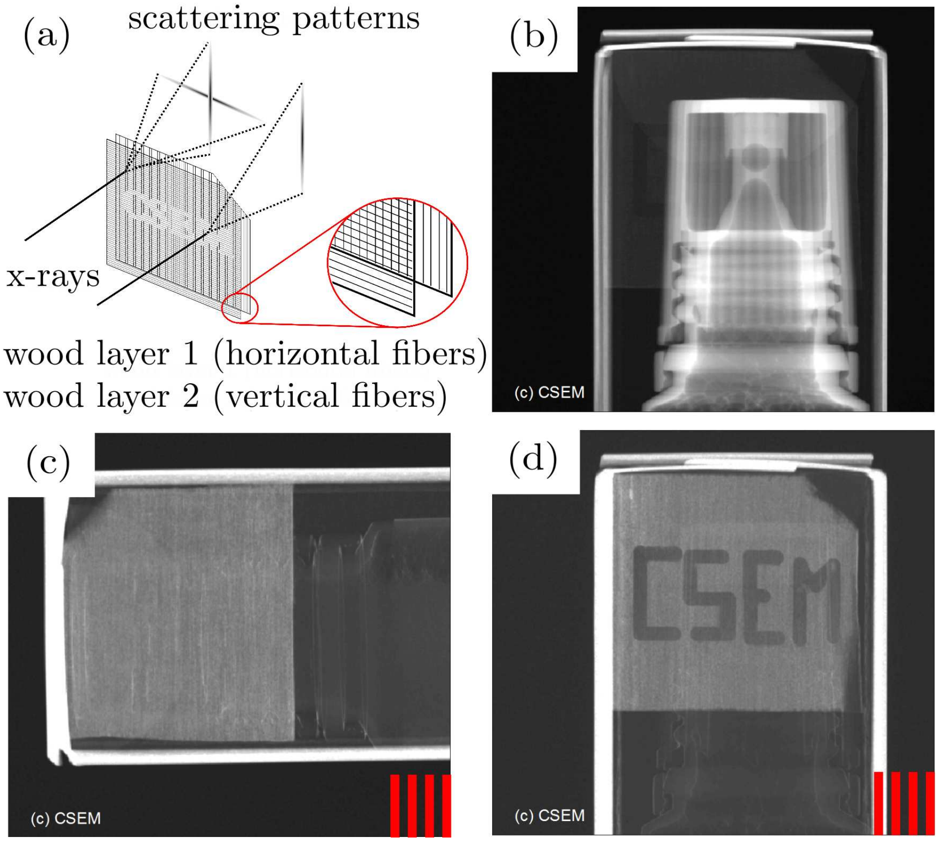

Figure 5.27: *(a) Schematic view of the marker, which consists of two layers of wood with fibers oriented perpendicular to each other. The acronym "CSEM" was written onto one of the layers by removing some material. (b) Absorption-based image T of the plastic drug bottle in its carton box. The marker is hardly visible since it nearly does not absorb the x-rays. (c) Scatter dark field image V of the marker with the fibers in layer 2 perpendicular to the gratings lines. (d) Same dark field image but with the fibers in layer 2 parallel to the gratings lines. Note that the grating lines' orientation is indicated by the red solid lines at the bottom right of each image (Revol et al. 2010a).*

of a sample at the micron scale. Actually, the scattering pattern also strongly depends on the shape of the inhomogeneities of the sample as introduced in Section 5.1.2.

The idea is to use this feature in order to produce markers to authenticate certain goods that are subject to forgery. The advantage of using x-rays over optical methods lies in the fact that the packet does not need to be opened to read the marker. This potentially saves some time and/or allows more packets to be screened.

A test marker was built as an example. It consists of two thin layers of wood. Since wood consists of multiple fibers that are oriented roughly along the same direction, the resulting ultra small angle scattering is extremely anisotropic. The fibers of both layers were oriented perpendicular to each other as shown on Figure 5.27-a. The acronym "CSEM" was then written onto layer 2 by milling while layer 1 was left intact. Consequently, the scattering pattern from a point in one of the letters is concentrated along one direction while it extends in both directions for a point in the background.

Since one-dimensional gratings are used, the Talbot-Lau interferometer (see Section 2.1.3) is only sensitive in the direction perpendicular to the grating lines (Jensen *et al.* 2010). As a result, when the marker is placed (in this example, in a drug box made of cartons) such that the fibers of layers 2 are parallel to the grating lines, the scattering image display the acronym "CSEM" (see Figure 5.27-d). In contrast, it does not appear when the fibers of layers 2 are perpendicular to the grating lines (see Figure 5.27-c).

For practical applications, more involved markers should be used, which have defined scattering signals along known directions. Such markers should also rely on complex, hardly reproducible fabrication processes. The results of this section are reported in (Revol *et al.* 2010a).

5.4 Summary and Conclusions

There are different ways to visualize the work carried out in this project. It has been presented here as a logical sequence of Chapters and Sections, each with a defined topic. In reality, most of the topics have been addressed in parallel and each new result triggered a series of questions and/or allowed new ideas to be tested. As such, I usually prefer to visualize this work as a closed cycle, where theoretical model, instrumentation, imaging methods and applications are strongly linked to another.

The first task consisted in reaching a starting point on this cycle. For this purpose, a literature survey was realized, both on the theoretical work produced in this field and on the fabrication processes available for the production of x-ray gratings. Then, an experimental bench was developed including both dedicated hardware and software. In parallel, a first set of x-ray gratings (**S20-4**) was manufactured in the clean rooms of CSEM in Neuchâtel. This grating set was designed to reach the performance of state-of-the-art systems (at that time).

The characterization of the results obtained with this first setup allowed for an extension of the understanding of the contrast formation. In particular, a model was suggested for the quantification of the sources of noise that impact on the measurement sensitivity. The artifacts present in the images have been summarized and correction algorithms were presented to compensate for their negative effects.

A large variety of samples could then be investigated and provided promising results. At the same time, these first inspections underlined the need for improvements in the instrumentation and prompted the developments of new measurement methods.

In terms of methods, three significant contributions could be implemented.

- ➢ The industrial needs in terms of robustness and short acquisition time call for image reconstruction techniques that do not require the gratings to be moved. For this reason, a method based on Moiré fringes was implemented, which allows phase contrast and dark field imaging while satisfying the previous requirements. Such a technique could be of benefit for non-destructive testing, in particular.
- ➢ The measurements of the specimens with an anisotropic micro-structure (like for example made of fibers) revealed that a large variation of the dark field signal was observed depending on the relative orientation of the sample with the gratings' lines. Thus, a method based on the measurement of the dark field signal for different relative orientations was developed in order to extract information on the anisotropy of the micro-structure. Such an inspection tool could represent a significant progress for the investigation of fiber-composite materials.
- ➢ Dual energy imaging is done routinely in combination with absorption contrast in order to gain insights into the elemental composition of the object studied. A grating interferometer was developed following a concept invented by (Kottler & Kaufmann 2009). It enabled to experimentally demonstrate the feasibility of dual energy phase contrast imaging. It is envisioned that a further improvement of the detection sensitivity could be achieved in this way.

From the instrumental point of view, three major improvements were realized in this work.

- ➢ From the measurements with biological specimens, it became clear that a higher sensitivity to variations of the refraction coefficient was required. A new setup (**S20-12**) using higher fractional Talbot orders was designed, which provided an increase of 50% (on average) of the contrast-to-noise ratio. Thus, new insights into the medical probes could be gained and highlighted the potential of phase contrast imaging for medical diagnostics.

- The thickness and density of the samples that could be imaged with setup **S20-4** were limited, since the design energy lay by 20 keV. Pushing this design energy up to 50 keV required a large effort in the optimization of the micro-fabrication processes but a new grating set **S50-4** was produced at CSEM Neuchâtel. It allowed denser objects (for example, out of aluminum) to be investigated.
- The compact setup **S25-1b** revealed the necessity of bending the gratings in order to compensate for the spherical divergence of the x-ray beam. Indeed, the latter results in an increase of the angular incidence at the sides of the gratings, and consequently, a decrease of the performance. This issue is particularly pronounced for compact setups with large fields of view. Thus, a new type of cylindrical frame was developed, which compensates for this effect. The tests proved the validity of the approach and removed the bottle neck in terms of size of the field of view.

A summary of the design parameters of all grating interferometer configurations used in this thesis is given in Table 5.5.

Finally, the data acquired on the numerous samples tested allowed conclusions to be drawn on the potential of phase contrast and dark field imaging.

- For medical diagnostics, human and animal organs were screened with phase contrast imaging and, in some cases, the data were verified by conventional techniques (for instance, by histology). In comparison to absorption-based imaging, a clear contrast improvement could be observed for soft tissues like the adrenal gland, tendons and blood vessels. Studies in the domain of cardiovascular diagnostics are on-going.
- In non-destructive testing and evaluation, important contrast enhancement could be proven with phase contrast imaging for the quality inspection of manufactured products, for example, for the detection of gluing defects in syringes. On the other hand, dark field imaging turned out to be an invaluable tool for the characterization of micro-structure: from the evaluation of sub-pixel porosity to the detection of crack or impact damage in fiber-composite materials. In another industry, phase contrast and dark field imaging proved to complement perfectly the conventional absorption-based radiography for the inspection of packaged food (detection of contaminants or defects in the sealing).
- In the domain of homeland security, the three channels of information (absorption, differential phase contrast and scatter dark field imaging) can be combined to form a material-dependent signature that is characteristic of the investigated material. This signature was used to distinguish explosives

from typical false alarm objects such as chocolate, soap and cheese. Furthermore, a concept was developed, where markers with a defined scattering pattern are used to authenticate certain products like drugs or perfumes in order to prevent forgery.

	Parameter	**S20-4**	**S25-1b**	**S20-12**	**S50-4**
General	Design Energy E_{des} [keV]	20	24.5	20	50
	Fractional Talbot order N	4	1	12	4
Distances	z_{01} [mm]	1310	515	1262	1610
	z_{12} [mm]	69	77	189	401
Source Grating	Periodicity [µm]	57	20	20	20
	Height [µm]	70	45	45	120
	Duty Cycle	0.2	0.2	0.2	0.2
Beam Splitter Grating	Periodicity [µm]	2.85	5.22	2.61	2.85
	Height [µm]	12.85	31.3	12.85	32.3
	Duty Cycle	0.5	0.5	0.5	0.5
Analyzer Grating	Periodicity [µm]	3	3	3	5
	Height [µm]	30	30	30	100
	Duty Cycle	0.5	0.5	0.5	0.5
Characteristics	Angular Range [µrad]	43.5	39.0	15.9	12.5
	Visibility v^r	0.4	0.28	0.22	0.18
	@ V_{tube}=	40kVp	40kVp	40kVp	60kVp

Table 5.5: *Summary of the parameters and characteristics of the grating interferometers*

OUTLOOK

Although the first x-ray phase contrast imaging instrument was already invented in 1965, the field really started to boom in the last decade. The number of research groups active in this domain surged and the progress realized has been tremendous. Among all techniques, a small number of methods have been shown to be compatible with standard x-ray sources and detectors. This feature was decisive to raise the interest of industry, since this means that the technology could potentially be implemented in industrial environments or in hospitals.

Our research focused on grating-based x-ray interferometry. This method allows for the measurement simultaneously of the refraction and ultra small angle scattering of the x-ray beam in the sample in addition to its absorption. These two additional contrast mechanisms provide complementary insights into the composition and micro-structure of the studied object. Our goal is to develop the technology up to a point where it can be industrialized.

The various experimental prototypes built and optimized during this work have demonstrated some real progress in terms of instrumentation and measurement techniques. Phase sensitive measurements can now be realized on a daily basis with a high sensitivity and significant contrast enhancements could be observed for a wide range of examples.

Thus, grating interferometry is at a stage where the conception of an industrial prototype is possible with certain limitations in terms of usable x-ray energies (up to 50 keV) and size of the fields of view (up to $5 \times 7\,\mathrm{cm}^2$). Even so, a large number of applications can be envisioned. For example, in the field of medical imaging, phase contrast imaging could be implemented for small animal imaging or as tool for the examination of specimens post mortem. In non-destructive evaluation, dark field imaging would be of great help in the study of composite materials.

The next decade will be pivotal in determining how far phase contrast imaging with a grating interferometer can penetrate the x-ray market and to what extent it can complement existing systems. This will depend largely on the progress realized in grating fabrication but also on the development of dedicated reconstruction algorithms, which take into account the particularities of the measured data and correct for the specific artifacts. Some contributions were introduced in this dissertation but much remains to be done in this particular domain.

The target applications in the medium term are still unknown but trends can already be drawn. For human medicine, mammography systems based on grating interferometry will be soon achievable from a technological point of view. Whether this technology can provide a sufficient contrast enhancement (or equivalently, a reduction of the ionization dose) is however still to be proven. For cardiovascular imaging, grating interferometry seems to offer a real advantage but its implementation lies even further away from the current technical limitations. The fierce competition in medical diagnostics with other imaging techniques like magnetic resonance imaging, positron emission tomography, ultrasound imaging without forgetting absorption-based x-ray imaging also makes the estimate more difficult.

The highest potential is to be found in my eyes in non-destructive testing and evaluation. In particular, the use of the scatter dark field image could be of benefit to a large number of inspection systems. The examples of aluminum welding and fiber-reinforced materials have been discussed and look promising. In the food industry, the detection of contaminants thanks to grating interferometry complements nicely the current x-raying systems, which are limited essentially to metallic impurities.

In terms of competition with other phase sensitive techniques, grating interferometry appears nowadays as the best compromise between sensitivity and complexity. Most of the research worldwide is concentrated on this technology, in particular in industry. The grating-based projection method is winning momentum but suffers from a lack of sensitivity, which restrains its use. The problem is even more acute for propagation-based imaging. At the other extreme, crystal interferometry and analyzer-based imaging are limited by their demands for monochromatic radiation.

However, the emergence of new closely related technologies could change the situation. I am thinking of the recent progress in energy-sensitive detectors. The latter could potentially revolutionize the field of x-ray imaging, as seems to be the case for spectral computed tomography for instance. On the source side, table-top synchrotron sources are consistently improving their performances (photon flux and monochromaticity in particular). Such sources would benefit strongly all phase contrast imaging techniques. Methods which were previously judged too restrictive could then become attractive.

APPENDIX

A

MEDICAL IMAGING: MORE EXAMPLES

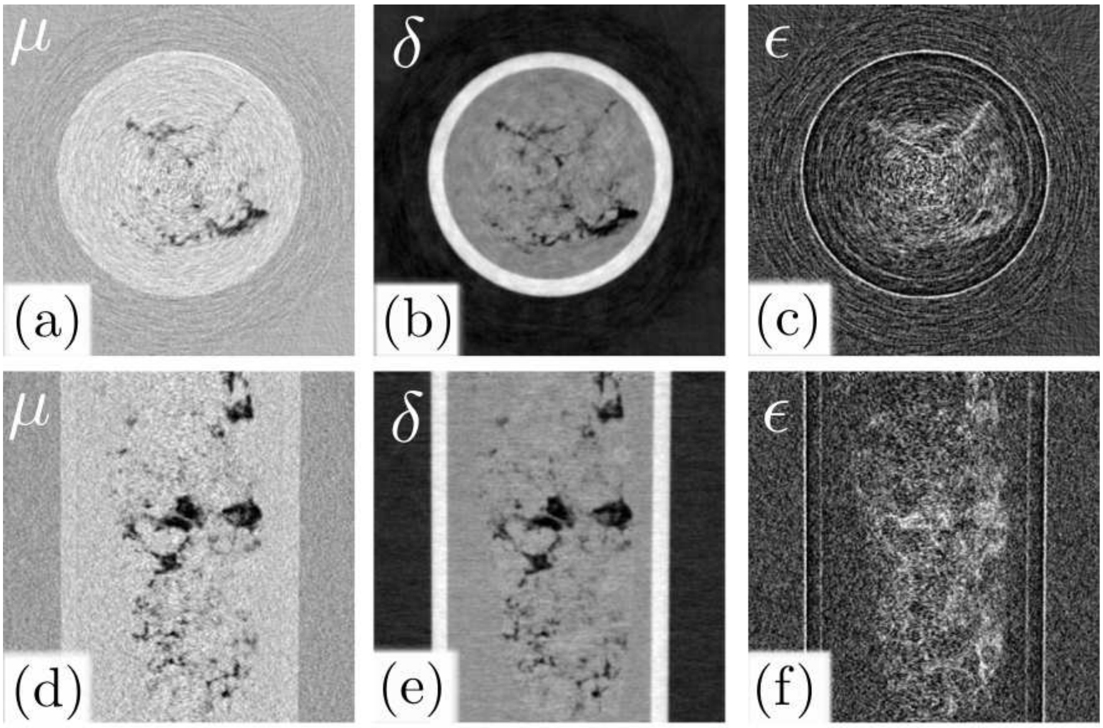

Figure A.1: *Human pancreas. (a), (b) and (c) (resp. (d), (e), (f)) show an axial (resp. longitudinal) cross section within the three-dimensional reconstructions of the linear absorption coefficient* μ*, the refraction coefficient* δ *and the linear scattering coefficient* ϵ *for a specimen composed of a piece of human pancreas. The sample was fixed in formalin, placed in a 2 cm-wide plastic tube and embedded in agarose gel. Few, non-identified, anatomical structures can be identified in all images. Note however that the cross sections of* δ *do show more levels of grays than the cross sections of* μ*.*

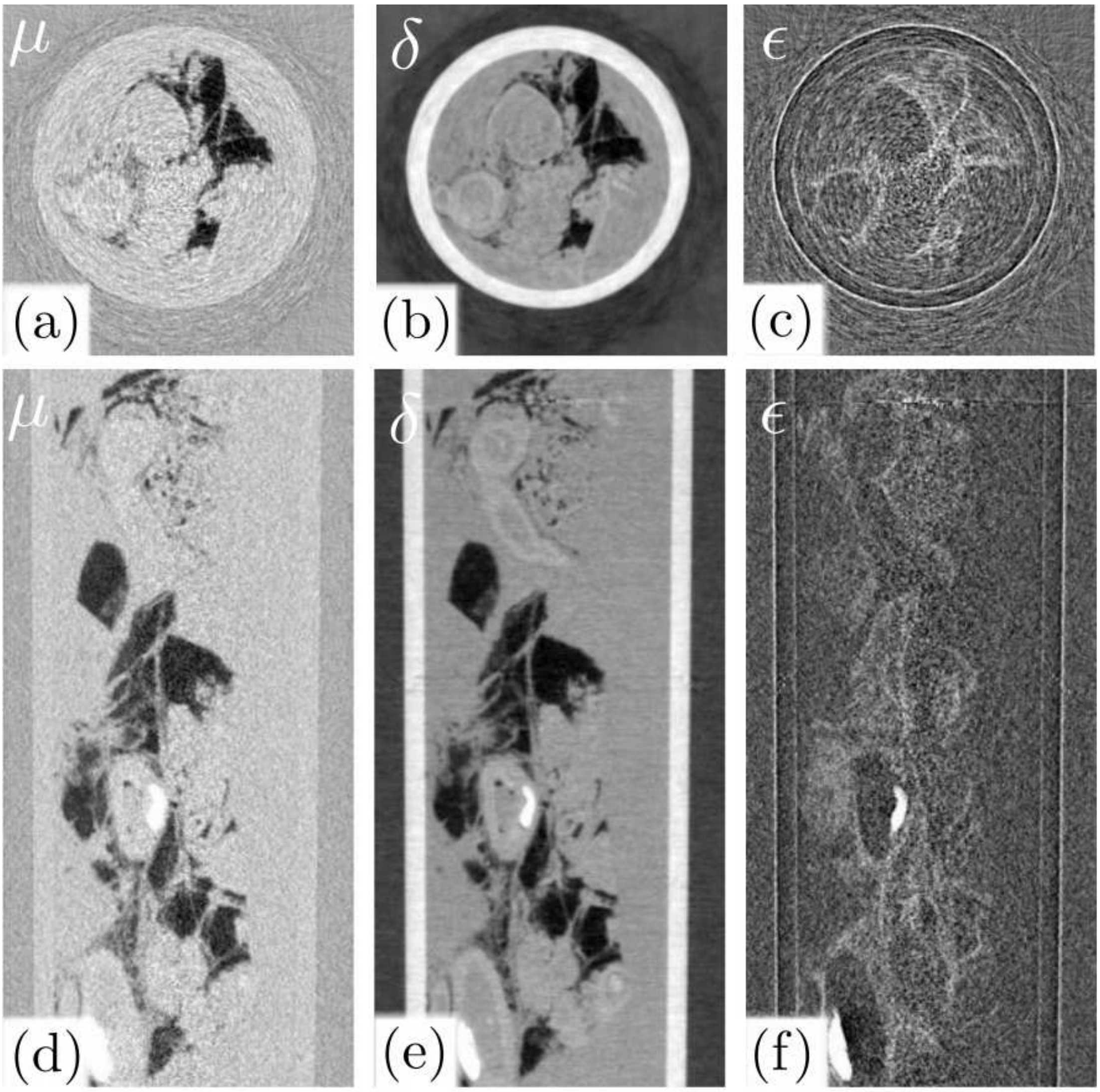

Figure A.2: *Human blood vessels. (a), (b) and (c) (resp. (d), (e), (f)) show an axial (resp. longitudinal) cross section within the three-dimensional reconstructions of the linear absorption coefficient μ, the refraction coefficient δ and the linear scattering coefficient ϵ for a specimen composed of a piece of human blood vessels. The sample was fixed in formalin, placed in a 2 cm-wide plastic tube and embedded in agarose gel. The fat and connective tissue, appearing dark in the images of μ and δ, can be identified. Furthermore, the bright structures in μ, δ and ϵ are presumably atherosclerotic plaques. However, note that the blood vessel structure can be visualized as light gray levels in the cross sections of δ, while they are invisible in the cross sections of μ.*

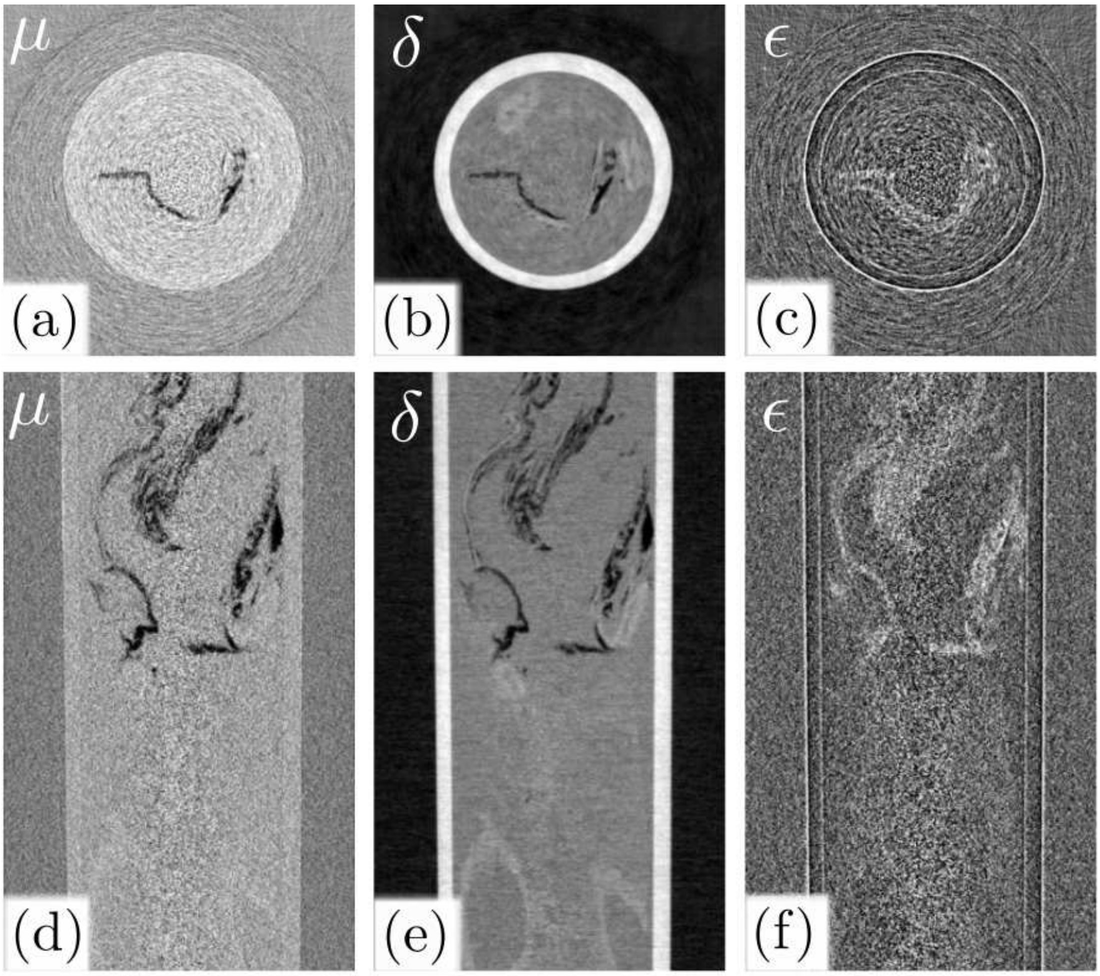

Figure A.3: *Human liver. (a), (b) and (c) (resp. (d), (e), (f)) show an axial (resp. longitudinal) cross section within the three-dimensional reconstructions of the linear absorption coefficient* μ*, the refraction coefficient* δ *and the linear scattering coefficient* ϵ *for a specimen composed of a piece of human liver. The sample was fixed in formalin, placed in a 2 cm-wide plastic tube and embedded in agarose gel. Some fat and connective tissue can be identified (dark levels in* μ *and* δ*) in the images. Some large blood vessels also do appear as light gray levels in* δ*. However the organ (liver) itself does not appear in these measurements.*

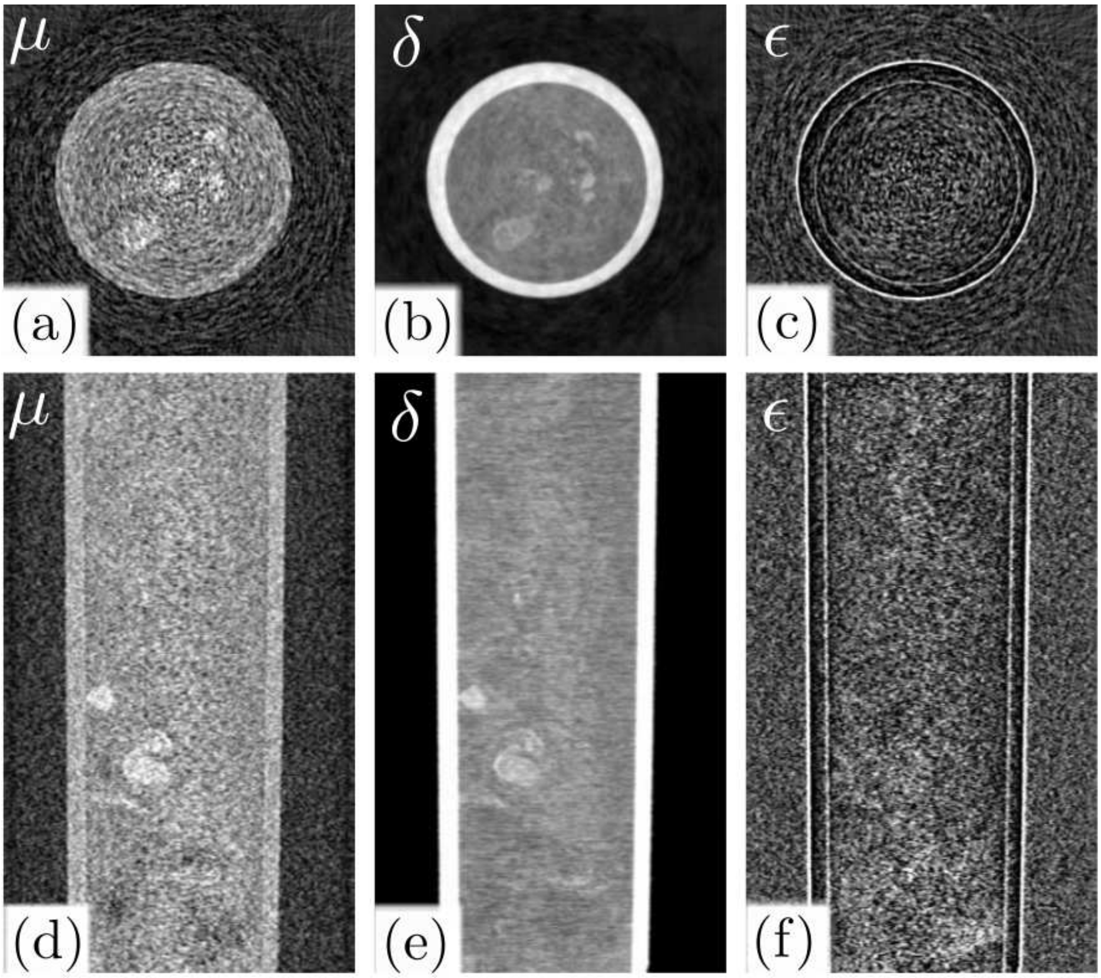

Figure A.4: *Human stomach. (a), (b) and (c) (resp. (d), (e), (f)) show an axial (resp. longitudinal) cross section within the three-dimensional reconstructions of the linear absorption coefficient* μ*, the refraction coefficient* δ *and the linear scattering coefficient* ϵ *for a specimen composed of a piece of human stomach. The sample was fixed in formalin, placed in a 2 cm-wide plastic tube and embedded in agarose gel. Few, non-identified, anatomical structure can be observed.*

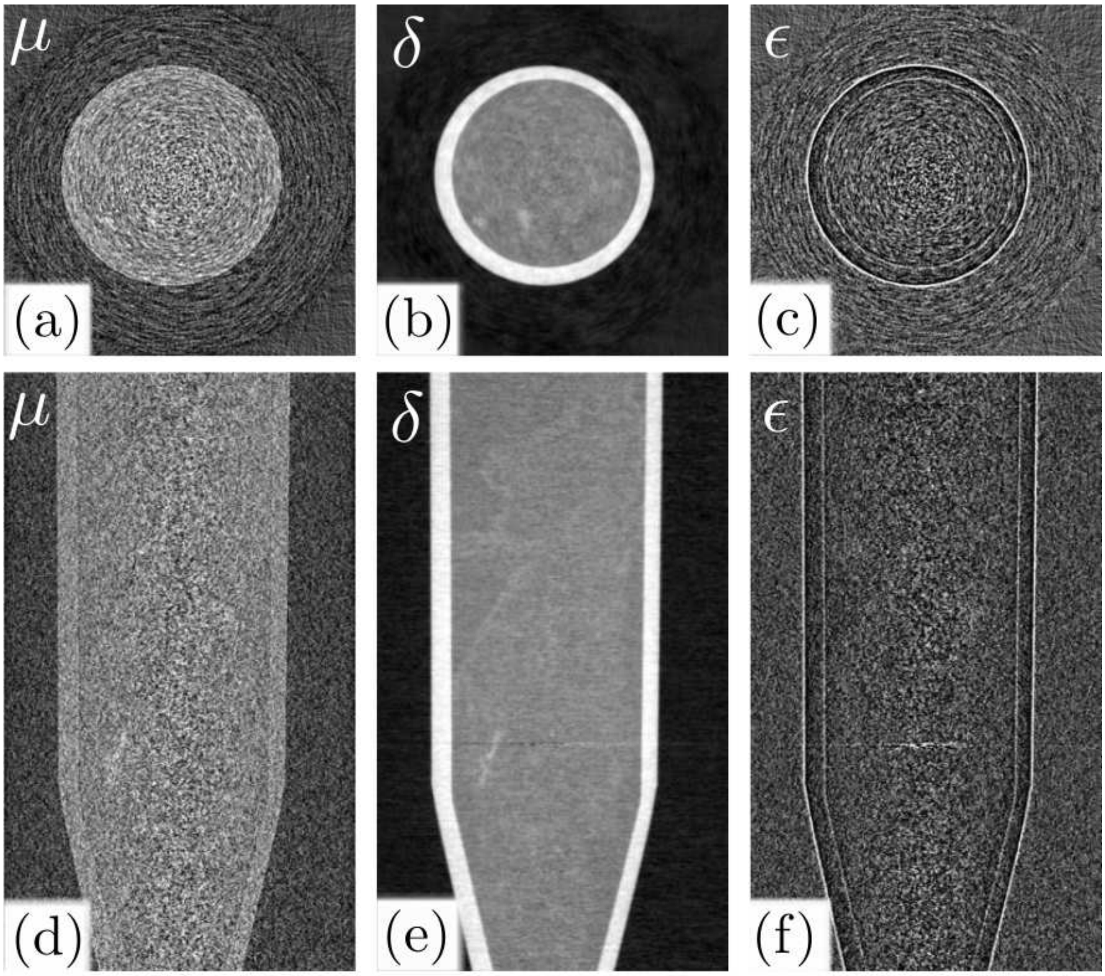

Figure A.5: *Human lungs. (a), (b) and (c) (resp. (d), (e), (f)) show an axial (resp. longitudinal) cross section within the three-dimensional reconstructions of the linear absorption coefficient μ, the refraction coefficient δ and the linear scattering coefficient ϵ for a specimen composed of a piece of human lungs. The sample was fixed in formalin, placed in a 2 cm-wide plastic tube and embedded in agarose gel. Nearly no anatomical structure can be observed.*

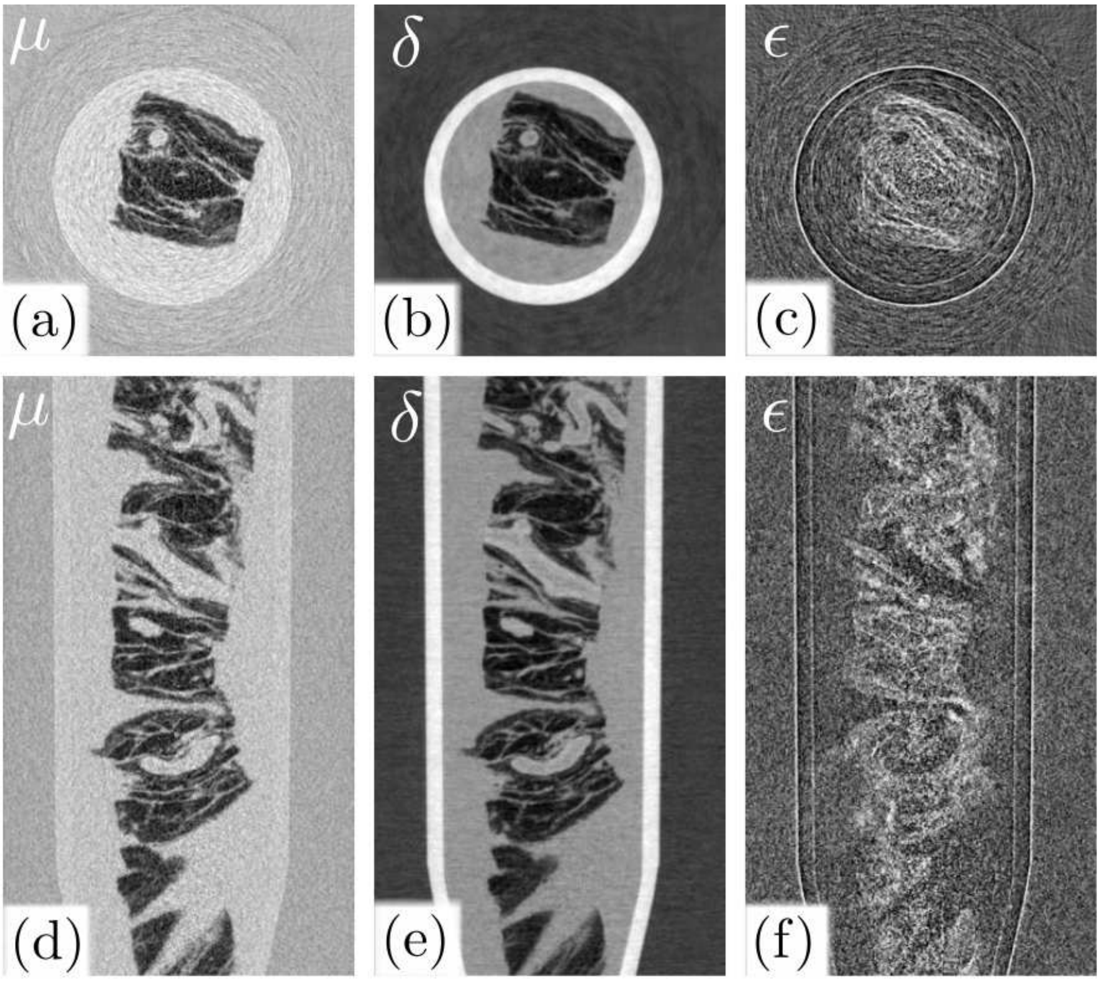

Figure A.6: *Human mesentery. (a), (b) and (c) (resp. (d), (e), (f)) show an axial (resp. longitudinal) cross section within the three-dimensional reconstructions of the linear absorption coefficient* μ*, the refraction coefficient* δ *and the linear scattering coefficient* ϵ *for a specimen composed of a piece of human mesentery. The sample was fixed in formalin, placed in a 2 cm-wide plastic tube and embedded in agarose gel. The fat and connective tissue (dark in* μ *and* δ*) can be observed in the images. Some blood vessels also do appear as light gray levels in* δ *while they are invisible in the cross sections of* μ*.*

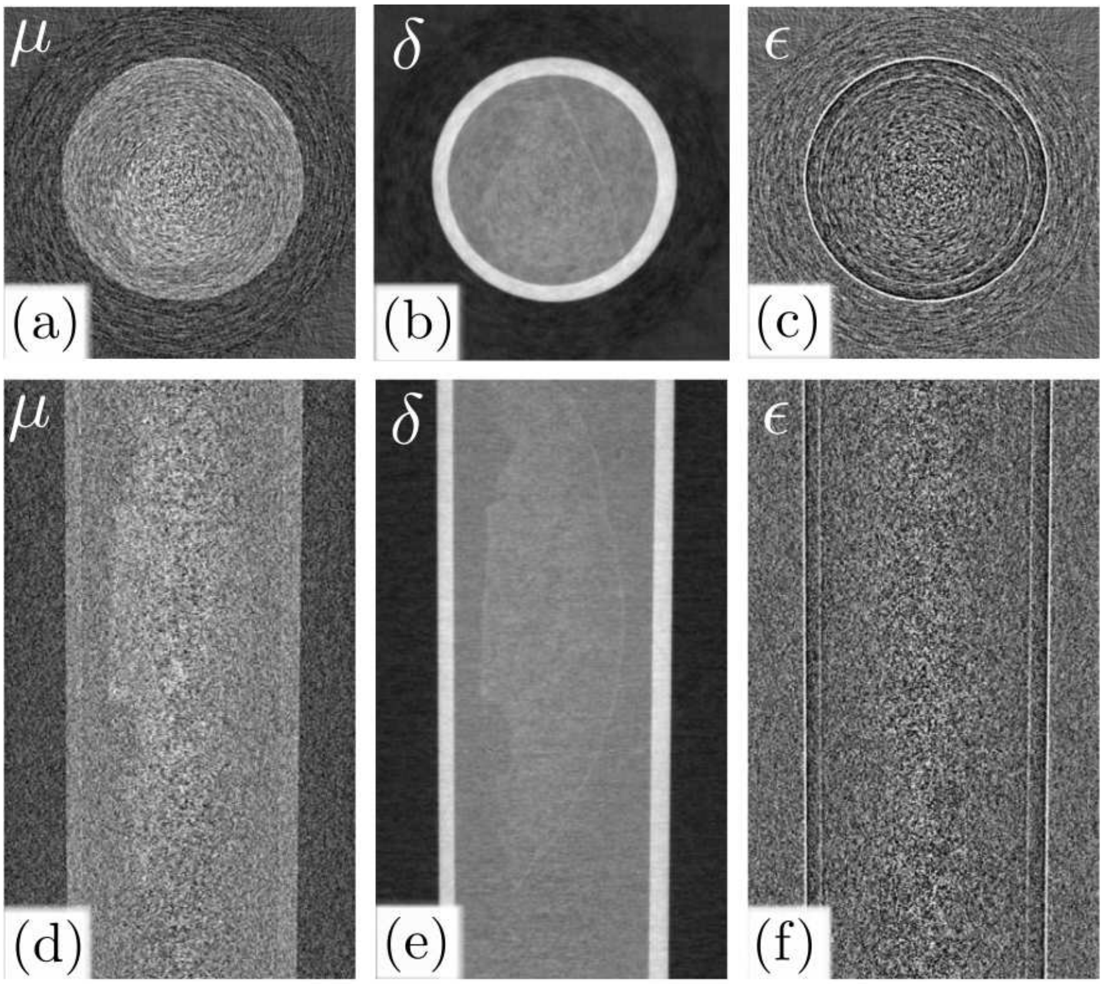

Figure A.7: *Human spleen. (a), (b) and (c) (resp. (d), (e), (f)) show an axial (resp. longitudinal) cross section within the three-dimensional reconstructions of the linear absorption coefficient μ, the refraction coefficient δ and the linear scattering coefficient ϵ for a specimen composed of a piece of human spleen. The sample was fixed in formalin, placed in a 2 cm-wide plastic tube and embedded in agarose gel. Nearly no anatomical structure can be observed.*

APPENDIX

B

NON-DESTRUCTIVE TESTING: MORE EXAMPLES

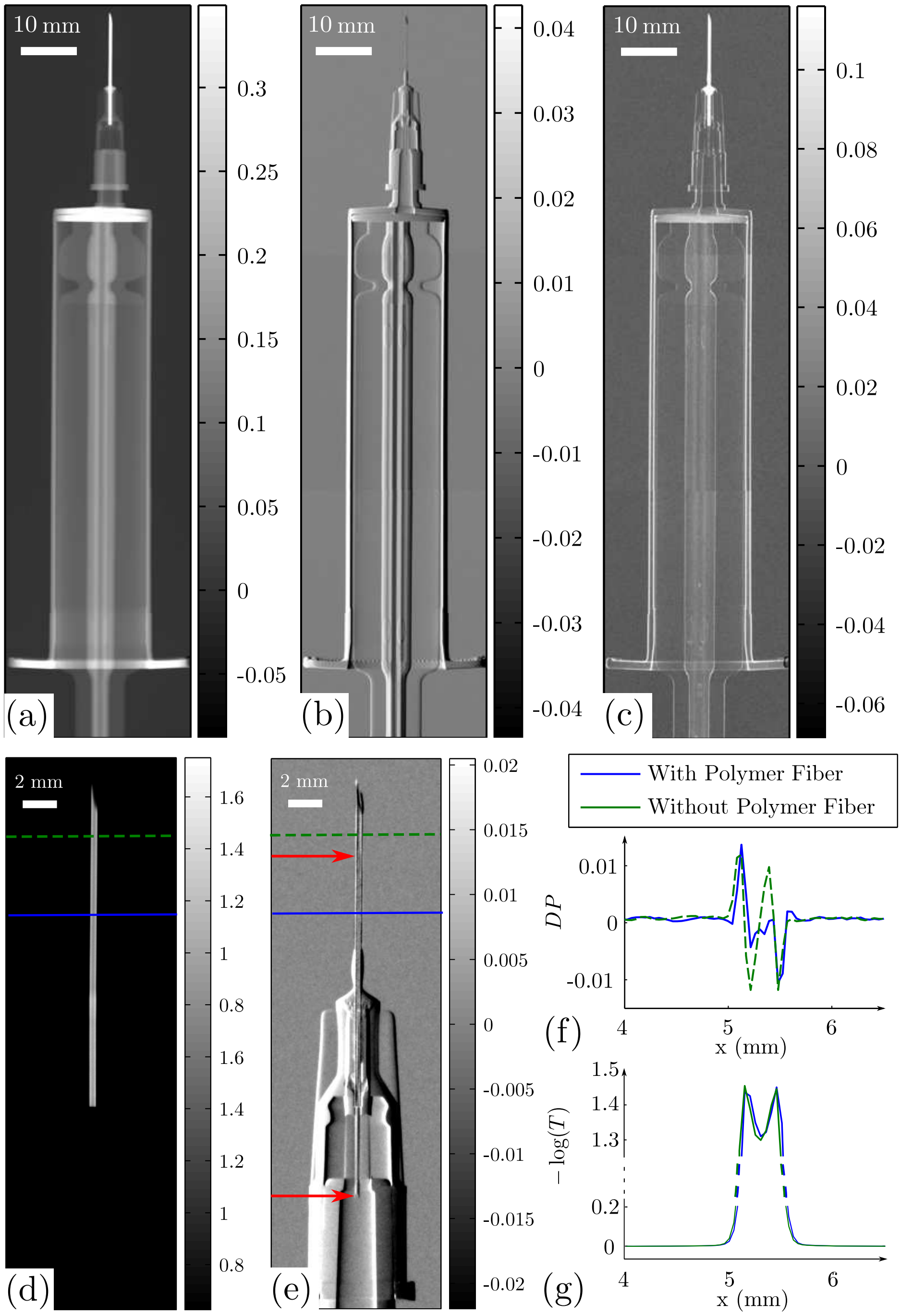

Figure B.1: *The aim of this measurement is to compare the potential of absorption-based imaging and differential phase contrast with respect to the detection of a thin polymer fibers inserted into a metal needle. (a), (b) and (c) show the transmission, differential phase contrast and dark field images of the test syringe, respectively. (d) and (e) are zoom in of (a) and (b), where the dynamic range has been chosen in order to visualized the metal needle. Clearly, the polymer fiber can not be observed in the transmission image while it appears in the differential phase contrast image. Its two ends are indicated by the two red arrows in (e). This is confirmed by looking at the cross-sections of the two signals in (f) and (g), once with the polymer fibers in the needle (blue solid line) and once without (green dotted line). A large signal change is observed in the differential phase signal* DP *but not in the normalized transmission signal* $-\log(T)$.

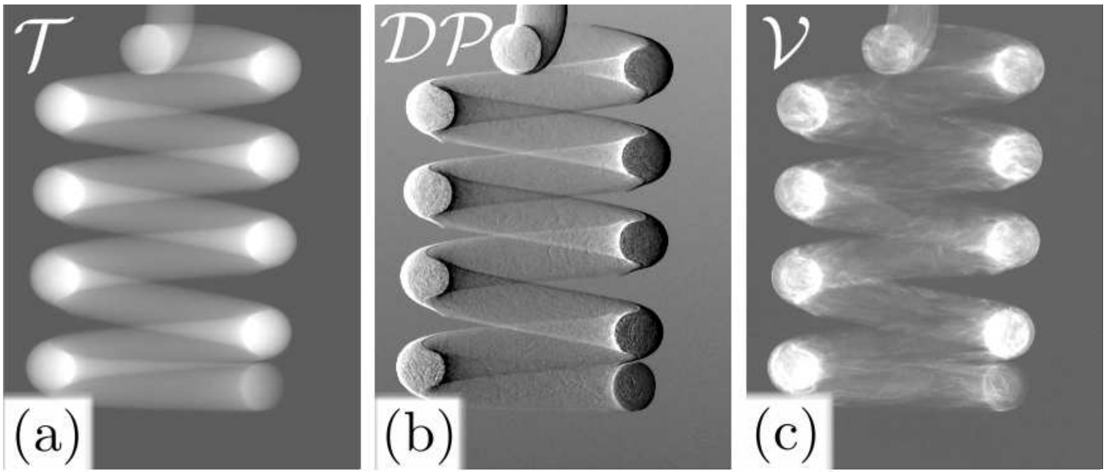

Figure B.2: *Normalized (a) transmission, (b) differential phase contrast and (c) dark field image of a spring made out of composite material (polymer fibers in a polymer binder). The distribution of fibers appears nicely in (c). Note that these are only two-dimensional projections and not the results of a computed-tomography. These results were obtained in collaboration with the Empa.*

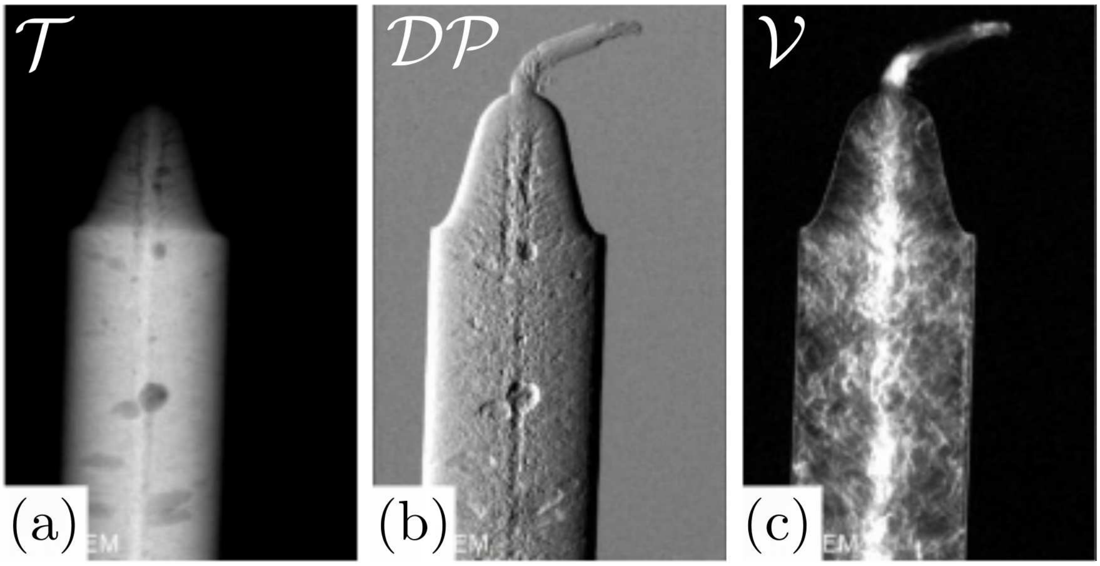

Figure B.3: *Normalized (a) transmission, (b) differential phase contrast and (c) dark field image of a candle. These results were obtained in collaboration with the Empa.*

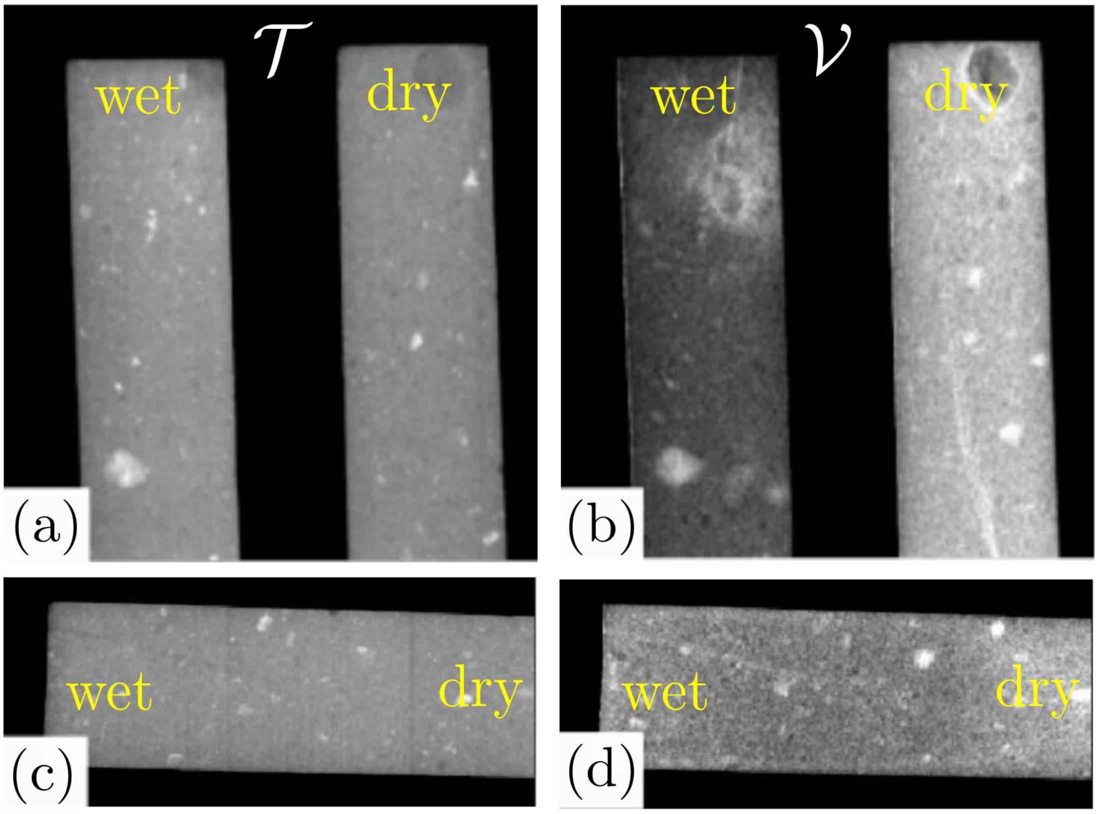

Figure B.4: *Normalized (a) transmission and (b) dark field image of two bricks, one being dry and the other wet. (c) and (d) shows the transmission and dark field image of one brick, where one end is wet and the other dry. This examples illustrates the potential of scatter dark field imaging for the study of the wetting properties of porous materials, such as the brick in the example. These results were obtained in collaboration with the Empa.*

LIST OF SYMBOLS AND ABBREVIATIONS

General

h	Planck constant	23
c	Speed of light	20
$\mathcal{F}_x(g)$	Fourier Transform of function g along the x-direction	36
$\mathcal{F}_{x,y}(g)$	Two-dimensional Fourier Transform of function g along the directions x and y	49
^{r}	Superscript r refers to a measurement without sample	25
^{s}	Superscript s refers to a measurement with sample	25
FFT	Fast Fourier Transform	41
CSEM	Centre Suisse d'Electronique et Microtechnique SA	14
EMPA	Eidgenössische Materialprüfungs- und ForschungsAnstalt	14

Symbols related to the gratings

G_0	Source grating	18
G_1	Beam splitter grating	18
G_2	Analyzer grating	18
p_0	Source grating periodicity	18
p_1	Beam splitter grating periodicity	18
p_2	Analyzer grating periodicity	18
H_0	Source grating height	18
H_1	Beam splitter grating height	18
H_2	Analyzer grating height	18
DC_0	Source grating duty cycle	18
DC_1	Beam splitter grating duty cycle	18
DC_2	Analyzer grating duty cycle	18
T_0^2	Intensity transmission function of grating G_0	37
T_1	Complex amplitude transmission function of grating G_1	20
T_1^0	Unit cell of transmission function T_1	22
T_2^2	Intensity transmission function of grating G_2	31
T_f^2	Intensity distribution of the source focal spot	20

a_ℓ	Complex Fourier coefficients of periodical function T_0^2	37
B_ℓ	Complex Fourier coefficients of periodical function T_1	20
c_ℓ	Complex Fourier coefficients of periodical function T_2^2	31
$\Delta\Phi$	Phase shift induced by a rectangular phase grating	23
λ_{des}	Design wavelength such that $\Delta\Phi = \pi/2$, in the case of a $\pi/2$-phase grating	23
E_{des}	Design energy defined as $E_{des} = hc/\lambda_{des}$	23
τ	Mutual coherence function of the radiation	36
τ_ℓ	Attenuation of the Fourier coefficient due to the mutual coherence function of the radiation	36
T_{12}	Value of the transmission through G_1 and G_2	83

Symbols related to distances

(x, y, z)	Coordinate system of the detector	21
(x_o, y_o, z_o)	Coordinate system fixed to the sample	26
(x_f, y_f, z_f)	Coordinate system fixed to the focal spot	36
$\mathbf{r}$	Vector position defined by coordinate (x,y,z)	20
z_{12}	Distance between gratings G_1 and G_2	31
z_{01}	Distance between gratings G_0 and G_1	33
z_s	Distance between the sample and G_1	34
M_g	Magnification of the gratings' periodicity	33
M_s	Magnification of the sample	34
D_T	Talbot distance equal to $2p_1^2/\lambda_{des}$	22
N	Talbot order defined as $N = 16z_{12}/D_T$	24
D_N	N^{th} fractional Talbot distance $D_N = ND_T/16$	24
d_N	N^{th} fractional Talbot distance corrected for the magnification M_g	33

Symbols related to the x-ray source

λ	Wavelength of the x-ray photons	19
E	Energy of the x-ray photons	4
$\mathcal{S}(\lambda)$	Number of photons emitted by the source at wavelength λ during the exposure time by unit solid angle	39
V_{tube}	Acceleration voltage of the electron beam in the x-ray tube	74

Symbols related to the x-ray detector

p_{pix}	Size of the detector pixel	31
$\mathcal{D}$	Gain of the detector pixel	31
DQE	Detective quantum efficiency	75
$PSF(x, y)$	Point spread function of the detector pixel	31
FPN	Fixed pattern noise of the detector	61
ADU	Arbitrary digital units	61

Symbols related to the wave propagation

$u(\mathbf{r},t)$	Scalar electromagnetic field at position $\mathbf{r}$ and time t	20
$U(\mathbf{r})$	Complex amplitude of the scalar field u($\mathbf{r}$,t)	20
I	Field intensity defined equal to $\lvert U\rvert^2$	21
k	Wave number	20
H_d	Fresnel kernel	21
$_{fr}$	Subscript fr refers to the interference fringes	22
$_{par}$	Subscript *par* refers to the parallel beam case	22
$_{pt}$	Subscript *pt* refers to the point source case	35
$_{pix}$	Subscript *pix* refers to the pixel intensity	31
b_ℓ	Complex Fourier coefficients of intensity I_{fr}	22
p_{fr}	Periodicity of the interference modulations I_{fr}	22
Q_ℓ	Amplitude coefficient of the phase stepping curve	39
ψ_ℓ	Phase coefficient of the phase stepping curve	39
ϑ	Rotation of G_2 with respect to G_1 around the optical axis	108
p_m	Periodicity of the Moiré fringes	110
Ω	Angle of incidence of the x-ray beam onto the gratings	119
Ω_M^i	Angular acceptance of grating G_i	120

Symbols related to the sample

t	Thickness of the sample	59
Z	Atomic number	4
n	Index of refraction $n = 1 - \delta + i\beta$	20
β	Extinction coefficient	20
$\Delta\beta$	Difference of the extinction coefficients between the sample and the medium	84
δ	Refraction coefficient	20
$\Delta\delta$	Difference of the refraction coefficients between the sample and the medium	83
$< E_\delta >$	Effective energy of a measurement δ for polychromatic radiation	102
μ	Linear attenuation coefficient	26
$\delta\mu$	Difference of the linear attenuation coefficients between the sample and the medium	83
$< E_\mu >$	Effective energy of a measurement μ for polychromatic radiation	102
ϵ	Linear scattering coefficient	55
$< E_\epsilon >$	Effective energy of a measurement ϵ for polychromatic radiation	103
O	Amplitude transmission function of the object	25
A	Attenuation function of the sample	25
$\bar{A}$	Attenuation function of the sample after averaging over one pixel	33
Φ	Integrated phase shift due to the sample	25
Φ_s	Part of the phase shift Φ slow compared to p_1	27
Φ_f	Part of the phase shift Φ fast compared to p_1	28
α_s	Angular deviation of the beam due to a phase gradient in Φ_s	27
φ	Phase shift of the interference pattern for monochromatic radiation	27
$\bar{\varphi}$	Phase shift of the interference pattern with pixel averaging	33

ψ	Phase shift of the interference pattern for polychromatic radiation	27
σ_{usas}	Ultra-small angle scattering cross section due to Φ_f	28
ρ	Electronic density	28
$\mathcal{R}$	Autocorrelation function of the electronic density	28
$\sigma^2_{\Phi_s}$	Variance of the fast phase shift variations	29
γ	Normalized autocorrelation function of the phase shift variations	29
S_ℓ	Scattering function for the ℓ coefficient	28
$\bar{S}_\ell$	Scattering function for the ℓ coefficient with pixel averaging	33
Q_ℓ	Fourier amplitude coefficient of the pixel intensity for polychromatic radiation	39
ψ_ℓ	Fourier phase coefficient of the pixel intensity for polychromatic radiation	39
PE	Polyethylene	72
PI	Polyimide	84
PA6	Polycaprolactam	72
PA66	Polyamid 6,6 or nylon	72
PMMA	Polymethyl-methacrylate or plexiglass	72
POM	Polyoxymethylene	72
PTFE	Polytetrafluoroethylene or teflon	72

Symbols related to the image reconstruction

T	Transmission image of the sample	43
$\mathcal{T}$	Normalized transmission image of the sample	52
DP	Differential phase contrast image of the sample	43
$\mathcal{DP}$	Normalized differential phase contrast image of the sample	54
v	Visibility of the phase stepping curve	43
V	Dark field image of the sample	43
$\mathcal{V}$	Normalized dark field image of the sample	55
USAS	Ultra-small angle x-ray scattering	28
FBP	Filtered Back Projection	47
Υ	Rotation angle of the sample compared to the gratings around the optical axis z	114
X_0	Mean of the directional dark field curve	114
X_1	Amplitude of the directional dark field curve	114
Λ_1	Phase of the directional dark field curve	114
$F = X_1/X_0$	Degree of anisotropy of the directional dark field curve	115

χ	Translation of the interference fringes along the x-direction	40
θ	Angle of projections during a tomographic acquisition	47
p_θ	Projection of a three-dimensional object onto a flat panel detector under angle θ	47
q_θ	Filtered projection of a three-dimensional object onto a flat panel detector under angle θ	50

Symbols related to the experimental bench

CAD	Computer Assisted Design	88
Tx_s	Translation of the sample along direction x	91
Ty_s	Translation of the sample along direction y	91
Ry_s	Rotation of the sample around direction y	91
Tx_{sr}	Translation of the source grating along direction x	91
Tz_g	Translation of grating G_2 along direction z	91
Rz_g	Rotation of the grating G_1 around direction z	91
VI	Virtual Instrument developed in NI Labview	93

Symbols related to the noise and artifacts

$_{det}$	Subscript *det* refers to the noise contributions from the detector	73
$_{jitter}$	Subscript *jitter* refers to the noise contributions from the mechanical jitter of the phase stepping stage	73
$\bar{X}$	Mean of variable X	73
σ_X	Standard deviation of variable X	73
SNR_X	Signal to noise ratio of variable X	75
CNR_X	Contrast to noise ratio of variable X of a given feature within a background medium	101
R	Penalization of phase contrast versus absorption imaging due to scattering samples	84

BIBLIOGRAPHY

[Als-Nielsen & McMorrow 2001] J. Als-Nielsen and D. McMorrow. Elements of modern x-ray physics. Wiley, Chichester, 2001.

[Arrizòn & Ojeda-Castaeda 1994] V. Arrizòn and J. Ojeda-Castaeda. *Multilevel phase gratings for array illuminators*. Appl. Opt., vol. 33, no. 25, page 5925, 1994.

[Arrizòn & Rojo-Velazquez 2001] Victor Arrizòn and Gustavo Rojo-Velazquez. *Fractional Talbot field of finite gratings: compact analytical formulation*. J. Opt. Soc. Am. A, vol. 18, no. 6, pages 1252–1256, 2001.

[Bech *et al.* 2010] M. Bech, O. Bunk, R. Feidenhans'l, C. David and F. Pfeiffer. *Quantitative x-ray dark-field computed tomography*. Phys. Med. Biol., vol. 55, pages 5529–5539, 2010.

[Berger *et al.*] M.J. Berger, J.H. Hubbell, S.M. Seltzer, J. Chang, J.S. Coursey, R. Sukumar, D.S. Zucker and K. Olsen. *XCOM: Photon Cross Sections Database*. Rapport technique, National Institute of Standards and Technology.

[Berry & Klein 1996] M. V. Berry and S. Klein. *Integer, fractional and fractal Talbot effects*. Journal of Modern Optics, vol. 43, pages 2139–2164, 1996.

[Berry *et al.* 2001] M. Berry, I. Marzoli and W. Schleich. *Quantum carpets, carpets of light*. Physics World, vol. 1, page 1, June 2001.

[Bonse & Hart 1965] U. Bonse and M Hart. *An x-ray interferometer*. Appl. Phys. Lett., vol. 6, pages 155–156, 1965.

[Bronnikov 2002] A. Bronnikov. *Theory of quantitative phase-contrast computed tomography*. J. Opt. Soc. Am. A, vol. 19, no. 3, pages 472–480, March 2002.

[Bronshtein *et al.* 2003] I. N. Bronshtein, K. A. Semendyayuv, G. Musiol and H. Muehlig. Handbook of mathematics, 4th ed. Springer, Berlin, 2003.

[Bunk *et al.* 2009] O. Bunk, M. Bech, T. Jensen, R. Feldenhans'l, T. Blnderup, A. Menzel and F. Pfeiffer. *Multimodal x-ray scatter imaging.* New Journal of Physics, vol. 11, page 123016, 2009.

[Buzug 2008] Thorsten M. Buzug. Computed tomography : From photon statistics to modern cone-beam ct. Springer, Berlin, 2008.

[Byrne 2007] C. L. Byrne. Applied iterative methods. CRC Press, 2007.

[Chabior *et al.* 2011] M. Chabior, T. Donath, C. David, O. Bunk, M. Schuster, C. Schroer and F. Pfeiffer. *Beam hardening effects in grating-based x-ray phase-contrast imaging.* Med. Phys., vol. 38, pages 1189–1195, 2011.

[Chapman *et al.* 1997] D. Chapman, W. Thomlinson, R. Johnston, D. Washburn, E. Pisano, N. Gmur, Z. Zhong, R. Menk, F. Arfelli and D. Sayers. *Diffraction enhanced x-ray imaging.* Phys. Med. Biol., vol. 42, pages 2015–2025, 1997.

[Chen *et al.* 2010] G-H Chen, N. Bevins, J. Zambelli and Z. Qi. *Small-angle scattering computed tomography (SAS-CT) using a Talbot-Lau interferometer and a rotating anode x-ray tube: theory and experiments.* Optics Express, vol. 18, pages 12960–12970, 2010.

[Christie & Cameron 1994] Ian. R. Christie and Brian P. Cameron. *Gold Deposition within the Electronics Industry.* Gold Bull., vol. 27, page 12, 1994.

[Clauser 1998] J. F. Clauser. *Ultrahigh resolution interferometric x-ray imaging.* Rapport technique, US Patent 5 812 629, 1998.

[Cloetens *et al.* 1996] P. Cloetens, R. Barrett, J. Baruchel, J.P. Guigay and M. Schlenker. *Phase objects in synchrotron radiation hard x-ray imaging.* J. Phys. D: Appl.Phys, vol. 29, pages 133–146, 1996.

[Coolidge 1916] William Coolidge. *Vacuum Tube.* Rapport technique, US Patent, 1916.

[Cormack 1963] Allen M. Cormack. *Representation of a function by its line integrals, with some radiological applications.* J. Applied Physics, vol. 34, page 2722, 1963.

[Cunningham *et al.* 1994] I. A. Cunningham, M. S. Westmore and A. Fenster. *A spatial-frequency dependent quantum accounting diagram and detective quantum efficiency model of signal to noise propagation in cascaded imaging systems.* Med. Phys., vol. 21, pages 417–427, 1994.

[David & Pfeiffer 2008] C. David and F. Pfeiffer. *X-ray interferometer for phase contrast imaging.* Rapport technique, European Patent EP1879020A1, 2008.

[David & Weitkamp 2006] C. David and T. Weitkamp. *Interferometer for Quantitative Phase Contrast Imaging and Tomography with an incoherent polychromatic x-ray source.* Rapport technique, European Patent EP1731099A1, 2006.

[David *et al.* 2002] C. David, B. Nöhammer and H. H. Solak. *Differential x-ray phase contrast imaging using a shearing interferometer.* Appl. Phys. Letters, vol. 81, pages 3287–3289, 2002.

[David *et al.* 2007] C. David, J. Bruder, T. Rohbeck, C. Grünzweig, C. Kottler, A. Diaz, O. Bunk and F. Pfeiffer. *Fabrication of diffraction gratings for hard X-ray phase contrast imaging.* Microelectronic Engineering, vol. 84, pages 1172–1177, February 2007.

[Donath *et al.* 2009] T. Donath, F. Pfeiffer, O. Bunk, W. Groot, M. Bednarzik, C. Grünzweig, E. Hempel, S. Popescu, M. Hoheisel and C. David. *Phase-contrast imaging and tomography at 60 keV using a conventional x-ray tube source.* Rev. Sci. Instrum., vol. 80, page 053701, 2009.

[Engelhardt *et al.* 2007] M. Engelhardt, J. Baumann, M. Schuster, C. Kottler, F. Pfeiffer, O. Bunk and C. David. *High-resolution differential phase contrast imaging using a magnifying projection geometry with a microfocus x-ray source.* Appl. Phys. Letters, vol. 90, page 224101, May 2007.

[Engelhardt 2008] M. Engelhardt. *Neue Verfahren in der Mikrofokus-Röntgen Radiographie und Computertomographie: Phasenkontrastbildgebung und Abbildung der Brennfleckintensitätsverteilung New techniques in microfocus x-ray radiography and computed tomography: Phase contrast imaging and determination of the focal spot intensity distribution.* PhD thesis, Technische Universität München, 2008.

[Faris & Byer 1988] G. W. Faris and R. L. Byer. *Three-dimensional beam-deflection optical tomography of a supersonic jet.* Appl. Opt., vol. 27, pages 5202–5212, 1988.

[Feldkamp *et al.* 1984] L. A. Feldkamp, L. C. Davis and J. W. Kress. *Practical cone-beam algorithm.* J. Opt. Soc. Am. A, vol. 1, no. 6, pages 612–619, Jun 1984.

[Goodman 2005] Joseph W. Goodman. Introduction to fourier optics. Roberts & Company, 2005.

[Gourrier *et al.* 2010] Aurélien Gourrier, Chenghao Li, Stefan Siegel, Oskar Paris, Paul Roschger, Klaus Klaushofer and Peter Fratzl. *Scanning small-angle X-ray scattering analysis of the size and organization of the mineral nanoparticles in fluorotic bone using a stack of cards model.* Journal of Applied Crystallography, vol. 43, no. 6, pages 1385–1392, Dec 2010.

[Hecht 2002] E. Hecht. Optics. Pearson, 2002.

[Hendee & Morgan 1984] W.R. Hendee and C.J. Morgan. *Magnetic Resonance Imaging Part I - Physical Principles.* West Journal of Medicine, vol. 141, pages 491–500, 1984.

[Hounsfield & Ambrose 1973] G. N. Hounsfield and J. Ambrose. *Computerized transverse axial scanning (tomography).* British Journal of Radiology, vol. 46, pages 1016–1027, 1973.

[Hounsfield 1972] G. N. Hounsfield. *A method of and apparatus for measuring X or gamma radiation.* In UK Patent 1283915, 1972.

[Ingal & Beliaevskaya 1995] V. N. Ingal and E. A. Beliaevskaya. *X-ray plane-wave topography observation of the phase contrast from a non-crystalline object.* J. Phys. D Appl. Phys., vol. 28, pages 2314–2317, 1995.

[Isola *et al.* 2010] A.A. Isola, A. Ziegler, D. Schäfer, T. Köhler, W.J. Niessen and M. Grass. *Motion compensated iterative reconstruction of a region of interest in cardiac cone-beam CT.* Computerized Medical Imaging and Graphics, vol. 34, no. 2, pages 149 – 159, 2010.

[Jackson 1999] J. D. Jackson. Classical electrodynamics, third edition. John Wiley & Sons, Inc., 1999.

[Jensen *et al.* 2010] T. H. Jensen, M. Bech, O. Bunk, T. Donath, C. David, R. Feidenhans'l and F. Pfeiffer. *Directional x-ray dark-field imaging.* Phys. Med. Biol., vol. 55, pages 3317–3323, 2010.

[Jerjen *et al.* 2010] I. Jerjen, V. Revol, C. Kottler, R. Kaufmann, T. Lüthi and U. Sennhauser. *Phase Contrast Cone Beam Tomography with an X-Ray Grating Interferometer.* Proceedings of the International Conference on Advanced Phase Measurement Methods in Optics and Imaging, vol. 1236, pages 227–231, 2010.

[Jerjen *et al.* 2011] Iwan Jerjen, Vincent Revol, Philipp Schuetz, Christian Kottler, Rolf Kaufmann, Thomas Luethi, Konstantins Jefimovs, Claus Urban and Urs Sennhauser. *Reduction of phase artifacts in differential phase contrast computed tomography.* Opt. Express, vol. 19, no. 14, pages 13604–13611, Jul 2011.

[Kak & Slaney 1999] Avinash C. Kak and Malcolm Slaney. Principles of computerized tomographic imaging. IEEE Press, 1999.

[Kendall 1979] Don. L. Kendall. *Vertical Etching of Silicon at Very High Aspect Ratios*. Ann. Rev. Mater. Sci., vol. 9, pages 373–403, 1979.

[Kitchen *et al.* 2007] M.J. Kitchen, K.M. Pavlov, K.K. Siu, R. Menk, G. Tromba and R.A. Lewis. *Analyser-based phase contrast image reconstruction using geometrical optics*. Phys. Med. Biol., vol. 52, pages 4171–4187, 2007.

[Kitchen *et al.* 2008] Marcus J. Kitchen, Konstantin M. Pavlov, Stuart B. Hooper, David J. Vine, Karen K.W. Siu, Megan J. Wallace, Melissa L.L. Siew, Naoto Yagi, Kentaro Uesugi and Rob A. Lewis. *Simultaneous acquisition of dual analyser-based phase contrast X-ray images for small animal imaging*. European Journal of Radiology, vol. 68, no. 3, Supplement 1, pages S49 – S53, 2008. Proceedings of the 5th Medical Application of Synchrotron Radiation 2007.

[Kitchen *et al.* 2011] Marcus J Kitchen, David M Paganin, Kentaro Uesugi, Beth J Allison, Robert A Lewis, Stuart B Hooper and Konstantin M Pavlov. *Phase contrast image segmentation using a Laue analyser crystal*. Physics in Medicine and Biology, vol. 56, no. 3, page 515, 2011.

[Kottler & Kaufmann 2009] C. Kottler and R. Kaufmann. *Interferometer device and method*. Rapport technique, European Patent EP 2 060 909 A1, 2009.

[Kottler *et al.* 2007a] C. Kottler, C. David, F. Pfeiffer and O. Bunk. *A two-directional approach for grating based differential phase contrast imaging using hard x-rays*. Optics Express, vol. 15, no. 3, pages 1175–1181, February 2007.

[Kottler *et al.* 2007b] C. Kottler, F. Pfeiffer, O. Bunk, C. Grünzweig, J. Bruder, R. Kaufmann, L. Tlustos, H.Walt, I. Briod, T. Weitkamp and C. David. *Phase contrast X-ray imaging of large samples using an incoherent laboratory source*. Physica Status Solidi (a), vol. 204, no. 8, page 2728?2733, August 2007.

[Kottler *et al.* 2007c] C. Kottler, F. Pfeiffer, O. Bunk, C. Grünzweig and C. David. *Grating interferometer based scanning setup for hard x-ray phase contrast imaging*. Rev. Sci. Instrum., vol. 78, no. 043710, page 043710, April 2007.

[Kottler *et al.* 2010a] C. Kottler, V. Revol, R. Kaufmann, K. Knop, U. Sennhauser, I. Jerjen, T. Lüthi, F. Cardot, P. Niedermann, J-P. Morel, C. Maake, H. Walt, E. Knop and N. Blanc. *Phase Sensitive Imaging: Towards its interdisciplinary applications*. Proceedings of the

International Conference on Advanced Phase Measurement Methods in Optics and Imaging - AIP Proceedings, vol. 1236, pages 213–218, 2010.

[Kottler *et al.* 2010b] C. Kottler, V. Revol, R. Kaufmann and C. Urban. *Dual Energy Phase Contrast X-ray Imaging with Talbot-Lau Interferometer.* J. Appl. Phys., vol. 108, page 114906, 2010.

[Kottler *et al.* 2010c] C. Kottler, V. Revol, C. Maake, R. Kaufmann and C. Urban. *Phase sensitive X-ray imaging: Towards medical applications.* In IEEE Medical Imaging Conference Record (NSS/MIC), 2010.

[Krejci *et al.* 2010a] Frantisek Krejci, Jan Jakubek and Martin Kroupa. *Hard x-ray phase contrast imaging using single absorption grating and hybrid semiconductor pixel detector.* Rev. Sci. Instrum., vol. 81, page 113702, 2010.

[Krejci *et al.* 2010b] Frantisek Krejci, Jan Jakubek and Martin Kroupa. *Low dose X-ray phase contrast imaging sensitive to phase effects in 2-D.* In Conference Record IEEE Medical Imaging Conference, 2010.

[Krestel 1990] E. Krestel. Imaging systems for medical diagnostics: Fundamentals, technology, image quality. Siemens/Publicis, 1990.

[Lang 1996] Walter Lang. *Silicon microstructuring technology.* Materials Science and Engineering R, vol. 17, pages 1–55, 1996.

[Lewis *et al.* 2005] R A Lewis, N Yagi, M J Kitchen, M J Morgan, D Paganin, K K W Siu, K Pavlov, I Williams, K Uesugi, M J Wallace, C J Hall, J Whitley and S B Hooper. *Dynamic imaging of the lungs using x-ray phase contrast.* Phys. Med. Biol., vol. 50, no. 21, pages 5031–5040, 2005.

[Lohmann & Silva 1971] A.W. Lohmann and D.E. Silva. *An interferometer based on the Talbot effect.* Optics Communications, vol. 2, no. 9, pages 413 – 415, 1971.

[Momose *et al.* 1996] A. Momose, T. Takeda, Y. Itai and K. Hirano. *Phase-contrast X-ray computed Tomography for observing biological soft tissues.* Nature Medicine, vol. 2, no. 4, pages 473–475, April 1996.

[Momose *et al.* 2001] A. Momose, T. Takeda, A. Yoneyama, I. Koyama and Y. Itai. *Phase-Contrast X-Ray Imaging Using an X-Ray Interferometer for Biological Imaging.* Analytical Sciences, vol. 17, no. supplement, pages 6355–6367, October 2001.

[Momose *et al.* 2008] A. Momose, W. Yashiro and Y. Takeda. *Sensitivity of X-ray Phase Imaging Based on Talbot Interferometry.* Jpn. J. Appl. Phys., vol. 47, pages 8077–8080, 2008.

[Momose *et al.* 2009] A. Momose, W. Yashiro, H. Maikusa and Y. Takeda. *High-speed X-ray phase imaging and X-ray phase tomography with Talbot interferometer and white synchrotron radiation.* Optics Express, vol. 17, page 12540, 2009.

[Momose 1995] A. Momose. *Demonstration of phase-contrast X-ray computed tomography using an X-ray interferometer.* Nuclear Instruments and Methods in Physics Research Section A: Accelerators, Spectrometers, Detectors and Associated Equipment, vol. 352, no. 3, pages 622 – 628, 1995.

[Momose 2003] A. Momose. *Phase-sensitive imaging and phase tomography using X-ray interferometers.* Opt. Express, vol. 11, page 2303, 2003.

[Momose 2005] A. Momose. *Recent Advances in X-ray Phase Imaging.* Jap. Journal Appl. Phys., vol. 44, no. 9A, pages 6355–6367, 2005.

[Newport] Newport. Technical data sheet of the linear stage uts.

[Nob 1967] Nobel lectures, physics 1901-1921. Elsevier Publishing Company, 1967.

[Nugent *et al.* 1996] K.A Nugent, T.E. Gureyev, D.F. Cookson, D. Paganin and Z. Barnea. *Quantitative Phase Imaging Using Hard X Rays.* Physical Review Letters, vol. 77, no. 14, pages 2961–2964, September 1996.

[Okunade 2002] Akintunde Akangbe Okunade. *Numerical models for comparing filter materials for diagnostic radiology.* Radiation Physics and Chemistry, vol. 65, no. 1, pages 1 – 9, 2002.

[Olivo & Speller 2007a] A. Olivo and R. Speller. *A coded-aperture technique allowing x-ray phase contrast imaging with conventional sources.* Applied Physics Letters, vol. 91, page 074106, 2007.

[Olivo & Speller 2007b] A. Olivo and R. Speller. *Modelling of a novel x-ray phase contrast imaging technique based on coded apertures.* Phys. Med. Biol., vol. 52, pages 6555–6573, 2007.

[Olivo *et al.* 2009] A Olivo, S.E. Bohndiek, J.A. Griffiths, A. Konstantinidis and R Speller. *A non-free-space propagation x-ray phase contrast imaging method sensitive to phase effects in two directions simultaneously.* Appl. Phys. Letters, vol. 94, page 044108, 2009.

[Pan & Kak 1983] S. X. Pan and A. C. Kak. *A computational study of reconstruction algorithms for diffraction tomography: Interpolation vs. filtered-backprojection.* IEEE Trans. Acoust. Speech Signal Processing, vol. ASSP-31, pages 1262–1275, 1983.

[Pfeiffer *et al.* 2006] F. Pfeiffer, T. Weitkamp, O. Bunk and C. David. *Phase retrieval and differential phase-contrast imaging with low-brilliance X-ray sources.* Nature Physics, vol. 2, pages 258 – 261, March 2006.

[Pfeiffer *et al.* 2007] F. Pfeiffer, C. Kottler, O. Bunk and C. David. *Hard X-Ray Phase Tomography with Low-Brilliance Sources.* Physical Review Letters, vol. 98, no. 10, pages 108105/1–4, March 2007.

[Pfeiffer *et al.* 2008] F. Pfeiffer, M. Bech, O. Bunk, P. Kraft, E. Eikenberry, Ch. Brönnimann, C. Grünzweig and C. David. *Hard-X-ray dark-field imaging using a grating interferometer.* Nature Materials, vol. 7, pages 134–137, February 2008.

[Poludniowski *et al.* 2009] G Poludniowski, G Landry, F DeBlois, P M Evans and F Verhaegen. *SpekCalc : a program to calculate photon spectra from tungsten anode x-ray tubes.* Physics in Medicine and Biology, vol. 54, no. 19, page N433, 2009.

[Rabbani *et al.* 1987] M. Rabbani, R. Shaw and R. Van Metter. *Detective quantum efficiency of imaging systems with amplifying and scattering mechanisms.* J. Opt. Soc. Am. A, vol. 4, pages 895–901, 1987.

[Radon 1986] Johann Radon. *On the Determination of Functions From Their Integral Values Along Certain Manifolds.* Medical Imaging, IEEE Transactions on, vol. MI-5, pages 170–176, 1986.

[Revol *et al.* 2010a] V. Revol, C. Kottler, R. Kaufmann, F. Cardot, P. Niedermann, I. Jerjen, T. Lüthi, U. Straumann, U. Sennhauser and C. Urban. *Sensing Small Angle Scattering with an X-ray Grating Interferometer.* In Nuclear Science Symposium Conference Record (NSS/MIC), 2010.

[Revol *et al.* 2010b] V. Revol, C. Kottler, R. Kaufmann, I. Jerjen, T. Lüthi, F. Cardot, P. Niedermann, U. Sennhauser, U. Straumann and C. Urban. *Application-Oriented X-ray Grating Interferometer.* Proceedings of the International Conference on Advanced Phase Measurement Methods in Optics and Imaging - AIP Proceedings, vol. 1236, pages 221–225, 2010.

[Revol *et al.* 2010c] V. Revol, C. Kottler, R. Kaufmann, U. Straumann and C. Urban. *Noise Analysis of Grating-Based X-ray Differential Phase Contrast Imaging.* Rev. Sci. Instrum., vol. 81, page 073709, 2010.

[Revol *et al.* 2011a] V. Revol, I. Jerjen, C. Kottler, P. Schütz, R. Kaufmann, T. Lüthi, U. Sennhauser, U. Straumann and C. Urban. *Sub-Pixel Porosity Revealed by X-Ray Scatter Dark Field Imaging.* J. Appl. Phys., vol. 110, page 044912, 2011.

[Revol *et al.* 2011b] Vincent Revol, Christian Kottler, Rolf Kaufmann, Iwan Jerjen, Thomas Lüthi, Francis Cardot, Philippe Niedermann, Ulrich Straumann, Urs Sennhauser and Claus Urban. *X-ray interferometer with bent gratings: Towards larger fields of view.* Nuclear Instruments and Methods in Physics Research Section A: Accelerators, Spectrometers, Detectors and Associated Equipment, vol. 648, no. Supplement 1, pages S302 – S305, 2011. NIMA 4th International Conference on Imaging techniques in Subatomic Physics, Astrophysics, Medicine, Biology and Industry.

[Röntgen 1896] W. Röntgen. *On a New Kind of Rays.* Nature, vol. 53, pages 274–276, 1896.

[Rosenfeld & Kak 1982] A. Rosenfeld and Avinash C. Kak. Digital picture processing, 2nd ed. New York, N.Y. Academic Press, 1982.

[Sandborg *et al.* 1994] M. Sandborg, C. Carlsson and G. Carlsson. *Shaping X-ray spectra with filters in x-ray diagnostics.* Med. & Biol. Eng. & Comput., vol. 32, pages 384–390, 1994.

[Snigirev *et al.* 1995] A. Snigirev, I. Snigireva, V. Kohn, S. Kuznetsov and I. Schelokov. *On the possibilities of x-ray phase contrast microimaging by coherent high-energy synchrotron radiation.* Review of Scientific Instruments, vol. 66, page 5486, 1995.

[Takeda *et al.* 1982] M. Takeda, H. Ina and S. Kobayashi. *Fourier-transform method of fringe-pattern analysis for computer-based topography and interferometry.* J. Opt. Soc. Am., vol. 72, pages 156–160, 1982.

[Takeda *et al.* 2000] T. Takeda, A. Momose, K. Hirano, S. Haraoka, T. Watanabe and Y. Itai. *Human Carcinoma: Early Experience with Phase-Contrast X-ray CT with Synchrotron Radiation - Comparative Specimen Study with Optical Microscopy.* Radiology, vol. 214, no. 1, pages 298–301, July 2000.

[Takeda *et al.* 2007] Y. Takeda, W. Yashiro, Y. Suzuki, S. Aoki, T. Hattori and A. Momose. *X-Ray Phase Imaging with Single Phase Grating.* Jpn. J. Appl. Phys., vol. 46, pages L89–L91, 2007.

[Talbot 1836] H. F. Talbot. *Facts relating to optical science.* Philos. Mag., vol. 9, 1836.

[Trtik *et al.* 2011] P. Trtik, B. Münch, W.J. Weiss, A. Kaestner, I. Jerjen, L. Josic, E. Lehmann and P. Lura. *Release of internal curing water from lightweight aggregates in cement paste investigated by neutron and X-ray tomography.* Nuclear Instruments and Methods in Physics Research Section A: Accelerators, Spectrometers, Detectors and Associated Equipment, vol. In Press, Corrected Proof, pages –, 2011.

[Tuohima 2007] H.M. Hertz Tuohima M. Otendal. *Phase-contrast x-ray imaging with a liquid-metal-jet-anode microfocus source.* Appl. Phys. Letters, vol. 91, page 174104, August 2007.

[Weitkamp *et al.* 2005] T. Weitkamp, A. Diaz, C. David, F. Pfeiffer, M. Stampanoni, P. Cloetens and E. Ziegler. *X-ray phase imaging with a grating interferometer.* Optics Express, vol. 13, no. 16, pages 6296–6304, August 2005.

[Weitkamp *et al.* 2006] T. Weitkamp, C. David, C. Kottler, O. Bunk and F. Pfeiffer. *Tomography with grating interferometers at low-brilliance sources.* Proc. SPIE, vol. 6318, pages 1–10, 2006.

[Wen *et al.* 2008] H. Wen, E. E. Bennett, M. Hegedus and S. Carroll. *Spatial Harmonic Imaging of X-ray Scattering: Initial Results.* IEEE Trans. on Med. Imaging, vol. 27, pages 997–1002, 2008.

[Wen *et al.* 2009] H. Wen, E. E. Bennett, M. Hegedus and S. Rapacchi. *Fourier X-ray Scattering Radiography Yields Bone Structural Information.* Radiology, vol. 251, pages 910–918, 2009.

[Wen *et al.* 2010] H. H. Wen, E. E. Bennett, R. Kopace, A. F. Stein and V. Pai. *Single-shot x-ray differential phase-contrast and diffraction imaging using two-dimensional transmission gratings.* Optics Letters, vol. 35, pages 1932–1934, 2010.

[Wernick *et al.* 2003] M. Wernick, O. Wirjadi, D. Chapman, Z. Zhong, N. Galatsanos, Y. Yang, J. Brankov, O. Oltulu, M. Anastasio and C. Muehleman. *Multiple-image radiography.* Phys. Med. Biol., vol. 48, pages 3875–3895, 2003.

[Wijesekera *et al.* 2010] Nevin T. Wijesekera, Mark K. Duncan and Simon P. G. Padley. *X-ray computed tomography of the heart.* British Medical Bulletin, vol. 93, no. 1, pages 49–67, 2010.

[Wilkins *et al.* 1996] S.W. Wilkins, T.E. Gureyev, D. Gao, A. Pogany and A.W. Stevenson. *Phase-contrast imaging using polychromatic hard X-Rays.* Nature, vol. 384, pages 335–338, November 1996.

[Winthrop & Worthington 1965] John T. Winthrop and C. R. Worthington. *Theory of Fresnel Images. I. Plane Periodic Objects in Monochromatic Light.* J. Opt. Soc. Am., vol. 55, pages 373–381, 1965.

[Yashiro *et al.* 2008] W. Yashiro, Y. Takeda and A. Momose. *Efficiency of capturing a phase image using conebeam x-ray Talbot interferometry.* J. Opt. Soc. Am. A, vol. 25, page 2025, 2008.

[Yashiro *et al.* 2010] W. Yashiro, Y. Terui, K. Kawabata and A. Momose. *On the origin of visibility contrast in x-ray Talbot interferometry.* Opt. Express, vol. 18, pages 16890–16901, 2010.

[Yoneyama *et al.* 2002] A. Yoneyama, A. Momose, I. Koyama, E. Seya, T. Takeda, Y. Itai, K. Hirano and K. Hyodo. *Large-area phase-contrast X-ray imaging using a two-crystal X-ray interferometer.* J. Synchrotron Radiation, vol. 9, pages 277–281, July 2002.

[Zanette *et al.* 2010] I. Zanette, T. Weitkamp, T. Donath, S. Rutishauser and C. David. *Two-Dimensional X-Ray Grating Interferometer.* Physical Review Letters, vol. 105, page 248102, 2010.

[Zauner 2006] Rudolf Zauner. *Micro powder injection moulding.* Microelectronic Engineering, vol. 83, no. 4-9, pages 1442 – 1444, 2006. Micro- and Nano-Engineering MNE 2005.

[Zernike 1934] F. Zernike. *Diffraction Theory of the Knife-Edge Test and its Improved Form, the Phase-Contrast Method.* Monthly Notices of the Royal Astronomical Society, vol. 94, pages 377–384, 1934.

[Zhu *et al.* 2010] P. Zhu, K. Zhang, Z. Wang, Y. Liu, Z. Wu, S. MacDonald, F. Marone and M. Stampanoni. *Low-dose, simple, and fast grating-based X-ray phase-contrast imaging.* Proc. Nation. Acad. Sci. USA, vol. 107, pages 13576–13581, 2010.

[Zweig 1965] H. J. Zweig. *Detective Quantum Efficiency of Photodetectors with some Amplification Mechanisms.* J. Opt. Soc. Am., vol. 55, pages 525–528, 1965.

CURRICULUM VITAE

Vincent Marcel Revol
Born 18. March 1984 in Grenoble, France
French Citizen

Education

1998 - 2001	Lycée B. De Laffemas, Valence, France
2001 - 2003	"Classes Préparatoires", Lycée Le Parc, Lyon, France Prepare entrance exams for French engineering schools
2003 - 2006	Ecole Polytechnique, Paris, France Majors in Electrical Engineering and Physics
2006	Diploma work at the Spintec laboratory of the Commissariat l'Energie Atomique (CEA), Grenoble, France "Chauffage Dynamique de Jonctions Tunnel Magnétiques"
2006 - 2007	Stanford University, United States of America Studies in Electrical Engineering
2007	Diploma work at the Center for Magnetic Nanotechnology, Stanford University, United States of America "Spin-valve based Current Transformer / Voltage Transformer"
2008 - 2011	PhD student in Physics at the University of Zürich and at the Centre Suisse d'Electronique et Microtechnique (CSEM)

Qualifications

2001	French Baccalaureate Type S (with very high honors)
2008	Master of Science in Electrical Engineering from the Stanford University (GPA 4.0 out of 4.0)
2008	Diplôme de l'Ecole Polytechnique (equivalent Master of Science)